University of Alberta

The Experimental Investigation of Vortex Wakes from Oscillating Airfoils

by

Mathew Bussière

A thesis submitted to the Faculty of Graduate Studies and Research
in partial fulfillment of the requirements for the degree of

Master of Science

Department of Mechanical Engineering

Fall 2012
Edmonton, Alberta

ABSTRACT

The ability to actively control large coherent vortices in the wake of an unsteady body is studied experimentally. This thesis initially considers a single airfoil in a uniform flow that is forced to oscillate sinusoidally about its aerodynamic center. The resulting wake is expected to be dominated by large coherent vortices (Bohl & Koochesfahani, 2009), (Schnipper, Andersen, & Bohr, 2009), (Jung & Park, 2005), (Godoy-Diana, Marais, Aider, & Wesfreid, 2009), (Gopalkrishnan, Triantafyllou, Triantafyllou, & Barrett, 1994). The wakes for several different oscillation waveforms are studied and a model describing the evolution of the vortices as they progress downstream is developed and compared to the experimental data. The investigation then expands to 2 airfoils in a tandem configuration where the upstream airfoil produces a predictable and well studied wake which the downstream airfoil attempts to modify in some prescribed manner. To interpret the resulting velocity field in both cases, custom vortex detection software is developed so that vortices may be accurately identified and characterized. The experiments take place in a re-circulating water channel and flow measurements are undertaken primarily using the particle image velocimetry (PIV) measurement technique. The vortex detection algorithm must, therefore, accommodate experimental PIV velocity vector fields. Given the large number of vector fields that are to be investigated, the detection algorithm should proficiently and automatically reject false vortices with minimal human intervention.

ACKNOWLEDGMENTS

I would like to thank my supervisor Dr. David Nobes for his support, patience and guidance and for providing me with a rich and rewarding academic experience. I would also like to thank my co-supervisor Dr. Bob Koch for his wisdom, and knowledge. David and Bob have participated in this project with much interest and enthusiasm and have inspired and motivated me.

My thanks and appreciation to Bernie Faulkner and Rick Conrad who have generously given their time and expertise to better my work. I thank them for their contribution and their good-natured support.

I must acknowledge my friends and colleagues,: Mona Abdorazaghi, Kevin Breton, Braden Rooke, Masoud Mashkournia, Mehdi Rezaei Saray, Debjyoti Sen, Miguel Balzán, David Terrien, Mark Roes, Joel Cadrin, Michel Godbout, Olivier Creurer, Rouzbeh Ghazi, Aleksey Baldygin, Mohammad Mahmoudi, Alireza Setayeshgar, Luis Ferraz, Richard Groulx, Chad Gawad, and Philipp Brändle who have all assisted, advised, and supported my research and writing efforts during this time, and also the Morrissette family for their support and genuine interest in my studies over the years.

A sincere thank you to Lisa Ulliac for her love, support and endless patience; and my brother Stéphane Bussière who's passion for engineering and science continues to inspire me.

Finally I wish to thank my parents whose boundless love and support has allowed me to pursue my wildest dreams.

TABLE OF CONTENTS

CHAPTER 1: Introduction 1

1.1 Motivation 1

1.2 Summary / thesis outline 4

CHAPTER 2: Experimental procedure 6

2.1 Introduction 6

2.2 Flow facility 6

2.3 Airfoil and support apparatus 12

2.3.1 Stepper motor control 15

2.3.2 Angular position trigger signal 16

2.4 PIV Method 17

2.4.1 Particle image velocimetry (PIV) 17

2.4.2 Imaging system 18

2.4.3 Calibration 22

2.4.4 Optimization of Δt 24

2.4.5 Image pre-Processing 24

2.4.6 Vector field correlation 26

2.4.7 Vector field post-processing 29

2.4.8 Vector field stitching 31

2.4.9 Measurement uncertainties 32

2.5 Summary 34

CHAPTER 3: Vortex detection and characterization 36

3.1 Introduction 36

3.1.1 Approaches to Vortex Detection 38

3.2 Development of a vortex detection algorithm 41

3.2.1 Maximum vorticity (MV) method 41

3.2.2 Cross sectional lines (CSL) method 47

3.2.3 Winding angle (WA) method 52

3.2.4 Other methods 61

3.2.5 The combinatorial vortex detection (CVD) method 63

3.3 Verification on a simulated flow field 66

3.4 Experimental Method 77

3.5 Results 78

3.5.2 WA: to detect errors in WA and CSL 82

3.5.3 Vorticity profiles 86

3.5.4 Circumferential velocity profiles 88

3.6 Conclusions 93

CHAPTER 4: Wake characteristics of an oscillating airfoil 95

4.1 Introduction 95

4.2 Background 100

4.3 Wake classification 109
  4.3.1 Flow visualization of the wake 109
  4.3.2 Phase diagram 113
4.4 Wake characterization of select regimes 118
  4.4.1 Wake arrangement 118
  4.4.2 Phase average vortex cross-sectional study 121
  4.4.3 Wake profiles 129
  4.4.4 Limitations of using phase-averaged fields 133
  4.4.5 Initial circulation estimates 136
  4.4.6 Detailed wake investigation 138
4.5 Conclusions 177

CHAPTER 5: Vortex interaction and wake characteristics of two oscillating airfoils in tandem 180

5.1 Introduction 180
5.2 Background 181
5.3 Experimental Procedure 185
5.4 Vortex characterization 190
  5.4.1 Single airfoil (forefoil) 191
  5.4.2 Tandem configuration 194
5.5 Differential pressure 208

5.5.1 Signal processing 208

5.5.2 Pressure signal 209

5.6 Conclusions.. 213

CHAPTER 6: Conclusions and future work 214

6.1 Summary 214

6.2 Future work.. 217

APPENDIX A: Instantaneous streaklines 226

APPENDIX B: Wake model calculations 239

APPENDIX C: Matlab Code 245

LIST OF TABLES

Table 2.1: Stepper motor specifications 16

Table 3.1: Comparison of physical quantity (PQ) and geometric vortex detection methods 63

Table 3.2: Grid resolution thresholds for simulated flow field 72

Table 3.3: Noise thresholds for simulated flow field 75

Table 4.1: Classification, St_d and A_d for various wake schemes 115

Table 4.2: Initial circulation estimates Γ_o for select wake types 137

Table 4.3:Summary of fit functions and coefficients for the 2S_vK wake from case A_1 151

Table 4.4: Summary of fit functions and coefficients for the 2S_A wake 161

Table 4.5:Summary of fit functions and coefficients for the 2S_ivK wake 170

Table 4.6: Summary of important wake parameters for the 2S_vK, 2S_ivK and the 2S_A wakes 176

Table C.1: Matlab code summary and description 245

LIST OF FIGURES

Figure 2.1: Flow facility and experimental setup panoramic photograph 7

Figure 2.2: Schematic of recirculating water channel (Top) 8

Figure 2.3: Flow facility component photographs. (a) centrifugal pump, (b) entrance plenum straightening veins.. 9

Figure 2.4: Flow facility component photographs. a) turbulence grid, b) converging section straightening veins 10

Figure 2.5: Orifice plate pressure transducer calibration curve 11

Figure 2.6: Airfoil photographs (a) view of wing tip and span, (b) airfoil coupler with pressure tap valves 13

Figure 2.7: Cross-section of the airfoil support apparatus 14

Figure 2.8: Stepper motor signal plot 15

Figure 2.9:Imaging system schematic... 20

Figure 2.10:Laser optics and sheet orientation schematic 21

Figure 2.11: a) laser mounting and b) 4 CCD cameras.. 22

Figure 2.12: Calibration target with associated camera viewing regions and airfoil position.. 22

Figure 2.13: Calibration target images from CCD No. 1 with (a) raw image and (b) de-warped image 24

Figure 2.14: Example 3D correlation map from raw PIV data on CCD No.1...... 27

Figure 2.15: 3D correlation maps for 32 pixel and 64 pixel square interrogation windows: Top left: poorly defined peak; top right: well defined peak in noisy background; bottom left: well defined peak; bottom right, well defined peak (best correlation). 29

Figure 2.16: Vector field stitching schematic 32

Figure 3.1: Result of multilevel threshold technique for two different cases on a supposed vorticity map 44

Figure 3.2: Multilevel threshold and image morphology algorithm schematic 46

Figure 3.3: Cross sectional lines procedure schematic 48

Figure 3.4: Cross sectional lines (CSL) algorithm flow chart 52

Figure 3.5: Computation of angle $\alpha k, i$ on streamline S_k for the winding angle algorithm 56

Figure 3.6: Computation of length Dse for the winding angle algorithm 57

Figure 3.7: Winding angle algorithm flow chart 60

Figure 3.8: Combinatorial (CVD) algorithm flow chart with the 3 individual algorithms displayed in green 64

Figure 3.9: Simulated velocity vector field showing every 6th vector with velocity magnitude v $(\mathrm{mm/s})$in the background. 67

Figure 3.10: Simulated velocity vector field with freestream $U\infty$ subtracted, showing every 6th vector and with vorticityω $(\mathrm{s} - 1)$ in the background. 68

Figure 3.11: Vortex radius rv vs. the number of velocity vectors per vortex diameter $vv/\emptyset v$ 69

Figure 3.12: Vortex circulation Γ vs. the number of velocity vectors per vortex diameter vv$/\emptyset v$.. 71

Figure 3.13:Circulation discretization error schematic....................................... 72

Figure 3.14: Vortex radius computed by CVD algorithm as a function of normalized velocity field noise n.. 74

Figure 3.15: Vortex circulation computed by CVD algorithm as a function of normalized velocity field noise n.. 75

Figure 3.16: Velocity vector field with vorticity background ω (1/s) and normalized velocity field noise n =0.0089. The detected vortex core shown as a white '×', and the vortex core boundary plotted in black. 1 every 11 velocity vectors are displayed.. 76

Figure 3.17: Airfoil dimensions and parameters characterizing its motion.......... 77

Figure 3.18:Airfoil wake schematic.. 79

Figure 3.19: Vortex cores (white '×') and radius (black circles) as computed with the WA and CSL algorithms plotted over the global vorticity map for $Re = 146$ a) $f = 1.6\ \mathrm{rad/s},\ \theta A = 8°$ b) and $f = 3.4\ \mathrm{rad/s},\ \theta A = 8°$. 82

Figure 3.20:Instantaneous streamlines from the sample vortex's reference velocity field (velocity field traveling with the centre of the vortex) plotted over the local vorticity field.. 84

Figure 3.21: Complying streamlines as defined by the winding angle algorithm's specifications along with cluster points (black ‘·’) and vortex core from CSL method (black ‘+’).. 85

Figure 3.22: Vorticity vs. the dimensionless vortex radius for the sample vortex, an ideal Burgers vortex and ideal Rankine vortex 87

Figure 3.23: Relative circumferential velocity vs. the dimensionless vortex radius for the sample vortex, an ideal Burgers vortex and ideal Rankine vortex 89

Figure 3.24: Instantaneous streamlines from sample vortices with overlapping cores from a local reference velocity plotted over the local vorticity field ω (1/s). 91

Figure 3.25: Vorticity vs. the dimensionless vortex radius for sample vortices with overlapping cores, along with an ideal Burgers vortex of similar peak vorticity and radius 92

Figure 3.26: Vorticity vs. the dimensionless vortex radius for sample vortices with overlapping cores, along with an ideal Burgers vortex and ideal Rankine vortices of similar peak vorticity and radius 93

Figure 4.1: Wake types of an oscillating airfoil... 97

Figure 4.2: Slurry injection flow visualization experimental setup schematic... 110

Figure 4.3: Instantaneous streakline images for A_d = 0.84 and a) St_d = 0.129 which fits the 2S_vK type wake, b) St_d = 0.201 a 2S_A type wake and c) St_d = 0.274 a 2S_ivK type wake. 112

Figure 4.4: Instantaneous streakline snapshots for St_d = 0.161 and a) A_d = 0.42 a 2S_vK type wake, b) A_d = 1.04 a 2S_A type wake and c) A_d = 1.47 a 2S_ivK type wake. 113

Figure 4.5: Dimensionless Strouhal number St_d based on chord width D, and dimensionless amplitude A_d map out various wake patterns which are the result of several oscillation frequency and amplitude combinations for the NACA 0012 airfoil in steady flow. The black dotted line indicates the boundary where the wake transitions from a 2S_vK to an 2S_ivK wake and the purple dotted line indicates where the wake transitions from 2S_ivK to 2S_ivKa. 114

Figure 4.6: Vorticity, ω $(s-1)$, for A_d = 0.84 and a) St_d = 0.129 a 2S_vK type wake, b) St_d = 0.201 a 2S_A type wake and c) St_d = 0.274 a 2S_ivK type wake. The suspected vortex cores along with their respective boundary radii are plotted on as white points and black circles respectfully.. 119

Figure 4.7: Vorticity, ω $(s-1)$, for St_d = 0.161 and a) A_d = 0.42 a 2S_vK type wake, b) A_d = 1.04 a2S_A type wake and c) A_d = 1.47 a 2S_ivK type wake. The suspected vortex cores along with their respective boundary radii are plotted on top as white points and black circles respectfully.. 121

Figure 4.8: Vorticity map of a sample vortex from the 2S_vK wake with A_d = 0.84 and St_d = 0.129 along with streamlines plotted from a moving reference frame equal to the suspected drift velocity of the vortex v_d.. 122

Figure 4.9: Vorticity profile for a sample vortex from the 2S_vK wake with A_d = 0.84 and St_d = 0.129 123

Figure 4.10: Vorticity map of a sample vortex from the 2S_A wake with $A_d = 0.84$ and $St_d = 0.201$ along with streamlines plotted from a moving reference frame equal to the suspected drift velocity of the vortex v_d. 124

Figure 4.11: Vorticity profile for a sample vortex from the 2S_vK wake with Ad = 0.84 and Std = 0.201 125

Figure 4.12: Vorticity map of a sample vortex from the 2S_A wake with $A_d = 0.84$ and $St_d = 0.274$ along with streamlines plotted from a moving reference frame equal to the suspected drift velocity of the vortex v_d. 126

Figure 4.13: Vorticity profile for a sample vortex from the 2S_vK wake with Ad = 0.84 and Std = 0.274 127

Figure 4.14: Circumferential velocity profile for a sample vortex from the 2S_vK wake with $A_d = 0.84$ and $St_d = 0.129$ 128

Figure 4.15:Circumferential velocity profile for a sample vortex from the 2S_vK wake with Ad = 0.84 and Std = 0.201 128

Figure 4.16: Circumferential velocity profile for a sample vortex from the 2S_vK wake with Ad = 0.84 and Std = 0.274 129

Figure 4.17: Time resolved average showing the wake velocity profiles with velocity magnitude in the background and velocity vectors plotted over top for $St_d = 0.161$ and a) $A_d = 0.42$ a 2S_vK wake type, b) $A_d = 1.04$ a 2S_A wake type and c) $A_d = 1.47$ a 2S_ivK wake type. 131

Figure 4.18: Velocity magnitude of time averaged fields along the streamwise symmetry line for St_d = 0.161 and a) A_d = 0.42 a2S_vK wake type, b) A_d = 1.04 a 2S_A wake type and c) A_d = 1.47 a 2S_ivK wake type 132

Figure 4.19:Velocity magnitude of time averaged fields along a transverse line at x = 100 mm for St_d = 0.161 and a) A_d = 0.42 a2S_vK wake type, b) A_d = 1.04 a 2S_A wake type and c) A_d = 1.47 a 2S_ivK wake type 133

Figure 4.20:Circulation vs. streamwise distance for Ad = 0.84 and Std = 0.129 (2S_vK wake) showing the inaccuracies of using phase averaged data to predict certain parameter 135

Figure 4.21: Vortex radius vs. streamwise distance for Ad = 0.84 and Std = 0.129 (2S_vK wake) showing the inaccuracies of using phase averaged data to predict certain parameter 136

Figure 4.22: Sample instantaneous vorticity fields, $\omega\ (s-1)$, for A_d = 0.84 and a) St_d = 0.129 a the 2S_vK wake type, b) St_d = 0.201 a 2S_A wake type and c) St_d = 0.274 a 2S_ivK wake type. The suspected vortex cores along with their respective boundary radii are plotted on as white crosses and black circles respectively. 139

Figure 4.23: Circulation vs. dimensionless streamwise distance for A_d = 0.84 and S_{td} = 0.129 ($f = 1.60$ rad/s and $\theta A/2 = 4°$) 140

Figure 4.24: Initial circulation estimate error vs. dimensionless streamwise distance for A_d = 0.84 and S_{td} = 0.129 ($f = 1.60$ rad/s and $\theta A/2 = 4°$) 141

Figure 4.25: Peak positive vorticity vs. dimensionless streamwise distance for A_d = 0.84 and S_{td} = 0.129 (f = 1.60 rad/s and $\theta A/2 = 4°$) 143

Figure 4.26: Analytical peak vorticity error vs. dimensionless streamwise distance for A_d = 0.84 and S_{td} = 0.129 (f = 1.60 rad/s and $\theta A/2 = 4°$) 145

Figure 4.27: Vortex boundary radii r_v vs. dimensionless streamwise distance for A_d = 0.84 and S_{td} = 0.129 (f = 1.60 rad/s and $\theta A/2 = 4°$) 147

Figure 4.28: Dimensionless streamwise drift velocity v_{drift} vs. dimensionless streamwise distance for A_d = 0.84 and S_{td} = 0.129 (f = 1.60 rad/s and $\theta A/2 = 4°$) 148

Figure 4.29: Streamwise vortex spacing S_x vs. dimensionless streamwise distance for A_d = 0.84 and S_{td} = 0.129 (f = 1.60 rad/s and $\theta A/2 = 4°$) 149

Figure 4.30: Transverse vortex spacing S_y vs. dimensionless streamwise distance for A_d = 0.84 and S_{td} = 0.129 (f = 1.60 rad/s and $\theta A/2 = 4°$) 150

Figure 4.31: Circulation vs. dimensionless streamwise distance for A_d = 0.84 and S_{td}=0.201 (f = 2.50 rad/s and $\theta A/2 = 4°$) 152

Figure 4.32: Analytical circulation error vs. dimensionless streamwise distance for A_d = 0.84 and S_{td}=0.201 (f = 2.50 rad/s and $\theta A/2 = 4°$) 153

Figure 4.33: Peak positive vorticity vs. dimensionless streamwise distance for A_d = 0.84 and S_{td}=0.201 (f = 2.50 rad/s and $\theta A/2 = 4°$) 154

Figure 4.34: Analytical peak vorticity error vs. dimensionless streamwise distance for A_d = 0.84 and S_{td}=0.201 (f = 2.50 rad/s and $\theta A/2 = 4°$) 156

Figure 4.35: Vortex boundary radii r_v vs. dimensionless streamwise distance for A_d = 0.84 and S_{td}=0.201 ($f = 2.50$ rad/s and $\theta A/2 = 4°$) 157

Figure 4.36: Dimensionless drift velocity vs. dimensionless streamwise distance for A_d = 0.84 and S_{td}=0.201 ($f = 2.50$ rad/s and $\theta A/2 = 4°$) 158

Figure 4.37: Streamwise vortex spacing S_x vs. dimensionless streamwise distance for A_d = 0.84 and S_{td}=0.201 ($f = 2.50$ rad/s and $\theta A/2 = 4°$) 159

Figure 4.38: Transverse vortex spacing S_y vs. dimensionless streamwise distance for A_d = 0.84 and S_{td}=0.201 ($f = 2.50$ rad/s and $\theta A/2 = 4°$) 160

Figure 4.39: Circulation vs. dimensionless streamwise distance for A_d = 0.84 and S_{td} = 0.274 ($f = 3.40$ rad/s and $\theta A/2 = 4°$) 162

Figure 4.40: Circulation error vs. dimensionless streamwise distance for A_d = 0.84 and S_{td} = 0.274 ($f = 3.40$ rad/s and $\theta A/2 = 4°$) 163

Figure 4.41: Positive peak vorticity vs. dimensionless streamwise distance for A_d = 0.84 and S_{td} = 0.274 ($f = 3.40$ rad/s and $\theta A/2 = 4°$) 164

Figure 4.42:Positive peak vorticity error vs. dimensionless streamwise distance for A_d = 0.84 and S_{td} = 0.274 ($f = 3.40$ rad/s and $\theta A/2 = 4°$) 165

Figure 4.43: Vortex boundary radiu r_v s vs. dimensionless streamwise distance for A_d = 0.84 and S_{td} = 0.274 ($f = 3.40$ rad/s and $\theta A/2 = 4°$) 166

Figure 4.44:Dimensionless drift velocity vs. dimensionless streamwise distance for A_d = 0.84 and S_{td} = 0.274 ($f = 3.40$ rad/s and $\theta A/2 = 4°$) 168

Figure 4.45:Streamwise vortex spacing S_x vs. dimensionless streamwise distance for $A_d = 0.84$ and $S_{td} = 0.274$ ($f = 3.40$ rad/s and $\theta A/2 = 4°$) 169

Figure 4.46: Transverse vortex spacing S_y vs. dimensionless streamwise distance for $A_d = 0.84$ and $S_{td} = 0.274$ ($f = 3.40$ rad/s and $\theta A/2 = 4°$) 170

Figure 4.47: Experimental curve fit of circulation vs. dimensionless streamwise distance for the 2S_vK, the 2S_A and the 2S_ivK wakes 173

Figure 4.48: Experimental curve fit of positive peak vorticity vs. dimensionless streamwise distance for the 2S_vK, the 2S_A and the 2S_ivK wakes 174

Figure 4.49:Experimental curve fit of vortex boundary radii vs. dimensionless streamwise distance for the 2S_vK, the 2S_A and the 2S_ivK wakes 175

Figure 4.50:Experimental curve fit of streamwise drift velocity vs. dimensionless streamwise distance for the 2S_vK, the 2S_A and the 2S_ivK wakes 176

Figure 5.1: A schematic of the tandem airfoil arrangement 186

Figure 5.2: Test section schematic showing the forefoil and hindfoil along with the pressure membrane 188

Figure 5.3: Vortex spacing arrangement for tandem airfoil schematic 190

Figure 5.4: Vorticity field for the wake with oscillation frequency and amplitude of 4 rad/s and $\theta A = 20°$ With a) showing the phase averaged field and b) showing a sample field. In addition, boundary radii for the detected vortices are shown black circles and the vortex cores are shown as white ‘×’. 192

Figure 5.5: Vorticity field for the wake with oscillation frequency and amplitude of 2 rad/s and $\theta A = 40°$. With a) showing the phase averaged field and b) showing a sample field. In addition, boundary radii for the detected vortices are shown black circles and the vortex cores are shown as white '×'. 193

Figure 5.6: Dimensionless Strouhal number St_d based on chord width D, and dimensionless amplitude A_d map out various wake patterns which are the result of several oscillation frequency and amplitude combinations for the NACA 0012 airfoil in steady flow. The black dotted line indicates the boundary where the wake transitions from a 2S_vK to an 2S_ivK wake and the purple dotted line indicates where the wake transitions from 2S_ivK to 2S_ivKa. 194

Figure 5.7: Vorticity field behind the hindfoil of wake type A for 8 phases $\Phi = 0° - 315°$ with detected vortex cores plotted as white x's and boundary radii as black circles. 196

Figure 5.8: Total combined circulation from all of the vortices averaged over 100 fields for each phase along with that of the single airfoil case. 197

Figure 5.9: Total combined circulation from all of the weak vortices ($\Gamma \leq 500$ (mm^2/s)) averaged over 100 fields for each phase. 199

Figure 5.10:Total combined circulation from all of the strong vortices (Γ>500 (mm2/s)) averaged over 100 fields for each phase. 200

Figure 5.11: Average number of detected vortices vs. the phase of the hindfoil along with the average number of detected vortices for the single airfoil case .. 201

Figure 5.12: Vorticity field behind the hindfoil of wake type B for 8 phases $\Phi = 0° - 315°$ with detected vortex cores plotted as white x's and boundary radii as black circles. 203

Figure 5.13: Total combined circulation from all of the vortices averaged over 100 fields for each phase along with that of the single airfoil case. 204

Figure 5.14: Total combined circulation from all of the weak vortices ($\Gamma \leq 500$ (mm^2/s)) averaged over 100 fields for each phase. 205

Figure 5.15:Total combined circulation from all of the strong vortices (Γ>500 (mm2/s)) averaged over 100 fields for each phase. 206

Figure 5.16: Average number of detected vortices vs. the phase of the hindfoil along with the average number of detected vortices for the single airfoil case .. 207

Figure 5.17: Filter response of the selected Chebyshev type II digital filter 209

Figure 5.18: Pressure membrane voltage output for various phases for wake type A plotted with the angular position of the hindfoil.. 211

Figure 5.19:Pressure membrane voltage output for various phases for wake type B plotted with the angular position of the hindfoil.. 212

Figure A.1: Instantaneous Streaklines for a) frequency of 1 rad/s and amplitude of 7degrees, b) frequency of 1 rad/s and amplitude of 8degrees and c) frequency of 1 rad/s and amplitude of 10degrees 227

Figure A.2: Instantaneous Streaklines for a) frequency of 1.2 rad/s and amplitude of 6degrees, b) frequency of 1.25 rad/s and amplitude of 10 degrees and c) frequency of 1.3 rad/s and amplitude of 8degrees 228

Figure A.3: Instantaneous Streaklines for a) frequency of 1.5 rad/s and amplitude of 1degrees, b) frequency of 1.5 rad/s and amplitude of 6degrees and c) frequency of 1.6 rad/s and amplitude of 4degrees 229

Figure A.4: Instantaneous Streaklines for a) frequency of 2 rad/s and amplitude of 2 degrees, b) frequency of 2 rad/s and amplitude of 4degrees and c) frequency of 2 rad/s and amplitude of 6degrees 230

Figure A.5: Instantaneous Streaklines for a) frequency of 2 rad/s and amplitude of 7degrees, b) frequency of 2 rad/s and amplitude of 10 degrees and c) frequency of 2 rad/s and amplitude of 2degrees 231

Figure A.6: Instantaneous Streaklines for a) frequency of 2.2 rad/s and amplitude of 1degree, b) frequency of 2.5 rad/s and amplitude of 4degrees and c) frequency of 2.7 rad/s and amplitude of 7 degrees 232

Figure A.7: Instantaneous Streaklines for a) frequency of 2.8 rad/s and amplitude of 4degrees, b) frequency of 3 rad/s and amplitude of 1degree and c) frequency of 3 rad/s and amplitude of 2degrees 233

Figure A.8: Instantaneous Streaklines for a) frequency of 3 rad/s and amplitude of 10degrees, b) frequency of 3.3 rad/s and amplitude of 5degrees and c) frequency of 3.4 rad/s and amplitude of 4 degrees 234

Figure A.9: Instantaneous Streaklines for a) frequency of 3.5 rad/s and amplitude of 5 degrees, b) frequency of 4 rad/s and amplitude of 1degree and c) frequency of 4 rad/s and amplitude of 2degrees 235

Figure A.10: Instantaneous Streaklines for a) frequency of 4 rad/s and amplitude of 5 degrees, b) frequency of 4 rad/s and amplitude of 7 degrees and c) frequency of 4 rad/s and amplitude of 10 degrees 236

Figure A.11: Instantaneous Streaklines for a) frequency of 5rad/s and amplitude of 1 degree, b) frequency of 5 rad/s and amplitude of 2 degrees and c) frequency of 5.5 rad/s and amplitude of 2degrees 237

Figure A.12: Instantaneous Streaklines for a) frequency of 6 rad/s and amplitude of 1 degree, b) frequency of 6 rad/s and amplitude of 2 degrees and c) frequency of 8 rad/s and amplitude of 4degrees 238

NOMENCLATURE

Acronyms

2C2D	2 Components 2 Dimensions
2D	2 Dimensional
2S_A	Aligned wake type
2S_ivK	inverted von Karman wake type
2S_ivKa	asymmetric inverted von Karman wake type
2S_vK	von Karman wake type
CCD	Charge-Coupled Device
CCW	Counter Clock-Wise
CSL	Cross Sectional Lines vortex detection algorithm
CVD	Combinatorial Vortex Detection algorithm
CW	Clock-Wise
DEG	Discriminant of non-real Eigenvalues of Gradient matrix
DNS	Direct Numerical Simulation
IM	Image Morphology
LHS	Left Hand Side
MTV	Molecular Tagging Velocimetry
MV	Maximum Vorticity vortex detection algorithm

Nd:YAG	Neodymium-doped Yttrium Aluminum Garnet
ONFR	Organized Near Field Region
PIV	Particle Image Velocimetry
PQ	vortex detection methods relying on Physical Quantities
PTU	Programmable Timing Unit
RHS	Right Hand Side
ROI	Region Of Interest
TIV	Threshold Intensity Vector
WA	Winding Angle vortex detection algorithm

Symbols

A_1	cross-sectional area of orifice plate
A_2	cross-sectional area of water channel return line
$\dot{Q}$	Volumetric flow rate of water channel
C_d	Orifice plate discharge coefficient
ΔP	differential pressure
ρ	density
V	voltage
m_{cal}	slope of differential orifice flow meter calibration curve
C	airfoil chord length
I_n	raw intensity distribution
$\vec{s}$	PIV displacement vector
ω	2D scalar vorticity

$\vec{\nabla}$	Gradient operator
$\vec{v}$	velocity vector
S_e	image morphology structuring element
ψ	row index of vortex core from CSL
ς	column index of vortex core from CSL
v_p	perpendicular velocity (used in CSL)
r_v	vortex boundary radius
v_{drift}	streamwise drift velocity of a vortex
S_k	streamline *k*
$\alpha_{w,k}$	winding angle of a streamline *k*
$P_{k,i}$	vertex *i* on a streamline *k*
D_{se}	distance between starting and ending points of a streamline
MP_k	cluster point for mapping a streamline *k*
D	airfoil thickness
A	distance traveled by airfoil trailing edge during oscillation
θ	airfoil angle of attack
Re	airfoil thickness based Reynolds number
U_∞	freestream velocity
ν	kinematic viscosity
f	frequency of airfoil oscillation
t	time
S_x	streamwise vortex spacing
S_y	transverse vortex spacing
Γ	circulation of a vortex

v_{θ}	circumferential velocity within a vortex
$\emptyset_{v}$	unit of vortex diameter
vv	number of velocity vectors
$\vec{v}_n$	velocity field noise vector
$\lvert n \rvert$	velocity magnitude limit of a velocity noise field $\vec{v}_n$
$\bar{\bar{n}}$	normalized velocity field noise
ω_n	vorticity induced by a velocity noise field $\vec{v}_n$
St_d	dimensionless airfoil oscillation frequency
A_d	dimensionless airfoil oscillation amplitude
w	axial velocity component in a vortex
ω_{peak}	peak vorticity within a vortex
y_{core}	transverse coordinate of a vortex core
x_{core}	streamwise coordinate of a vortex core
ω_{μ}	average peak vorticity of all vortices in a flow field
Γ_o	circulation of a vortex at the trailing edge of the airfoil
ω_o	peak vorticity of a vortex at the trailing edge of the airfoil
x_c	dimensionless streamwise spatial coordinate
Γ_{BL}	circulation generated from the airfoil boundary layer
Γ_{TE}	circulation generated from the airfoil trailing edge

Accents

$\bar{\mathrm{P}}$	a fit for experimental parameter P
$\hat{\mathrm{P}}$	analytical model of parameter P
$\tilde{\mathrm{P}}$	normalized error of parameter P

CHAPTER 1: Introduction

1.1 Motivation

The work presented in this thesis is motivated by 3 primary topics: the importance of quantitatively investigating the vortical wake of unsteady bodies; the importance of manipulating such wakes in a way that enhances the strength of its vortices with active control; and the importance of manipulating such wakes in a way that suppresses the strength of its vortices with active control.

Flow over unsteady streamlined bodies is an important topic in modern fluid mechanics. Initially motivated by phenomenon such as wing flutter and dynamic stall (Bohl & Koochesfahani, 2009), it has since progressed to include more recent studies focusing on biological applications related to propulsion of aquatic organisms (Shukla, Govardhan, & Arakeri, 2009) (Gopalkrishnan et al., 1994). For example (Ozen & Rockwell, 2010) investigate the vortical structures on a flapping wing with the intention of gaining a deeper understanding of control concepts used by swimming fish and mammals such as the humpback whale. There is believed to be a substantial connection between the kinematics of these biological swimmers and the structure of the associated wakes they generate (Bohl & Koochesfahani, 2009). Therefore, accurate characterization of the wake structure of oscillating bodies is an important topic and can lead to significant advancements in the development of biologically inspired aquatic and aeronautical propulsion.

Actively enhancing the relative strength, size or quantity of vortices in a given flow has several advantages. Namely, in optimizing mixing processes (Gopalkrishnan et al., 1994), (Kwon & Choi, 1996), (Seidel, Siegel, Fagley, Cohen, & McLaughlin, 2009) and in energy harvesting within turbulent flows. Several studies have appeared on the subject of using active control to stabilize/destabilize unsteady flow regimes (Roussopoulos, 2006), (Jukes & Choi, 2009), (Seidel et al., 2009). Destabilizing a wake may prove to be useful in energy harvesting systems such as the ones presented by (Akaydin, Elvin, & Andreopoulos, 2010) and (Nelson, 2010) where a peizo-electric cantilever dynamically deforms under the pressure forces imposed by nearby vortices. Enhancing the strength of these vortices may yield higher power output from such devices.

Actively suppressing the strength size or quantity of vortices in a given flow is also advantageous. The undesirable and potentially destructive periodic loading that vortices impose on structures creates a need for vortex suppression. Vortex suppression was first attempted with passive control strategies, most of which consisted of geometric modifications made to a vortex generating cylinder (Gopalkrishnan et al., 1994). Simple examples of geometric modifications to the flow include the installation of rigid (Akilli, Sahin, & Filiztumen, 2005), (Kwon & Choi, 1996) and hinged splitter plates (Shukla et al., 2009) in the near field wake of the cylinder. This led to passive open-loop control, in which the geometric modifications were driven by some preset time dependant signal (Gopalkrishnan et al., 1994), (Tang & Aubry, 2000) and eventually closed-loop control where the driving signal is replaced with some real-time measurement of the flow response (Roussopoulos, 2006), (Keles, 2002) (Muddada & Patnaik, 2010).

The current work aims to suppress of enhance the strength of fully formed vortices, without interfering with the formation process, through active open-loop control. This is a valuable study for applications where the vortex source cannot be altered or controlled.

A quantitative study of these wake structures requires dependable and robust vortex detection algorithms. In addition to being a required component of the wake characterization study, vortex detection and specifically that performed with experimental PIV vector fields, is an important research area on its own. Vortex detection has received considerable attention in the literature and is a valuable tool for studying the characteristics of vortices as they interact with rotor-craft blades, aircraft wings and turbo machine blades (Ari Sadarjoen, 2000), (Vollmers, 2001). This extends to a much larger scale as scientists depend heavily on vortex detection methods for understanding ocean circulation currents (Ari Sadarjoen, 2000). Given the large amount of experimental velocity fields made available through particle image velocimetry (PIV) (Vollmers, 2001), accurate and automated vortex detection tailored for experimentally generated vector fields is of significant importance.

1.2 Summary / thesis outline

Three major experiments are performed in this thesis. These experiments are related to: the development of a vortex detection and characterization algorithm, wake characterization of a single oscillating airfoil and the wake characterization of 2 oscillating airfoils in tandem. They are individually presented and discussed in *chapters 3, 4* and *5* respectively.

The basic experimental procedure for this thesis is described in *chapter 2*. Each of the three experiments is accompanied by slight variations to the basic setup which will be discussed in their respective chapters. The following items are outlined in the experimental procedure chapter: a description of the flow facility; a description of the basic setup for the airfoil support and driving apparatus and a description of the PIV measurement technique and of the imaging system used.

A vortex detection and characterization algorithm is developed and tested in *chapter 3*. The algorithm is developed for use in interrogating experimental PIV data. It combines 3 separate algorithms to ensure robust and accurate vortex detection. In this chapter the algorithm is broken down into its essential components in order to clearly describe how it works. The algorithm is tested on a simulated velocity field with a Burgers vortex at its centre. The effect of changing the grid resolution and of adding velocity field noise to the simulated field is tested.

A detailed investigation of the vortical wake of an oscillating airfoil is shown in *Chapter 4*. In this chapter, a qualitative investigation of the wake identifies and characterizes the basic wake types that arise from an oscillating airfoil. This information is used to develop a phase map which serves to locate the various wake types and their corresponding transitions in terms of dimensionless amplitude and frequency of airfoil oscillation. Then a quantitative assessment with PIV measurement is performed for select wake types which were identified by the phase map as important transitions. Finally, vortex evolution is compared to an analytical model by investigating the change in peak vorticity with streamwise distance.

Two airfoils oscillating in tandem are studied in *Chapter 5*. The downstream airfoil is expected to actively modify and rearrange the vortices shed from the upstream airfoil through open-loop control. The airfoils oscillate at the same frequency and amplitude and the effect of changing their relative phase is quantified by investigating the wake of the downstream airfoil. The differential pressure measured across the downstream airfoil's aerodynamic centre produces a dynamic signal that is unique to each phase. This could later be used to expand the current system from open-loop control to closed-loop control.

Important conclusions as well as potential improvements for experiments and methodology are outlined in *Chapter 6*. The thesis is concluded with an appendix that includes wake images (Appendix A), mathematical derivations (Appendix B) and code from the detection algorithm (Appendix C).

CHAPTER 2: Experimental procedure

2.1 Introduction

The experimental facility consisted of a recirculating waterchanel with low turbulence characteristics (T.L. Hilderman, 2004). The airfoil(s) was suspended vertically such that it hangs down through the free surface into the water channel, perpendicular to the upstream flow direction. PIV is employed to calculated two-component velocity vectors on a two dimensional region-of-interest (2C2D).

2.2 Flow facility

The flow facility used to develop the general flow in all experiments is an open re-circulating water channel with low turbulence characteristics (T.L. Hilderman, 2004). A photograph of the waterchanel is shown in Figure 2.1. The center of the channel test section is located 3100 mm downstream from the turbulence grid. The four CCD cameras are directly above the test section. A schematic of the water channel is shown in Figure 2.2. The entrance and exit plenums are located at the left and right sides of the schematic respectively. The water flows out of the entrance plenum through the two sets of straightening veins and past the turbulence grid before entering the channel's test section.

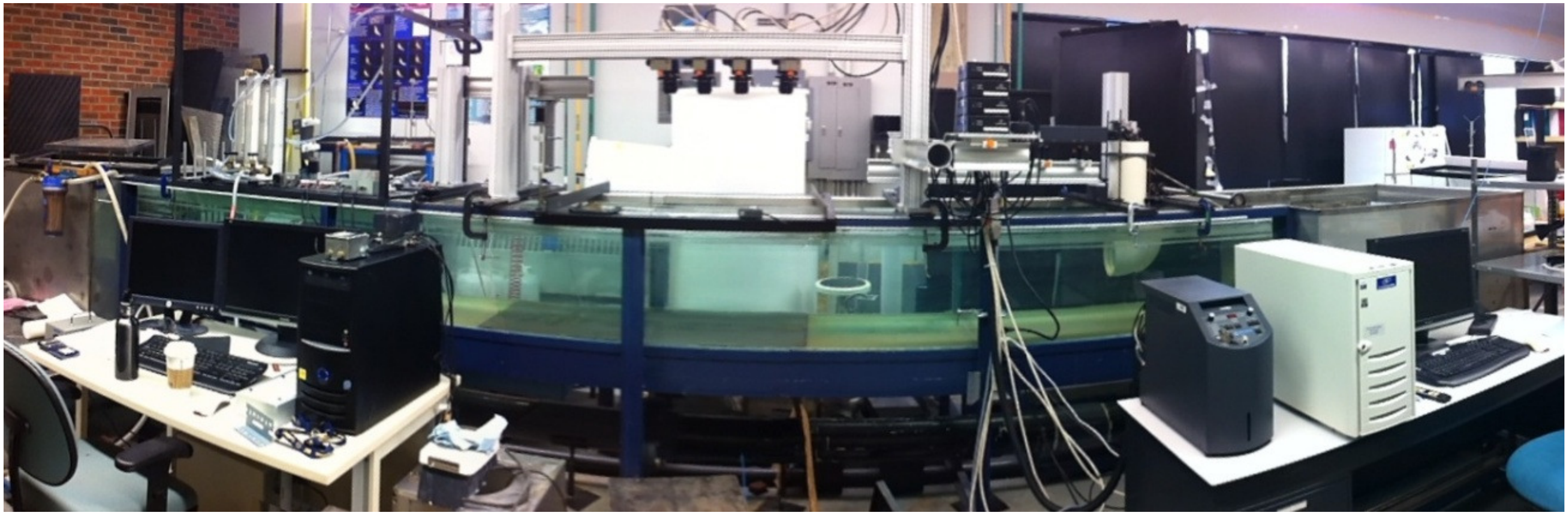

Figure 2.1: Flow facility and experimental setup panoramic photograph

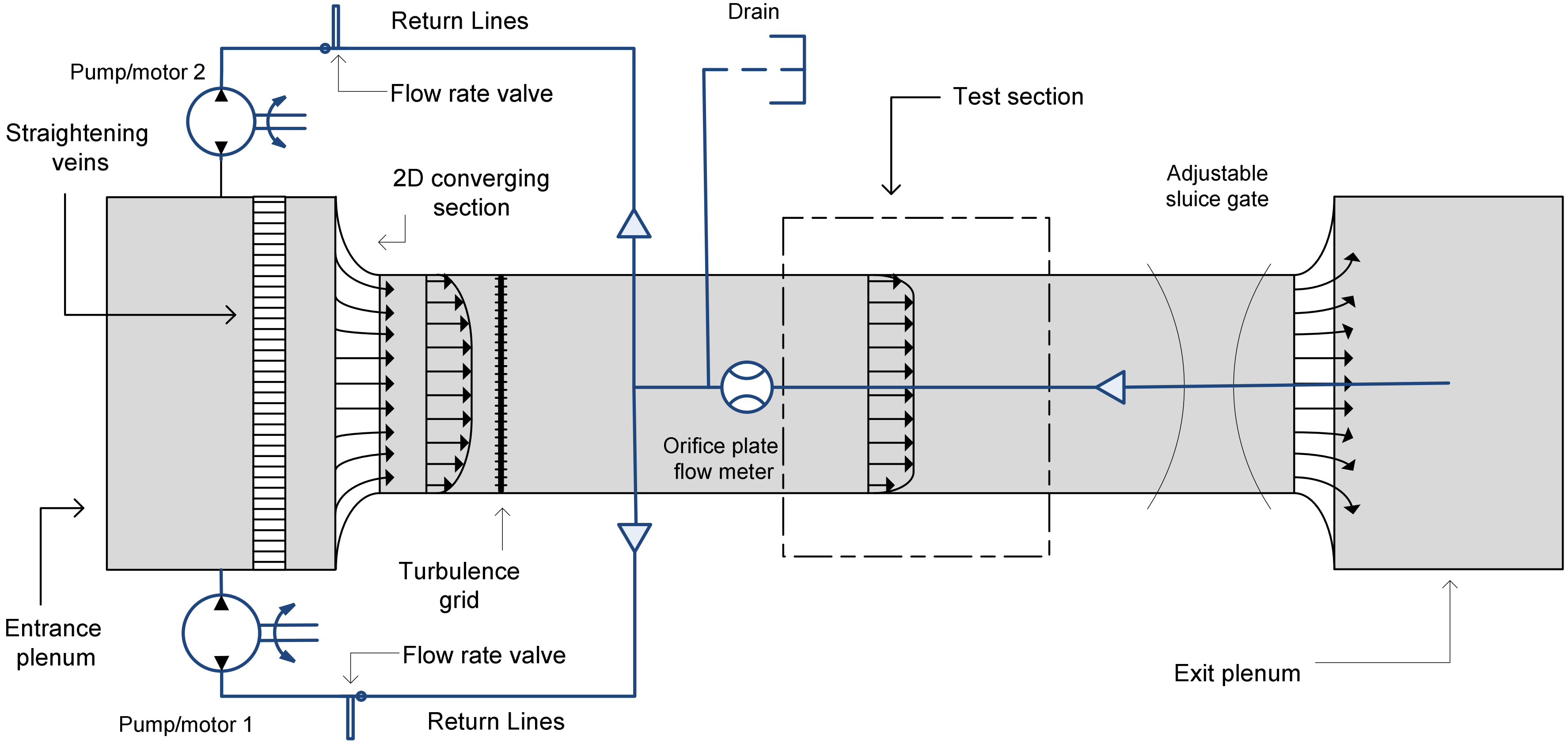

Figure 2.2: Schematic of recirculating water channel (Top)

The turbulence grid is placed at the inlet of the waterchanel and consists of flat stainless steel bars that have a cross-section of 19.2 mm× 5 mm. The bars are arranged in a square grid with a mesh spacing of 76.2 mm to form a total open area of 56%. The turbulence grid generates a uniform streamwise velocity profile with variations of 5% and turbulence intensity for the mean horizontal of 4% at the test section (T.L. Hilderman, 2004). The flow of water continues past the turbulence grid, through the test section and over the weir into the exit plenum. Photographs of one of the two identical pumps and the entrance plenum straightening veins are shown in Figure 2.3 and photographs of the turbulence grid and converging section straightening veins shown in Figure 2.4.

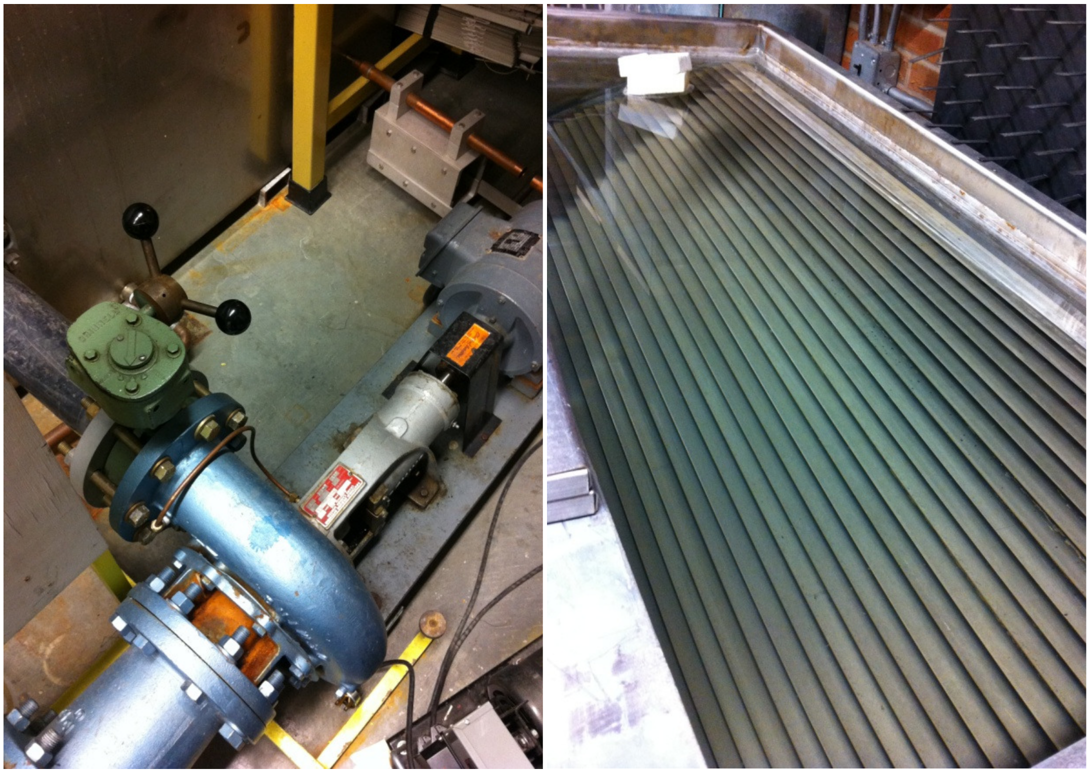

(c) (d)

Figure 2.3: Flow facility component photographs. (a) centrifugal pump, (b) entrance plenum straightening veins

(a) (b)

Figure 2.4: Flow facility component photographs. a) turbulence grid, b) converging section straightening veins

Two centrifugal pumps in parallel drive the water flow and are supplied through a single inlet at the bottom of the exit plenum. Water travels through the supply pipe of area $A_1 = 0.0187$ m^2 then through an orifice plate of area $A_2 = 0.0117$ m^2, before splitting into the two pump inlets. The pump outlets feed water into either side of the entrance plenum. The flow rate is controlled by two flow rate valves located on each pump directly after the outlet. The orifice pressure taps on either side of the orifice plate are connected to a differential pressure transducer (DP215, Validyne) and the flow rate $\dot{Q}$ is derived from the transducer output voltage V using:

$$\dot{Q} = C_d A_2 \sqrt{\frac{\Delta P/\rho}{1-(A_2/A_1)^2}} \tag{2.1}$$

Where,

$$\Delta P = 98.1 \cdot 2 m_{cal} V \tag{2.2}$$

The density of water ρ is taken to be 1000 kg/m^3 and the 98.1 factor in *eqn. (2.2)* converts centimeters of water (cm H_2O) into Pascals (Pa). The calibration curve of the differential pressure transducer was derived with a 200 cm water manometer and is shown in Figure 2.5. The measured voltage out of the differential pressure transducer is plotted against the measured water column height Δh in the manometer.

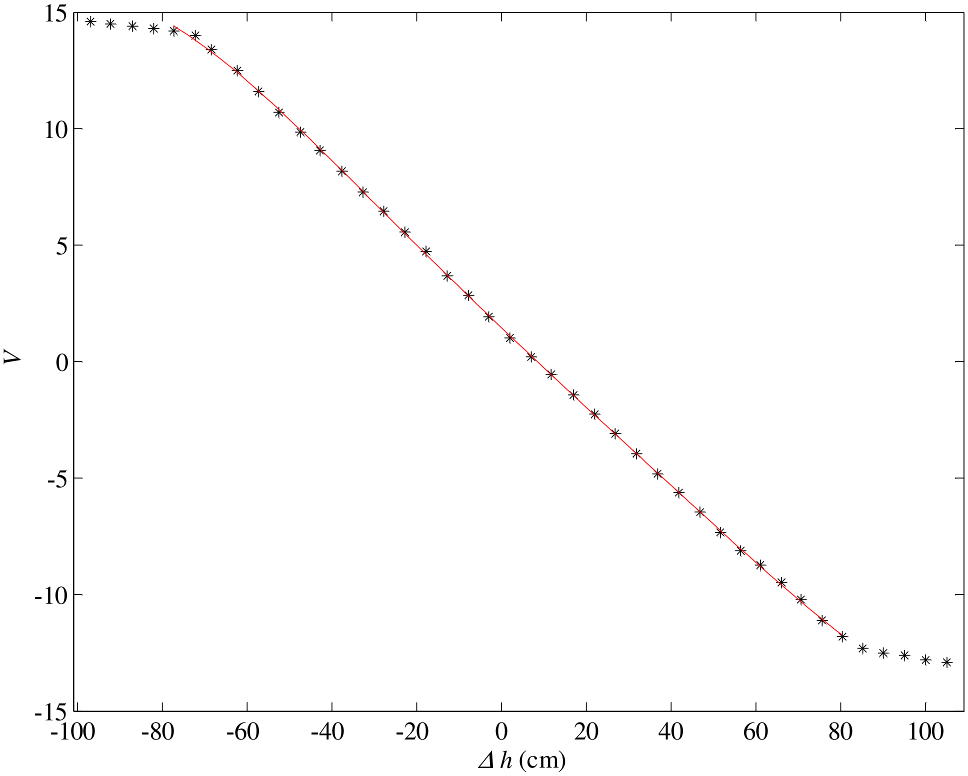

Figure 2.5: Orifice plate pressure transducer calibration curve

The slope in the linear region of the curve is $m_{cal} = -0.1706$ V/cm. The discharge coefficient for the orifice plate is C_d = 0.63. The channel velocity is approximated with *eqn. (2.1)* and a more accurate value is obtained later with PIV measurements.

2.3 Airfoil and support apparatus

The airfoil support apparatus consisted of a frame that anchors to the water-channel frame and serves as a rigid base for mounting the wing or airfoil, the acrylic sheet that is used to allow viewing through the surface, the stepper motor and the pressure transducer. Photographs of the airfoil are shown in Figure 2.6 showing the wing tip facing the bottom of the channel in Figure 2.6 (a) and the wing coupler with airfoil shaft socket and pressure tap valves in Figure 2.6 (b). The aluminum airfoil was constructed from a continuous extrusion with a cross-sectional NACA 0012 shape and a chord length C = 75mm. This was suspended on a solid shaft driven by a stepper motor (PK258-02Dl, Oriental Motor) that passes through the airfoil's aerodynamic center allowing for controlled pitch oscillations of any wave form. The airfoil was suspended vertically such that it hangs down through the free surface into the water channel, perpendicular to the upstream flow direction.

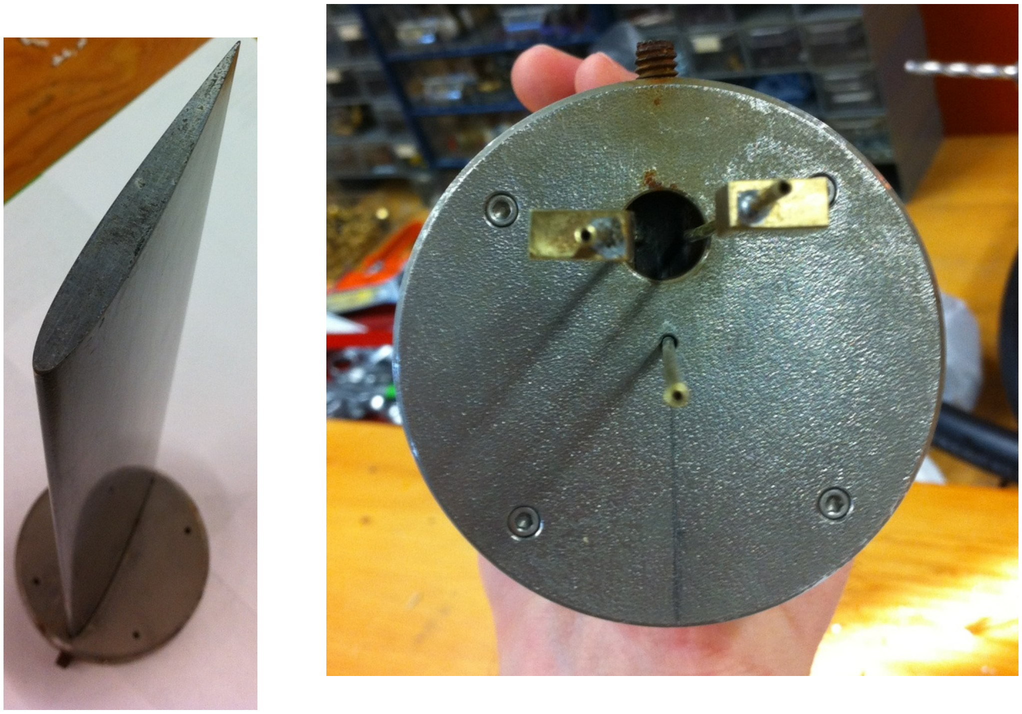

(a) (b)

Figure 2.6: Airfoil photographs (a) view of wing tip and span, (b) airfoil coupler with pressure tap valves

A symmetric cross-section of the support apparatus is shown in Figure 2.7. The airfoil shaft, made of solid ½” diameter brass and is held in place with two concentric radial polypropylene bearings which are bolted to the mounting plate. The shaft fits into the airfoil coupler socket and is secured by a set screw. The airfoil fits into a socket on the bottom of the airfoil coupler and is secured with 4 set screws that surround the airfoil. An acrylic water block fits around the brass shaft, against the acrylic sheet and prevents water from spilling onto the acrylic viewing window. The stepper motor is bolted to the mounting plate and its output shaft fits into a socket on the top of the brass airfoil shaft and is secured with a set screw. A pressure transducer is used to measure the differential pressure across the airfoil’s aerodynamic centre and will be discussed further in *Chapter 5*. To keep the tubes connecting the pressure ports to the pressure transducer short, the transducer was bolted to the opposite side of the mounting plate as seen in the figure. It may also be bolted to the airfoil shaft allowing the connecting tubes to move with the airfoil and prevent any unwanted tube deformation during airfoil motion. Finally, the acrylic viewing window hangs from four set screws attached to the support frame allowing to adjust the height of the acrylic sheet and to level it. The purpose of the acrylic sheet is to break the free surface of the water and allow the cameras to observe the flow in the plane of interest free of any diffractive effects which are linked to the water's free surface.

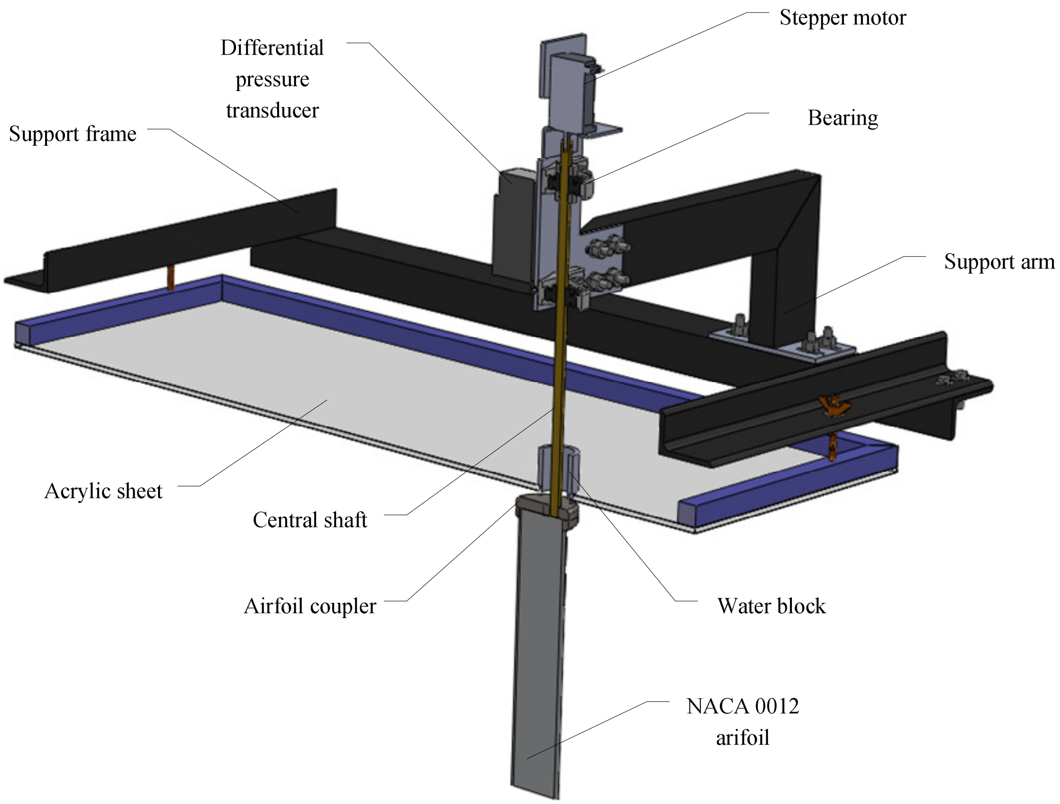

Figure 2.7: Cross-section of the airfoil support apparatus

2.3.1 Stepper motor control

Airfoil motion is driven by a stepper motor attached to the airfoil shaft at the aerodynamic center. Driving the airfoil with a stepper motor allows for a user defined input waveform. Provided the external forces on the airfoil do not exceed the maximum holding torque of the stepper motor, no slip will occur and an optical encoder is not needed. A stepper motor approximates the reference input signal by rotating clockwise (CW) or counter-clockwise (CCW) in fixed quantities called steps. Figure 2.8 illustrates how a stepper motor approximates sinusoidal motion given a reference sine wave input.

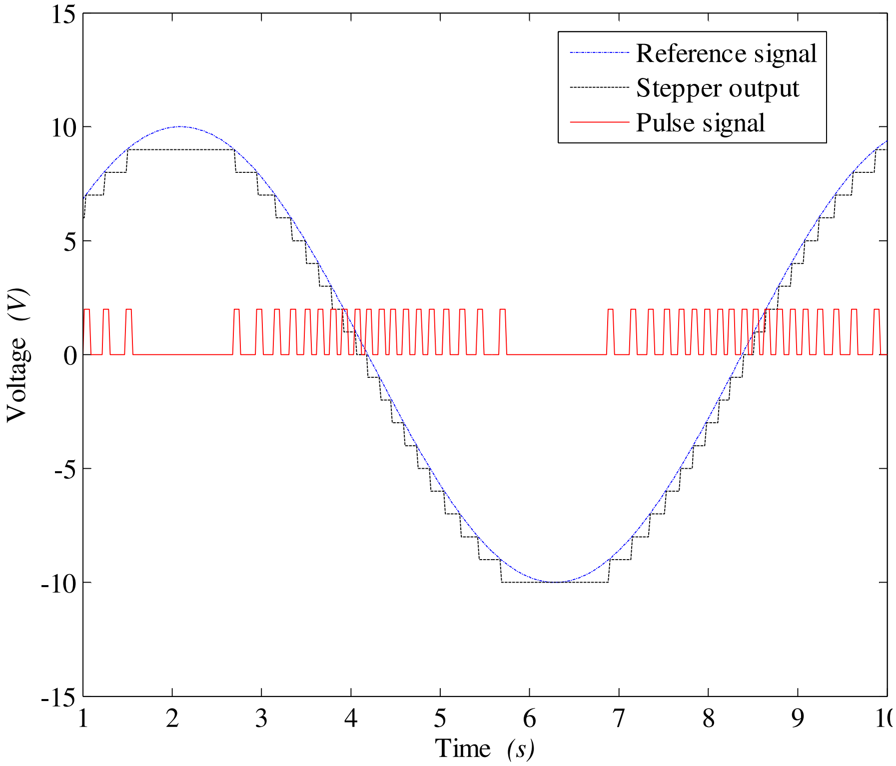

Figure 2.8: Stepper motor signal plot

The stepper motor used in this study (PK258- 02Dl, Oriental Motor) has 200 steps per revolution providing a resolution of 1.8°/step; however, the resolution can be increased to 0.1125°/step when the driver operates in micro-stepping mode. To generate smooth motion and minimize undesirable flow brought on by sudden changes in angular position caused by angular steps, the smallest step size is used. However, the minimum pulse width of 5μs imposes constraints on the step resolution for high oscillation amplitudes and frequencies. A step resolution that depends on the amplitude and frequency of the input signal to provide the best resolution while respecting the minimum pulse width is used. The available micro-stepping resolutions are found in Table 2.1.

Table 2.1: Stepper motor specifications

Number of divisions	Resolution (counts/rev)	Step angle (degree)
1	200	1.8°
2	400	0.9°
4	800	0.45°
8	1600	0.225°
16	3200	0.1125°

2.3.2 Angular position trigger signal

The angular position of the airfoil is monitored by counting the pulses that are sent to the stepper motor driver eliminating the need for an encoder. This assumes that the torque on the stepper motor does not exceed the maximum holding torque of the stepper motor. For this particular stepper motor, micro-stepping does not reduce the maximum holding torque of the stepper motor. The control interface (dSPACE Inc, DS1104) generates a 5 VDC output pulse signal when the airfoil reaches a desired position. This can be set for positive angles, negative angles or both (for positive CCW rotation). This signal is primarily used for triggering the imaging system which allows for consistent characterization of the wake at a prescribed angular position of the airfoil.

2.4 PIV Method

All experiments are performed with the base experimental setup described in this section. Slight modifications from the basic setup are needed for each chapter and are discussed as needed. The main flow diagnostic is 2C2D PIV which is used to determine the velocity field.

2.4.1 Particle image velocimetry (PIV)

PIV is an optical flow measurement method which characterizes the flow by computing instantaneous velocity vector fields within a plane of interest (Adrian & Westerweel, 2011). The fluid is seeded with particles designed to follow the flow field. The flow within a defined space is illuminated and the seed particles in that area are subsequently imaged. Laser pulses generate short, intense bursts of light and are used for illuminating the seed particles. In this study the flow is characterized with 2C2D vector fields and so the laser is focused into a thin sheet to ensure that only seed particles contained within the 2D plane of interest are imaged. The cameras record 2 consecutive instantaneous images separated by a known Δt that is short relative to the flow speed. Correlation algorithms are then used to compute the velocity vectors (Raffel, Willert, Wereley, & Kompenhans, 1998). PIV allows for a global characterization of the flow field (Adrian & Westerweel, 2011) and is therefore a powerful tool for tracking and characterizing large scale structures such as vortices which are believed to be global features (Jiang, 2002).

2.4.2 Imaging system

The major components of the imaging system are shown in Figure 2.9 and consist of:

Seed particles, hollow glass spheres 18µm in diameter (Sphericel 60P18, Potters Industries) which have a density of 0.6g/cc and at the flow conditions used are nearly neutrally buoyant in water.

A double pulsed Nd:YAG laser (Solo III-15z, New Wave) is a double cavity laser with a nominal maximum power of 50mJ/pulse and pulse duration of 7ns. Its two pulses illuminate the seed particles separated by a known Δt. The laser first passes through a refracting telescope to focus the beam and a low focal length cylindrical lens which spreads the beam into sheet. As shown in the cross-section in Figure 2.10, and a photograph of the laser/optics setup shown in Figure 2.11 (a) the light sheet is redirected into the water channel by two 45^o mirrors. The first mirror sits above the channel and its orientation can be adjusted to ensure that the light sheet is level and coincides precisely with the measurement plane. The second is inside a periscope extending down into the channel to bring the light sheet to the same height as the measurement plane. The periscope is 3.75 m downstream from the airfoil, ensuring that it does not disturb the flow in the test section.

Four fast frame-transfer CCD cameras (Imager Pro X 4M, LaVision) have 2112 x 2072 pixel resolution CCDs are dual frame and store data in 14-bit. They are mounted above the channel and oriented to image through the top of the channel as show in Figure 2.9 The two frames capture scattered light from the two laser pulses. The cameras were fitted with 50mm SLR lenses (Nikkor) to image the region-of-interest. Each CCD camera observes a different region on the measurement plane and the resulting vector fields from the four images pairs are stitched together in post-processing to produce one global field. A photograph of the camera setup is shown in Figure 2.11 (b)

A programmable timing unit (PTU) is a timing card which is housed in the control computer. It generates timing pulses that are used to accurately control the timing of laser pulses with the exposure to the two frames of the cameras.

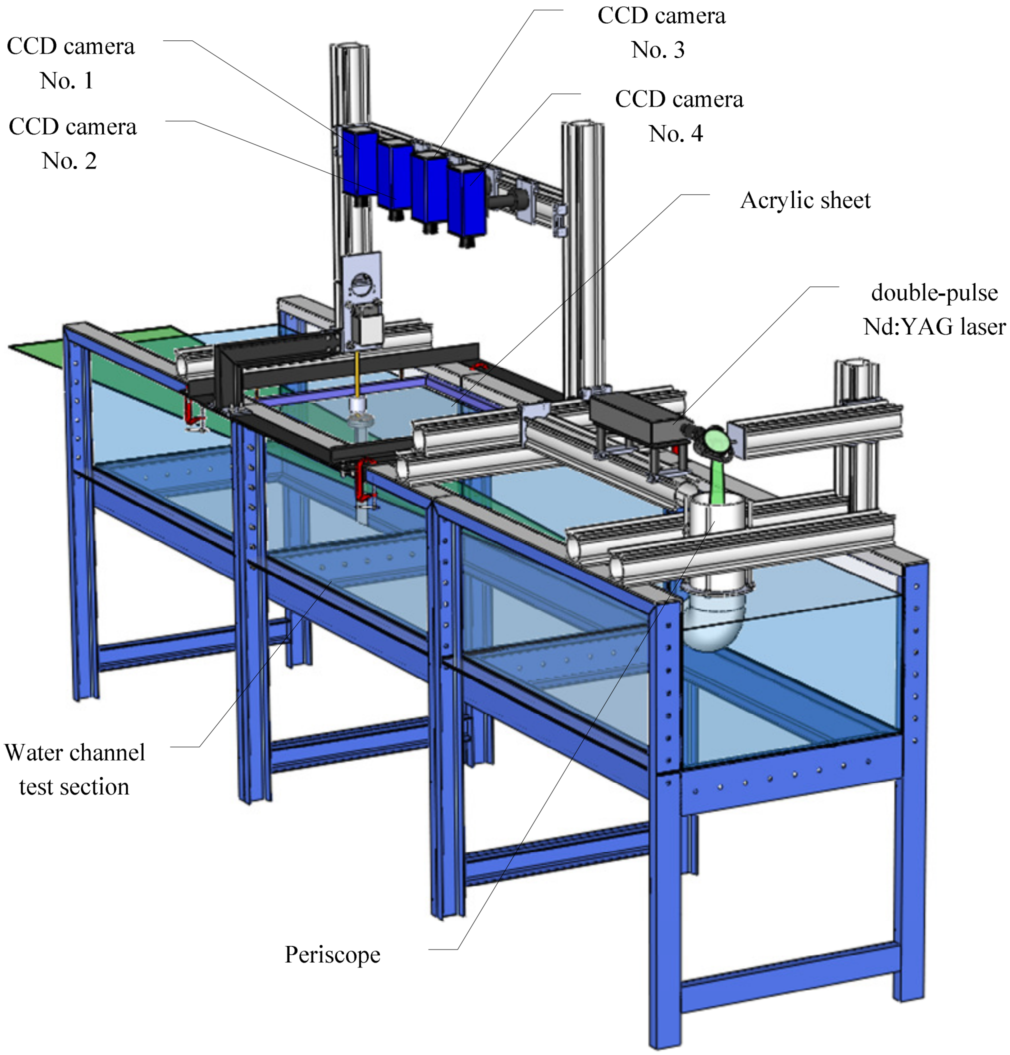

Figure 2.9:Imaging system schematic

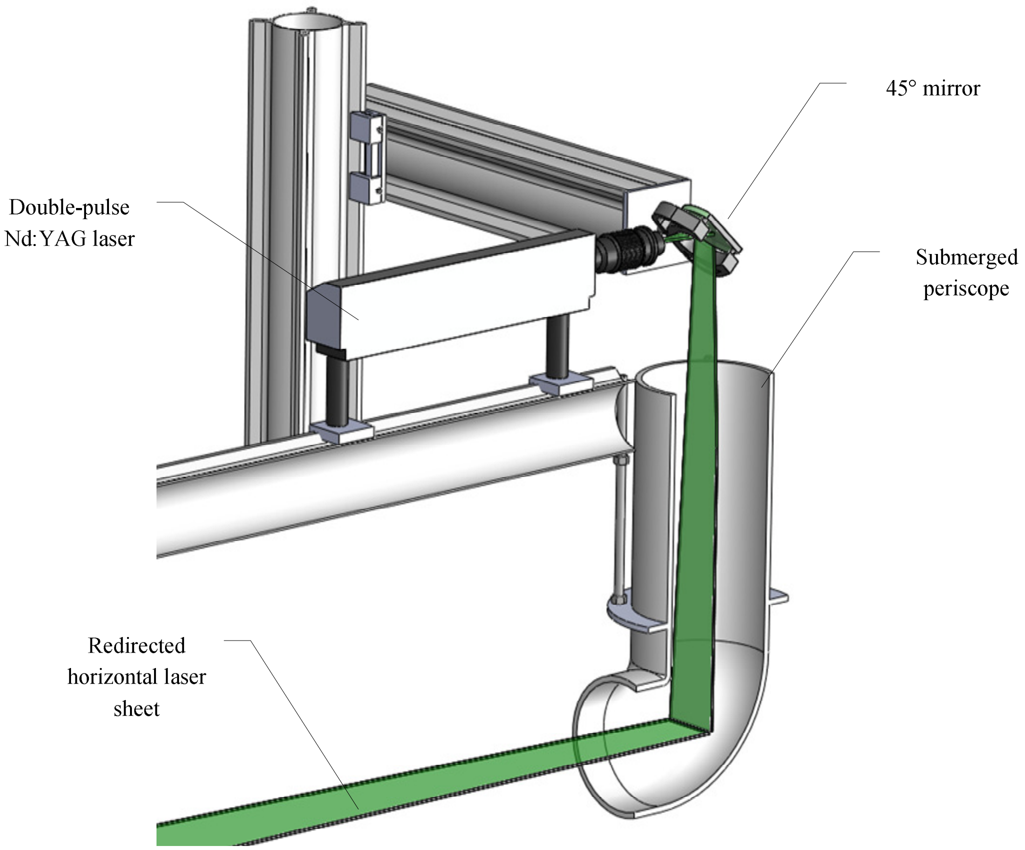

Figure 2.10:Laser optics and sheet orientation schematic

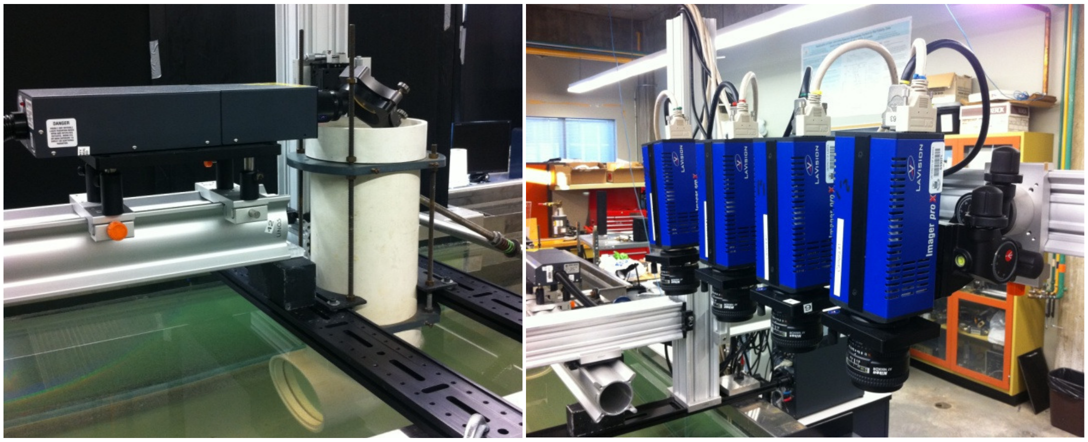

(a) (b)

Figure 2.11: a) laser mounting and b) 4 CCD cameras

2.4.3 Calibration

Calibration of the images generated by the cameras is used to map data from pixel space to real space and to remove optical and perspective distortion. Calibration is performed using a custom 300 mm × 800 mm 2D calibration target. The target is comprised of several equally spaced black dots 1.3 mm in diameter and spaced 3 mm on a square lattice. The calibration target is placed into the water channel such that its surface is coincident with the measurement plane. Due to the varying angles of each of the 4 CCD cameras with respect to the measurement plane, they have warped fields-of-view. Figure 2.12 is a schematic of the calibration target with the warped fields-of-view for the 4 CCD cameras along with the location of the NACA 0012 airfoil.

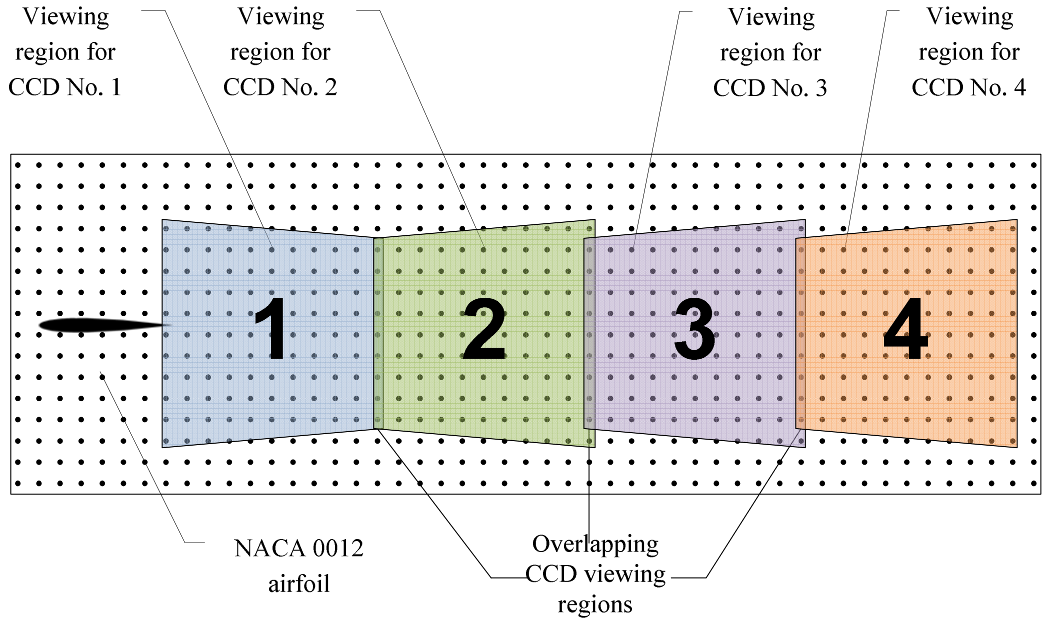

Figure 2.12: Calibration target with associated camera viewing regions and airfoil position

Cameras No. 2, 3 and 4 have similarly shaped fields-of-view which are slightly in forward scatter. Camera No. 1 however is different since its angle relative to the measurement plane is opposite to the other cameras. Camera No. 1 is relatively close to the mounting plate and must be oriented in this manner to avoid line-of-sight obstructions. An implication of this arrangement is that cameras No. 2,3, and 4 have similar intensity images while camera No.1 which is in slight back scatter will always have a lower intensity image. The cameras each take images of a distinct section of the flow; however, a small overlap region is used to perform accurate image stitching.

The images collected from the 4 cameras for calibration are processed by commercial PIV software (LaVision GmbH, DaVis 8.05) where the dots are identified and compared to their known distances on the calibration target. A third order polynomial mapping function was computed and the images collected by the cameras were de-wrapped. The calibration image taken from camera No.1 along with the associated de-warped image is shown in Figure 2.13.

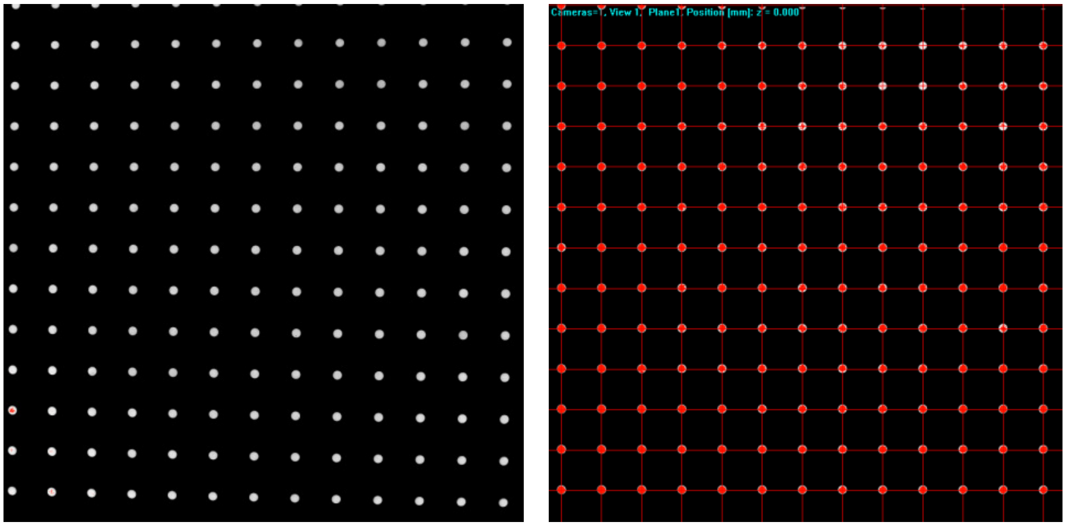

(a) (b)

Figure 2.13: Calibration target images from CCD No. 1 with (a) raw image and (b) de-warped image

2.4.4 Optimization of Δt

The Δt was optimized for every set of flow conditions with a built in function within the commercial software (LaVision GmbH, DaVis 8.05). This function takes several image pairs with varying Δt and computes the optimal Δt .

2.4.5 Image pre-Processing

Prior to cross-correlation of the image pairs, the raw images are preprocessed with commercial software (LaVision GmbH, DaVis 8.05). This step often gives rise to enhanced particle intensity and shape and ultimately leads to better correlation (Raffel et al., 1998), (Honkanen & Nobach, 2005). The correlation strength is often affected by disparity in the image intensity arising from light sheet non-uniformities, shadows, reflections or variations in particle size (Raffel et al., 1998).

In this thesis correlation strength is improved with the following image pre-processing methods: background intensity subtraction, sliding minimum subtraction and min-max filter for intensity normalization. In the equations that follow, I_n denotes the raw intensity distribution and I'_n denotes the preprocessed intensity distributions for the n^{th} of N raw PIV images. The subscripts ψ and ϕ refer to the x and y Cartesian coordinate of a given pixel in a $\Psi \times \Phi$ pixel image.

The background intensity subtraction method aims to reduce the effects of laser flare, shadows and other temporally consistent effects (Raffel et al., 1998). It does so by subtracting a background image that is recorded before the fluid is seeded. However this is often impractical and background subtraction is frequently achieved by subtracting the minimum intensity from each pixel from a sufficiently large set of raw images (Raffel et al., 1998). This is expressed mathematically by:

$$I'_{n_{\psi,\phi}} = I_{n_{\psi,\phi}} - \min\left[I_{n1_{\psi,\phi}} \dots I_{N_{\psi,\phi}}\right] \tag{2.3}$$

Merely subtracting the minimum intensity from each pixel is limited by its inability to track temporal variations in the background since it is essentially averaged over a large number of raw images. The sliding minimum subtraction method builds on the principles of background intensity subtraction. However, rather than subtracting the minimum intensity pixel as shown in *eqn. (2.3)* , it uses a sliding minimum filter given by:

$$I'_{n_{\psi,\phi}} = I_{n_{\psi,\phi}} - \mathrm{minA} \tag{2.4}$$

where:

$$A = \begin{bmatrix} I_{n_{\left(\psi-\frac{a-1}{2}\right),\left(\phi-\frac{a-1}{2}\right)}} & I_{n_{\left(\psi-\frac{a-1}{2}+1\right),\left(\phi-\frac{a-1}{2}\right)}} & \cdots & I_{n_{\left(\psi+\frac{a-1}{2}\right),\left(\phi-\frac{a-1}{2}\right)}} \\ I_{n_{\left(\psi-\frac{a-1}{2}\right),\left(\phi-\frac{a-1}{2}+1\right)}} & I_{n_{\left(\psi-\frac{a-1}{2}+1\right),\left(\phi-\frac{a-1}{2}-1\right)}} & \cdots & I_{n_{\left(\psi-\frac{a-1}{2}\right),\left(\phi-\frac{a-1}{2}-1\right)}} \\ \vdots & \vdots & \ddots & \vdots \\ I_{n_{\left(\psi-\frac{a-1}{2}\right),\left(\phi+\frac{a-1}{2}\right)}} & I_{n_{\left(\psi-\frac{a-1}{2}+1\right),\left(\phi-\frac{a-1}{2}\right)}} & \cdots & I_{n_{\left(\psi+\frac{a-1}{2}\right),\left(\phi-\frac{a-1}{2}\right)}} \end{bmatrix} \tag{2.5}$$

The reference background obtained with *eqns. 2.4* and *2.5* track changes in the background both temporally and spatially (Honkanen & Nobach, 2005),(A. M. Madej, 2010) and works with raw PIV data where the background is not always constant in time.

The min-max filter for intensity normalization method normalizes the intensities of particles by calculating the minimum and maximum intensity values of each pixel within a given *a* × *a* window. It then replaces each pixel within that window with the difference of these two values. The window size should be larger than an individual particle diameter, yet small enough to remove any significant spatial disparity in the background (Raffel et al., 1998).

2.4.6 Vector field correlation

The correlation was performed with commercial software (LaVision GmbH, DaVis 8.05). The primary goal of the correlation is to calculate the most statistically probable displacement between two groups of particles. The intensity distributions are subdivided into interrogation windows of fixed size and shape. All equivalent interrogation windows from the 2 frames of a given camera are cross-correlated with one-another giving rise to a correlation function. The correlation function is evaluated and its peak corresponds to a displacement vector $\vec{s}$. The velocity corresponding to a given interrogation window is approximated to first order by $\vec{u} = \vec{s}/\Delta t$ (Raffel et al., 1998). Figure 2.14 is a sample correlation function from a raw PIV data set taken from a 64×64 pixel interrogation window from camera No.1. The figure shows a strong correlation peak surrounded by relatively low noise.

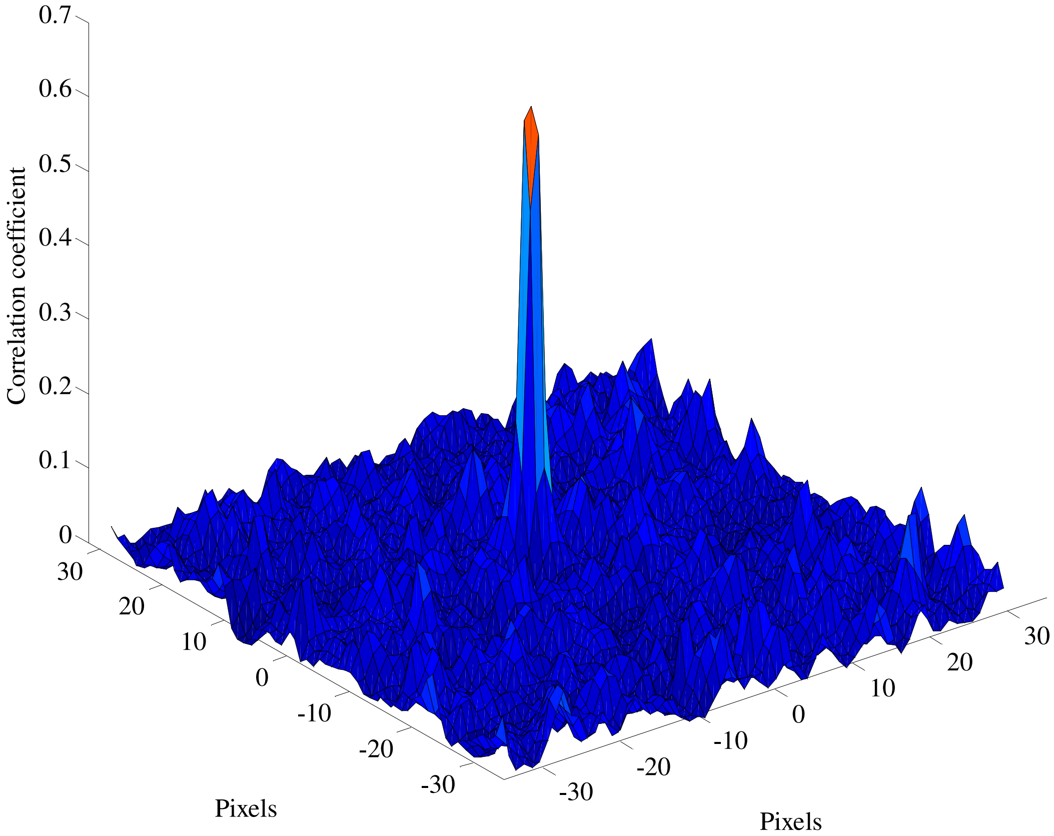

Figure 2.14: Example 3D correlation map from raw PIV data on CCD No.1

The noise floor seen in the Figure 2.14 can be reduced by performing a multiple pass interrogation. Essentially, a second interrogation pass is performed with a window offset that is equal to the displacement vector of the previous pass (Raffel et al., 1998). The current study employs 3 passes; the first pass with a 64×64 pixel interrogation window and the next two passes with 32×32 pixel interrogation windows and 50% overlap. The overlap refers to the percentage of the interrogation window that is common to 2 consecutive passes.

Figure 2.15 illustrates potential challenges in choosing appropriate interrogation window size based on the magnitude of local velocity gradients. The raw PIV intensity image for camera No.1 and frame No. 1 is shown and the trailing edge of the airfoil is seen on the left side of the figure. The flow immediately behind the airfoil experiences relatively large velocity gradients and the resulting 32×32 pixel interrogation window yields a poor correlation peak. In contrast, a larger 64×64 pixel interrogation window produces a much stronger correlation peak. Interrogation windows further downstream produce the strongest peaks, even for small interrogation windows; however, the interrogation window size is determined by the areas with large velocity gradients such as immediately behind the airfoil.

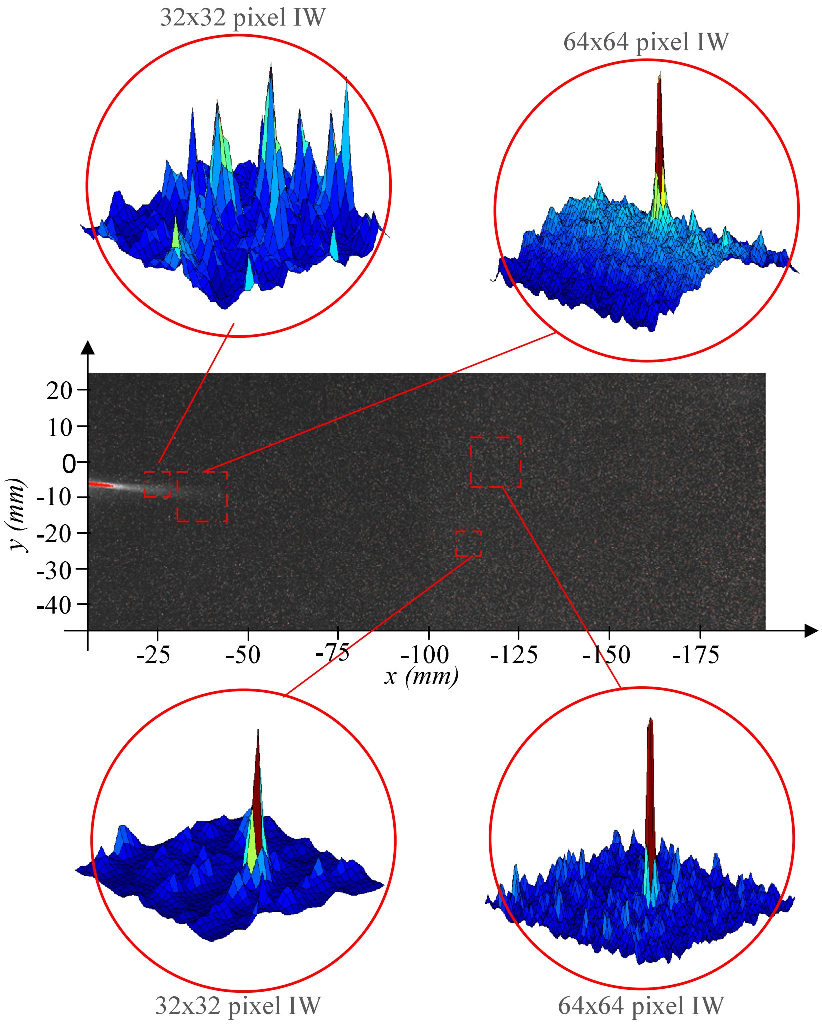

Figure 2.15: 3D correlation maps for 32 pixel and 64 pixel square interrogation windows: Top left: poorly defined peak; top right: well defined peak in noisy background; bottom left: well defined peak; bottom right, well defined peak (best correlation).

2.4.7 Vector field post-processing

In general, the vector fields obtained directly from the cross-correlation need to be smoothed and verified before other parameters such as vorticity and streamlines are calculated (Brown, Jones, Middleton, & Jones, n.d.). In this work the vector fields are post-processed with commercial PIV (LaVision GmbH, DaVis 8.05) and mathematical software (Mathworks Inc, Matlab). Visual inspection of the raw vector fields usually reveals incorrect velocity vectors having vastly different direction and/or magnitude compared to the neighboring vectors. Vector field post-processing automatically detects and replaces spurious vectors and generates a smooth field for future computation of derived quantities and statistical values (Raffel et al., 1998). The vector post-processing used in this study consists of a median test and Gaussian low-pass spatial filtering. In the *eqns.* to follow, $u_{i,j}$ and $v_{i,j}$ are the *x* and *y* components for the velocity vector $\vec{V}$ with Cartesian coordinates *i* and *j* in an $I \times J$ vector field array.

The median test rejects vectors whose magnitude or components of magnitude exceed a certain threshold ε_{thresh} when compared to the median of neighboring vectors (Raffel et al., 1998), (Adrian & Westerweel, 2011). The median velocity components of the surrounding vectors are defined by u_{med} and v_{med} , and valid vectors are expressed mathematically by:

$$\left|u_{med} - u_{i,j}\right| < \epsilon_{thresh} \tag{2.6}$$

and

$$\left|v_{med} - v_{i,j}\right| < \epsilon_{thresh} \tag{2.7}$$

Rejected vectors are replaced either by alternative correlation peaks or by interpolation (Adrian & Westerweel, 2011). Linear interpolation is among the simplest methods for replacing spurious vectors and is express mathematically by:

$$\tilde{u}_{i,j} = \frac{1}{2}\left(u_{i+1,j} + u_{i-1,j}\right) \tag{2.8}$$

and

$$\tilde{v}_{i,j} = \frac{1}{2}\left(v_{i+1,j} + v_{i-1,j}\right) \tag{2.9}$$

The fundamental properties of fluids mechanics impose a reasonable degree of continuity or coherency on PIV vector fields (Raffel et al., 1998). Linear interpolation may not produce entirely smooth vector fields if, for example, some nearby spurious vectors are considered in the calculation of *eqns. 2.8* and *2.9* (Raffel et al., 1998). To ensure smoothness in the vector field, a spatial Gaussian low-pass filter with $\sigma = 1$ is used in addition to the median test to further remove high frequency noise in the vector field.

2.4.8 Vector field stitching

The four individual vector fields obtained above were reassembled into one global coherent vector field with custom code (see Appendix C) developed with commercial mathematics software (Mathworks Inc, Matlab). Gaussian smoothing was only applied once and all four vector fields were stitched ensuring smooth transitions at the seams where the individual fields overlap. The stitching code receives input values for both x and y offsets for vectors fields generated from cameras No. 2, 3 and 4 relative to camera No.1. The offsets shown in Figure 2.16 are determined by visually inspecting a test image which has been de-warped according to the current calibration. Then, with all four fields of view displayed together, small manual adjustments are made to the various offsets until the image appears as a single coherent illustration. Overlap in the figure is exaggerated for the purpose of clearly conveying the offset dimensions. The overlapping regions assume the value of the downstream vector field and the edges are trimmed to produce a rectangular shaped vector field.

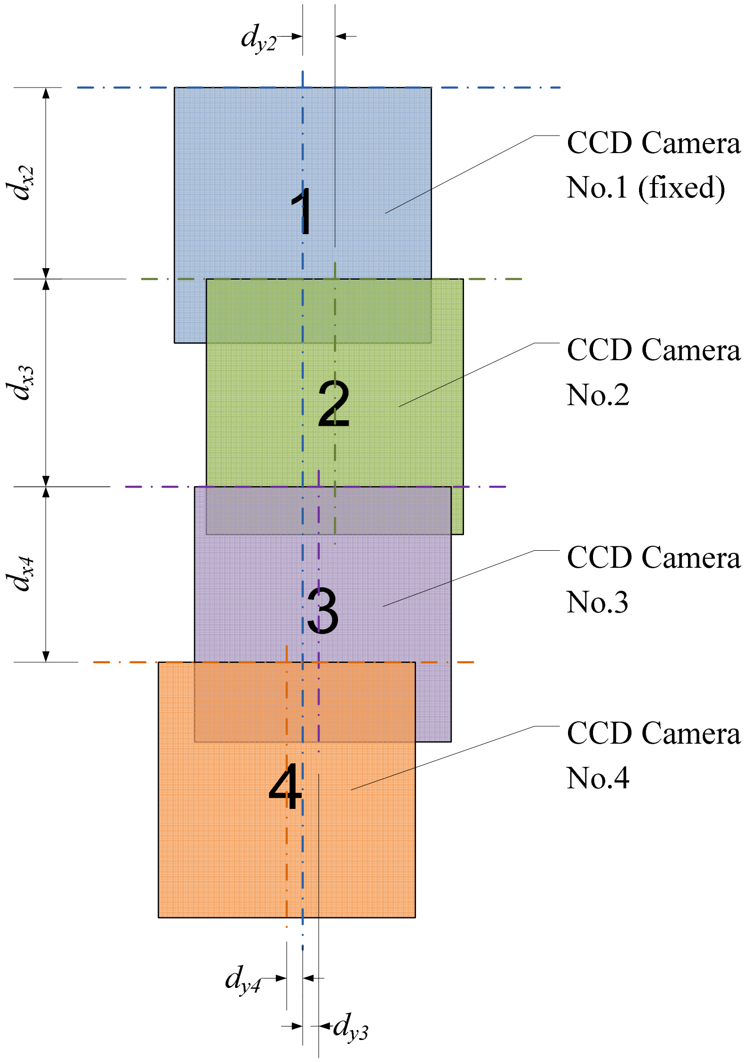

Figure 2.16: Vector field stitching schematic

2.4.9 Measurement uncertainties

An estimation of the PIV measurement uncertainty is used to assess the final accuracy of the measured velocity field. The individual components of the PIV system each contribute to the overall uncertainty in the system.

Uncertainty arises from the fidelity of the seed particle motion to represent local fluid motion. This uncertainty is due to particle slip in which the seed particles lag behind the fluid motion by some finite quantity. The slip velocity is computed to first order by (Adrian & Westerweel, 2011):

$$|v - u| = \left[\frac{(\bar{\rho} - 1)g\tau_o}{\bar{\rho}}\right] \tag{2.10}$$

with gravitational constant $g = 9.81\text{m/s}^2$, seed particle diameter $d_p = 18\mu\text{m}$ and time constant

$$\tau_o = \frac{\rho_p d_p^2}{18\nu_w \rho_w} \tag{2.11}$$

$\bar{\rho}$ is the density ratio taking into account the density of the seed particle and of water , $\rho_p = 600\text{kg/m}^3$ and $\rho_f = 998\text{kg/m}^3$ respectively.

$$\bar{\rho} = \rho_p/\rho_w \tag{2.12}$$

The slip velocity error of 0.47% relative to the freestream velocity of $U_\infty = 0.017\text{mm/s}$ is approximated to first order with *eqn. (2.10)*. Uncertainty due to varying image magnification over the image domain is corrected by calibrating with a calibration target; however, image magnification also varies over the thickness of the light sheet and the associated magnification uncertainty is on the order of 0.3% for most PIV arrangements (Adrian & Westerweel, 2011). The measurement uncertainty in determining the location of the correlation peak for a 8 pixel particle displacement is about 1-2% of the full scale velocity for similar planar PIV systems (Adrian & Westerweel, 2011), (A. Madej, Babazadeh, &

Nobes, 2011). Finally, uncertainty in the timing of events has a resolution of 10 ns and a jitter of less than 1 ns. (A. Madej et al., 2011).

2.5 Summary

An experiment apparatus designed to study the wake of a sinusoidally pitching NACA 0012 airfoil in a steady uniform flow of water is described. The flow facility consists of an open recirculating water channel with low turbulence characteristics. The mean waterchanel flow rate was monitored by a differential pressure transducer connected to an orifice plate flow meter on the main return line of the water channel.

The airfoil was driven about its aerodynamic center with a micro-stepping motor. The stepper motor has sufficiently high holding torque to avoid slipping or skipping steps under the dynamic pressure forces imposed on the airfoil by the moving fluid. The angular position of the airfoil is calculated to within one step angle by using the number of pulses sent to the stepper motor driver by the control board and multiplying by the applicable stepping resolution.

The flow velocity of a 2D slice parallel to the flow direction and across the water channel was characterized with a commercial PIV system comprising of four dual-frame CCD cameras for imaging, a two pulse Nd:YAG laser for illumination, and neutrally buoyant hollow glass spheres as seed particles. The raw PIV images were then preprocessed by:

- background intensity subtraction, for images with temporally constant backgrounds;
- sliding minimum subtraction, for images with temporally variant backgrounds;
- and min-max filters for normalizing the intensity of particles within an image.

The raw vector fields are computed with a multi-pass cross-correlation performed with commercial software. The raw vector fields were then post processed using a median test to remove any spurious vectors. The four individual vector fields were stitched together using custom code, and the global vector field was then passed a spatial Gaussian low-pass filter to further smooth the vector field and remove any discontinuities in the field, especially at the stitching seams.

This experimental procedure is the basis for the work presented throughout this thesis. Experiments from each chapter are accompanied by minor modifications to the basic setup which will be introduced and discussed in as needed.

CHAPTER 3: Vortex detection and characterization

3.1 Introduction

Vortices are essential flow features in a number of fluid flow applications. Vortex formation in the wake of airfoils and other streamlined bodies is important both in research and in practice. For example, numerous turbulent flow regimes are dominated by temporally evolving, spatially coherent structures which are generally regarded as vortices (Jeong & Hussain, 2006).

The study of flow around a pitching airfoil is useful for understanding undesirable effects such as wing flutter (Bohl & Koochesfahani, 2009) and more recently, for understanding biologically inspired aquatic propulsion (Schnipper et al., 2009), (Sarkar & Venkatraman, 2006). In this study a NACA 0012 airfoil submersed in a vertically aligned uniform flow field, is forced to oscillate sinusoidally about its aerodynamic center which is roughly the quarter chord distance. For the flow velocities tested, the wake downstream of the airfoil is comprised of coherent structures which separate from the trailing edge of the airfoil and travel downstream at a given drift velocity. For this type of flow, accurate detection and characterization of the coherent structures in the wake is a central focus for previous research (Bohl & Koochesfahani, 2009), (Gostelow, Platzer, & Carscallen, 2006), (Lai & Platzer, 1999). For a given Reynolds number, it is possible to generate several different wake schemes which are described by vortex position and organization in the wake (Schnipper et al., 2009).

The classification of the vortex populated wake is usually summarized using a phase diagram that maps the important wake transitions as a function of two independent dimensionless parameters. These are the Strouhal number based on the flapping frequency and dimensionless amplitude based on chord length (Godoy-Diana et al., 2009), (Schnipper et al., 2009). To generate these phase diagrams a reliable and accurate identification of the vortices in the wake is required. In addition to reliably detecting vortices, it is important to be able to compute several parameters that are used to describe the flow by aerodynamicists. In particular these include vortex core coordinates, vortex drift velocity, maximum vorticity, circulation, boundary radius and maximum circumferential velocity (Vollmers, 2001).

Approaches for vortex detection are often developed and tested on data obtained through direct numerical simulation (DNS) (Jiang, 2002), (Robinson, 1991). Performing vortex detection on PIV data can be more difficult because of measurement noise and experimental uncertainty in the data (Saikrishnan, Marusic, & Longmire, 2006). Measurement noise is usually attenuated by filtering prior to running a detection algorithm (Vollmers, 2001) but, thresholds must be carefully selected as not to overlook weak or small vortices (Saikrishnan et al., 2006). In addition, the flow field near the centre of the vortex experiences substantial gradients which can lead to seeding issues and poor correlation in the PIV data (Vollmers, 2001). While DNS data can employ local mesh refinement (Moin & Mahesh, 1998) to increase the spatial resolution in specific locations such as the vortex core, PIV detection algorithms must find other ways to overcome the sharp gradients near the core. Often, due to camera resolution, PIV data must be collected using a number of independent cameras which results in images that need to be de-warped and stitched together. This can introduce discontinuities in the flow-field image. Such discontinuities could contribute to elevated local vorticity which could be falsely identified as a vortex (Jeong & Hussain, 2006). PIV data is becoming increasingly available to experimentalists (Vollmers, 2001) and consequently, robust vortex detection and characterization algorithms that are specifically tailored for PIV data is an important topic in modern experimental fluid mechanics.

In this chapter a vortex detection algorithm has been developed by combining selected features from 3 individual algorithms. The algorithm must efficiently analyze the data and successfully detect and locate vortices as well as calculate characteristic vortex parameters. It is also essential to automatically diagnose and detect a false positive vortex without human intervention. This chapter explores the effectiveness of the proposed algorithm by studying the vortices in the well documented wake of a pitching symmetric airfoil (Bohl & Koochesfahani, 2009), (Godoy-Diana et al., 2009). The algorithm is also tested on a simulated Burgers vortex where the effects of adding white noise and of changing the grid resolution are studied.

3.1.1 Approaches to Vortex Detection

A precise definition of a vortex does not exist (Jeong & Hussain, 2006) and this makes them difficult to detect in practical flows. The most straightforward and widespread definition of a vortex is merely the perception of swirling movement of fluid about a central point (Jiang, 2002). It is difficult to translate such an intuitive notion, which is based on human perception, into a strict numerical characterization which can be detected by numerically driven algorithms.

Lugt (1979) suggested that "*A vortex is the rotating motion of a multitude of material particles around a common center*". This is consistent with the earlier definition however it does not introduce any new criteria for characterizing vortical structures, nor does it provide a valuable definition from which a vortex detection algorithm can be developed. Building upon the former definition, Robinson (1991) proposes that "*A vortex exists when instantaneous streamlines mapped onto a plane normal to the vortex core exhibit a roughly circular or spiral pattern, when viewed from a reference frame moving with the center of the vortex core*". This definition provides a precise geometric characterization however, detection of a vortex using this approach requires *a priori* information about the location of its core, making it difficult to implement a sensible systematic vortex detection procedure. It can, however, be a useful basis for developing an automated vortex verification algorithm. Jeong & Hussain (2006) also suggest that *"A vortex core must have a net vorticity, hence net circulation"*. This requirement excludes potential flow regions from vortex cores ultimately suggesting that an irrotational vortex is one with zero cross-section. This provides an instant means for identifying regions where vortices may reside without any previous knowledge of the location or drift velocity of a vortex core. Scalar vorticity fields are easily computed from the velocity vectors and regions of interest can then be generated and labeled. This definition combined with the definition of Robinson (1991) is a sensible foundation for developing a robust vortex detection algorithm.

Vortex detection methods are often carefully tailored to work with specific data types and specific flow-fields. As a result, they are tuned to detect precise structures based on unambiguous definitions of the vortices of interest (Jiang, 2002). The algorithms can be quite sensitive to parameters such as vortex spacing, should there be multiple vortices in a given flow-field, vortex size, angular velocity and the presence of shear flow (Vollmers, 2001).

Ari Sadarjoen (2000) suggests that the various vortex detection algorithms reported in the literature can be divided into two distinct groups. The first is a more traditional class of vortex detection algorithms based on evaluating physical quantities of the flow-field at specific points. Common parameters to measure are velocity, vorticity, pressure and the velocity gradient tensor. Ari Sadarjoen (2000) stressed that a major shortcoming of this class is that the algorithms are less sensitive to large, slow rotating vortices. For example, the maximum vorticity method (Jiang, 2002) defines a vortex core as a local maximum of vorticity magnitude. This method inherently ignores regions where the vorticity falls below a defined threshold and will likely fail to detect weak, slow rotating vortices.

A second group based on geometric methods represents a relatively new set of vortex detection algorithms. These algorithms rely on geometric features, such as streamlines and pathlines, rather than scalar properties evaluated at individual grid points (Jiang, 2002). While being more computationally demanding, they make up for a common deficiency in traditional methods with their ability to automatically distinguish false positives from actual vortices (Jiang, 2002), (Ari Sadarjoen, 2000).

3.2 Development of a vortex detection algorithm

The basic concepts and approaches to vortex detection that can be used in developing an algorithm can be explored by reviewing three vortex detection methods that have been used in the literature. These are the maximum vorticity (MV) method (Strawn, Kenwright, & Ahmad, 1999), the cross sectional lines (CSL) method (Vollmers, 2001) and the winding angle (WA) method (Portela, 1999). The following section discusses the main aspects of each which will be used to develop a combinatorial vortex detection (CVD) method for use on PIV data.

3.2.1 Maximum vorticity (MV) method

Strawn et al. (1999) proposed that a vortex core exists where there is a local maximum of vorticity magnitude. Maximum vorticity successfully identifies vortices in close proximity, where the cores may be overlapping (Jiang, 2002). However, a major drawback to this method is that vorticity does not only identify vortices, it also identifies regions where shearing activity occurs (Jeong & Hussain, 2006). This makes it more challenging to develop a vortex detection algorithm based solely on vorticity fields for non free-shear flow regimes (Jeong & Hussain, 2006), (Jiang, 2002). Alternatively, vorticity fields can provide a means of outlining a region-of-interest (ROI) where potential vortices might be located, and other algorithms will be used to evaluate these ROI individually.

For the CVD, a Gaussian low pass spatial filter was applied to the velocity data to produce a smooth field and eliminate any small scale fluctuations which could cause local spikes in the vorticity field. Scalar vorticity ω, computed numerically at every grid point, is defined from the two-dimensional velocity field $\vec{v}$ by:

$$\omega = \vec{\nabla} \times \vec{v} \tag{3.1}$$

In order to detect weak vortices with relatively low vorticity, a low vorticity threshold must be applied; however, this runs the risk of lumping stronger, closely spaced vortices into one single ROI where it would be evaluated as a single vortex structure. To circumvent this, multilevel thresholds are used and the resulting indexed image is analyzed with logical operators and image morphology (IM) techniques.

Multilevel threshold and image morphology algorithm

A multilevel threshold is applied with the intention that weak vortices may be identified without preventing the ability to distinguish strong vortices with overlapping cores or that are simply in close proximity. Figure 3.1 illustrates on two test case vorticity fields, how a three level threshold can be applied. The resulting indexed image along with a desired ROI map is shown for the two sample vorticity fields. The images in the left column of Figure 3.1 are the resulting indexed images where i=1,2,3 while the right column represents the desired ROI map that is to be extracted from the corresponding indexed image. Without a multilevel threshold, only one of the three threshold levels would be used and would lead to one of the following scenarios:

- When only threshold level 1 is used: The larger region, which clearly has two distinct peaks of vorticity, is lumped into one single ROI and is treated as a single potential vortex. However, this region has two distinct peaks and should be treated as two individual ROIs.
- When only threshold level 3 is used: The weaker vortices, do not meet the vorticity ω_{peak} level 3 threshold, are not considered to be ROIs and are not identified as potential vortices.

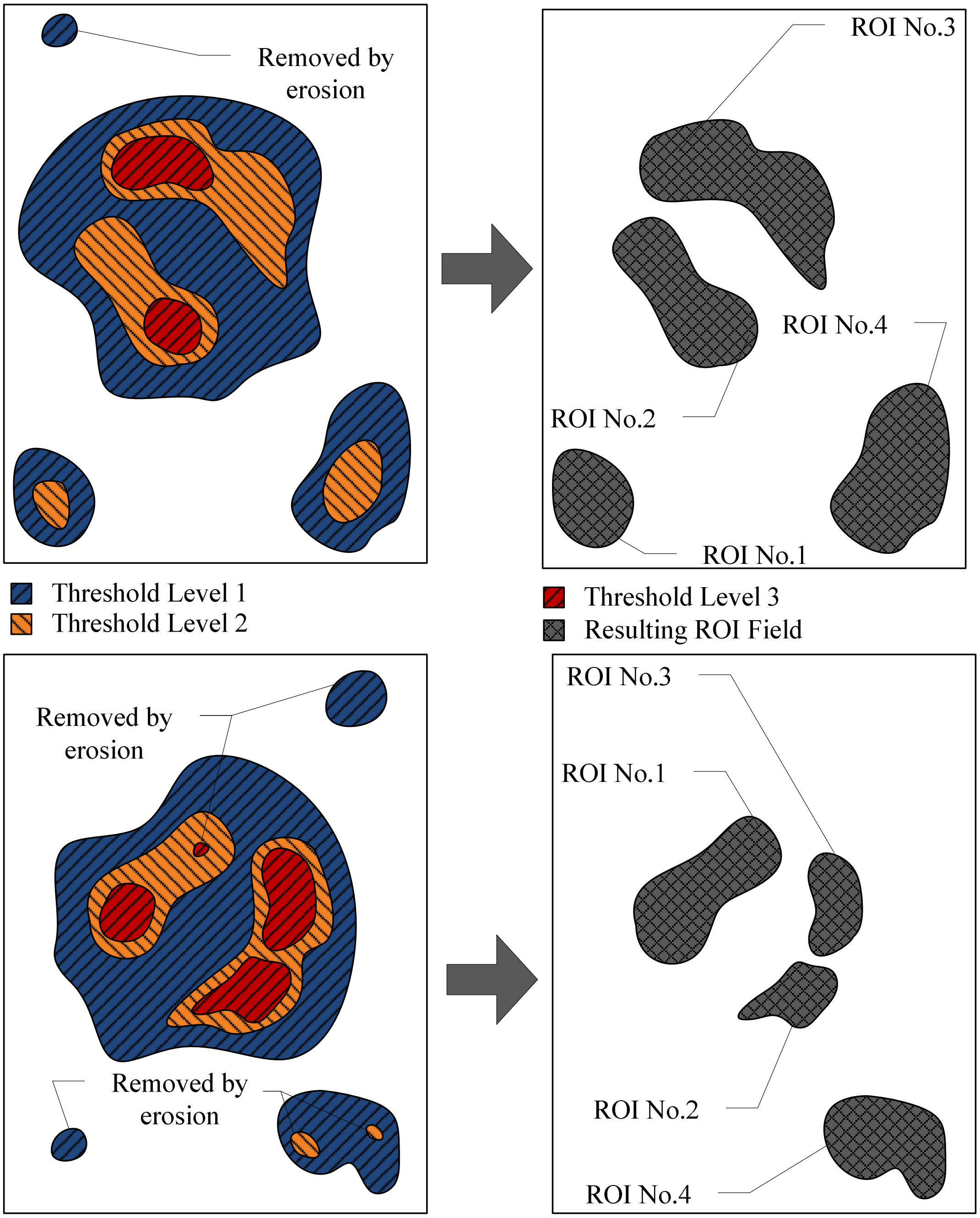

Figure 3.1: Result of multilevel threshold technique for two different cases on a supposed vorticity map

To overcome some of these major limitations of using a single level threshold to identify ROIs, an ROI map is generated with the algorithm outlined in Figure 3.2. The proposed algorithm thresholds the vorticity field returning an indexed image using the threshold values defined by the threshold intensity vector (TIV):

$$TIV = \langle TI_1, TI_2, TI_3 \rangle \tag{3.2}$$

Morphological opening is performed for each of the thresholds defined in *eqn. (3.2)*. It is a process which combines two basic image morphology techniques, erosion and dilation, and executes them in a specific order. First, the image is eroded with a diamond shaped structuring element of size $S_{e.}$ Clusters of pixels smaller than S_e are removed and those larger than size S_e are made smaller. Then dilation is performed with the same structuring element S_e to restore the clusters of pixels that were not removed by erosion to their original size.

Groups of connected pixels formed by index I_1 are first morphologically opened with an IM diamond shaped structuring element of size S_{e1} then they are labeled and investigated individually. Structures from index I_2 are first morphologically opened with an IM diamond shaped structuring element of size S_{e2}, then sub-labeled within each of the labeled groups from index I_1. If no groups from index I_2 are contained within a given group from index I_1 then the algorithm terminates and the group of pixels from index I_1 becomes a ROI. However, if at least one group from index I_2 is detected within a given index I_1 group, then pixels from index I_3 are morphologically opened with an IM diamond shaped structuring element of size S_{e3}, and subsequently sub-labeled within each of the index I_2 groups. At this point the algorithm counts the number of groups at each level. If multiple index I_3 groups are detected within an index I_2 cluster, then each individual index I_3 group forms a ROI. If only one index I_3 group is counted, then the algorithm falls back a level and considers the number of index I_2 clusters. Again, if multiple index I_2 groups are detected then each individual index I_2 group forms a ROI and, if only one index I_2 label is detected, the index I_1 group becomes the ROI. In this manner, the ROIs will always consider the largest possible area, but will separate into multiple ROIs when multiple distinct, higher vorticity peaks are detected.

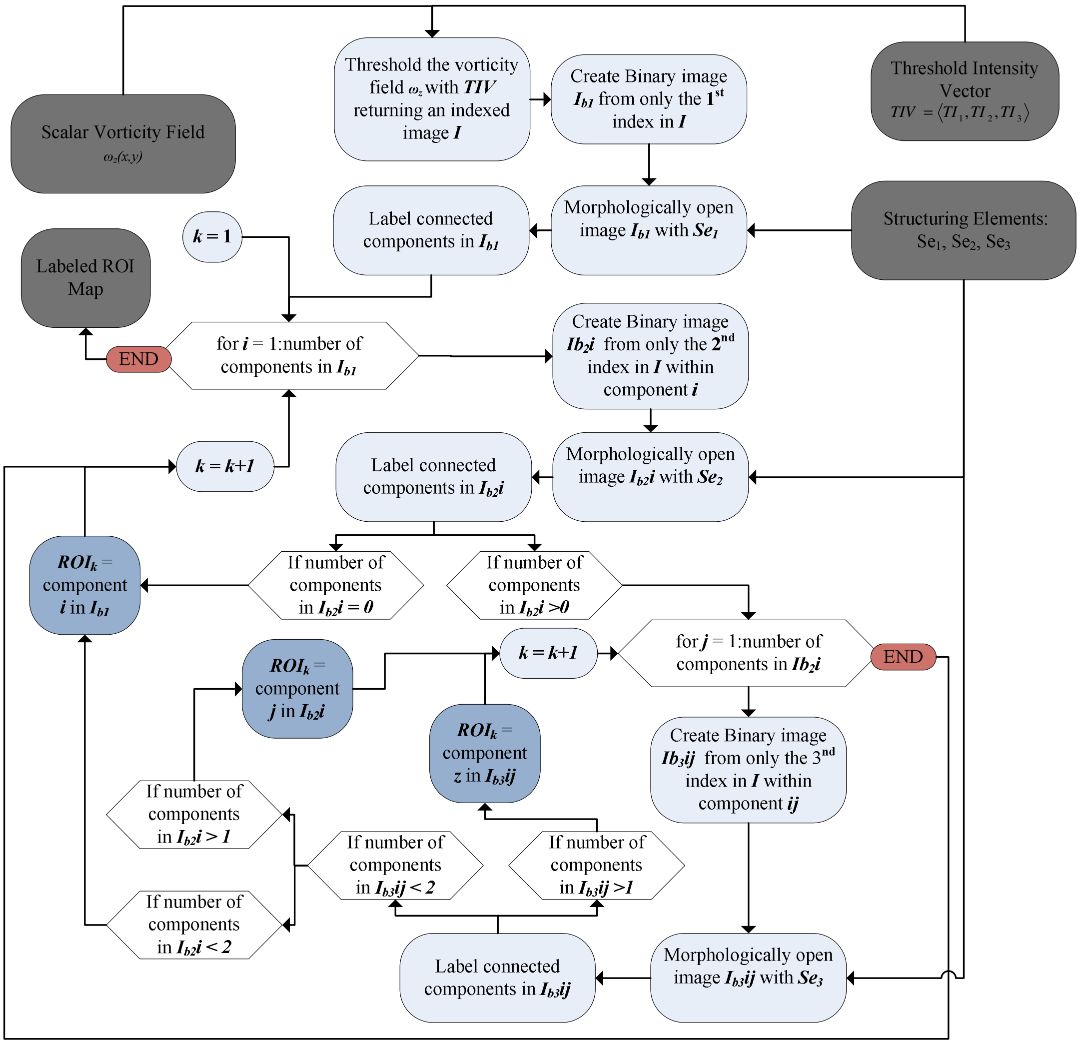

Figure 3.2: Multilevel threshold and image morphology algorithm schematic

3.2.2 Cross sectional lines (CSL) method

This method locates a potential vortex core in a given ROI by measuring the velocity component perpendicular to parallel straight lines (CSLs) cutting the ROI at an arbitrary angle (Vollmers, 2001). The cross sectional lines method is implemented and inspected for its ability to accurately and consistently locate vortex cores in ROIs which were identified and labeled with the MV algorithm. It is important to recognize that the CLS method does not detect vortices. It merely locates potential vortex cores and boundary radii. The method will output the two dimensional coordinates of a core whether or not a vortex actually exists in the current ROI.

A CSL algorithm similar to the one described by Vollmers (2001) is performed for each of the labeled ROI. A schematic outlining the essential CSL procedure is shown in Figure 3.3 where a sample vortex is shown. The concentric circles represent vorticity contours and the core is shown as a red '×'.

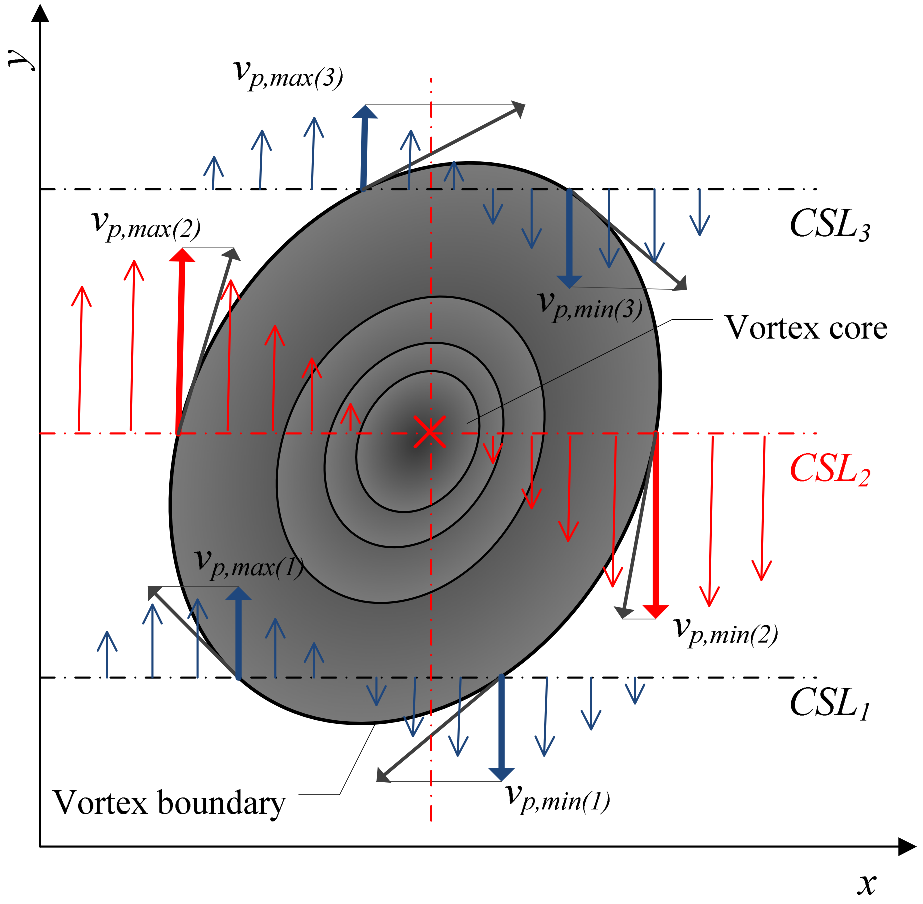

Figure 3.3: Cross sectional lines procedure schematic

For an $A \times B$ vector velocity field, the y-component of velocity $v_{y(i,j)}$ is evaluated for columns $i = 1,2,3 \ldots A$ and rows $j = 1,2,3 \ldots B$ along every row in each of the ROIs. When discussing the CSL method, velocity $v_{y(i,j)}$ is referred to as the perpendicular velocity $v_{p(i,j)}$. The maximum and minimum perpendicular velocities for each row j within a given ROI are defined as:

$$v_{p,\max(j)} = \max(v_{p(A_s,j)}, v_{p(A_s+1,j)}, \ldots, v_{p(A_e,j)}) \qquad (3.3)$$

and

$$v_{p,\min(j)} = \min(\, v_{p(A_s,j)},\, v_{p(A_s+1,j)}, \dots,\, v_{p(A_e,j)}) \tag{3.4}$$

The indices A_s and A_e refer to the first and last velocity vectors within a ROI on a given row respectively. The row ψ within the ROI with the largest difference $\left|v_{p,\max(j)} - v_{p,\min(j)}\right|$ is referred to as the critical CSL written as CSL_{ψ} and it represents the *y*-coordinate of a vortex core, should one exist in the ROI under evaluation. The perpendicular velocity along this row is then written as $v_{p(i,\psi)}$. The *x*-coordinate of the vortex core is the location on CSL_{ψ} where the velocity is:

$$v_{p(\varsigma,\psi)} = \frac{\left(v_{p,\max(\psi)} + v_{p,\min(\psi)}\right)}{2} \tag{3.5}$$

and the coordinates of the vortex core are then given by (ς, ψ).

For simplicity, the hypothetical vortex shown in Figure 3.3 only reveals three rows/lines of the v_y velocity field. The critical perpendicular line is $CSL_{\psi} = CSL_2$ and is plotted in red. A comparison with the other two lines reveals that CSL_2 has the largest difference between its maximum and minimum perpendicular velocities $v_{p,\max(2)}$ and $v_{p,\min(2)}$. Consequently, the *y*-coordinate for the hypothetical vortex core is $\psi = 2$. Evaluation of *eqn.* (3.5) along CSL_2 gives velocity $v_{p(\varsigma,2)}$. The algorithm searches for $v_{p(\varsigma,2)}$ along CSL_2 to find ς. The two computed coordinates locate the vortex core of a potential vortex in the ROI; however it does not determine whether the ROI truly does contain a vortex. Other vortex detection methods should be used to verify that a particular ROI contains a vortex. The CSL method provides an estimation of vortex size by fitting a circle of radius r_v centered at the core with length (Vollmers, 2001):

$$r_v = \frac{\left|\varsigma_{v,\max(\psi)} - \varsigma_{v,\min(\psi)}\right|}{2} \tag{3.6}$$

where, $\varsigma_{v,\max(\psi)}$ refers to the column index on row ψ where the velocity vector $v_{p,\max(\psi)}$ is located and $\varsigma_{v,\min(\psi)}$ refers to the column index on row ψ where the velocity vector $v_{p,\min(\psi)}$ is located. Finally, Vollmers (2001b) proposed that the transverse and streamwise components of the drift velocity $\vec{v}_{drift} = \langle v_{drift,x}, v_{drift,y}\rangle$ are respectively the *x* and *y* components of velocity evaluated at the core coordinate (ς, ψ).

Geometric methods such as the winding angle method require a reference frame moving at the core velocity of a vortex. This is especially challenging when the vortices do not have similar drift velocities and different sets of streamlines must be calculated for each reference frame belonging to each of the different drift velocities. Unlike most geometric methods, the CSL method can locate stationary and dynamic vortex cores and hence, a fixed reference frame is not necessary. In short, performing CSL does not require *a priori* knowledge of the location or velocity of the vortex core; it only requires pre-defined ROI where suspect vortices are potentially located. The CSL method is ideally suited for locating vortex cores and estimating vortex size and drift velocity in flow fields where little is known about the vortical structures present. The algorithm is performed on pre-defined ROI which are computed with the MV method. The CSL algorithm used in this study is summarized in the flow chart shown in Figure 3.4. The algorithm is comprised of two primary nested loops; one for the individual ROI and the second for the individual CSLs in each ROI. The input (shown as grey boxes) is comprised of the 2C2D global velocity field and the labeled ROI map.

A shortcoming of the CSL method is its inherent inability to reject false positives by identifying a vortex core in a ROI which does not contain a vortex. To overcome this problem, a hybrid detection algorithm comprised of the MV, CSL and a geometric method is proposed. Since geometric methods can effectively identify and reject false positives often ignored by other methods, when combined with geometric detection method and CSL method, a more robust detection method is obtained. The proposed geometric detection method is the winding angle (WA) method.

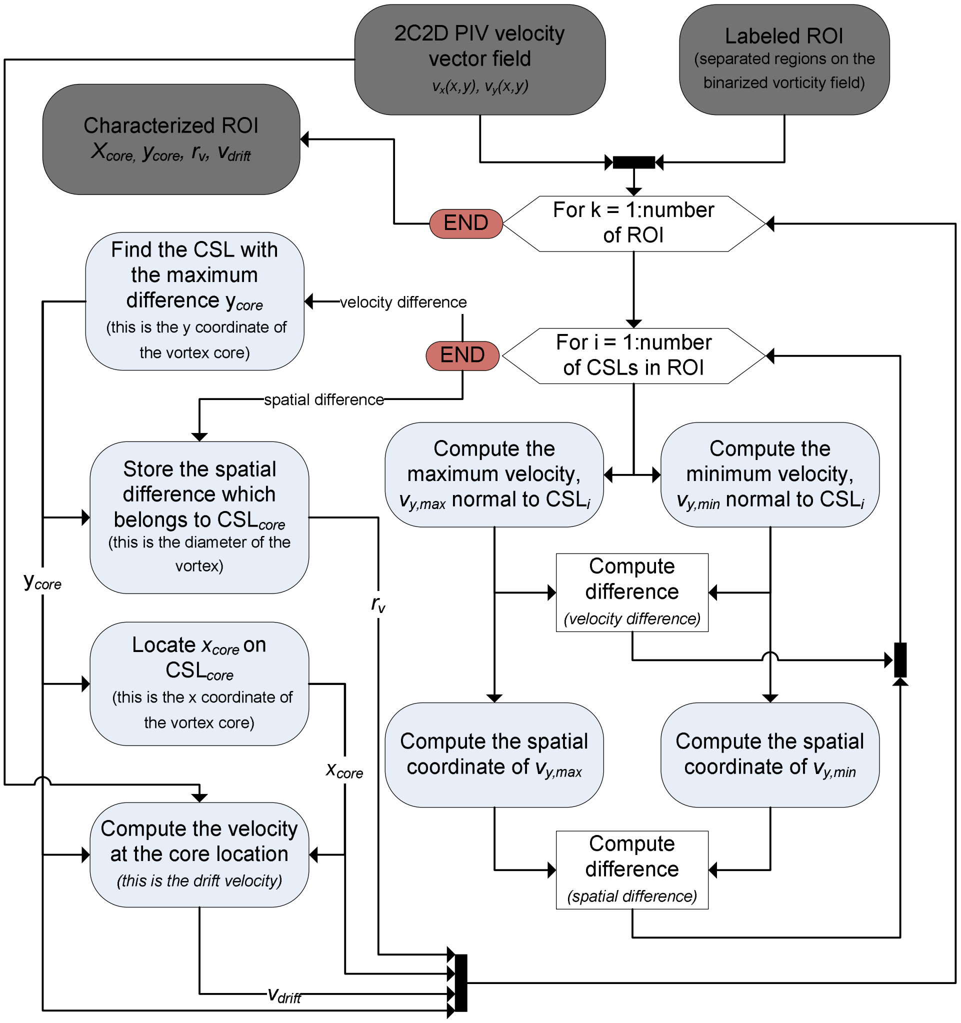

Figure 3.4: Cross sectional lines (CSL) algorithm flow chart

3.2.3 Winding angle (WA) method

The WA method, first proposed by Portela (1999), is a geometric vortex detection method which evaluates discretized streamlines and determines if they belong to a vortex. Ari Sadarjoen (2000) suggested that a streamline must satisfy two criteria to be considered part of a vortex. Firstly, the winding angle α_w along a streamline must be $\alpha_w \geq n2\pi$, where $(n = 1,2,3 \dots)$. Here the winding angle for streamline S_k is defined as the sum of all the angles ($\angle$) between line segments of a discretized streamline composed of *N* connected points P_k:

$$\alpha_{w,k} = \sum_{i=1}^{N-1} \angle\left(P_{k,i-1}, P_{k,i}, P_{k,i+1}\right) \tag{3.7}$$

A streamline belonging to a vortex is characterized by a closed semi elliptic path (Jeong & Hussain, 2006)(Ari Sadarjoen, 2000), (Pagendarm, Henne, & Rutten, 1999), (Perry & Chong, 1996) and the winding angle criterion alone is not enough to satisfy this requirement (Ari Sadarjoen, 2000). It is possible for a streamline to have a sufficiently large winding angle yet not follow a closed path; therefore, a second provision is necessary. The second criterion states that the distance between the starting and the ending point of a streamline should be reasonably small (Ari Sadarjoen, 2000). This second requirement is unfortunately qualitative since it depends on the length scale of the flow-field as well as the total length of the calculated streamlines.

Streamlines that comply with the two criteria above are then linked to a precise vortical structure. An automated process which groups all of the streamlines meeting the above criteria and tags them according to which vortex they are believed to belong to is described by Ari Sadarjoen (2000). This is done by mapping each streamline to a cluster point and then grouping all cluster points that are in close proximity. Each cluster point is the arithmetic average of the vertices which make up a given streamline. A maximum separation determines how far apart a cluster point must be from other points before it is marked as a new group. One particular limitation of this method is the separation distance must be specified *a priory* and it depends heavily on the vortex spacing of the flow field.

This method is well suited for detection of multiple vortices given suitable starting points for streamlines and predefined ROI with local velocity vector fields (Jiang, 2002). The local velocity vector fields must have a reference velocity that matches the drift velocity of the core. For this reason the WA method cannot be performed on a global field since the vortices can potentially have different drift velocities (Vollmers, 2001). As a constituent of the geometric vortex detection class, the WA method is computationally taxing (Jiang, 2002). However, for 2D flow fields computation time is not typically an issue. In addition, geometric methods are robust and unlike other traditional methods they can reliably distinguish false positives from true vortices (Jiang, 2002).

Closed streamline criteria

The WA method searches for streamlines that form closed paths by evaluating two specific requirements. It then groups the complying streamlines according to which vortex they are believed to belong to. The first requirement is that the 2D winding angle $\alpha_{w,k}$ for streamline S_k must be $|\alpha_{w,k}| = n2\pi$ where n is a positive integer (Ari Sadarjoen, 2000) The signed angle $\alpha_{k,i}$ between vectors $\overrightarrow{V_1}$and $\overrightarrow{V_2}$ on a given streamline is given by:

$$\alpha_{k,i} = \frac{\cos^{-1}\left(\overrightarrow{V_1} \cdot \overrightarrow{V_2}\right)}{\left|\overrightarrow{V_1}\right|\left|\overrightarrow{V_2}\right|}\left(\frac{\overrightarrow{V_n} \cdot \left(\overrightarrow{V_1} \times \overrightarrow{V_2}\right)}{\left|\overrightarrow{V_n} \cdot \left(\overrightarrow{V_1} \times \overrightarrow{V_2}\right)\right|}\right) \tag{3.8}$$

where,

$$\overrightarrow{V_1} = \langle (P_{x,(i-1)} - P_{x,(i-2)}), (P_{y,(i-1)} - P_{y,(i-2)}), 0 \rangle \tag{3.9}$$

and

$$\overrightarrow{V_2} = \langle (P_{x,i} - P_{x,(i-1)}), (P_{y,i} - P_{y,(i-1)}), 0 \rangle \tag{3.10}$$

and

$$\overrightarrow{V_n} = \langle 0,0,1 \rangle \tag{3.11}$$

Here, P_x and P_y are the respective (*x*,*y*) location on a given streamline and $\overrightarrow{V_n}$ is a unit vector normal to the flow-field of interest. Figure 3.5 demonstrates how the individual angles $\alpha_{k,i}$ are calculated on a section from streamline S_k. Here, the angle $\alpha_{k,i}$ measured from $\overrightarrow{V_1}$to $\overrightarrow{V_2}$ is CW. By the same convention, the next angle $\alpha_{k,(i+1)}$ would be CCW positive. The winding angle $\alpha_{w,k}$ for streamline S_k is determined by summing for all points on the streamline as follows:

$$\alpha_{w,k} = \sum_{i=2}^{N} \alpha_{k,i} \tag{3.12}$$

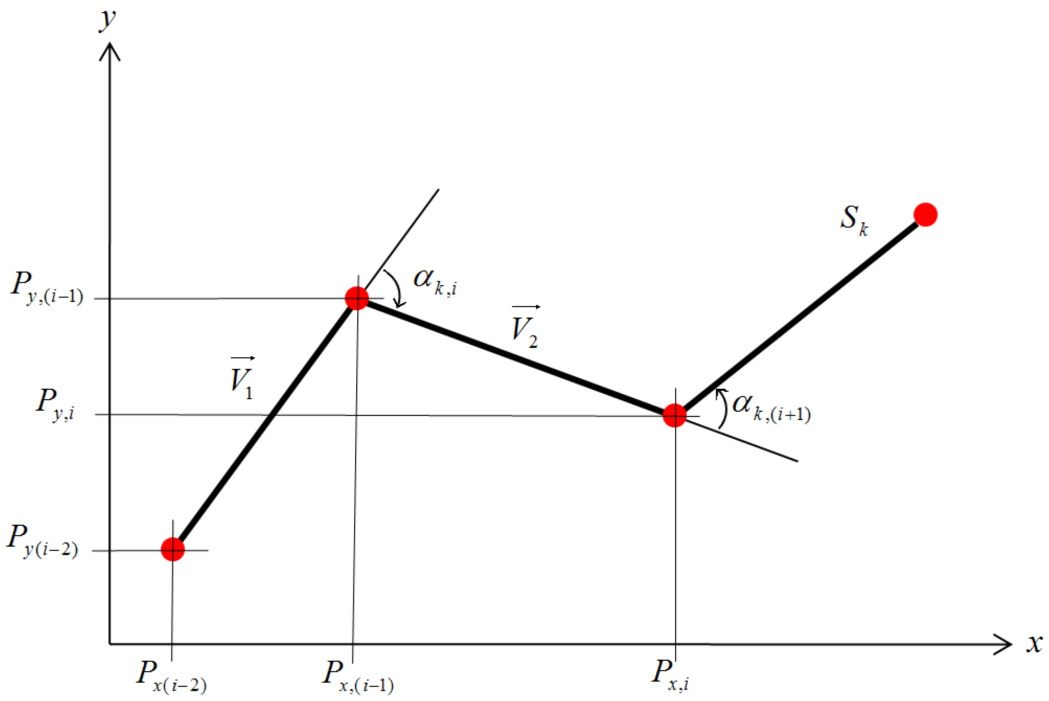

Figure 3.5: Computation of angle $\alpha_{k,i}$ on streamline S_k for the winding angle algorithm

The second requirement states that a streamline which is part of a vortex must have its starting and ending points relatively close together (Ari Sadarjoen, 2000). The distance between the starting ($P_{x,1}$, $P_{y,1}$) and ending point ($P_{x,N}$, $P_{y,N}$) of a streamline S_k shown in Figure 3.6 is given by:

$$D_{se} = \sqrt{\left(P_{x,N} - P_{x,1}\right)^2 + \left(P_{y,N} - P_{y,1}\right)^2} \qquad (3.13)$$

The starting location of a streamline is pre-defined and each streamline is comprised of a fixed number of points and a set spacing between them. Consequently, a streamline on a closed path can start and end anywhere on the path since the length of the streamline is a predefined value. Then, the maximum distance separating the start and end points of an arbitrary streamline on a closed circular path would be equal to the diameter of the circle defining that path. This identifies a major challenge for defining a D_{se} threshold, since streamlines on larger vortices require a large D_{se}; however, too large of a D_{se} threshold could lead to non-vortical streamlines being incorrectly associated to vortices. This is remedied by splitting streamlines when the cumulative sum of angles reaches the highest multiple of 2π. In this manner, the start and end points of a streamline on a closed path will always be a minimum.

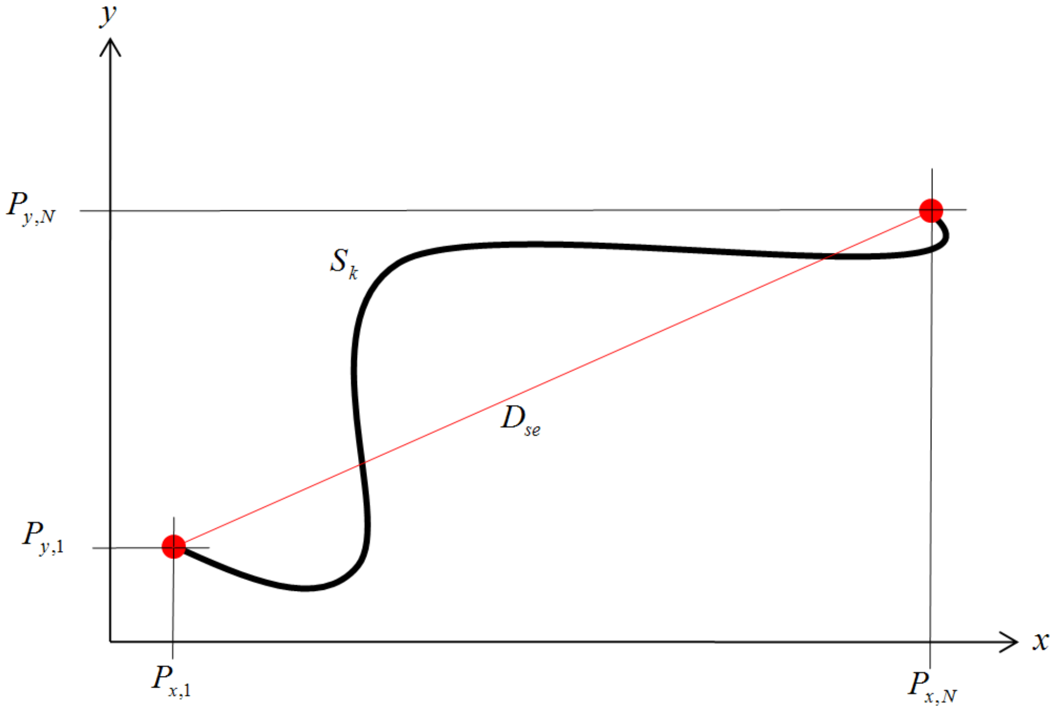

Figure 3.6: Computation of length D_{se} for the winding angle algorithm

Although the winding angle threshold is defined as $|\alpha_{w,k}| = n2\pi$; a suitable value for the threshold D_{se} must be selected. The D_{se} threshold depends on the length scale of the vortical structures present which unfortunately requires *a priori* knowledge of the expected size and spacing of the vortices in the flow field. The ROIs defined previously can be used to define a sensible threshold for D_{se}. Circles of radius r_v are fitted to the suspected vortices in each ROI. This parameter is a sensible length scale for coherent structures in the flow field of interest and a reasonable choice for the D_{se} threshold. This ensures that a streamline with a sufficiently large distance between its starting and ending points is not considered to be part of a vortex since its length scale would be much larger than any other structure in the current flow field.

The final task of the algorithm is to determine whether the individual streamlines conform to the specified thresholds. Streamlines that pass all the required criteria are marked and numbered. The sign of the winding angle $\alpha_{w,k}$ for each streamline determines the direction of rotation of the vortex associated to that streamline.

Mapping each streamline to a point and clustering

It is possible for an ROI to enclose multiple vortices. If this is the case it becomes necessary to label all of the closed streamlines accordingly. This is done by first mapping each of the closed streamlines to a point, then labeling clusters of closely grouped points (Ari Sadarjoen, 2000). The vortical streamlines S_k are mapped to points MP_k in the following manner:

$$MP_{x,k} = \frac{1}{N}\sum_{i=1}^{N} P_{x,i} \tag{3.14}$$

and

$$MP_{y,k} = \frac{1}{N}\sum_{i=1}^{N} P_{y,i} \tag{3.15}$$

The distance between MP_k and some other point $MP_{k'}$ is calculated as follows:

$$D_{MP_{k,k'}} = \sqrt{\left(MP_{x,k} - MP_{x,k'}\right)^2 + \left(MP_{y,k} - MP_{y,k'}\right)^2} \tag{3.16}$$

The first point MP_1 defines the first cluster group. If the distance between MP_1 and MP_2 is within a prescribed tolerance, then MP_2 is labeled as group 1, if the distance exceeds the tolerance, then MP_2 defines a new group. For point MP_3 , both distances $D_{MP_{3,1'}}$ and $D_{MP_{3,2}}$ are calculated. If neither value is within tolerance, then MP_3 defines a new cluster group. However, if either $D_{MP_{3,1'}}$ or $D_{MP_{3,2}}$ are within tolerance then MP_3 will belong to the closest group. All other points are labeled in this manner. Finally, once all of the streamlines are labeled, their arithmetic average is computed for each cluster group.

The WA algorithm used in this study is summarized by way of the flow chart shown in Figure 3.7. The algorithm is comprised of three nested loops: one investigates the ROIs, the second is for the instantaneous streamlines within each ROI and the third loop is concerned with the individual grid-points comprising each streamline. The input consists of the streamlines calculated from local velocity fields having a reference velocity equal to the drift velocity of the corresponding ROI.

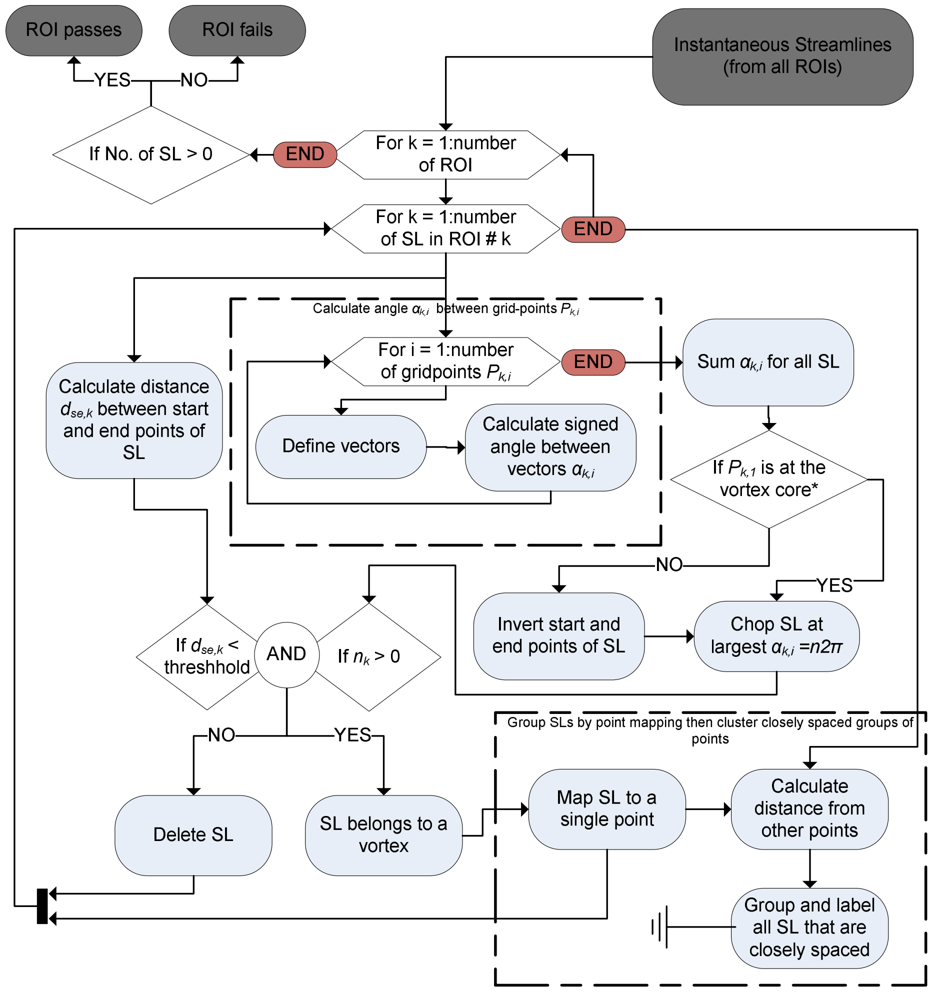

Figure 3.7: Winding angle algorithm flow chart

Limitations

The winding angle method is particularly sensitive to the reference velocity chosen for the computation of the required streamlines and hence, does not provide accurate estimates of vortex boundary in the event that the reference velocity is not precisely that of the vortex core. While the WA method does not generally provide a good estimate of vortex size and shape, it is extremely robust when it comes to eliminating false positives (Ari Sadarjoen, 2000).The WA method serves as a means of verifying if other detection techniques are accurate. The most apparent way to determine if a detection algorithm truly locates a vortex is by visual inspection. However, this seems counter intuitive since automation is the primary value of detection algorithms. For this reason, the WA method serves as a swirling flow verification once potential vortex core location and drift velocity are computed via other detection methods.

3.2.4 Other methods

A brief discussion of other vortex detection methods is presented for completeness. However, only the three methods discussed above will be used for the combinatorial detection algorithm.

Curvature centre method

Ari Sadarjoen (2000) developed the curvature centre method to locate vortex cores in two-dimensional flows. This method suggests that the centers of curvature for each grid-point on a streamline which belongs to a vortex should accumulate at a single point. The center of curvature points for all points on streamlines S_k of vortex V_i are calculated. These points form a new scalar field called the curvature density field (Ari Sadarjoen, 2000). It is possible to estimate the location of vortex cores by locating peaks in the curvature density field. Perhaps the most important limitation of this method is its tendency to detect false peaks when the streamlines are not perfectly circular. Ellipsoid shaped vortices are fairly common, especially if two closely spaced vortices are in the process of merging. For this reason the curvature centre method is not an ideal choice for core detection in the flow field of interest.

Discriminant of non-real eigenvalues of gradient matrix (*DEG*)

Vortices exist for imaginary eigenvalues of the gradient matrix of the velocity field. By this logic, Vollmers 2001 suggested that vortices can be separated from other patterns by evaluating the sign of the discriminant d_2 of non-real eigenvalues of the gradient matrix of velocity. The gradient matrix of velocity G and its discriminant of non-real eigenvalues d_2 are expressed as:

$$G = \begin{bmatrix} \frac{\partial u}{\partial x} & \frac{\partial u}{\partial y} \\ \frac{\partial v}{\partial x} & \frac{\partial v}{\partial y} \end{bmatrix} \tag{3.17}$$

and

$$d_2 = \left(\frac{\partial u}{\partial x} + \frac{\partial v}{\partial y}\right)^2 - 4\left(\frac{\partial u}{\partial x}\frac{\partial v}{\partial y} - \frac{\partial u}{\partial y}\frac{\partial v}{\partial x}\right) \tag{3.18}$$

The gradient matrix of velocity is calculated numerically at every grid-point and vortices are believed to exist where d_2 is negative. The evaluation of the derivatives may require smoothing of the data field. Unlike the maximum vorticity method, DEG does not confuse shear regions with vortices, but it also does not provide the direction of rotation of vortices. While the DEG method is able to distinguish most shear regions from vortices, it may still confuse circular or elliptic shaped shear and boundary layers for vortices. In addition it cannot distinguish two vortices with overlapping cores as can the MV method with appropriate use of multilevel thresholds.

Comparison

Table 3.1 compares the relevant vortex detection methods discussed. The various vortex detection methods are categorized by class as being either physical quantities or geometric, the required input data and their ability to detect multiple vortices. Summarizing remarks are included.

Table 3.1: Comparison of physical quantity (PQ) and geometric vortex detection methods

Detection Method	Class	Input	Detection of multiple vortices	Remarks
MV	PQ	vorticity field	yes	Inability to distinguish between a vortex and high shear regions.
CSL	PQ	velocity field	in predefined ROI	Provides drift velocity core location and boundary radius
WA	geometric	streamlines	in predefined ROI	Ability to detect false positives, but requires calculation of several streamlines.
DEG	PQ	velocity gradient	yes	Cannot distinguish vortices with overlapping cores.
CCD	geometric	streamlines	in predefined ROI	Only works with circular shaped vortices.

3.2.5 The combinatorial vortex detection (CVD) method

The CVD method was developed using a combination of the first three detection algorithms and simple image morphology techniques. An aim in the development of the method was that it must consistently detect and characterize multiple vortices from PIV generated velocity vector maps. It must label each vortex in the flow field and locate the vortex cores, the drift velocity, the circulation, the peak vorticity and boundary radii of the individual vortical structures. Ultimately, the method must reduce the size of the original dataset, by accurately conserving important vortex parameters.

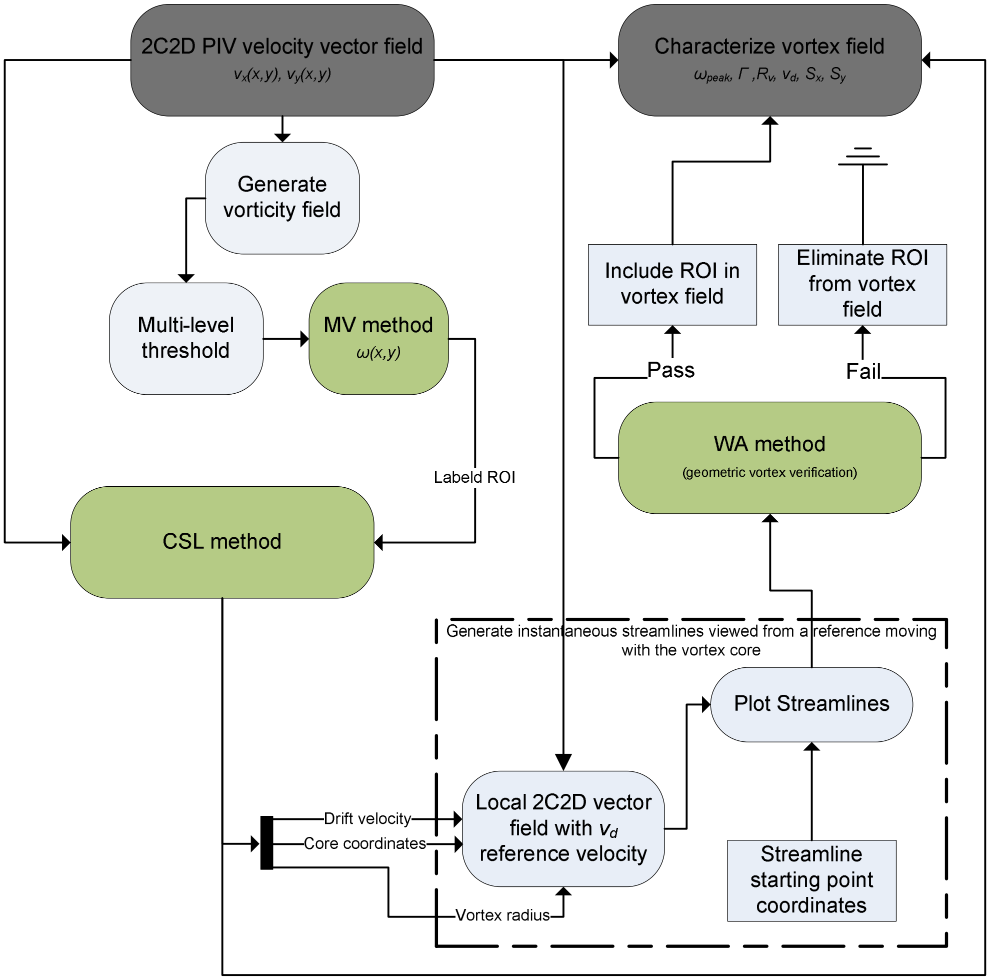

Figure 3.8: Combinatorial (CVD) algorithm flow chart with the 3 individual algorithms displayed in green

The CVD algorithm is summarized in the flow chart shown in Figure 3.8. The three individual detection algorithms are displayed as green boxes and the input and outputs (grey boxes) are the 2C2D velocity vector field and the characterized vortex field respectively. The 2D scalar vorticity field is generated from the global velocity map. The vorticity field is indexed by the multilevel threshold algorithm. Combined with the MV technique, sensible ROI are generated and labeled. The CSL method evaluates each ROI individually and outputs coordinates for the vortex core, the boundary radius and the drift velocity. It is important to remember that the CSL algorithm will report these vortex parameters regardless of a vortex being present emphasizing the CSL method's inability to determine if a vortex exists within a given ROI. This shortcoming suggests a third algorithm be used to validate the presence of a vortex in a ROI. The WA method can achieve this by searching each individual ROI for closed streamlines and automatically confirm or deny the presence of one or multiple vortices. To be consistent with the definition given by Robinson (1991), the WA method requires instantaneous streamlines computed from a reference frame traveling with the vortex core (Vollmers, 2001). This implies that there must be *a priori* knowledge of the vortex, specifically its core coordinates and drift velocity. This is particularly challenging since unlike CSL and MV, WA cannot be performed on the global coordinate system. Instead, local velocity vector maps must be generated for each ROI where the drift velocity, calculated from CSL is subtracted prior to computing the streamlines. Finally, the WA method either accepts a ROI and labels it as a vortex, or it rejects it.

3.3 Verification on a simulated flow field

The CVD algorithm is tested on a simulated 15 mm × 15 mm flow field containing an axisymmetric Burgers vortex at the center of the region.

The Burgers vortex solution is a vortex model often used to illustrate important elements of modern turbulence theory (Gibbon, 1999). The Burgers vortex represents an exact solution to the cylindrical Navier-Stokes equations where flow on a cylindrical vortex core inducing a circulation Γ_∞ at large distances is modeled (Drazin & Riley, 2006). The circumferential velocity v_θ and vorticity distribution ω of an axisymmetric Burgers vortex in a fluid with kinematic viscosity ν and radius r_v is (Prochazka & Pullin, 1998):

$$v_\theta(r) = \frac{\Gamma_\infty}{2\pi r}\left(1 - e^{-\frac{\gamma r^2}{4\nu}}\right) \tag{3.19}$$

and

$$\omega(r) = \frac{\gamma\Gamma_\infty}{4\pi\nu}\left(e^{-\frac{\gamma r^2}{4\nu}}\right) \tag{3.20}$$

Where γ describes the axial strain $\partial w/\partial z$ in a velocity field $\vec{u}$ described by an irrotational, pure strain, component $\vec{u}_s = (\alpha x, \beta y, \gamma z)$ and a rotational component confined to the xy plane $\vec{u}_w = (u_x, u_y, 0)$. For the case of an axisymmetric Burgers vortex $\gamma > 0$ and $\beta = \alpha = -\gamma/2$ (Prochazka & Pullin, 1998).

The simulated field has $I \times J$ velocity vectors. The $i^{\text{th}} \times j^{\text{th}}$ velocity vector, where i refers to indices in the x direction and j in the y direction, is expressed by $\vec{v}_{(i,j)} = (v_{x(i,j)}, v_{y(i,j)})$. The vortex travels in the negative y direction at the freestream velocity of $U_\infty = -2.25\ \mathrm{mm/s}$. The vortex has a peak vorticity of $\omega_{peak} = -3.96\ \mathrm{s}^{-1}$, a boundary radius of $r_v = 3.18\ \mathrm{mm}$ and induces a circulation of $\Gamma_\infty = 100\ \mathrm{mm}^2/\mathrm{s}$ at far distances. The effects of changing the flow field's grid resolution and adding white noise to the velocity vectors are investigated. This simulation is useful in determining the minimum grid resolution and the maximum velocity field noise for accurate use of the CVD algorithm on a universal flow field. The simulated vector field is shown in Figure 3.9 and the background color map indicates velocity magnitude. Figure 3.10 shows the simulated velocity field with the freestream velocity subtracted and with a background color map of vorticity.

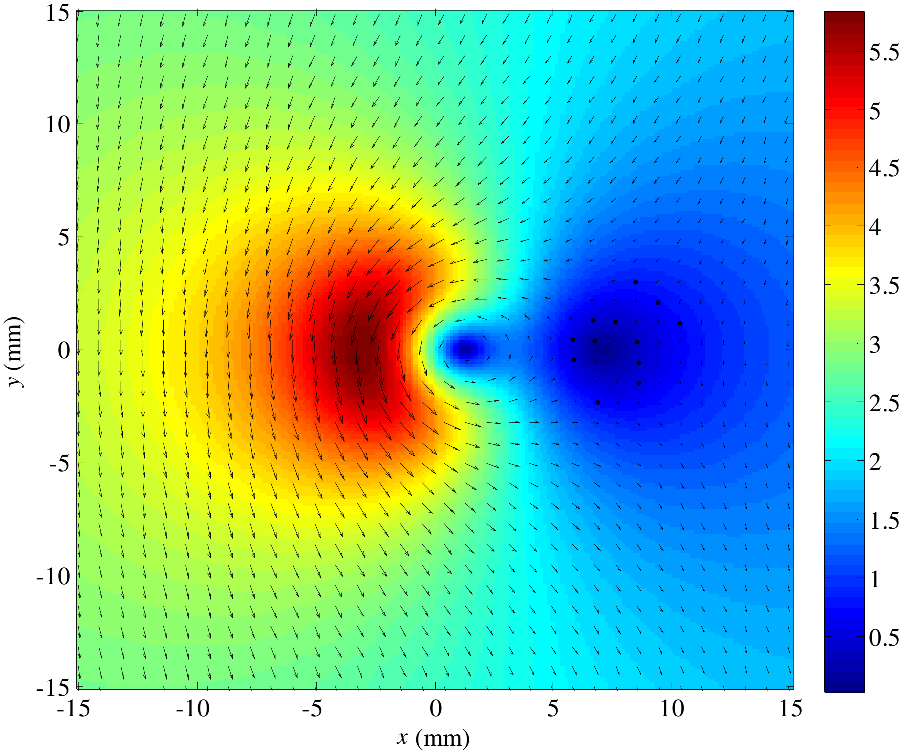

Figure 3.9: Simulated velocity vector field showing every 6th vector with velocity magnitude $\|v\|$ (mm/ s)in the background.

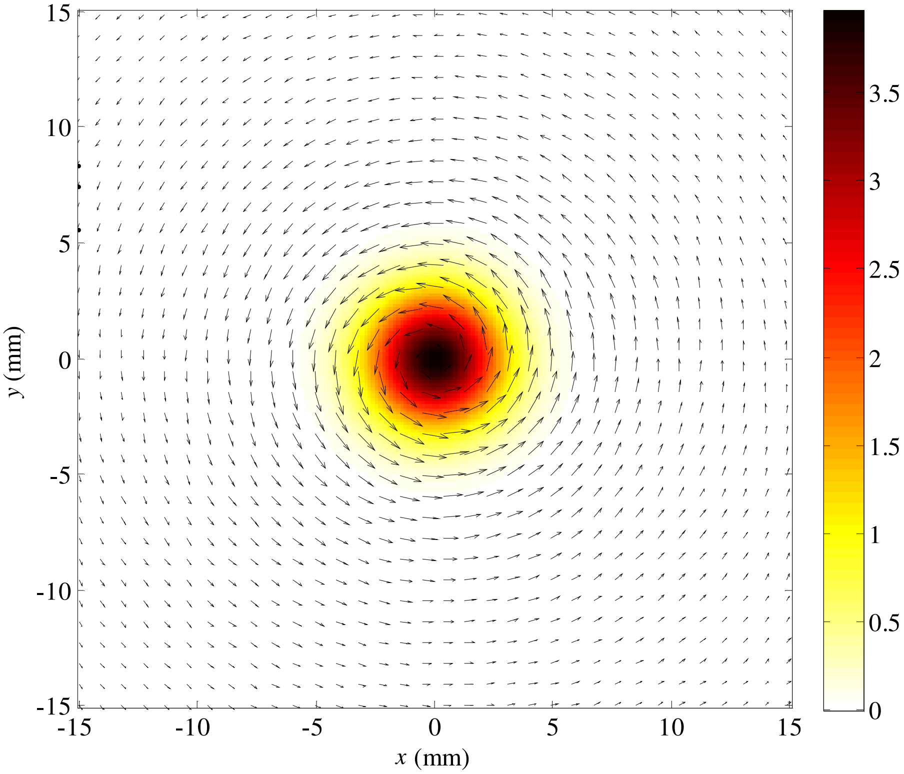

Figure 3.10: Simulated velocity vector field with freestream U_∞ subtracted, showing every 6th vector and with vorticity ω (s^{-1}) in the background.

The resolution is expressed by the number of velocity vectors (*vv*) that span the vortex diameter $\emptyset_v = 2r_v$ with the ratio $vv/\emptyset_v$. This identifies the minimum number of velocity vectors spanning the diameter of a vortex that are required to accurately identify and characterize it. Figure 3.11 shows the vortex radius computed by the CVD algorithm for various values of $vv/\emptyset_v$. Vortices with $vv/\emptyset_v < 5$ are rejected by the WA and considered to be type II errors. Based on the expected radius of $r_v = 3.18$ mm, computation of vortex radius for $r_v = 3.18 \text{ mm} \pm 5\%$ occurs for $vv/\emptyset_v > 17$.

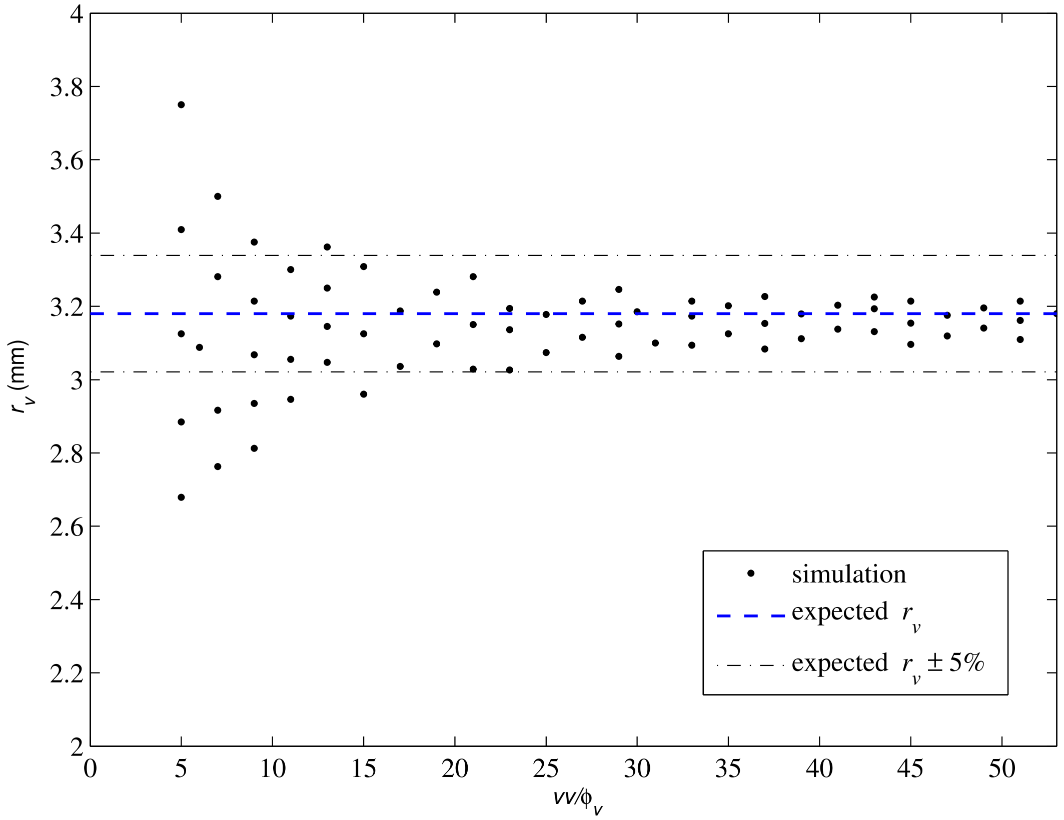

Figure 3.11: Vortex radius r_v vs. the number of velocity vectors per vortex diameter $vv/\emptyset_v$

Figure 3.12 shows the vortex circulation Γ computed by the CVD algorithm for various values of $vv/\emptyset_v$. No circulation is calculated for $vv/\emptyset_v < 5$ since the WA rejects the associated vortices. The circulation computed with the CVD is the core-region circulation. It represents only the circulation induced within the vortex boundaries (for $-r_v \geq r \geq r_v$) This value is expected to be smaller than $\Gamma_\infty = 100\ \mathrm{mm}^2/\mathrm{s}$ which is the circulation induced by the vortex at large distances (as $r \rightarrow \infty$). Using circulation $\Gamma_\infty = 100\ \mathrm{mm}^2/\mathrm{s}$ is impractical for this work since neighboring vortices prevent it from being obtained experimentally. Core-region circulation is a more practical way of measuring vortex strength since it can be calculated within a finite circle of radius r_v in which most of the vorticity is confined (Ponta, 2010). From this point forward the circulation of a vortex Γ refers to its core region circulation. The expected core-region circulation is then obtained by:

$$\Gamma_{core} = \int_{\theta=0}^{\theta=2\pi} \int_{r=-r_v}^{r=r_v} \frac{\gamma\Gamma_\infty}{4\pi\nu}\left(e^{-\frac{\gamma r^2}{4\nu}}\right) r dr d\theta \tag{3.21}$$

Substituting $r_v = 3.18\,\mathrm{mm}$ into *eqn 3.21*, the expected core circulation of the simulated vortex is found to be $\Gamma = 71\,\mathrm{mm}^2/\mathrm{s}$. Computation of core circulation for $\Gamma = 71\,\mathrm{mm}^2/\mathrm{s} \pm 5\%$ occurs for $vv/\emptyset_v > 25$. For lower values of $vv/\emptyset_v$ the circulation is always underestimated. This is because of the discretizing error involved in summing the vorticity pixels contained within the vortex boundaries. This is illustrated in Figure 3.13 where only the blue pixels are considered for the computed circulation. The area in red accounts for the difference between expected circulation and computed circulation. The grid resolution thresholds are summarized in Table 3.2.

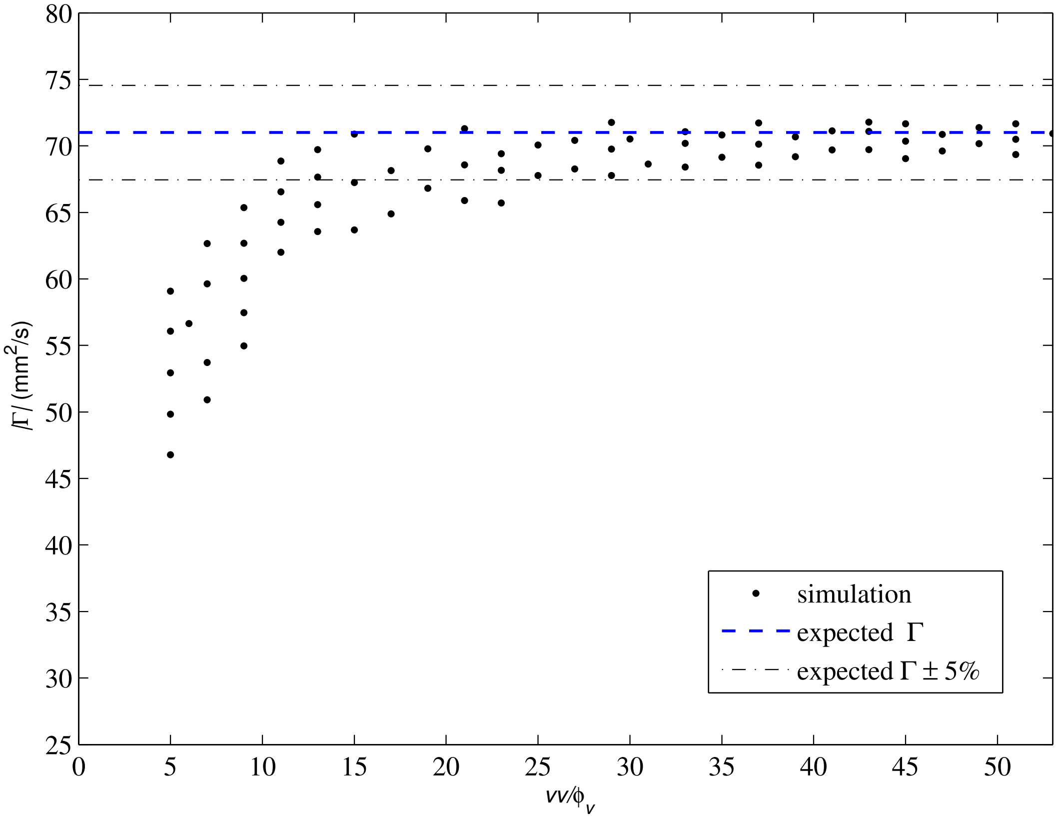

Figure 3.12: Vortex circulation Γ vs. the number of velocity vectors per vortex diameter $vv/\emptyset_v$

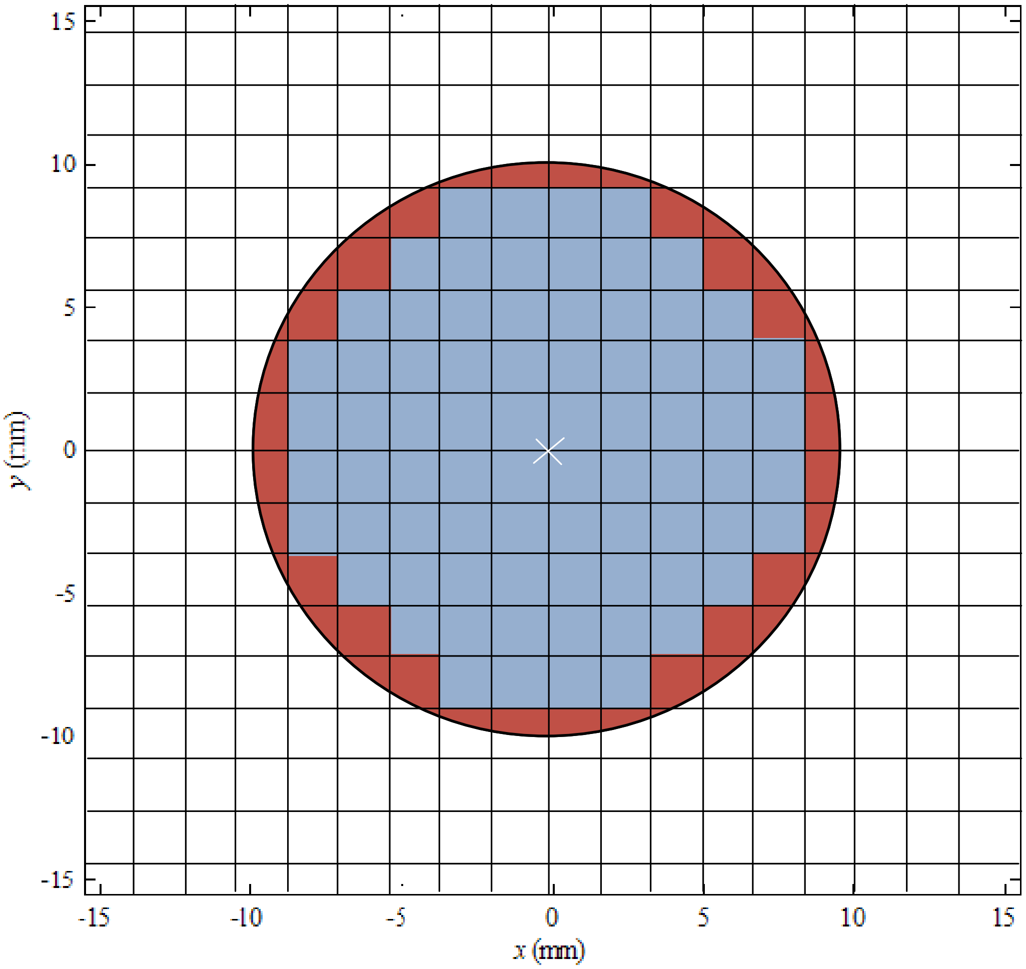

Figure 3.13:Circulation discretization error schematic

Table 3.2: Grid resolution thresholds for simulated flow field

Threshold	$\mathbf{vv/\emptyset_v}$
Type II error	$\mathrm{vv}/\emptyset_v < 5$
Computation of $r_v$within 5% of true value	$\mathrm{vv}/\emptyset_v > 17$
Computation of Γ within 5% of true value	$\mathrm{vv}/\emptyset_v < 25$

White noise was added to the simulated vector field. $I = J = 200$ such that $vv/\emptyset_v = 43$ is sufficiently large for accurate computation of circulation and radius.

White noise $\vec{v}_{n(i,j)} = (v_{nx(i,j)}, v_{ny(i,j)})$, is added to each respective component of velocity $\vec{v}_{(i,j)}$ of the original simulated vector field. The length of all v_{nx} and v_{ny} is normally distributed between $-n$ and n and the resulting velocity of the simulated vector field $\vec{v}'_{(i,j)} = ({v_{x(i,j)}}', {v_{y(i,j)}}')$ is:

$$\vec{v}_{(i,j)}{}' = \vec{v}_{(i,j)} + \vec{v}_{n(i,j)} \tag{3.22}$$

The effect of added noise is quantified by looking at the normalized velocity field noise $\bar{\bar{n}} = \|n\|/\|v\|_{\mu}$. This is the ratio of maximum velocity noise magnitude $\|n\| = \sqrt{2n^2}$ and the mean, pre-noise, velocity magnitude $\|v\|_{\mu}$ of the simulated velocity field. It expresses the added velocity noise in terms of the average velocity vector length of the simulated field. In the following figures the resolution is set to $vv/\emptyset_v = 43$ which is above the required thresholds from Table 3.2.

In Figure 3.14 the vortex radius r_v, computed with the CVD algorithm, is plotted against the normalized velocity field noise. Computation of vortex radius for $r_v = 3.18\,\mathrm{mm} \pm 5\%$ occurs for $\bar{\bar{n}} < 0.05$ and for $r_v = 3.18\,\mathrm{mm} \pm 8\%$ occurs for $\bar{\bar{n}} < 0.19$. For $\bar{\bar{n}} \geq 0.19$ the algorithm either reports a type II error or grossly underestimates the value of r_v.

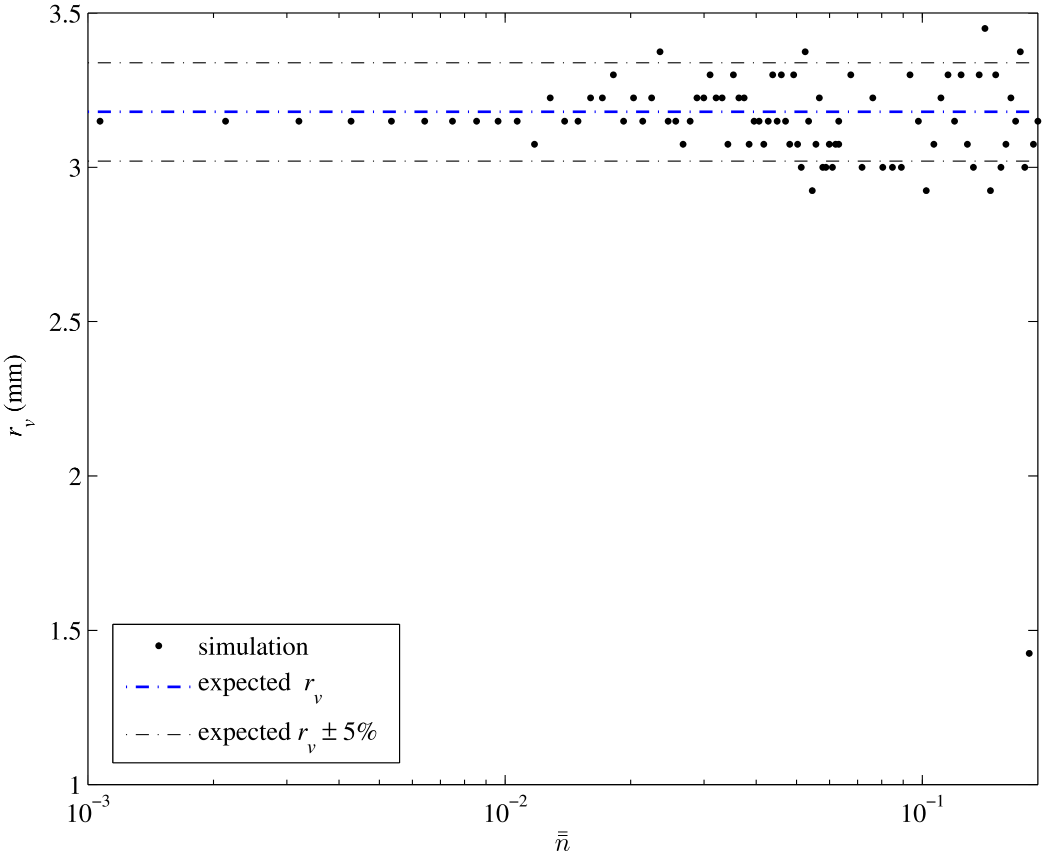

Figure 3.14: Vortex radius computed by CVD algorithm as a function of normalized velocity field noise $\bar{\bar{n}}$

In Figure 3.15 the vortex core circulation Γ computed with the CVD algorithm, is plotted against the normalized velocity field noise $\bar{\bar{n}}$. Computation of vortex core circulation for $\Gamma = 71\ \mathrm{mm}^2/\mathrm{s} \pm 5\%$ occurs for $\bar{\bar{n}} < 0.05$ and for $\Gamma = 71\ \mathrm{mm}^2/\mathrm{s} \pm 8\%$ occurs for $\bar{\bar{n}} < 0.19$. As with the computation of r_v, for values of $\bar{\bar{n}} \geq 0.19$ the algorithm either reports a type II error or grossly underestimates the value of Γ. The normalized velocity vector noise thresholds are summarized in Table 3.3.

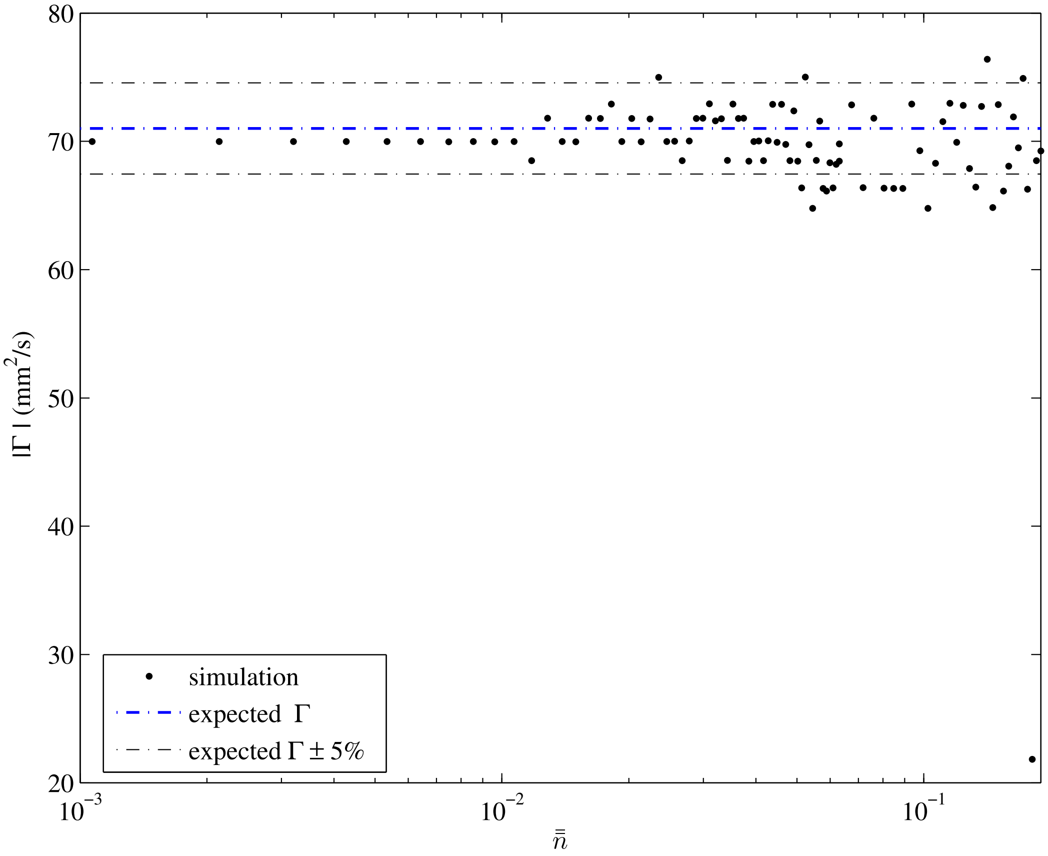

Figure 3.15: Vortex circulation computed by CVD algorithm as a function of normalized velocity field noise $\bar{\bar{n}}$

Table 3.3: Noise thresholds for simulated flow field

Threshold	$\bar{\bar{n}}$
Type II error	$\bar{\bar{n}} > 0.19$
Computation of $r_v$within 5% of true value	$\bar{\bar{n}} < 0.05$
Computation of $r_v$within 8% of true value	$\bar{\bar{n}} < 0.19$
Computation of Γ within 5% of true value	$\bar{\bar{n}} < 0.05$
Computation of Γ within 8% of true value	$\bar{\bar{n}} < 0.19$

Vorticity of $\omega_n = \vec{\nabla} \times \vec{v}_n$ is generated as a result of the added velocity field noise. At $\bar{\bar{n}} = 0.19$, ω_n is sufficiently high to split the potential ROI formed from index I_1 of threshold level TI_1 into smaller, disconnected groups of pixels.

These small clusters of pixels are either removed by the IM process or rejected by the WA algorithm. This forces the CVD algorithm to perform CSL on a smaller ROI obtained only from index I_2 of the TI_2 threshold and explains why the computed vortex radius and circulation suddenly drops for $\bar{\bar{n}} \geq 0.19$.

The velocity vector field of a simulated axisymmetric Burgers vortex with a vorticity background color map is shown in Figure 3.16. The added velocity field noise is less apparent in the individual velocity vectors but the vorticity generated from the noise appears yellow in the background color map.

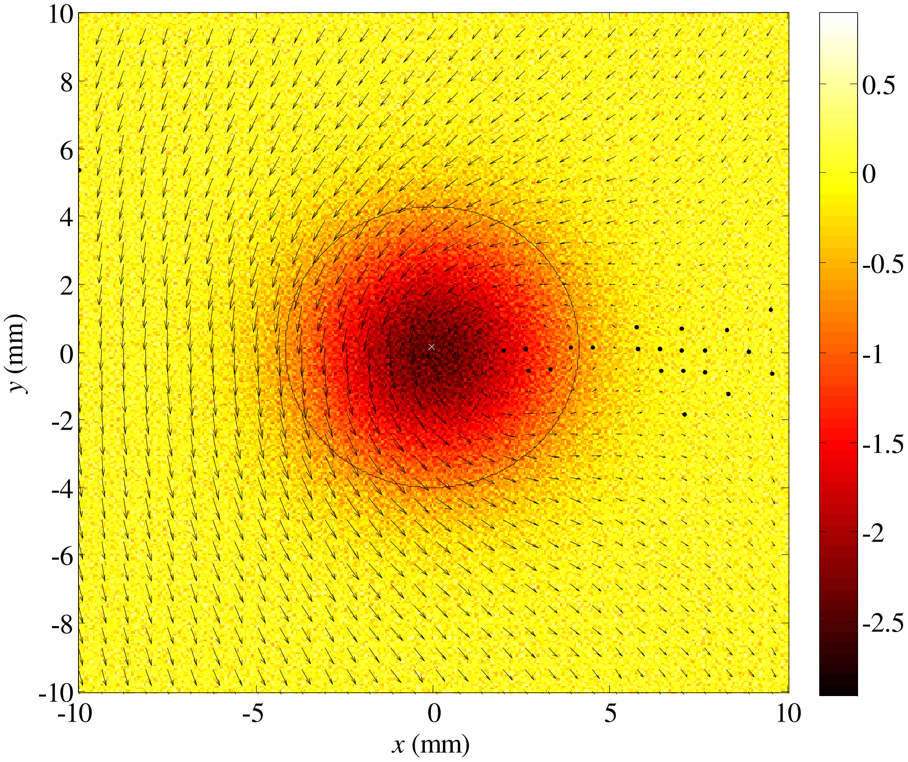

Figure 3.16: Velocity vector field with vorticity background ω (1/s) and normalized velocity field noise $\bar{\bar{n}}$ =0.0089. The detected vortex core shown as a white '×', and the vortex core boundary plotted in black. 1 every 11 velocity vectors are displayed.

3.4 Experimental Method

The basic experimental setup from *Chapter 2* was used to capture the velocity vector field immediately downstream from a flapping NACA 0012 airfoil. The CVD approach was used to identify and characterize the vortical structures present. The airfoil dimensions as well as parameters describing its motion are shown in Figure 3.17.

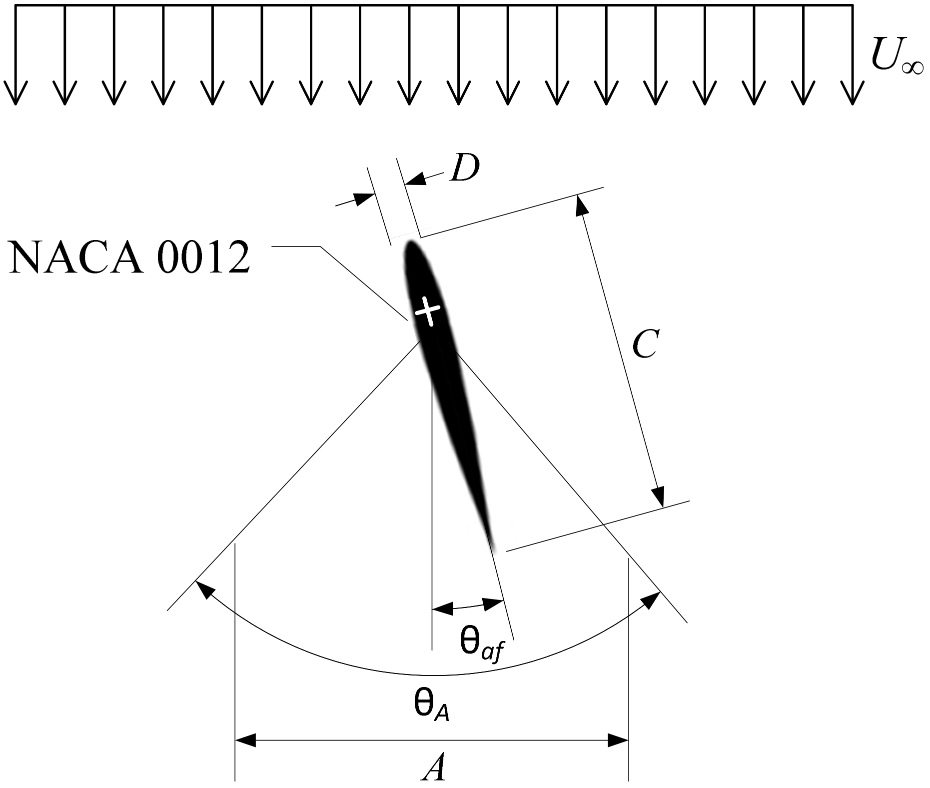

Figure 3.17: Airfoil dimensions and parameters characterizing its motion

The airfoil of chord length C was limited to small pitch oscillation amplitudes ($\theta_A \leq 8^o$) to prevent the creation of leading edge vortices, which would appear in the wake. A Reynolds number can be defined in terms of airfoil chord thickness D to characterize the flow as:

$$Re = \frac{U_\infty D}{\nu} \qquad (3.23)$$

where for the experiments performed in this study, the free stream velocity U_∞ is held constant at 17mm/s with an airfoil thickness of $D = 8.6$ mm and kinematic viscosity of water is 1×10^{-6} m^2/s so that $Re = 146$. The oscillation waveform is described by $\theta_{af}(t) = (\theta_A/2)\sin(2\pi f t)$ and several wake conditions are achieved by changing the oscillation amplitude θ_A and frequency f. The amplitude A is used later to non-dimensionalize the airfoil amplitude.

3.5 Results

A schematic of the oscillating airfoil and its wake is illustrated in Figure 3.18 and shows the airfoil in relation to generated vortices. Small airfoil oscillation amplitudes allow for an orderly wake with precisely two counter rotating vortices shed per oscillation cycle (Bohl & Koochesfahani, 2009). The airfoil of chord length C is shown along with the uniform flow of velocity U_∞. The vortices are arranged into two distinct rows which are aligned with the flow and separated by distance S_y. Similarly, the vortices on a given row are separated by S_x. Vortex core coordinates are labeled and a core boundary radius r_v is defined. The drift velocity $\vec{v}_{drift} = (v_{drift,x}, v_{drift,y})$ is the instantaneous velocity vector at the grid point coinciding with the vortex core. The vortices are also characterized by means of peak vorticity ω_{peak} and circulation Γ. Here, the circulation is calculated by summing the vorticity at each velocity measurement location determined by PIV within the radius r_v of a vortex as:

$$\Gamma = \iint_s (\vec{\nabla} \times \vec{v})\, ds = A_{pixel} \sum_{i=1}^{N_i} \sum_{j=1}^{N_j} \omega_{i,j} \tag{3.24}$$

Here *s* refers to the surface integral over area *ds* and A_{pixel} is the surface area of a rectangle formed from the coordinates of 4 adjacent velocity vectors.

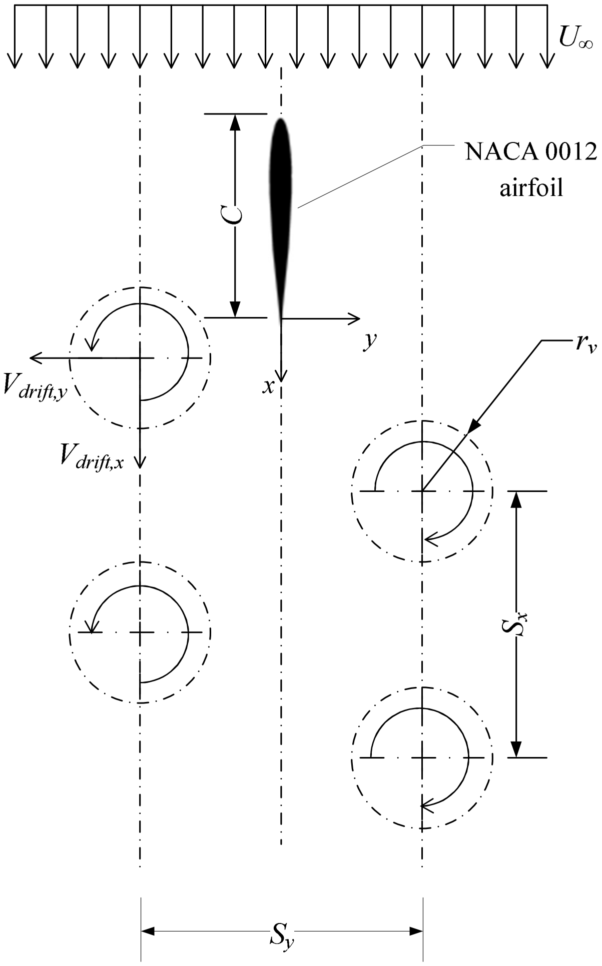

Figure 3.18:Airfoil wake schematic

By varying θ_A and *f*, it is possible to achieve different wake arrangements. Common wake schemes for sinusoidal pitching symmetric airfoils are **von Karman**, as is shown in Figure 3.18 which is typical for vortex shedding from a cylinder; **aligned**, where the transverse separation distance S_y approaches zero; and **inverted von Karman**, is when the sign of rotation for each row is inverted when compared to the von Karman wake (Godoy-Diana et al., 2009). These wake classifications will be described in more detail in *Chapter 4*.

Instantaneous velocity vector fields are computed for 100 wake data sets collected at an airfoil pitch of 0^o. These fields are averaged to produce a single field hereby referred to as a phase averaged field since all of the data is collected at a fixed oscillation phase. The WA and CSL methods are performed for two phase averaged fields. In Figure 3.19, the potential vortex cores and vortex boundary radii obtained from the CSL method are plotted over the vorticity field as white crosses and black circles respectively. In order to show the weak vortices clearly, the color map saturates at $|\omega| = 0.8\ \mathrm{s}^{-1}$ in Figure 3.19 (a) and at $|\omega| = 1.6\ \mathrm{s}^{-1}$ in Figure 3.19 (b). The von Karman wake shown in Figure 3.19(a) is the result of sinusoidal pitching at $f = 1.6\ \mathrm{rad/s}$ and $\theta_A = 8°$, and the inverted von Karman wake in Figure 3.19(b) is the result of sinusoidal pitching at $f = 3.4\ \mathrm{rad/s}$ and $\theta_A = 8°$. These two wakes at $Re = 146$ illustrate the extreme cases of wake vorticity for $\theta_A = 8°$.

The von Karman wake generally produces weak vortices with low peak vorticity and circulation. It exhibits the least vortex decay as a function of downstream distance and has larger stream wise spacing S_x. In comparison, vortices from the inverted von Karman wake have the highest peak vorticity and circulation. They have the highest vortex decay rate and they have relatively small stream wise spacing S_x. These two wake conditions are used as test cases to assess the CVD algorithm's ability to detect and characterize vortices over the range of flow conditions expected in this current low Reynolds number flow ($Re < 200$).

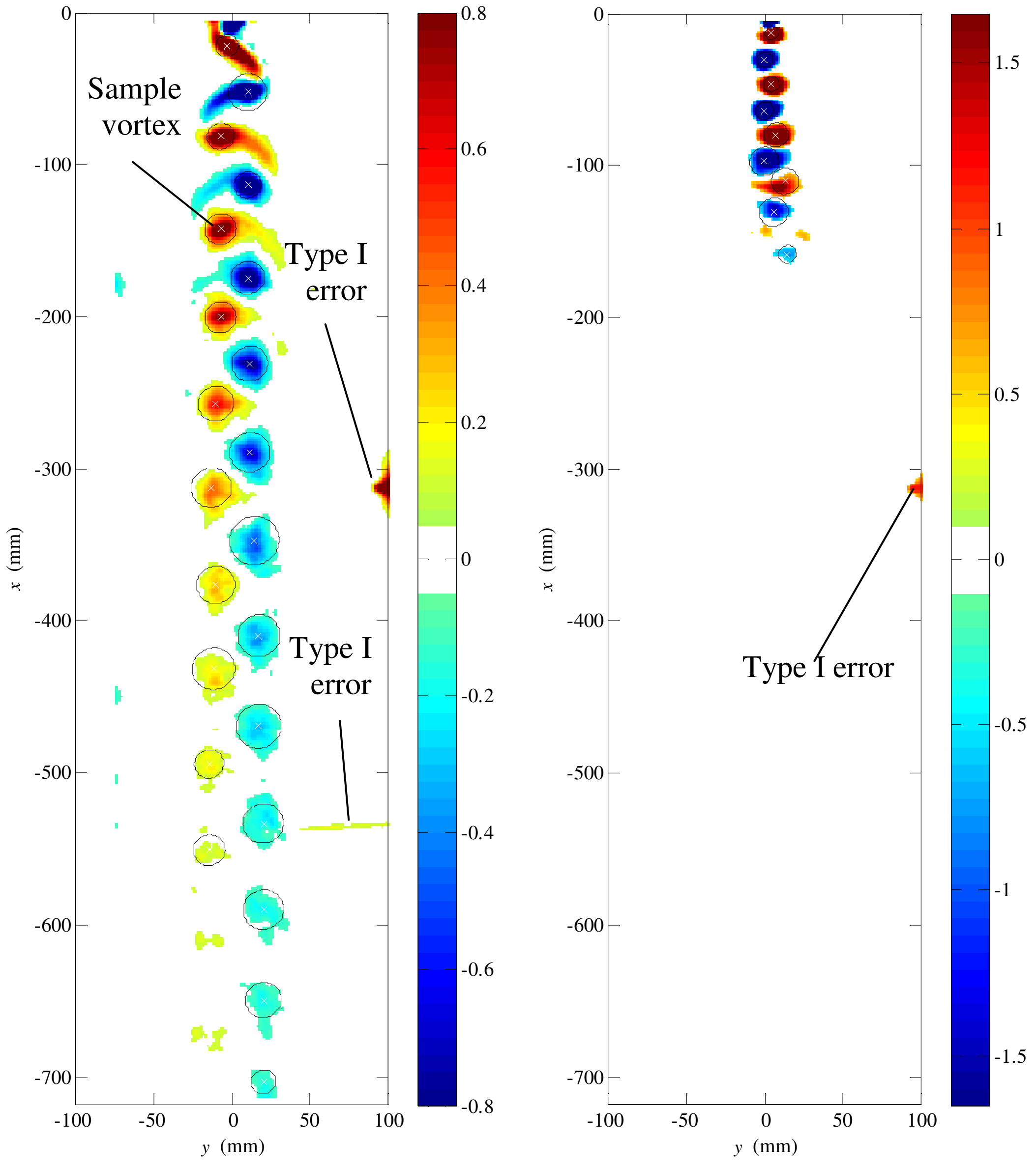

(a) (b)

Figure 3.19: Vortex cores (white ‘×’) and radius (black circles) as computed with the WA and CSL algorithms plotted over the global vorticity map for $Re = 146$ a) $f = 1.6\ \mathrm{rad/s},\ \theta_A = 8°$ b) and $f = 3.4\ \mathrm{rad/s},\ \theta_A = 8°$.

3.5.2 WA: to detect errors in WA and CSL

A false positive vortex diagnostic, or a **type I error,** occurs when an algorithm identifies a vortex that does not truly exist (Jiang, 2002), be it due to local shear flow, boundary effects or image stitching errors. Two examples type I errors are annotated in Figure 3.19 thereby demonstrating the CSL method’s inherent inability to reject a ROI which does not enclose a vortex. Once the data from Figure 3.19 is run through the WA algorithm, the false positive is rejected since its streamlines do not form semi-closed, semi-elliptic paths.

A sample vortex is labeled in Figure 3.19. A local velocity field, centered on the sample vortex core with a moving reference frame equal to the sample vortex's drift velocity as per the pre-WA section of the combinatorial algorithm of Figure 3.8 is calculated. Figure 3.20 shows the streamlines that are generated from this velocity field plotted over the local vorticity field. In Figure 3.21, 5 streamlines meeting the WA requirements are plotted. In addition, each complying streamline is mapped to a point (black '·') along with the vortex core which was previously computed with the CSL method (black '+'). The WA algorithm confirms that the sample ROI contains a vortex that is consistent with the vortex definition of Robinson (1991). It also confirms that only one vortex exists in the sample ROI and that the core location computed by CSL agrees well with the geometric centre of all the complying streamlines. Should the WA algorithm identify multiple vortices in a single ROI, then the vortex with the largest number of complying streamlines becomes the ROI's primary vortex and the other clusters of streamlines are associated to **type II errors**.

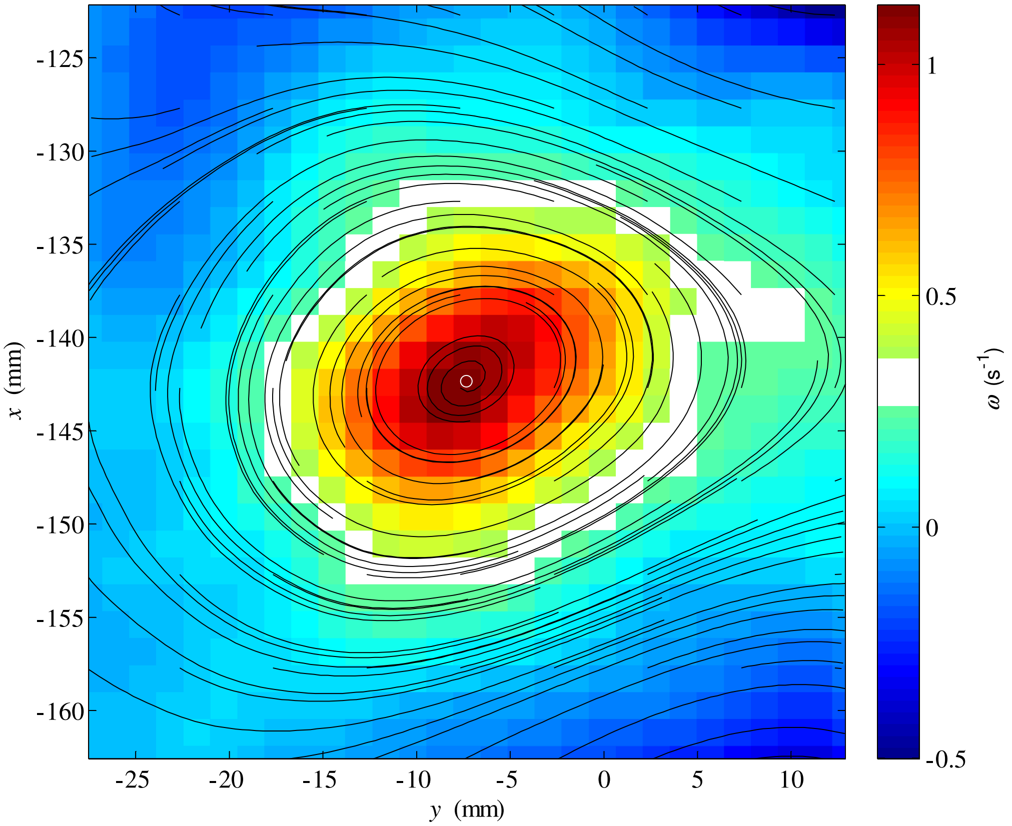

Figure 3.20:Instantaneous streamlines from the sample vortex's reference velocity field (velocity field traveling with the centre of the vortex) plotted over the local vorticity field

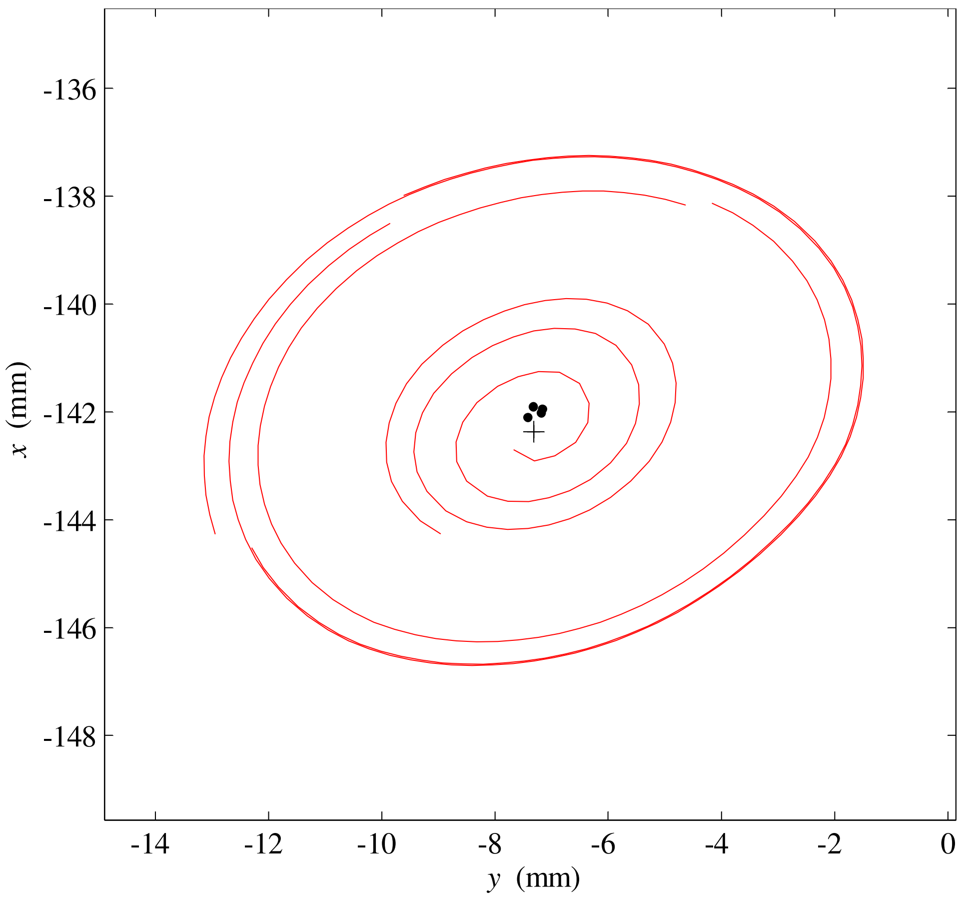

Figure 3.21: Complying streamlines as defined by the winding angle algorithm's specifications along with cluster points (black '·') and vortex core from CSL method (black '+').

A false negative, or a **type II error**, is a vortex which is present in the flow, but goes undetected by the algorithm. Unfortunately, due to the *a priori* knowledge required by the WA algorithm, it cannot avoid type II errors for vortices which are not in the predefined ROI. However, if multiple vortices are in a single ROI, the WA algorithm can identify a type II error, but only if the drift velocity of the false positive vortex is similar to that of the detected vortex. Type II errors for the proposed CVD algorithm may only be minimized through two mechanisms:

1) Wider threshold bounds in the TIV defined in *eqn. (3.2)* for the MV algorithm: Weaker vortices (vortices with low vorticity) are now enclosed by ROI and are consequently considered by the CSL and WA algorithms

2) Smaller sized IM structuring elements in the erosion process: Smaller vortices (vortices with small values of r_v) remain intact during the erosion process and consequently become enclosed by ROI and are considered by the CSL and WA algorithms

Implementing these modifications can cause significant increases in computation time; therefore, defining a minimum vortex size $r_{v,min}$ and strength $\omega_{peak,min}$ prior to running the algorithm is recommended. In doing so, weak and/or small vortices below the threshold are deliberately ignored and the algorithm requires less computation. Both the threshold defined in *eqn. (3.2)* and the sizes of IM structuring element S_{e1}, S_{e2} and S_{e3} are selected on the basis of minimizing type II errors and computation time.

3.5.3 Vorticity profiles

Vorticity distribution profiles of fully formed vortices are valuable characterization tools. They are useful for evaluating the accuracy of the vortex radius r_v, vortex shape and symmetry and for fitting analytical models to the vortex under consideration. Figure 3.22 shows the vorticity of the sample vortex presented in Figure 3.20 plotted against the dimensionless radius $(y - y_c)/r_v$ along a line of constant y passing through the vortex core. The vorticity profile suggests a Gaussian distribution with slight asymmetry, perhaps due to some interaction with the nearby counter rotating vortex.

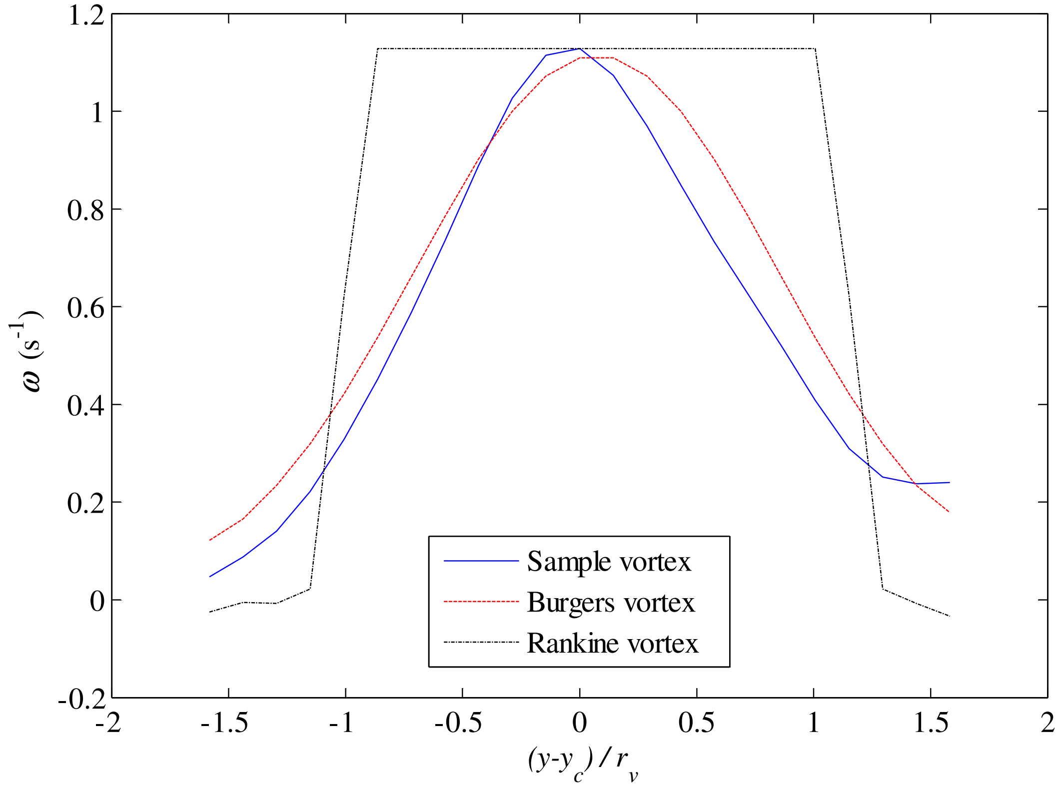

Figure 3.22: Vorticity vs. the dimensionless vortex radius for the sample vortex, an ideal Burgers vortex and ideal Rankine vortex

Also plotted in Figure 3.22 are the vorticity profiles for an ideal Burgers and Rankine vortices having the same peak vorticity and radii as those computed by CSL. The Burgers vortex was described above with *eqns. 3.19* and *3.20*, and the Rankine vortex is a simple model which attempts to simulate a real vortex by separating it into two regions, namely the inner core region and the outer core region. Vorticity in the core region is uniform and resembles a forced vortex while the outer core region is free of vorticity thus simulating an irrotational or free vortex (Giaiotti & Stel, 2006).

The vorticity distribution plot in Figure 3.22 reveals that the sample vortex closely resembles a Burgers vortex having the same radius and peak vorticity as the values computed by the CSL algorithm. This is validation that the CSL algorithm can effectively predict the radius and core coordinates of a vortex from a PIV generated velocity vector field. There is a slight spatial offset between the experimental vortex and the Burgers vortex. This is the result of the CSL algorithm which reads $v_{p(\varsigma,\psi)}$ from *eqn. (3.5)* sequentially from left to right. If the true core coordinate is between two velocity vectors, the algorithm will always chose the leftmost value.

3.5.4 Circumferential velocity profiles

In addition to vorticity profiles, circumferential velocity profiles prove to be equally useful for characterizing vortical flow structures. Circumferential, or azimuthal velocity is the component of velocity that is perpendicular to any straight line passing through the vortex core. Figure 3.23 compares circumferential velocity profiles of the sample vortex, a Rankine vortex and a Burgers vortex.

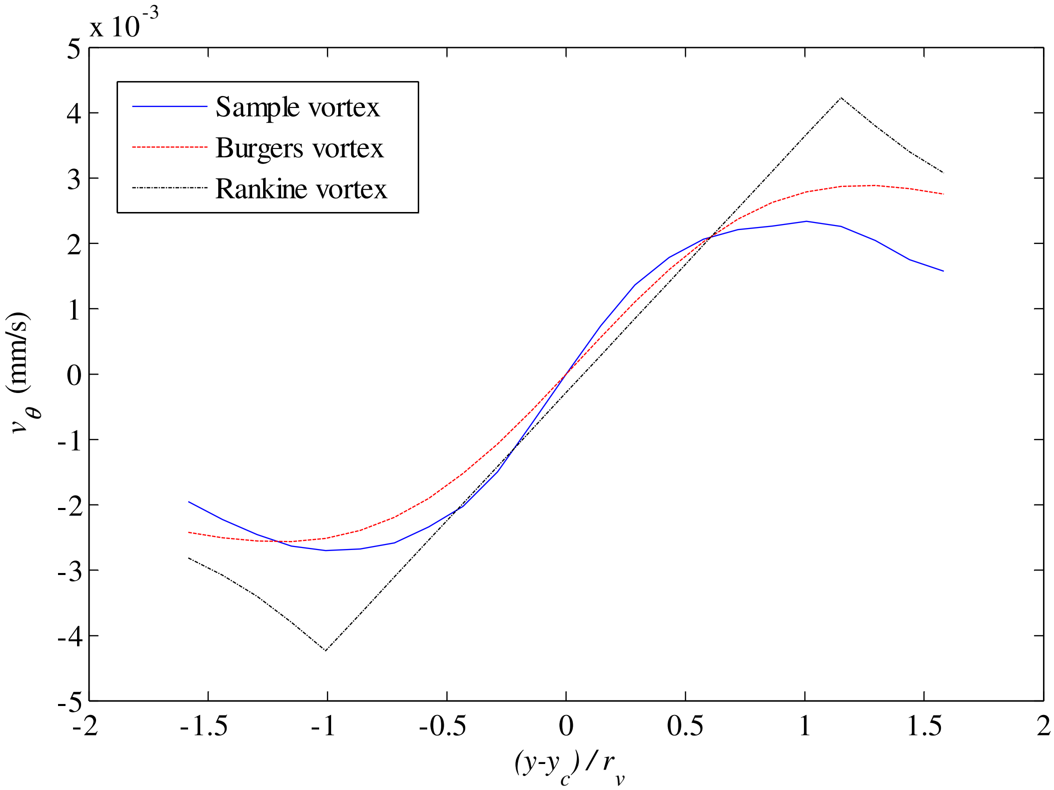

Figure 3.23: Relative circumferential velocity vs. the dimensionless vortex radius for the sample vortex, an ideal Burgers vortex and ideal Rankine vortex

Figure 3.23 shows that the sample vortex circumferential velocity resembles the Burgers vortex model. It can be observed in Figure 3.22 that defining a vortex boundary radius with a vorticity profile, essentially with the MV method alone, requires an arbitrary cutoff (Jeong & Hussain, 2006). However, within a vortex radius, the circumferential velocity magnitude is believed to increase with increasing radius and reach a maximum precisely at the vortex boundary r_v (Jeong & Hussain, 2006). This observation is clearly visible in Figure 3.23 and it highlights a significant advantage in using circumferential velocity profiles to define vortex boundaries. In addition, locating a vortex core in this manner does not require computation of parameters at or near the core itself.

Rather, it infers the location of the core based on velocity measurements taken at the outer boundaries of the core, where the gradients are much lower. Circumferential velocity profiles demonstrate how the CSL algorithm can clearly identify the boundary of a vortex core as the radial location of maximum absolute circumferential velocity. This definition of core boundary radius is less ambiguous than one derived from vorticity profiles and hence serves as a superior method for computing vortex boundary radii.

Three sample vortices with overlapping cores, taken from experimental data from a wake with at $f = 4$ rad/s and $\theta_A = 20°$, are shown in Figure 3.24. The three vortices are made visible by the distinct vorticity peaks shown in the color map representation of the vorticity field. The CSL algorithm was performed for a single ROI encompassing all three vortices and as a result only the primary core is detected and shown as a white circle. The instantaneous streamlines are generated from a reference frame moving with the primary core which is shown as a white circle. This figure was deliberately created with a single threshold in the MV algorithm to highlight the limitations that could arise from doing so when multiple vortices are in close proximity.

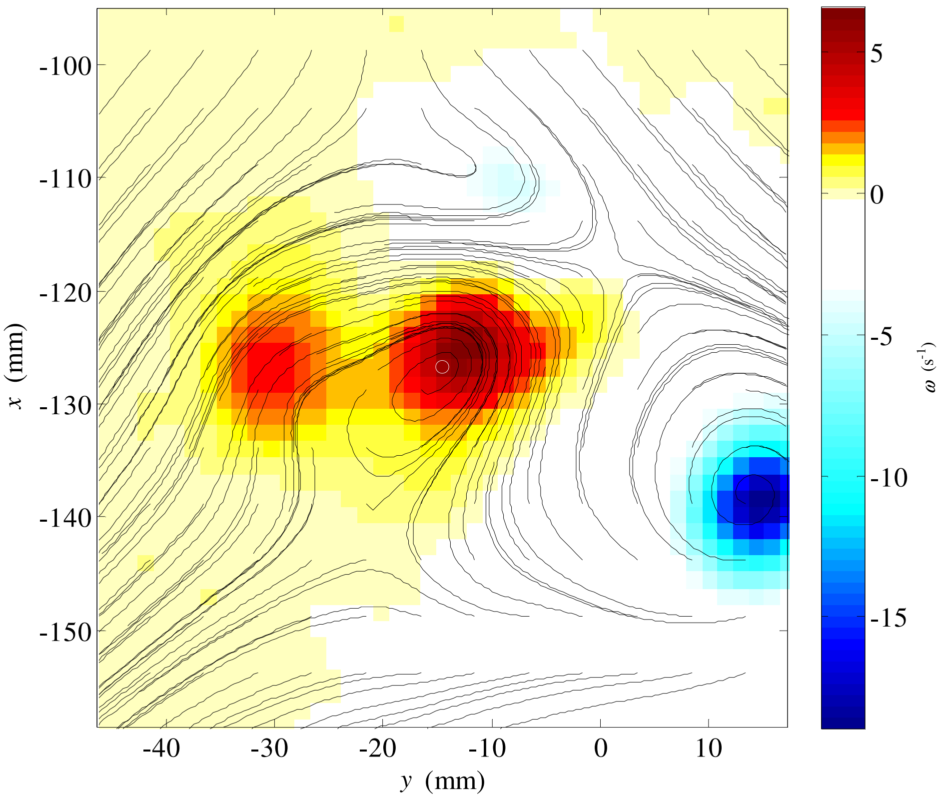

Figure 3.24: Instantaneous streamlines from sample vortices with overlapping cores from a local reference velocity plotted over the local vorticity field *ω* (1/s).

Figure 3.25 shows the vorticity profile for the above ROI for a line of constant *x* passing through the detected core (white ‘○’ in Figure 3.24).

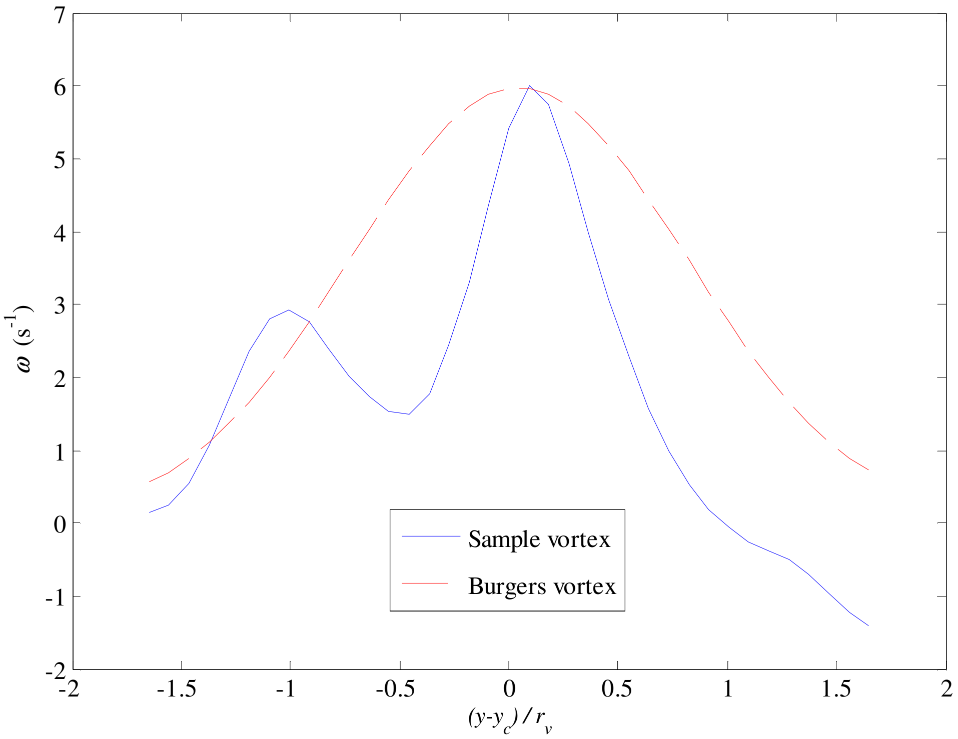

Figure 3.25: Vorticity vs. the dimensionless vortex radius for sample vortices with overlapping cores, along with an ideal Burgers vortex of similar peak vorticity and radius

The figure reveals that fitting a single Burgers vortex to the ROI is not a suitable model. In contrast, Figure 3.26 shows the vorticity profile for the same vortex pair; however, the MV algorithm uses an appropriately tuned multilevel threshold. The two vorticity peaks seen in Figure 3.24 are now enclosed by individual ROI and the CSL algorithm is able to accurately locate the two individual cores and calculate appropriate boundary radii and core coordinates. The secondary vortex in Figure 3.26 is described with less velocity vectors than the primary vortex and the Burgers model for the secondary vortex is, therefore, noticeably less accurate than that of the primary vortex. Nonetheless, comparison of Figure 3.25 and Figure 3.26 illustrates that evaluating the vortices as two separate ROI produces a significantly more accurate model.

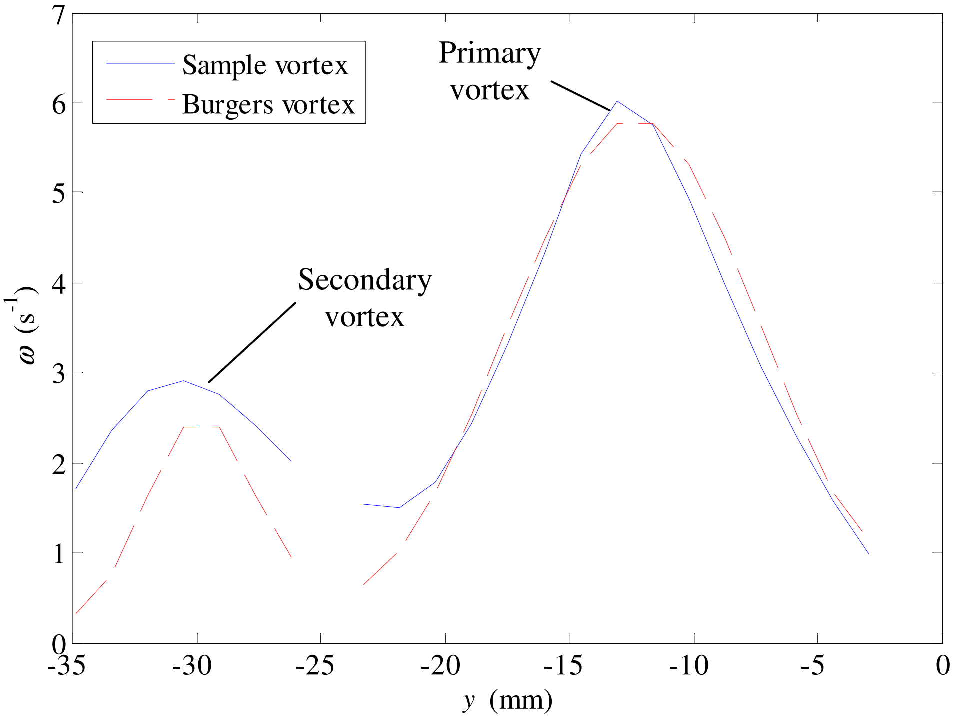

Figure 3.26: Vorticity vs. the dimensionless vortex radius for sample vortices with overlapping cores, along with an ideal Burgers vortex and ideal Rankine vortices of similar peak vorticity and radius

3.6 Conclusions

A vortex detection and characterization algorithm is developed and tested on 2C2D velocity vector fields taken from the wake of an oscillating NACA 0012 airfoil in a uniform flow. Vortex detection for experimental data is particularly challenging since it is often accompanied by measurement uncertainty and noise (Saikrishnan et al., 2006). Also, substantial gradients are present near the centre of the vortex often leading to seeding and correlation issues (Vollmers, 2001). The algorithm overcomes these limitations in the data sets by making use of three separate detection methods to provide dependable vortex detection for the von Karman and inverted von Karman wakes. The algorithm makes use of the CSL method for characterizing the vortex's core coordinates, boundary radius and drift velocity. The Burgers vortex model most closely matches the vortical structures for this flow so it will be used as a basis for validating the experimental vortex decay results. Vorticity and circumferential velocity profile plots were used to evaluate the CSL algorithm's ability to accurately locate a vortex core, to define the vortex boundary radius and to compute the vortex drift velocity vector. The WA algorithm proved to be a useful verification method for reliably identifying and subsequently eliminating false positives.

Future improvements to the CVD algorithm include development of a more advanced and automated method for tuning threshold intensity vectors *TIV* and for the image morphology parameters. In addition, the CSL method could supply the CVD with a second choice for the core coordinates. In the event that the ROI is rejected by the WA algorithm, the second choice could be used. These modifications aim to reduce true negatives and improve accuracy while minimizing computation time. Finally, a statistical assessment of the combinatorial algorithm's accuracy and repeatability could be compared with those of the individual algorithms to further understand the advantages of using a combinatorial detection approach with experimental PIV data.

CHAPTER 4: Wake characteristics of an oscillating airfoil

4.1 Introduction

A NACA 0012 airfoil is submersed vertically to align with a flow field in the waterchanel as described in *Chapter 2*. A stepper motor is used to pitch the airfoil about its aerodynamic center (roughly the quarter chord distance) with a periodic signal. The sinusoidal pitching motion of the airfoil is described by $\theta_{af}(t) = (\theta_A/2)\sin(2\pi f)$ and was shown in Figure 3.9. The wake generated by this motion is essentially 2D and is comprised of coherent structures which separate from the trailing edge of the airfoil and travel downstream at a given drift velocity.

The complex wake flow can be parameterized by:

- The spatial arrangement of vortices in the wake
- The spatial coordinates of vortex cores relative to the airfoil
- The vortex size, r_v defined by a circle fitted to the vortex
- The vortex drift velocity , $\vec{v}_{drift} = (v_{drift,x}\,, v_{drift,y})$
- Core region circulation of individual vortices, Γ
- The peak vorticity of individual vortices, ω_{peak}

These parameters are complex functions of: the Reynolds number *Re*, defined in *eqn. (3.23)* and the airfoil's oscillation waveform amplitude θ_A and frequency *f*.

The wake's spatial arrangement is divided into categories. Figure 4.1 shows the various vortex wake categories where the blue circles represent vortices with positive CCW rotation and those in red represent vortices with negative CW rotation. A von Karman wake (2S_vK) is show in Figure 4.1(a) and is defined by two vortices of opposite rotation that are shed alternately every oscillation period (Schnipper et al., 2009). This wake has two distinct rows of opposite signed vortices that are symmetric about the airfoil chord line. With increasing flapping frequency at a set amplitude, the lateral vortex spacing decrease until a unique condition is achieved where the vortices align in the wake of the airfoil. This is shown in t vortices with negative CW rotation. A von Karman wake (2S_vK) is show in Figure 4.1 (b) and is classified as an aligned wake (2S_A) where the two vortex rows coincide and the vortices effectively line up along the airfoil chord line. The inverted von Karman wake (2S_ivK) is shown in t vortices with negative CW rotation. A von Karman wake (2S_vK) is show in Figure 4.1 (c) and is defined as a von Karman wake in which the sign of vorticity in each of the two rows is reversed. These three wake schemes are the focus of this chapter and belong to the 2S family meaning that only two single vortices are shed per oscillation cycle.

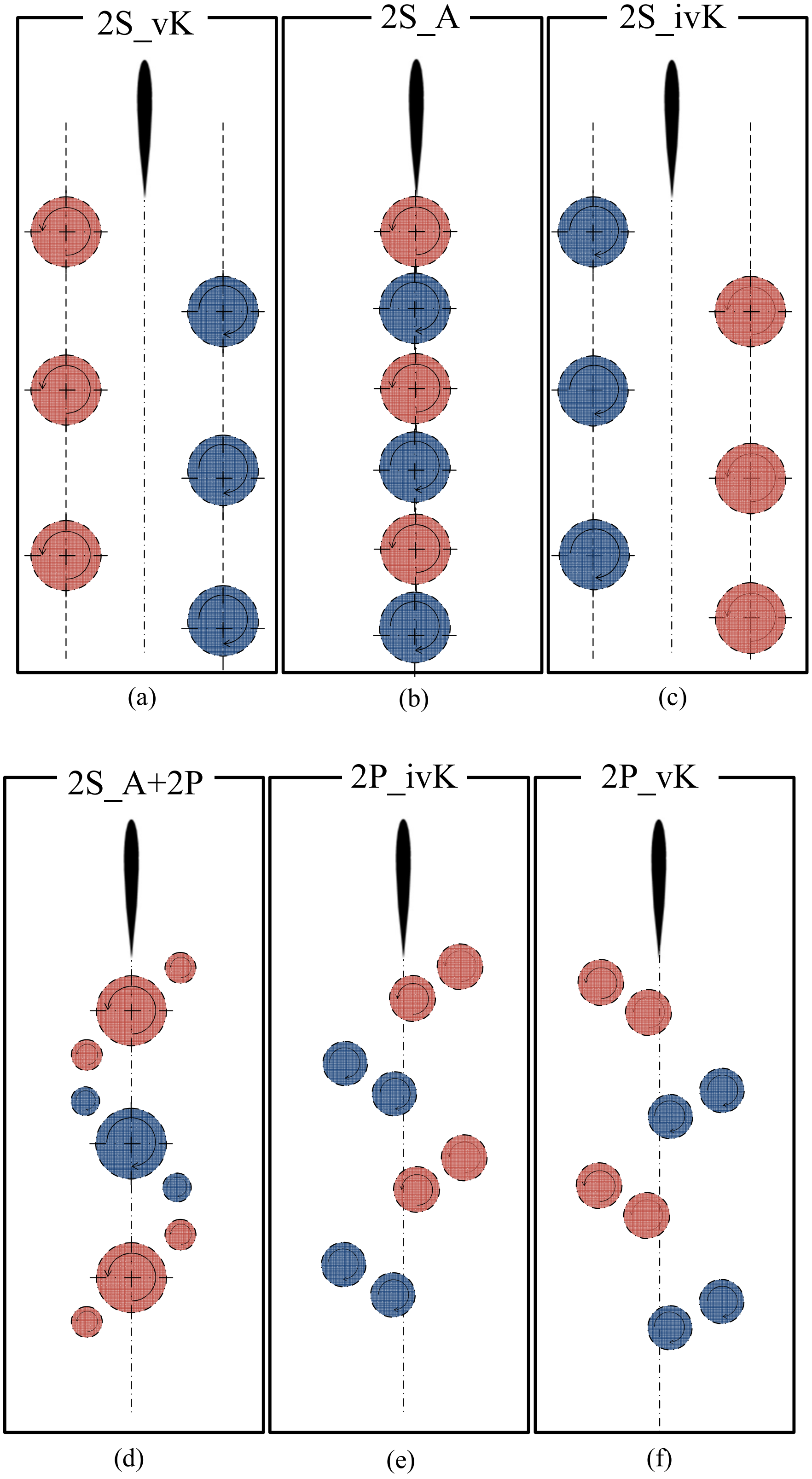

(a) (b) (c)

(d) (e) (f)

Figure 4.1: Wake types of an oscillating airfoil

For larger values of θ_A, more complicated wakes can occur in which multiple pairs of vortices are shed per oscillation cycle. When two pairs of vortices are generated every oscillation cycle this is referred to as a 2P wake and similarly, when four pairs are generated per oscillation cycle it is denoted a 4P wake. Additionally, combinations such as 2P+2S wakes are possible; such a wake would consist of two single vortices (2S), either in a 2S_vK, 2S_ivK or 2S_A configuration, each surrounded by a pair (2P) of vortices. These vortex wakes are shown in Figure 4.1(d-f). The vortices in these wakes vary in size and this is attributed to the different sources of vorticity on the airfoil and will be discussed in more detail later.

The 2S_vK type wakes frequently accompany stationary bluff bodies whereas more complicated spatial arrangement schemes such as 2S_ivK, 2S_A, 2P or 2P+2S are more commonly associated to oscillating structures (Schnipper et al., 2009). Several wake arrangements ranging from simple 2S schemes, to more complex schemes consisting of 16 vortices per oscillation cycle have been identified in the literature (Schnipper et al., 2009). The various wake arrangements are attributed to two distinct sources of vorticity on the airfoil. The round leading edge gives rise to flow separation at maximum pitch causing a leading edge vortex to advect along the side of the airfoil. Similarly, the trailing edge of the airfoil produces vorticity as it swings periodically. Naturally, the production of vortices at the trailing edge depend on the amplitude and frequency of the pitching oscillations, whereas the leading edge vortices tend to be a function of the free stream velocity (Schnipper et al., 2009).

The focus of this chapter is to characterize the wake behind a NACA 0012 airfoil which is driven by a periodic signal. The effect of changing both frequency f and amplitude θ_A of oscillation is studied. The wake's spatial arrangement can be identified using flow visualization techniques where instantaneous photographs of the flow are taken. These require minimal processing since they are visually interpreted. For this initial exploration and characterization of the flow, seed particles are injected upstream of the wing and a laser pulse freezes the motion of the flow. Instantaneous streaklines are captured by overhead CCD cameras. The other parameters which include vortex shape, core coordinates, drift velocity, circulation, peak vorticity and wake symmetry are experimentally evaluated with 2D PIV data in detail for a few cases. This detailed characterization is carried out using the vortex detection/characterization software that was presented in *Chapter 3*.

4.2 Background

Oscillating airfoils have generated much interest in resent literature largely due to its association with biological propulsion of flying and aquatic organisms (Bohl & Koochesfahani, 2009), (Shukla et al., 2009), (Gopalkrishnan et al., 1994), (Ozen & Rockwell, 2010) . These types of flows inherently produce thrust and the associated downstream flow conditions are described as a 2S_ivK wake which has a velocity excess or jet profile in its wake. This differs from the 2S_vK wake which has a velocity deficit, or a wake profile (Schnipper et al., 2009). In the 2S_vK wake the vortices left of the airfoil have positive, rotation and the vortices right of the airfoil have negative rotation as seen in t vortices with negative CW rotation. A von Karman wake (2S_vK) is show in Figure 4.1. The 2S_ivK wake is structured in a similar fashion; however, the direction of rotation in each row is reversed (Bohl & Koochesfahani, 2009).

The wake of an oscillating airfoil is dependent on the harmonic motion of the airfoil (Godoy-Diana et al., 2009). A 2D airfoil performing both periodic heaving and pitching motions with an arbitrary oscillation waveform can have an extremely complicated three dimensional wake. Heaving is where the aerodynamic centre of the airfoil moves perpendicular to the free stream flow, while pitching is when the airfoil's angle of attack is changed. Airfoil motion limited to sinusoidal pitch oscillations is investigated in this study and shown schematically in Figure 3.17. In the literature, 2D spatial arrangements of wakes generated by a NACA 0012 airfoil subject to sinusoidal pitch oscillations used these three independent dimensionless parameters to characterize the flow (Schnipper et al., 2009):

$$Re = \frac{U_\infty D}{\nu} \tag{4.1}$$

and

$$St = \frac{fD}{U_\infty} \tag{4.2}$$

and

$$A_D = A/D \tag{4.3}$$

Here Re is the Reynolds number, which is defined based on the airfoil thickness D (not chord length since the study is limited to small oscillation amplitudes). The kinematic viscosity of the fluid ν and the free stream velocity U_∞. The thickness based Strouhal number is defined as St where f is the frequency of pitching oscillation. Finally A_D is the dimensionless amplitude of oscillation and A is shown in Figure 3.17.

To gain insight into the wake flow, a wake map is used. A wake map is a phase diagram plotting a dependant variable as a function of two other independent variables, St and A_D. The wake map used to categorize the wake arrangement of oscillating structures was originally proposed by Williamson & Roshko (1988) who mapped the various wake arrangements of flow over a laterally oscillating cylinder. The wake map allows for the examination of important wake transitions such as the 2S to 2P transition and the 2S_vK to 2S_ivK transition. The qualitative composition of the wake map is independent of

Reynolds number in the range of 100 to 10,000 (Schnipper et al., 2009). Providing the basis for constructing a wake map for the pitching airfoil in steady flow examined here. The study by (Schnipper et al., 2009) uses a tow tank whereas the current study uses a re-circulating water channel which has higher freestream turbulence levels which should cause the vortices to experience accelerated decay.

Godoy-Diana et al. 2009 also investigate the vortex streets produced by pitching airfoils and use similar dimensionless parameters to the study by Schnipper et al. (2009). They produce a phase map which extends into the range where the wake becomes asymmetric which is useful for tandem airfoil configurations where the vortices from an upstream airfoil interact with a second downstream airfoil. They calculate circulation and vorticity of vortices in the wake of the airfoil, but only up to 3.3 chord lengths downstream. They focus more on describing the asymmetric wake transition characterized by 2S_ivK to 2S_ivKa.

In another study, Bohl & Koochesfahani 2009 experimentally investigated an oscillating 12cm chord NACA 0012 airfoil in a closed-return water tunnel. They do not develop a wake map but they measure the transition from the 2S_vK wake to the 2S_ivK wake using molecular tagging velocimetry (MTV). In their study, leading edge vortices were eliminated by using small pitching amplitudes ($\theta_A < 4°$) thus only producing 2S type wake arrangements. Defining the reduced frequency $k = (2\pi f C)/2U_\infty$ the 2S_vK to 2S_ivK transition occurs for $k > 5.7$ which interestingly does not coincide with the transition from a resulting drag force on the airfoil to a thrust force. In addition, they investigated the change in vortex intensity through two mechanisms; vortex stretching (I) and viscous diffusion (II). These two mechanisms are expressed in the 2D vorticity transport equation in cylindrical coordinates:

$$\frac{\partial \omega_z}{\partial t} = \underbrace{\omega_z \frac{\partial w}{\partial z}}_{\text{I}} + \underbrace{\nu \left(\frac{\partial^2 \omega_z}{\partial r^2} + \frac{1}{r} \frac{\partial \omega_z}{\partial r} \right)}_{\text{II}} \tag{4.4}$$

This equation is derived from the 2D Navier-Stokes equation assuming incompressible 2D fluid with no concentrated torques or line forces. Here ω_z is the in-plane vorticity, w is the axial component of velocity within the vortex, z is the axial coordinate and r is the radial coordinate. For subsequent analysis the flow is assumed to be predominantly 2D and for simplicity ω_z will be expressed as ω. The $\partial w / \partial z$ term corresponds to the change in axial velocity with respect to the axial coordinate (axial strain) which is assumed to be constant and negligible compared to the in-plane vorticity magnitude. The $\partial w / \partial z$ term will be approximated experimentally in later sections.

Bohl & Koochesfahani (2009) showed that the vorticity distribution of their experimental vortices approximate a Gaussian function centered at the vortex core. This is characteristic of a Burger vortex (Drazin & Riley, 2006). Its vorticity distribution as a function of the radial coordinate r at some time t is expressed by:

$$\omega(r) = \omega_{peak} \exp\left(-\frac{r^2}{r_c^2}\right) \tag{4.5}$$

where, ω_{peak} is the maximum local vorticity within the vortex boundaries $r \leq r_c$. Similar instantaneous vorticity profiles were plotted in the current work and were compared to the ideal Burger and Rankine vortex models.

Substituting *eqn. (4.5)* into *eqn. (4.4),* the change of vorticity within a vortex described by *eqn. (4.5)* with respect to *r* becomes:

$$\frac{\partial \omega}{\partial t} = \omega_{peak} \exp\left(-\frac{r^2}{r_c^2}\right)\frac{\partial w}{\partial z} + \frac{4\omega_{peak}\nu}{r_c^2} \exp\left(-\frac{r^2}{r_c^2}\right)\left(\frac{r^2}{r_c^2} - 1\right) \tag{4.6}$$

The time evolution of peak vorticity $\omega_{peak}(t)$ provides important information about the decay of a vortex. Considering $\omega_{peak}(t)$ rather than $\omega(r,t)$ removes the local *r* dependency from *eqn. (4.6)* and makes the data far more manageable when considering multiple vortices. This allows for a clear comparison between wake types.

In a Gaussian vorticity distribution ω_{peak} coincides with $r = 0$. Making the substitution $r = 0$ into *eqn. (4.6)* gives rise to the following expression for the time evolution of peak vorticity:

$$\frac{\partial \omega_{peak}}{\partial t} = \omega_{peak}\left(\frac{\partial w}{\partial z}\right) - \omega_{peak}\left(\frac{4\nu}{r_c^2}\right) \tag{4.7}$$

This indicates that the decay of peak vorticity of a Burgers vortex is driven by two mechanisms expressed individually by the two terms on the right hand side (RHS) of *eqn. (4.7).* Bohl & Koochesfahani (2009) indicate that the 1st term corresponds to axial stretching of the vortex and is responsible for axial flow toward the centre span. As a result, they assumed some constant $\partial w/\partial z < 0$ which was later determined experimentally. The second term in the LHS of *eqn. (4.7)* is the viscous decay of vorticity which corresponds to an exponentially decreasing vorticity with time.

The circulation Γ in a Burgers vortex (Gaussian vorticity distribution) is expressed as:

$$\Gamma = \iint_s (\vec{\nabla} \times \vec{v})\, ds = \int_0^{2\pi} \int_0^{r_c} \omega_{peak} \exp\left(-\frac{r^2}{r_c^2}\right) r dr d\theta \qquad (4.8)$$

The solution of this surface integral under the assumption of a Gaussian vorticity distribution is:

$$\Gamma = \pi r_c^2 \omega_{peak} (1 - e^{-1}) \qquad (4.9)$$

rearranging and solving for r_c^2 gives:

$$r_c^2 = \frac{\Gamma}{\pi \omega_{\mathrm{peak}} (1 - \mathrm{e}^{-1})} \qquad (4.10)$$

The circulation Γ is assumed to be constant since none of the vorticity is destroyed, it is merely diffused by viscous action through the body of the fluid. Under this assumption, the circulation Γ at any time *t* is simply the initial circulation Γ_{o} (Ponta, 2010). Substitution of *eqn. (4.10)* into *eqn. (4.7)* and replacing Γ with Γ_{o} yields:

$$\frac{\partial \omega_{peak}}{\partial t} = \omega_{peak} \left(\frac{\partial w}{\partial z}\right) - \omega_{peak}^2 \left(\frac{4\pi\nu}{\Gamma_{\mathrm{o}}}\right) (1 - e^{-1}) \qquad (4.11)$$

Assuming $\partial w/\partial z$ is constant the differential *eqn. (4.11)* has the following general solution:

$$\omega_{peak}(t) = \frac{\beta e^{\beta t}}{K e^{\beta t} - C} \tag{4.12}$$

where

$$K = \frac{4\pi\nu}{\Gamma_o}(1 - e^{-1}) \tag{4.13}$$

and

$$\beta = \frac{\partial w}{\partial z} \tag{4.14}$$

The constant of integration C is found by substituting $\omega_{peak}(0) = \omega_o$ into *eqn.(4.12)*, *C* is then:

$$C = K - \beta/\omega_o \tag{4.15}$$

Substitution of *C* from *eqn. (4.15)* into *eqn. (4.12)* gives:

$$\omega_{peak}(t) = \frac{\beta e^{\beta t}}{K e^{\beta t} - K + \left(\frac{\beta}{\omega_o}\right)} \tag{4.16}$$

This result will be used to generate an analytical model to predict vortex decay under the stated assumptions and to evaluate under which conditions, and particularly within how many chord lengths, these assumptions remain valid.

Bohl & Koochesfahani 2009 determined that vortices with the highest circulation and peak vorticity occur in the 2S_ivK type flow and that this type of flow also experiences the highest decay of peak vorticity ω_{peak}. Their study incorporates many elements related to the current work namely, a NACA 0012 airfoil with comparable chord length positioned in a uniform velocity of water. However, only the effect of changing the reduced frequency is investigated which makes it difficult to generate a comprehensive wake map to study the effects of both amplitude and frequency of oscillation on the wake arrangement. Also they only show the validity of the analytical model for the 2S_vK wake type and only for 1 chord length downstream.

The literature discussed above is summarized as follows:

Schnipper et al. 2009 qualitatively investigate the vortex wake of a NACA 0012 up to 10 oscillation periods downstream. They express the wake types on a phase diagram; however they don't quantify vortex decay or other important parameters.

Godoy-Diana et al. 2009 investigate the wake of a symmetric airfoil by studying circulation and vorticity 3.3 chord lengths downstream. They express the wake types on a phase diagram which agrees well with the one from Schnipper et al. 2009. However, they don't compare the vortex decay or boundary inflation to analytical models. In general they focus more on explaining the 2S_ivK to 2S_ivKa transition.

Bohl & Koochesfahani 2009 quantitatively investigate the vortex wake of a NACA 0012 up to 1 chord length downstream. They found that the vortex decay in the experimental data can be predicted with the 2D vorticity transport equation but don't investigate the accuracy of this model further downstream. They express the wake type in terms of reduced frequency where only the effect of the airfoil's oscillation frequency can be shown. Finally they study the time resolved wake profile and report whether a thrust producing wake or a drag producing wake.

Based on the discussed literature the objectives of this chapter are to:

- Quantitatively investigate the wake of an oscillating NACA 0012 airfoil up to 10 chord lengths downstream.
- Express wake types on a phase map in terms of dimensionless frequency St_d and dimensionless amplitude A_d of oscillation.
- Analytically predict the vortex decay for the 2S_vK, 2S_A and 2S_ivK wake types in terms of peak vorticity and determine for what downstream range this is valid.
- Analytically predict the vortex boundary inflation 2S_vK, 2S_A and 2S_ivK wake types in terms of radius r_v and determine for what downstream range this is valid.
- Further classify the wake as thrust producing, neutral or drag producing and compare with the qualitative wake classification from the phase diagram.

4.3 Wake classification

4.3.1 Flow visualization of the wake

A dense slurry composed of glass spheres (18µm diameter hollow glass spheres for PIV seeding) and water is injected through 2 small visualization ports on either side of the airfoil at the quarter chord distance as shown in Figure 4.2. The slurry is contained in a reservoir located at a height *h* above the visualization ports. The visualization ports are located 100 mm beneath the free surface and the reservoir height *h* is adjusted such that the velocity at which the slurry leaves the ports is virtually identical to that of the fluid passing over the airfoil's surface at that location. In this manner the streaklines generated from the slurry are as laminar as possible.

Instantaneous wake photographs are taken with four overhead CCD cameras. A thin laser sheet (double pulse Nd:YAG laser) is fired upstream, scattering light off the dense slurry and into the four CCD cameras. The images are stitched together with calibrated offsets to produce one single image with a global coordinate system with its origin at the trailing edge of the airfoil. These images were visually inspected and the wake type for each identified. Visualizing the wake in this manner made it possible to efficiently analyze and subsequently characterize various wake schemes by making fine adjustments to both the frequency and the amplitude of oscillation until a transition is observed. This method also makes it possible to collect snapshots of several wake schemes and generate a complete phase map covering the range of interest.

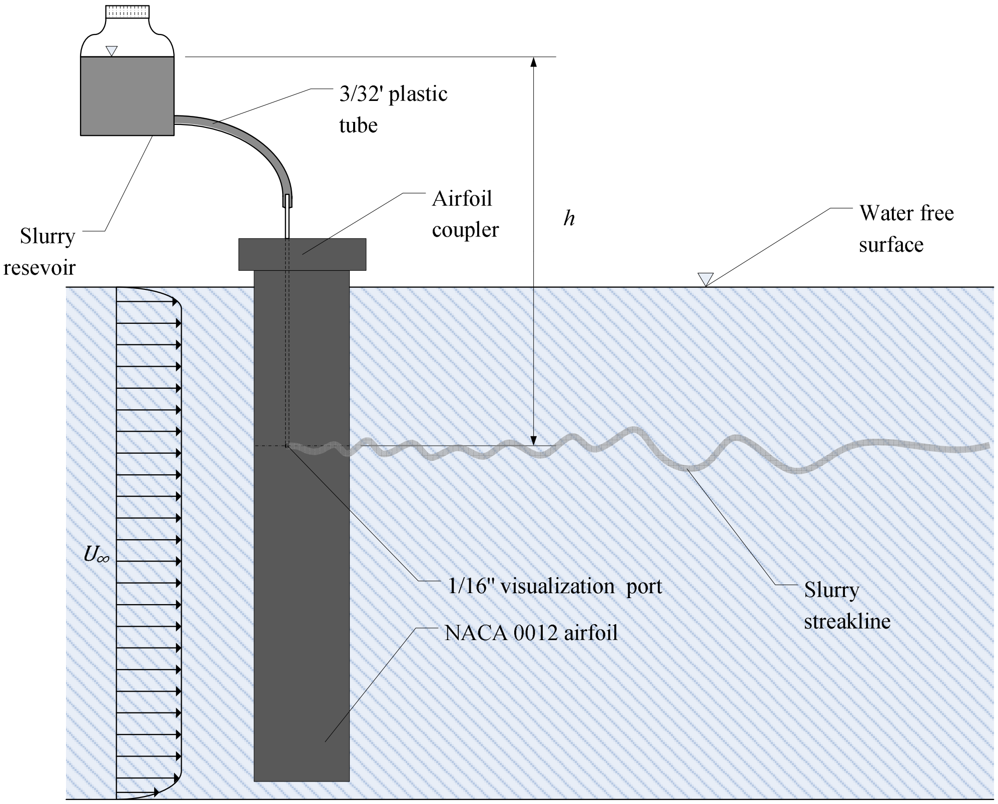

Figure 4.2: Slurry injection flow visualization experimental setup schematic

The instantaneous wake images reveal the vortices' spatial organization in a given wake so as to identify the type of wake in the image. To quantitatively understand wake transition phenomena, PIV is used on selected wake measurement. Then a more detailed wake analysis, which goes beyond simple wake classification based on spatial organization of visibly dominant structures, is performed. The instantaneous streakline images serve as a starting point and allow for targeted use of the PIV imaging technique.

Select examples of the instantaneous wake photographs are shown in Figure 4.3 and Figure 4.4. These images capture the three primary wake types under investigation: the 2S_vK wake, the 2S_A wake and the 2S_ivK wake, which are shown from left to right respectively. The freestream velocity is maintained at 0.017m/s and the airfoil has a chord thickness D of 0.0086 m yielding a Reynolds number of 146.

In Figure 4.3, the three wake types are achieved by varying the frequency of oscillation f while maintaining constant amplitude of A_d = 0.84. The 2S_vK, 2S_A and the 2S_ivK have St_d of 0.129, 0.201 and 0.274 respectively. In Figure 4.4, the three wake types are achieved by varying the amplitude of oscillation while maintaining a constant frequency of St_d = 0.161. Here the amplitudes A_d of 0.42, 1.04 and 1.47 are used for the 2S_vK, 2S_A description and the 2S_ivK wake types respectively. The images show the vortices and how they are arranged in the wake. Lines linking the individual vortices, called connecting braids, are visible in the images. The braids reveal the direction of rotation of the vortices and allow the associated wakes type to be identified. As the vortices progress downstream they grow in diameter and the particle slurry diffuses into the surrounding fluid making the vortices increasingly less visible. While difficult to compute the rate or exact magnitudes of vortex decay from the images quantitatively, it appears that the vortices decay much faster in the 2S_A and 2S_ivK compared to the 2S_vK. In total 37 wake images are used to characterize the various wake conditions.

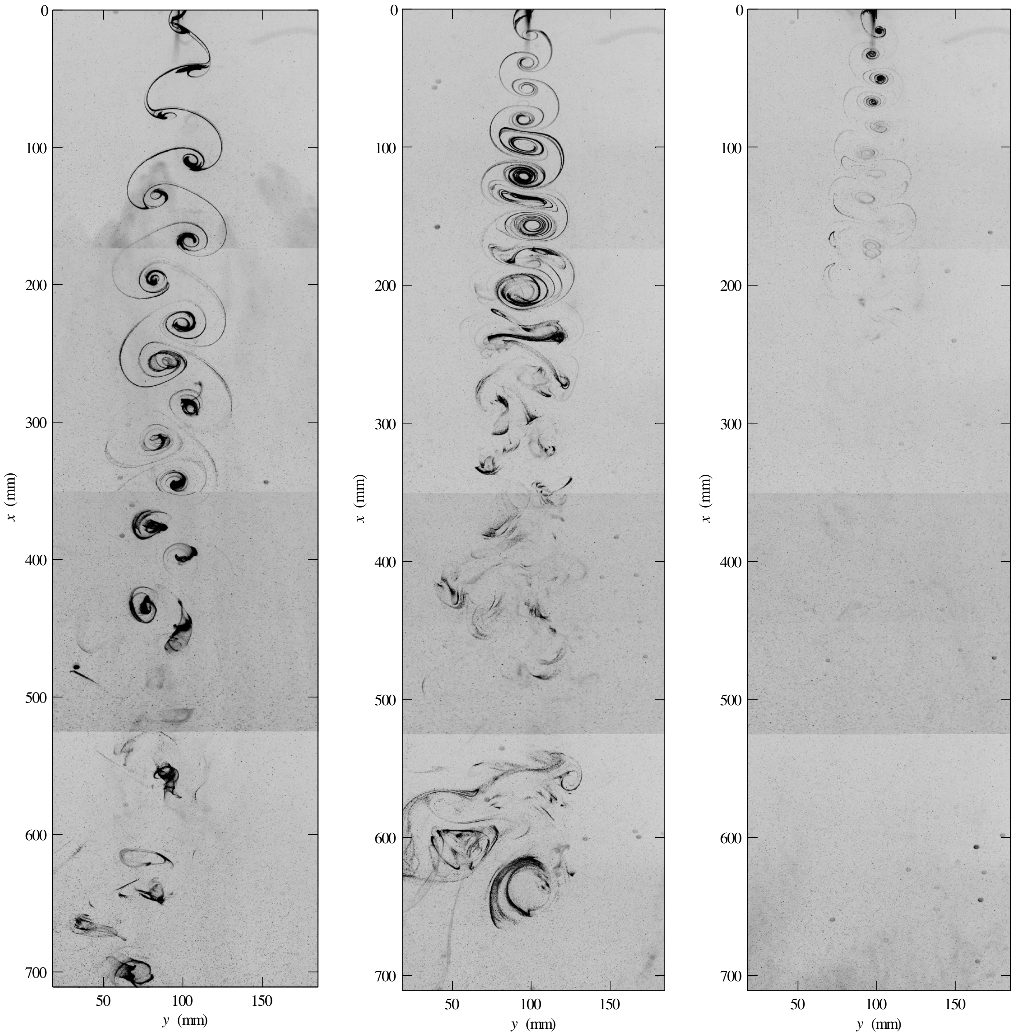

a) b) c)

Figure 4.3: Instantaneous streakline images for A_d = 0.84 and a) St_d = 0.129 which fits the 2S_vK type wake, b) St_d = 0.201 a 2S_A type wake and c) St_d = 0.274 a 2S_ivK type wake.

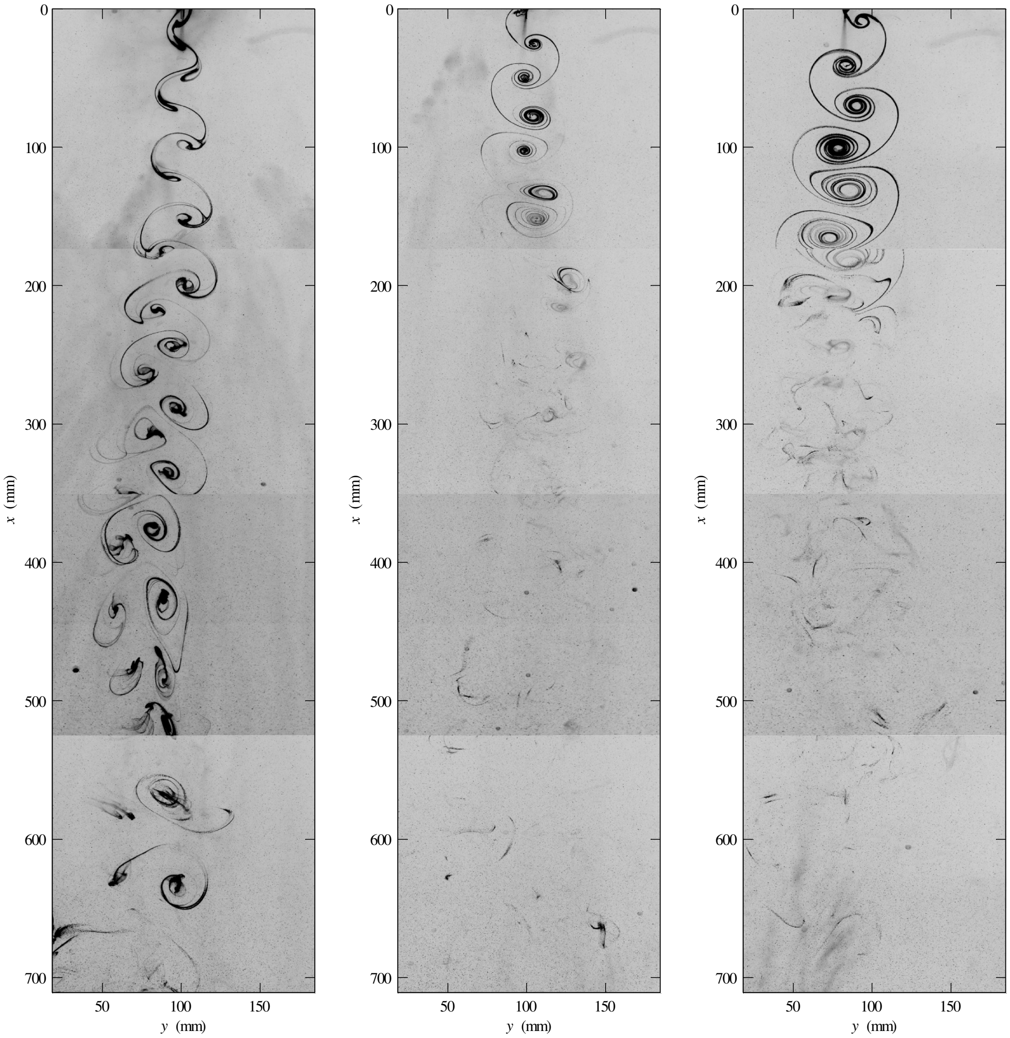

(a) (b) (c)

Figure 4.4: Instantaneous streakline snapshots for St_d = 0.161 and a) A_d = 0.42 a 2S_vK type wake, b) A_d = 1.04 a 2S_A type wake and c) A_d = 1.47 a 2S_ivK type wake.

4.3.2 Phase diagram

The values for θ_A, f, St_d , A_d and the corresponding wake type for the 37 test cases captured using flow visualization are identified and summarized in Table 4.1. The images are then divided into 4 types of wakes: 2S_vK, 2S_A, 2S_ivK and asymmetric inverted von Karman (2S_ivKa). The phase map in Figure 4.5 is a graphical representation of the data in Table 4.1. The individual wake types are plotted with dimensionless frequency St_d as the horizontal axis and dimensionless amplitude A_d as the vertical axis. This phase map serves to predict important transitions between the 4 wake types and demonstrates how variations in St_d and A_d affect the spatial organization of large structures in the wake of an oscillating airfoil. The 2S_A wake type may be viewed as a transitional region where the 2 vortex rows coincide. 2S_A wake type is marked as black squares '□' and the transitional region is estimated by a spline curve fit between these points. This curve tends to a minimum A_d = 0.42 indicating that at small oscillation amplitudes, the wake type is 2S_vK and independent of oscillation frequency.

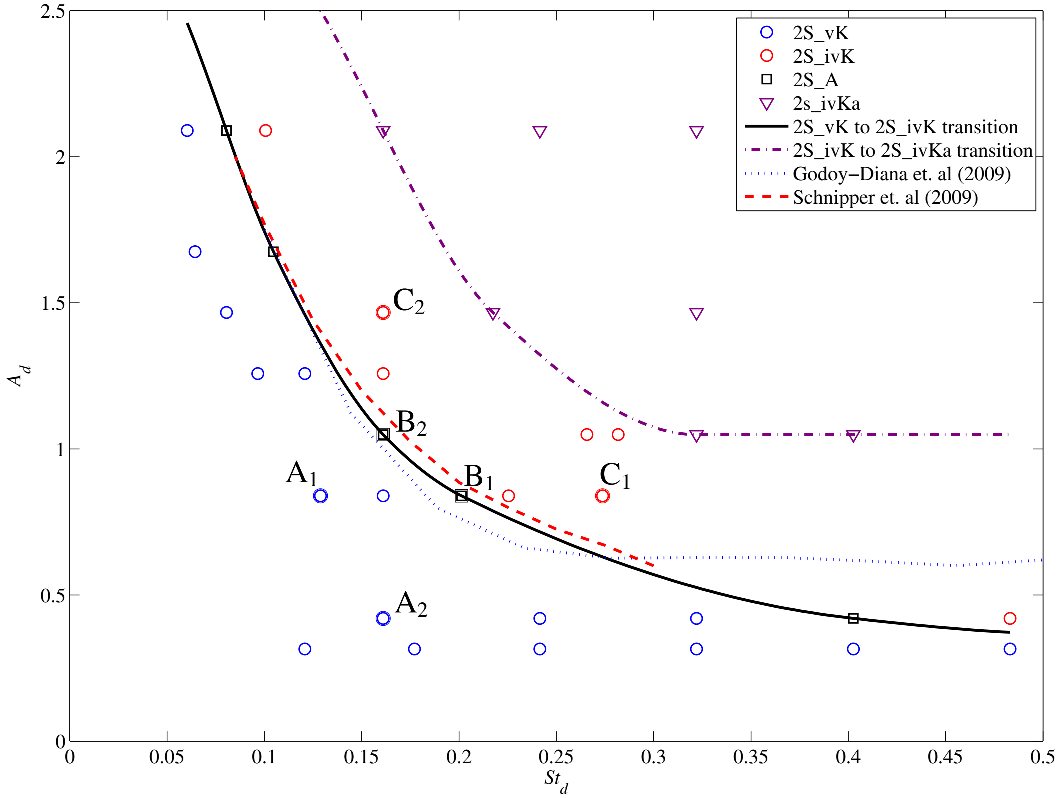

Figure 4.5: Dimensionless Strouhal number St_d based on chord width *D*, and dimensionless amplitude A_d map out various wake patterns which are the result of several oscillation frequency and amplitude combinations for the NACA 0012 airfoil in steady flow. The black dotted line indicates the boundary where the wake transitions from a 2S_vK to an 2S_ivK wake and the purple dotted line indicates where the wake transitions from 2S_ivK to 2S_ivKa.

The 2S_vK to 2S_ivK transition curves obtained by Schnipper et al. (2009) and by Godoy-Diana et al. (2009) are compared to the one obtained in this study. Schnipper et al. (2009) shows good agreement throughout, whereas Godoy-Diana et al. (2009) only shows good agreement for $St_d < 0.175$. This is likely due to an insufficient number of data points in the range of $0.4 < A_d < 0.6$ for the Godoy-Diana et al. (2009) study.

Table 4.1: Classification, St_d and A_d for various wake schemes

Wake No.	$\theta_A/2$ (degrees)	f (rad/s)	St_d	A_d	Classification
1	1.5	1.50	0.121	0.32	2S_vK
2	1.5	2.20	0.177	0.32	2S_vK
3	1.5	3.00	0.242	0.32	2S_vK
4	1.5	4.00	0.322	0.32	2S_vK
5	1.5	5.00	0.403	0.32	2S_vK
6	1.5	6.00	0.483	0.32	2S_vK
7 (**A_2**)	2	2.00	0.161	0.42	2S_vK
8	2	3.00	0.242	0.42	2S_vK
9	2	4.00	0.322	0.42	2S_vK
10	2	5.00	0.403	0.42	2S_A
11	2	6.00	0.483	0.42	2S_ivK
12 (**A_1**)	4	1.60	0.129	0.84	2S_vK
13	4	2.00	0.161	0.84	2S_vK
14 (**B_1**)	4	2.50	0.201	0.84	2S_A
15	4	2.80	0.225	0.84	2S_ivK
16 (**C_1**)	4	3.40	0.274	0.84	2S_ivK
17 (**B_2**)	5	2.00	0.161	1.04	2S_A
18	5	3.30	0.226	1.04	2S_ivK
19	5	4.00	0.322	1.04	2S_ivKa
20	5	3.50	0.282	1.04	2S_ivKa

21	5	5.00	0.403	1.04	2S_ivKa
22	6	1.20	0.097	1.26	2S_vK
23	6	1.50	0.121	1.26	2S_vK
24	6	2.00	0.161	1.26	2S_ivK
25	7	1.00	0.081	1.47	2S_vK
26 (**C_2**)	7	2.00	0.161	1.47	2S_ivK
27	7	2.70	0.217	1.47	2S_ivKa
28	7	4.00	0.322	1.47	2S_ivKa
29	8	0.80	0.064	1.67	2S_vK
30	8	1.00	0.081	1.67	2S_vK
31	8	1.30	0.105	1.67	2S_A
32	10	0.75	0.060	2.09	2S_vK
33	10	1.00	0.081	2.09	2S_A
34	10	1.25	0.101	2.09	2S_ivK
35	10	2.00	0.161	2.09	2S_ivKa
36	10	3.00	0.242	2.09	2S_ivKa
37	10	4.00	0.322	2.09	2S_ivKa

A second wake transition is observed when the deflection angle of the mean jet flow of the 2S_ivK wake becomes non-zero. Wakes in this region of the phase map are referred to as 2S_ivKa and are defined by (Godoy-Diana et al., 2009). Wakes of this variety typically occurs at higher frequencies and amplitudes and are similar in structure to the 2S_ivK wake, with the exception that the two vortex rows have some non-zero angle relative to the flow direction. (Godoy-Diana et al., 2009) refer to this transitional region as the symmetry-breaking threshold. Since the intention is to expand the current study to a tandem airfoil configuration, the wake conditions will be kept well below this transitional threshold. This approach leads to zero jet flow deflection and allows for future tandem alignment for the two airfoils.

PIV measurements are only performed for select points on the phase map and are marked $\mathbf{A_1}$, $\mathbf{B_1}$, $\mathbf{C_1}$, $\mathbf{A_2}$, $\mathbf{B_2}$ and $\mathbf{C_2}$ in Table 4.1 and Figure 4.5. The wakes types selected for the PIV study cover the three main wake types; 2S_vK, 2S_A and 2S_ivK. The cases are selected to vary one of A_d or St_d so as to examine the effect of varying only A_d at constant St_d, or St_d at constant A_d. This is done to examine the effect of each variable on wake type while holding the other constant.

4.4 Wake characterization of select regimes

4.4.1 Wake arrangement

For the cases denoted $\mathbf{A_1}$, $\mathbf{B_1}$, $\mathbf{C_1}$, $\mathbf{A_2}$, $\mathbf{B_2}$ and $\mathbf{C_2}$ in Table 4.1 and Figure 4.5, a more in depth investigation was performed. This analysis is performed using the PIV measurement technique described in *Chapter 3*. For each case, 100 PIV images are taken when the airfoil angle reaches $\theta_{af} = 0°$ through a CW half-cycle rotation. Phase averaging is used to reduce noise in the experimental data. However, caution must be employed using phase averaged data for calculating global parameters such as circulation. This will be described in more detail in a later section.

The first set of data points ($\mathbf{A_1}$, $\mathbf{B_1}$, $\mathbf{C_1}$) represent a horizontal path in Figure 4.5 intersecting the 2S_vk to 2S_ivK transition curve (black dotted line) in the phase map. Figure 4.6 illustrates three phase averaged vorticity fields along with vortex cores as white '×' and vortex boundaries as circles of radius r_v in black. These vortex parameters were computed with the CVD characterization algorithm described in *Chapter 3*. The wake types in Figure 4.6 (a), (b) and (c) correspond to cases $\mathbf{A_1}$, $\mathbf{B_1}$, $\mathbf{C_1}$ and cover the 2S_vK, 2S_A and 2S_ivK wake types respectively.

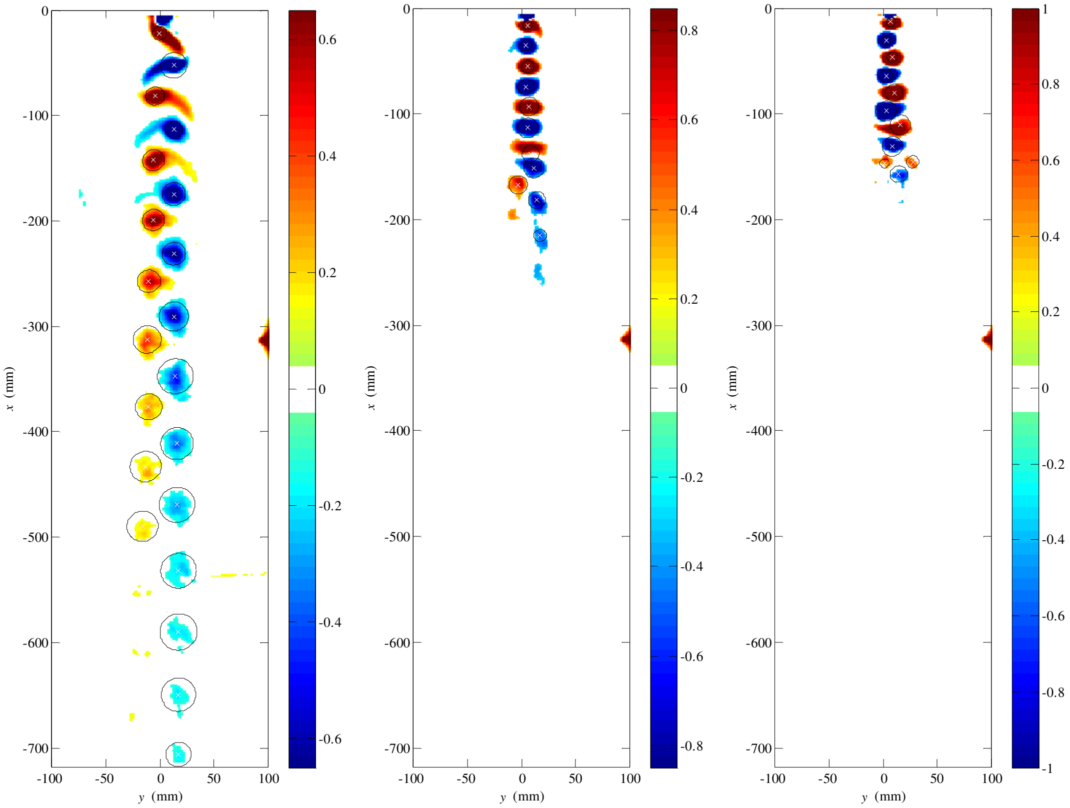

(a) (b) (c)

Figure 4.6: Vorticity, ω (s^{-1}), for A_d = 0.84 and a) St_d = 0.129 a 2S_vK type wake, b) St_d = 0.201 a 2S_A type wake and c) St_d = 0.274 a 2S_ivK type wake. The suspected vortex cores along with their respective boundary radii are plotted on as white points and black circles respectfully.

The vorticity thresholds were selected based on principles that were discussed in *Chapter 3* and essentially depend on the number of velocity vectors that span an average vortex diameter ϕ_v. Increasing the frequency from St_d = 0.121 to St_d = 0.201 causes the two separate vortex rows from case $\mathbf{A_1}$ to overlap and coincide with the airfoil chord line. In case $\mathbf{B_1}$ the vortices exhibit higher vorticity and experience faster decay than for case $\mathbf{A_1}$. In case $\mathbf{C_1}$ the frequency is further increased to St_d = 0.274 and it is observed that the vortex rows fall out of alignment and drift apart in the transverse direction opposite compared to the

2S_vK wake in case $\mathbf{A_1}$. In addition, the vortex rows of case $\mathbf{C_1}$ are still symmetrically oriented about the chord line confirming that the wake has not yet transitioned to the 2S_ivKa type. The vorticity indicated by the color map in Figure 4.6 shows that the vortices in wake $\mathbf{C_1}$ have the highest vorticity and the highest decay rate.

Figure 4.7 illustrates three phase averaged vorticity maps along with vortex cores as white points and vortex boundaries in black. The wake types in Figure 4.7 (a), (b) and (c) correspond to cases $\mathbf{A_2}$, $\mathbf{B_2}$, $\mathbf{C_2}$ and cover the 2S_vK, 2S_A and 2S_ivK wake types respectively. Here the oscillation frequency is fixed and the amplitude is varied. The general wake types observed in Figure 4.7 appear to match the corresponding cases in Figure 4.6. However, this only occurs for small amplitude oscillations and frequencies.

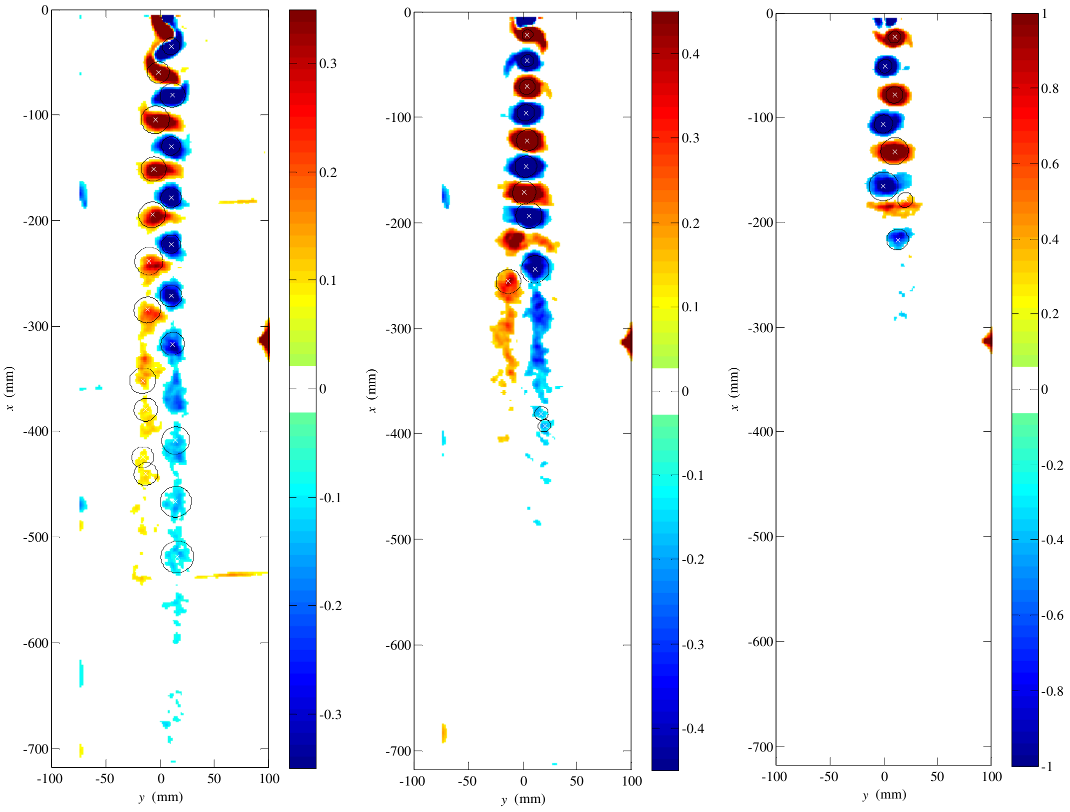

(a) (b) (c)

Figure 4.7: Vorticity, ω (s^{-1}), for St_d = 0.161 and a) A_d = 0.42 a 2S_vK type wake, b) A_d = 1.04 a2S_A type wake and c) A_d = 1.47 a 2S_ivK type wake. The suspected vortex cores along with their respective boundary radii are plotted on top as white points and black circles respectfully.

4.4.2 Phase average vortex cross-sectional study

Vorticity distribution profiles are used as vortex characterization tools. In *Chapter 3* the vorticity distribution profile is shown to be useful for evaluating the accuracy of the vortex radius r_v, and to validate the CSL method. Here they are used to compare vortex shape and vortex symmetry in the 2S_vK, 2S_A and the 2S_ivK wake types and for selecting appropriate analytical models to predict vortex time evolution trends.

A sample vortex from the 2S_vK wake (Case $\mathbf{A_1}$ from

Table 4.1) is shown in Figure 4.8. Streamlines generated from a reference frame moving with the vortex core are plotted over the vorticity background and the position of the vortex core appears as a white circle. The vortex in Figure 4.8 appears to be relatively circular in shape. Any neighboring vortices are sufficiently far and as a result, they do not seem to distort or bend the streamlines away from its core a significant amount. The computed core coincides with both the peak vorticity and the visible center of curvature of the WA compliant streamlines.

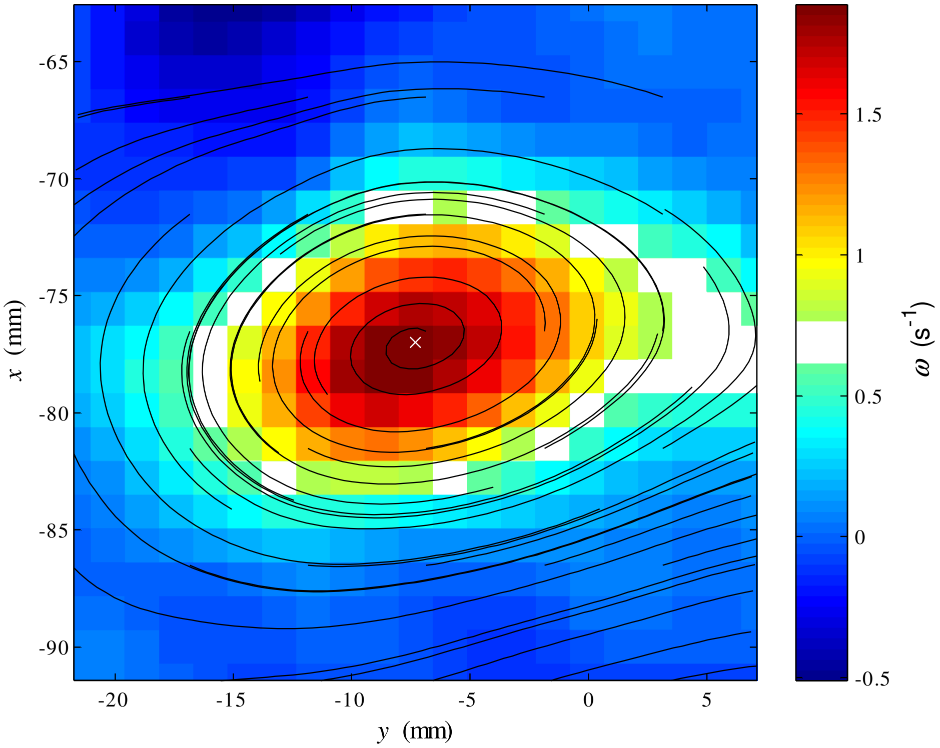

Figure 4.8: Vorticity map of a sample vortex from the 2S_vK wake with A_d = 0.84 and St_d = 0.129 along with streamlines plotted from a moving reference frame equal to the suspected drift velocity of the vortex v_d.

The vorticity distribution for this vortex and for an ideal Burgers and Rankin vortices are shown in Figure 4.9. The vorticity is plotted against the dimensionless radius $(y - y_{core})/r_v$ along a transverse line of constant *y* passing through the vortex core. The experimental phase average vorticity distribution matches the shape of a Gaussian distribution so the vortices in the 2S_vK wake can be modeled as Burgers vortices.

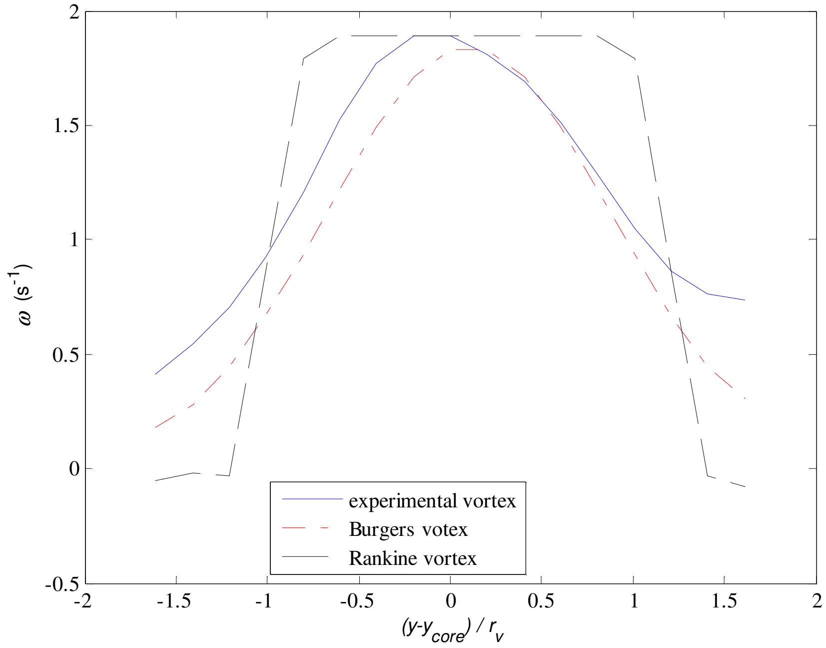

Figure 4.9: Vorticity profile for a sample vortex from the 2S_vK wake with A_d = 0.84 and St_d = 0.129

A sample phase average vortex from the 2S_A wake (Case $\mathbf{B_1}$ from Table 4.1) is shown in Figure 4.10. Streamlines generated from a reference frame moving with the vortex core are plotted over the phase average vorticity background and the vortex core appears as a white circle. As with the 2S_vK sample vortex, the 2S_A vortex is relatively circular in shape and the computed core coincides with both the peak vorticity and the visible center of curvature of the WA compliant streamlines. Neighboring vortices are closer than in the 2S_vK wake in Figure 4.8 but overlap into the sample vortex's boundary is not observed.

However, streamlines further away from the core demonstrate irregular curvature suggesting that an influence from neighboring vortices may exist.

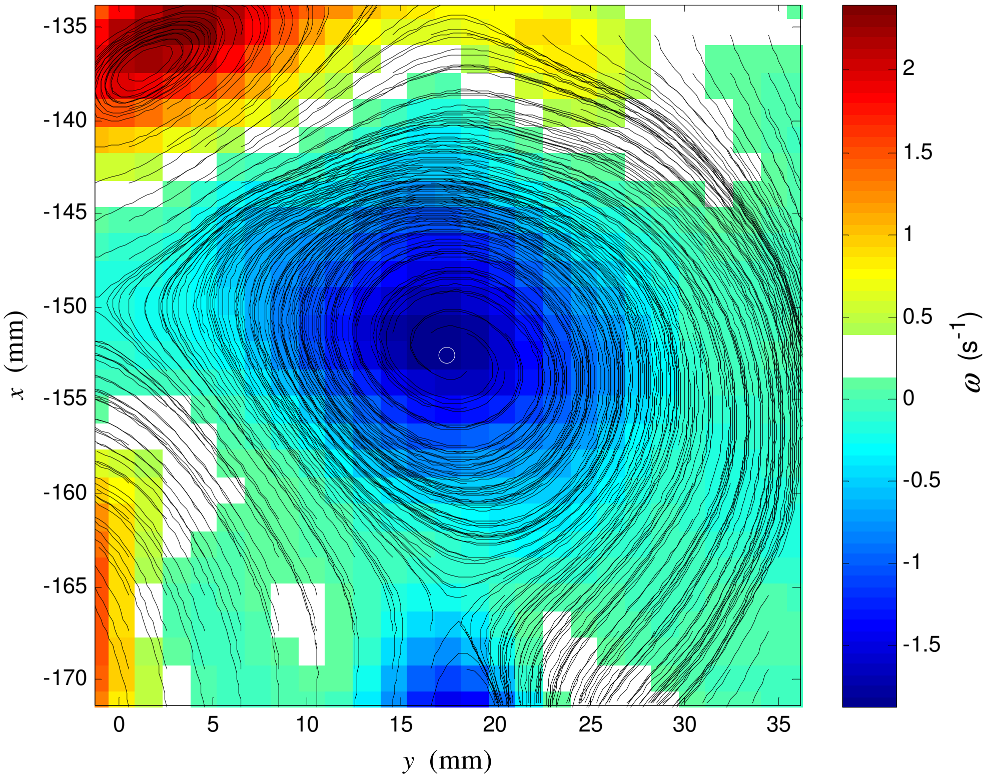

Figure 4.10: Vorticity map of a sample vortex from the 2S_A wake with A_d = 0.84 and St_d = 0.201 along with streamlines plotted from a moving reference frame equal to the suspected drift velocity of the vortex v_d.

The phase average vorticity distribution profile for this vortex and for ideal Burgers and Rankin vortices are shown in Figure 4.11. The phase average vorticity and circumferential velocity profiles are plotted using the same method as the 2S_vK wake. A Gaussian vorticity distribution for the vortices in the 2S_A wake results in a Burgers model for this case.

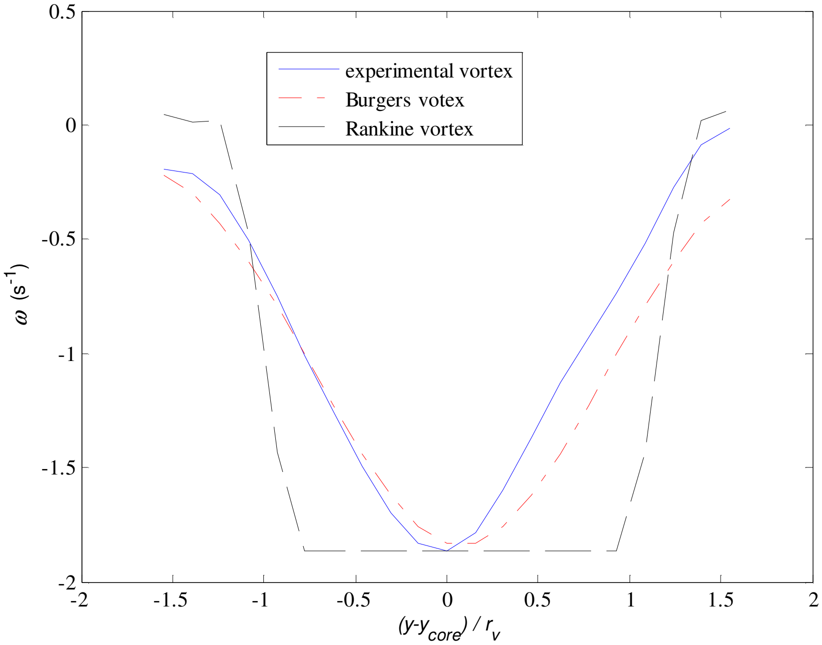

Figure 4.11: Vorticity profile for a sample vortex from the 2S_vK wake with Ad = 0.84 and Std = 0.201

Finally, a sample phase average vortex from the 2S_ivK wake (Case $\mathbf{C_1}$ from Table 4.1) is shown in Figure 4.12. Streamlines generated from a reference frame moving with the vortex core are plotted over the phase average vorticity background and the vortex core appears as a white circle. As with the previous two wakes, the current sample vortex is relatively circular in shape and the computed core coincides with both the peak vorticity and the visible center of curvature of the WA compliant streamlines. Neighboring vortices are closer than in the 2S_vK wake however the boundary radius is expected to be the smallest for this wake (Schnipper et al., 2009); for this reason there is not any vortex boundary overlap.

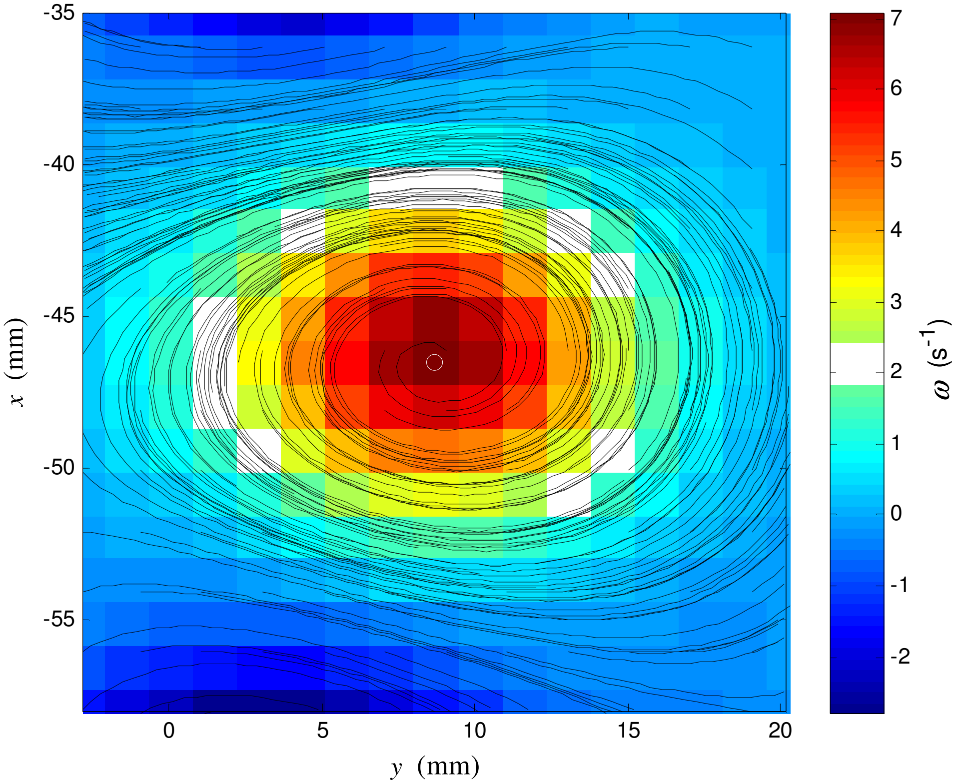

Figure 4.12: Vorticity map of a sample vortex from the 2S_A wake with $A_d = 0.84$ and $St_d = 0.274$ along with streamlines plotted from a moving reference frame equal to the suspected drift velocity of the vortex v_d.

The vorticity distribution profile for this phase average vortex and for ideal Burgers and Rankin vortices are shown in Figure 4.13. The phase average vorticity and circumferential velocity profiles are plotted using the same method as the 2S_vK and 2S_A wakes. A Gaussian vorticity distribution for the vortices in the 2S_ivK wake results in a Burgers model for this case.

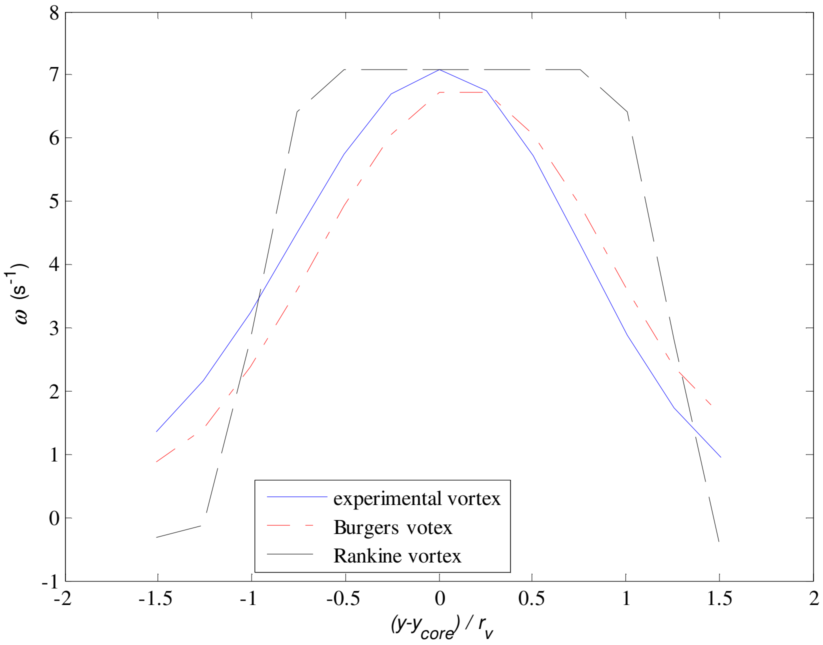

Figure 4.13: Vorticity profile for a sample vortex from the 2S_vK wake with Ad = 0.84 and Std = 0.274

Phase average circumferential velocity profiles corresponding to the 2S_vK, 2S_A and the 2S_ivK wake types, as well as Rankine and Burgers vortices are shown in Figure 4.14, Figure 4.15 and Figure 4.16 respectively. These figures provide further evidence that the vortices in all of the wake schemes may be fit with the Burgers model which ultimately validates the use of *eqn. (4.16)* enabling analytical prediction of vortex decay with time.

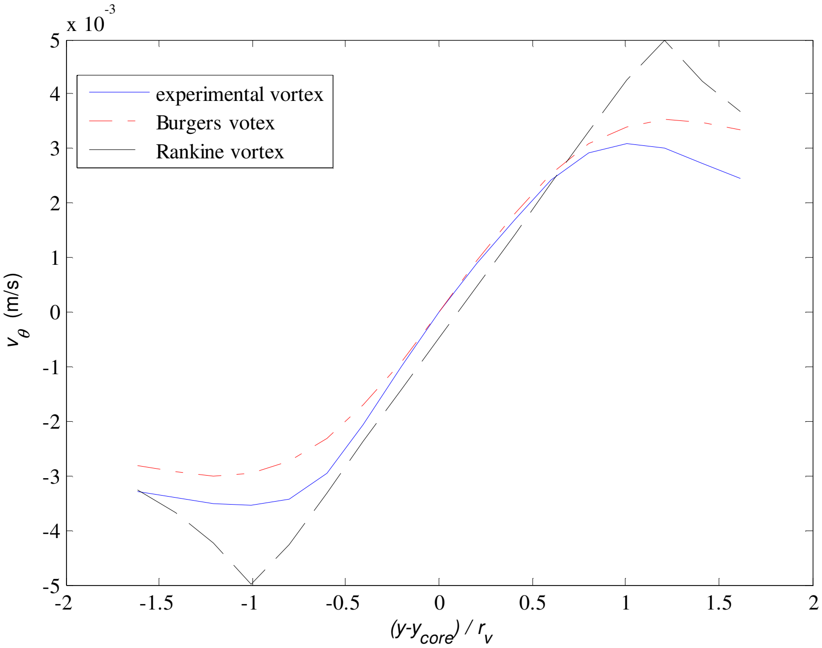

Figure 4.14: Circumferential velocity profile for a sample vortex from the 2S_vK wake with A_d = 0.84 and St_d = 0.129

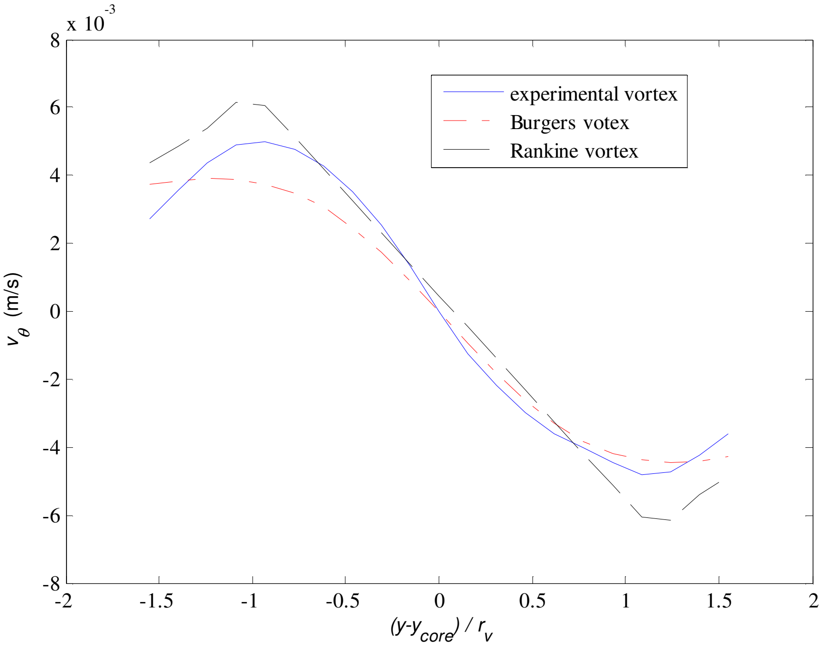

Figure 4.15:Circumferential velocity profile for a sample vortex from the 2S_vK wake with Ad = 0.84 and Std = 0.201

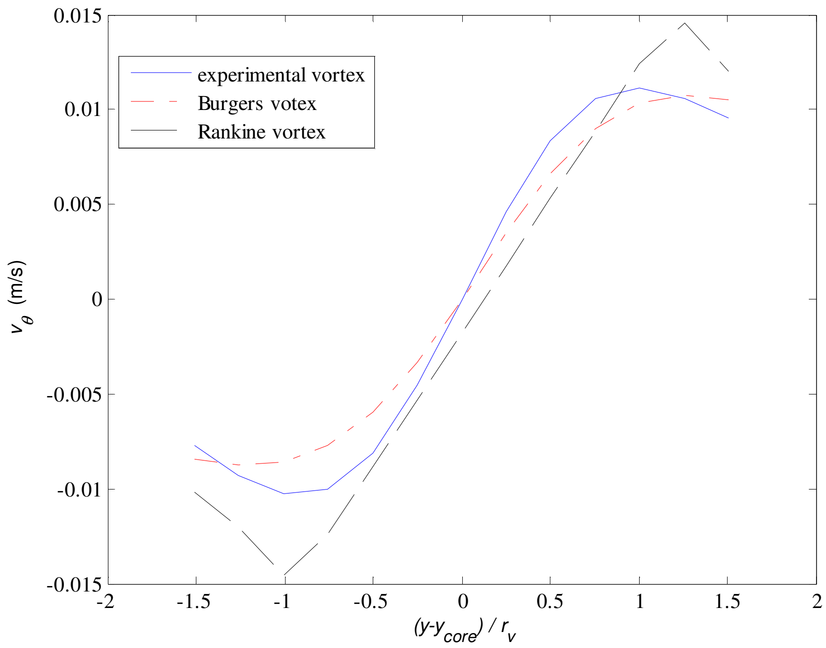

Figure 4.16: Circumferential velocity profile for a sample vortex from the 2S_vK wake with Ad = 0.84 and Std = 0.274

4.4.3 Wake profiles

Wake profiles are generated by time averaging 100 instantaneous vector fields for each of the three wake types described by cases $\mathbf{A_2}$, $\mathbf{B_2}$ and $\mathbf{C_2}$. Rather that imaging at $\theta_{af} = 0°$ as is the case with phase averaging, the time averaged wake profiles are the result of several instantaneous vector fields separated by a constant time 0.15 s. Wake profiles are used to classifying the three wake types as either; drag producing velocity deficit wakes, thrust producing velocity excess wakes, or velocity neutral wakes.

Figure 4.17 shows the wake profiles for cases $\mathbf{A_2}$, $\mathbf{B_2}$ and $\mathbf{C_2}$. The velocity magnitude $\|v\| = \sqrt{v_x^2 + v_y^2}$ m/s is plotted as a background color map and the velocity vectors are plotted over-top. The 2S_vK wake (Figure 4.17 (a) case $\mathbf{A_2}$)

has a distinct velocity deficit extending up to 6 chord lengths downstream. For the 2S_A wake (Figure 4.17 (b) case **B₂**) with $x/C < 2.75$ the flow field has a velocity neutral wake and beyond $x_c = 2.75$ it is characterized by a velocity deficit. For the 2S_ivK wake (Figure 4.17 (c) case **C₂**) a jet profile is observed and at $x_c = 2.5$ it bends slightly in the positive y direction. These findings are consistent with the literature (Bohl & Koochesfahani, 2009) which ultimately suggests that the 2S_vK wake is drag producing and the 2S_ivK wake is thrust producing, while the 2S_A wake has zero velocity deficit for most of the streamwise range except for a small 'dip' where it has a velocity deficit. This 'dip' is believed to coincide with the streamwise location where the vortices in the 2S_A wake essentially fall out of alignment and acquire some finite transverse spacing (Bohl & Koochesfahani, 2009).

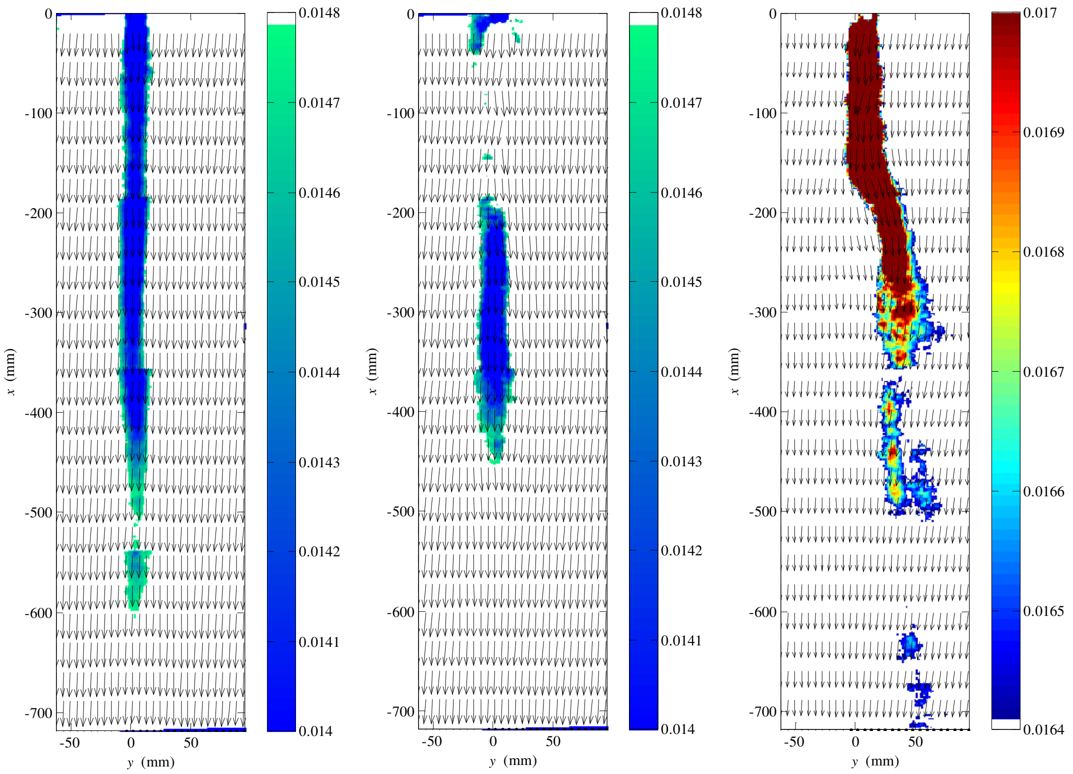

(a) (b) (c)

Figure 4.17: Time resolved average showing the wake velocity profiles with velocity magnitude in the background and velocity vectors plotted over top for St_d = 0.161 and a) A_d = 0.42 a 2S_vK wake type, b) A_d = 1.04 a 2S_A wake type and c) A_d = 1.47 a 2S_ivK wake type.

In Figure 4.18 the dimensionless velocity magnitude $\|v\| / U_\infty$ is plotted along the wake's streamwise centerline for the three wake types in Figure 4.17. This figure captures the distinct velocity deficit accompanied by the 2S_vK wake from case **A₂**, the velocity excess in the 2S_ivK wake from case **C₂** and the velocity neutral profile in the 2S_A wake from case **B₂**. Additionally, it quantifies the differences in velocity magnitude between the three wake types, and it shows the streamwise location of flow recovery.

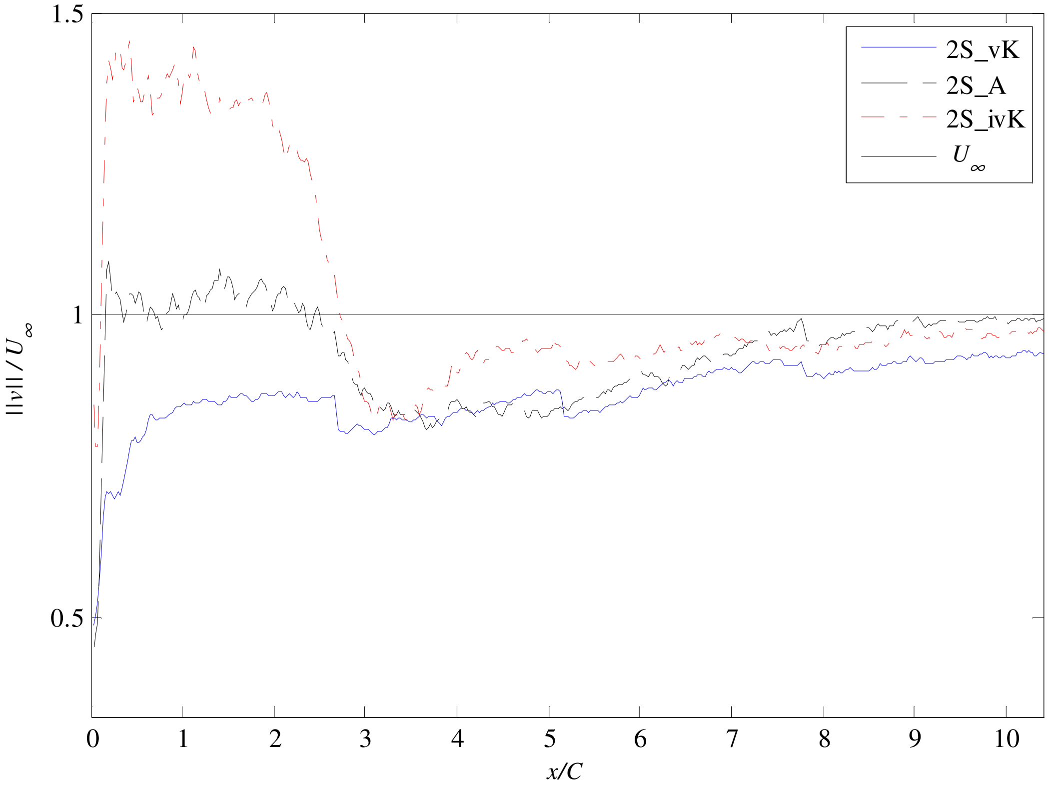

Figure 4.18: Velocity magnitude of time averaged fields along the streamwise symmetry line for St_d = 0.161 and a) A_d = 0.42 a2S_vK wake type, b) A_d = 1.04 a 2S_A wake type and c) A_d = 1.47 a 2S_ivK wake type

In Figure 4.19 the dimensionless velocity magnitude $\|v\| / U_\infty$ is plotted along a transverse line at *x/C* = 1.45 for the three wake types. Outside of the wake profile, the 2S_ivK wake has the lowest velocity magnitude, however as the transverse coordinate approaches the wake centerline, its velocity magnitude quickly surpasses the free stream velocity reaching a maximum value of $\|v\| / U_\infty = 1.35$. In these three wake schemes the oscillation frequency is held constant at 2 rad/s and the wake transitions are achieved by increasing the oscillation amplitude. Given the sinusoidal oscillation waveform, the velocity magnitude of the trailing edge decreases as it moves away from the streamwise centerline, eventually reaching zero and momentarily obstructing the flow at its maximum amplitude. This effect is more prominent in the 2S_ivK wake since it has the largest oscillation amplitude, and explains why far away from the streamwise centerline it has the lowest velocity magnitude.

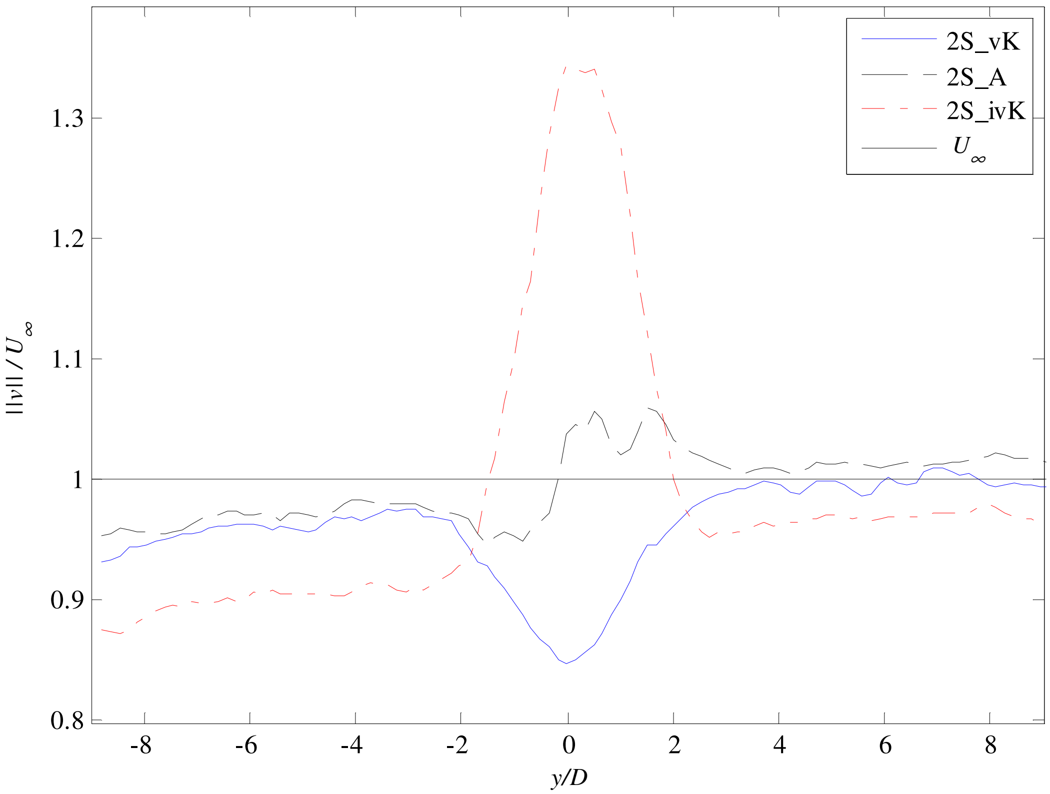

Figure 4.19:Velocity magnitude of time averaged fields along a transverse line at x = 100 mm for St_d = 0.161 and a) A_d = 0.42 a2S_vK wake type, b) A_d = 1.04 a 2S_A wake type and c) A_d = 1.47 a 2S_ivK wake type

4.4.4 Limitations of using phase-averaged fields

In general, vortices in the near field wake of this flow are more spatially consistent than those further downstream. In other words, vortex cores relatively close to the trailing edge are consistently in the same position from one oscillation period to another; but, structures further downstream experience more spatial variation. When several vector fields are phase averaged, the spatially consistent structures tend to preserve their magnitudes while the spatially varying structures tend to be reduced by lower magnitudes in the background field.

The circulation for 25 vector fields of the 2S_vK wake form case $\mathbf{A_1}$, when the airfoil position is $\theta_{af} = 0°$ during a positive CCW rotation, is plotted against the dimensionless downstream distance in Figure 4.20. The circulation Γ for the individual fields are plotted as black dots and the circulation Γ for the phase averaged field is shown as red circular marker. This illustrates the increasing variability of the vortex core's streamwise spatial coordinate x_c with downstream distance. In the near field $x_c = x/C < 2$, the data is grouped in tight vertical lines indicating consistently located vortices; however with increasing streamwise distance, the vortex location becomes variable to the point where the individual groups of data points are no longer discernible. As a result, the phase averaged data underestimates the circulation magnitude when compared to each instantaneous vector field.

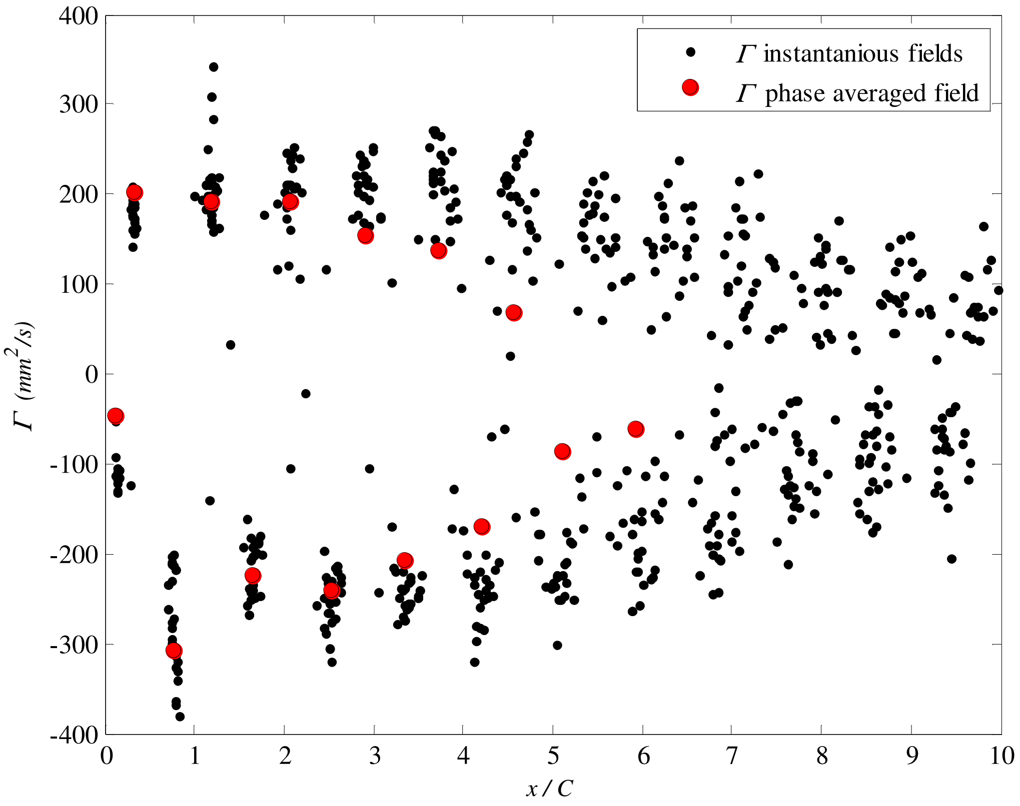

Figure 4.20:Circulation vs. streamwise distance for Ad = 0.84 and Std = 0.129 (2S_vK wake) showing the inaccuracies of using phase averaged data to predict certain parameter

Figure 4.21 illustrates the vortex boundary radii r_v as a function of the streamwise spacing for the same 25 sample fields as well as the phase averaged field. The radii obtained from phase averaged vector fields tend to be larger than in the instantaneous fields. Again, this is attributed to the spatial inconsistency of the vortices at high streamwise distances, leading to exaggerated vortex boundaries in the phase averaged field.

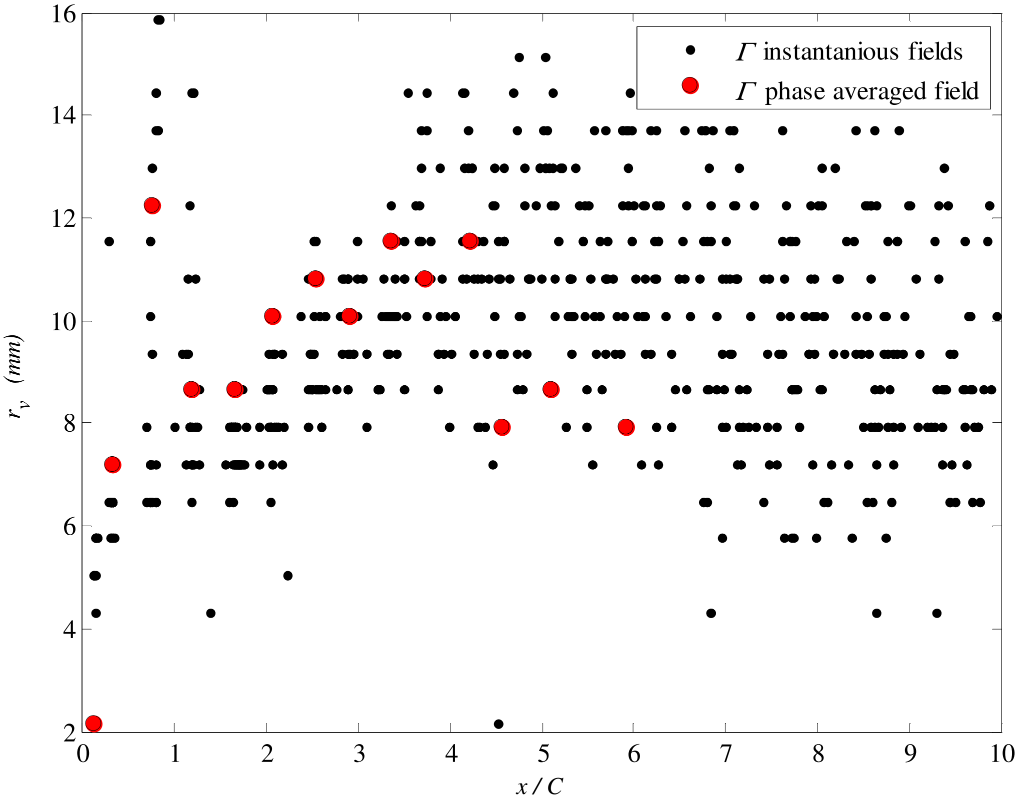

Figure 4.21: Vortex radius vs. streamwise distance for Ad = 0.84 and Std = 0.129 (2S_vK wake) showing the inaccuracies of using phase averaged data to predict certain parameter

4.4.5 Initial circulation estimates

Initial circulation Γ_o is estimated by studying the different sources of vorticity on the airfoil. Schnipper et al. 2009 suggest that the magnitude of the initial circulation on an oscillating airfoil is a result of both boundary layer circulation Γ_{BL} formed on one side of the foil during a half-cycle and trailing edge circulation $\Gamma_{TE,}$ produced as a result of the flapping motion of the foil. It is believed that the initial circulation in a 2S_vK wake is dominated by Γ_{BL} since the free-stream velocity U_∞ is relatively high compared to the flapping velocity of the airfoil. This coupled with the no-slip condition at the airfoil boundary leads to the following estimate for initial circulation Γ_o in a 2S_vK wake:

$$\Gamma_{BL} = \frac{1}{2}\int_0^{\frac{1}{2f}} U_\infty^2 dt = \frac{U_\infty}{4f} = \frac{DU_\infty}{4St_D} \tag{4.17}$$

Similarly, Schnipper et al. 2009 suggest that the initial circulation in an 2S_ivK wake is dominated by Γ_{TE} since the inherently higher oscillation amplitudes and frequencies lead to high airfoil tip velocities at the trailing edge effectively dwarfing the free stream velocity. The Γ_{TE} estimate is calculated by neglecting the free stream flow and considering only the motion of the trailing edge as follows:

$$\Gamma_{TE} = \frac{1}{2}\int_0^{\frac{1}{2f}} V_{TE}^2(t) dt \approx \frac{\pi^2 f \theta_A^2 C_{AC}^2}{2} = \frac{\pi^2 St_D U_\infty C_{AC}^2}{2D} \sin^{-1}\left(\frac{A_D D}{2C_{AC}}\right) \tag{4.18}$$

where V_{TE} is the magnitude of velocity of the trailing edge and C_{AC} is the length from the aerodynamic centre of the airfoil to the trailing edge. Table 4.2 lists the estimated initial circulation magnitudes for the select wake types using these equations. The initial circulation estimate for the 2S_A wake is closer to experimental values when the Γ_{TE} method is used.

Table 4.2: Initial circulation estimates Γ_o for select wake types

Wake type	ST_D	A_D	Γ_o (mm²/s)	Method
2S_vK (case **A₁**)	0.129	0.84	283	Γ_{BL}
2S_A (case **B₁**)	0.201	0.84	366	Γ_{TE}
2S_ivK (case **C₁**)	0.274	0.84	500	Γ_{TE}
2S_vK (case **A₂**)	0.161	0.42	227	Γ_{BL}
2S_A (case **B₂**)	0.161	0.104	363	Γ_{TE}
2S_ivK (case **C₂**)	0.161	0.147	515	Γ_{TE}

4.4.6 Detailed wake investigation

A detailed wake investigation is performed for the PIV data from cases $\mathbf{A_1}$, $\mathbf{B_1}$ and $\mathbf{C_1}$. Several important wake parameters are evaluated and compared to relevant literature and to theoretical predictions. The parameters evaluated are; circulation Γ, peak vorticity ω_{peak}, vortex boundary radii r_v, vortex streamwise drift velocity v_{drift}, streamwise vortex spacing S_x and transverse vortex spacing S_y. Vortex detection and characterization is performed on 25 vector fields per type. Phase averaged fields are not used for reasons discussed above. This experimental methodology requires almost 25 times the computation per flow type compared to a single phase averaged field. It is however a necessary procedure to ensure accurate representation of the vortical nature of the flow field.

One arbitrarily chosen flow field per flow regime is used for discussion. Figure 4.22 contains the three sample fields which correspond to cases $\mathbf{A_1}$, $\mathbf{B_1}$ and $\mathbf{C_1}$ covering the 2S_vK, 2S_A and 2S_ivK wake types respectively. While similar to the vorticity fields in Figure 4.6 and Figure 4.7, these are not phase averaged fields. Annotations are also included in Figure 4.22 that will be used in discussion, later in this chapter.

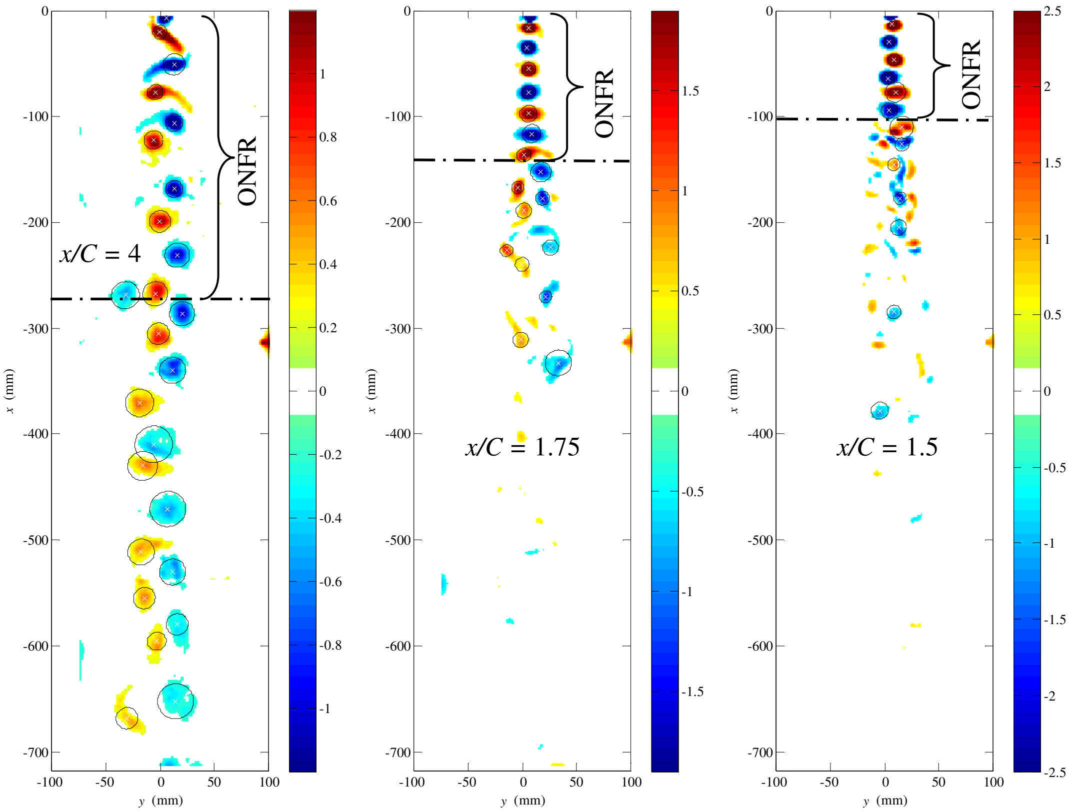

(a) (b) (c)

Figure 4.22: Sample instantaneous vorticity fields, ω (s^{-1}), for A_d = 0.84 and a) St_d = 0.129 a the 2S_vK wake type, b) St_d = 0.201 a 2S_A wake type and c) St_d = 0.274 a 2S_ivK wake type. The suspected vortex cores along with their respective boundary radii are plotted on as white crosses and black circles respectively.

2S_vK wake type (case A_1)

The circulation Γ for the 2S_vK wake from case $\mathbf{A_1}$ in Table 4.1 is shown in Figure 4.23 for the 25 instantaneous velocity fields. The vortices from the sample field shown in Figure 4.22(a) are highlighted with red circles and the results from the 25 instantaneous fields are fitted to a 2nd order exponential curve as follows:

$$\bar{\Gamma}(x_c) = ae^{bx_c} + ce^{dx_c} \tag{4.19}$$

The relevant fit coefficients are listed in Table 4.3. In order to predict the analytical time evolution of peak vorticity $\widehat{\omega}_{peak}(t)$, *eqns. 3.12-3.16* suggest that a constant value for initial circulation Γ_o must be assumed. $\Gamma_o = 200$ mm^2/s is plotted in Figure 4.23.

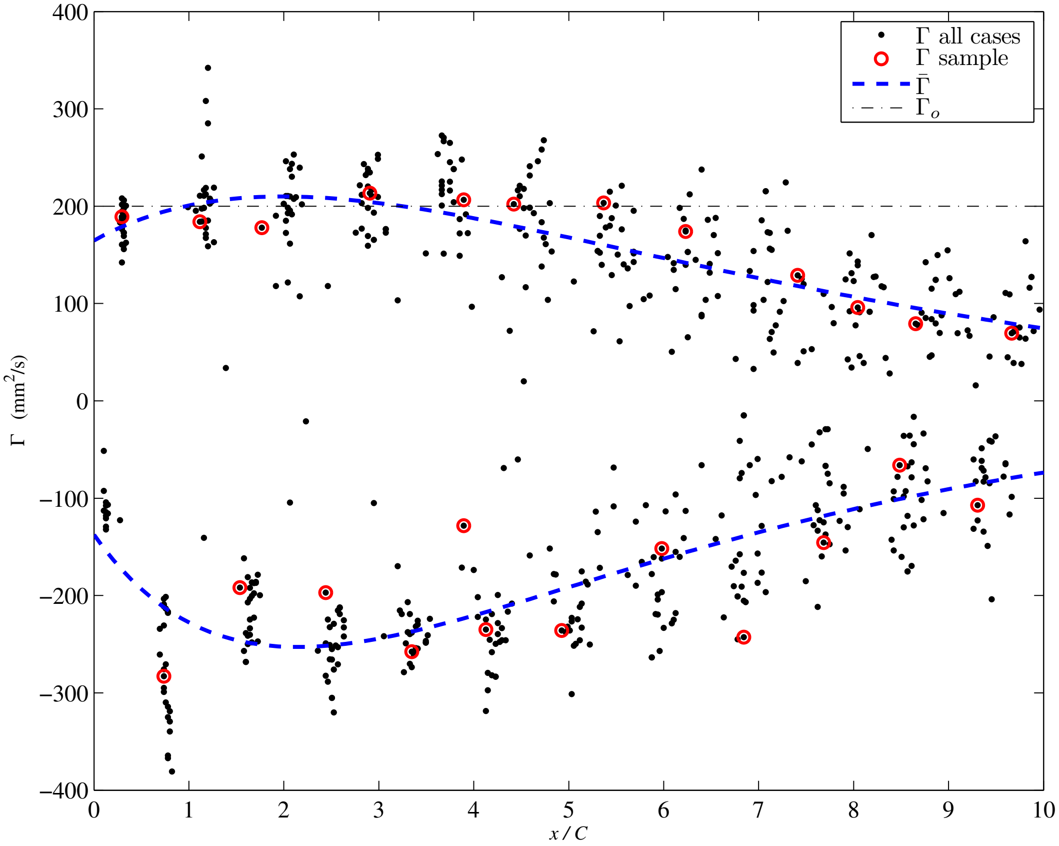

Figure 4.23: Circulation vs. dimensionless streamwise distance for A_d = 0.84 and S_{td} = 0.129 (f = 1.60 rad/s and $\theta_A/2 = 4°$)

A circulation error can be defined by $\tilde{\Gamma_o} = |\,\Gamma_o - \bar{\Gamma}|/\,\Gamma_o$ and is plotted in Figure 4.24. It remains within 0.05 for streamwise distances of 0.5< *x/C* <3.85. However, it begins to increase appreciably when *x/C* is increased beyond 4 chord lengths. This increase is attributed to vortex core overlap, in which an aged vortex diffuses into the viscous core of a neighboring vortex (Ponta, 2010).

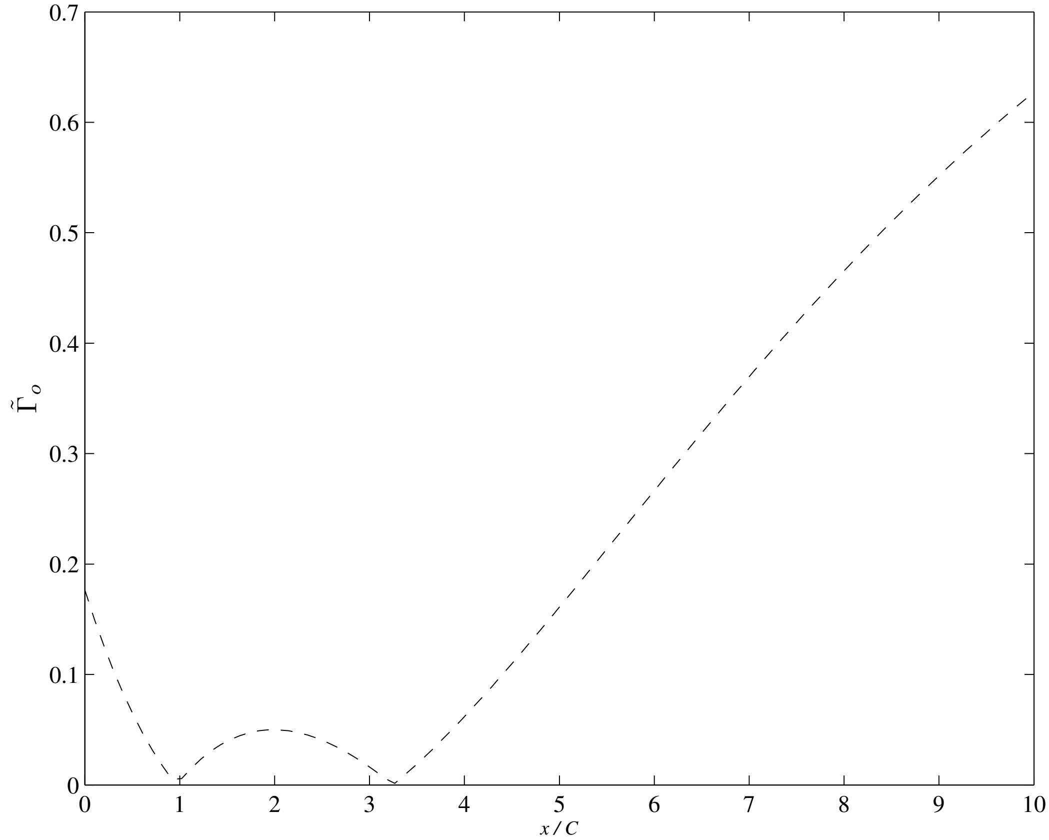

Figure 4.24: Initial circulation estimate error vs. dimensionless streamwise distance for A_d = 0.84 and S_{td} = 0.129 ($f = 1.60$ rad/s and $\theta_A/2 = 4°$)

The trend in Figure 4.23 for near field distances *x/C* < 4, is consistent with the literature which ultimately suggests that circulation is expected to remain relatively constant for a certain distance, typically before the onset of core overlap, since in such flows the vorticity is not destroyed, it is merely diffused by viscous action through the body of the fluid (Ponta, 2010).

The evolution of peak vorticity ω_{peak} for the 2S_vK wake from case $\mathbf{A_1}$ in Table 4.1 is shown in Figure 4.25 for the 25 instantaneous velocity fields. The peak vorticity for vortices in the sample field are highlighted as red circles and all of the data is fitted with an exponential curve based on the analytical prediction in *eqn. (4.16)* as follows:

$$\overline{\omega}_{peak}(x_c) = \frac{ae^{ax_c}}{be^{ax_c} - b + \left(\frac{a}{c}\right)} \tag{4.20}$$

The relevant fit coefficients are reported in Table 4.3. The analytical time evolution of peak vorticity $\widehat{\omega}_{peak}(t)$ for positive vortices is estimated using *eqn. (4.16)*. In order to compare the analytical peak vorticity with experimental data, it is necessary to rearrange *eqn. (4.16)* so that the independent variable is the dimensionless streamwise distance $x_c = x/C$ rather than time t. This is accomplished by using the average streamwise drift velocity v_{drift} = 0.153 m/s and substituting:

$$t = x_c\left(\frac{C}{v_{drift}}\right) \tag{4.21}$$

into *eqn. (4.16)*. Then $\widehat{\omega}_{peak}(t)$ is expressed in terms of the dimensionless streamwise coordinate x_c as follows:

$$\widehat{\omega}_{peak}(x_c) = \frac{\beta e^{\beta x_c\left(\frac{C}{v_{drift}}\right)}}{\frac{4\pi\nu}{\Gamma_o}(1 - e^{-1})e^{\beta x_c\left(\frac{C}{v_{drift}}\right)} - \frac{4\pi\nu}{\Gamma_o}(1 - e^{-1}) + \left(\frac{\beta}{\omega_o}\right)} \tag{4.22}$$

The peak vorticity at $x_c = 0$ is $\widehat{\omega}_{peak}(0) = \omega_o = 2.92$ s^{-1}, the kinematic viscosity of water ν is 1×10^{-6} m^2/s and, as mentioned, the initial circulation $\Gamma_o = 200$ mm^2/s was found from Figure 4.23. The β term, which represents the change in axial velocity with the axial coordinate of the vortex is chosen such that the to be, $\beta = \partial w/\partial z = -0.0165$ s^{-1} which was determined to yield the optimal agreement between the analytical model and the experimental results. This is relatively small compared to the velocity gradients embodied by the experimental peak vorticity, which for the current flow regime had an average value of ω_μ = 0.963 s^{-1}, confirming that the flow is predominantly 2D.

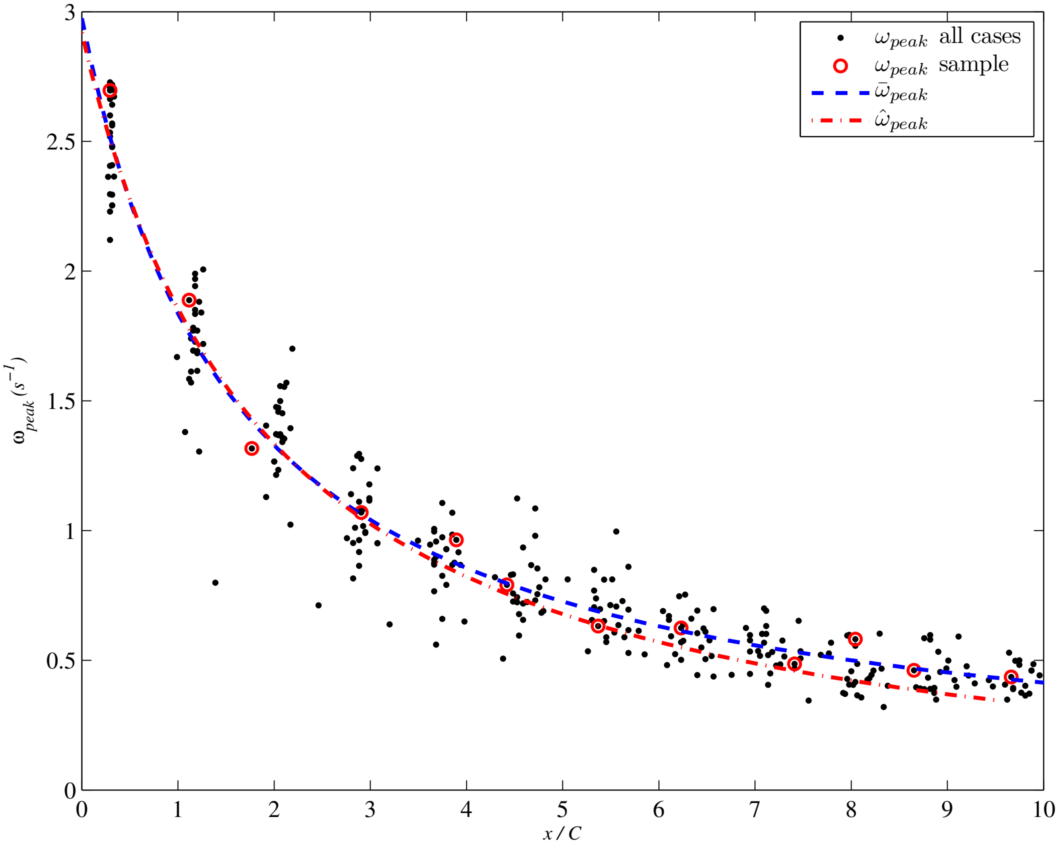

Figure 4.25: Peak positive vorticity vs. dimensionless streamwise distance for A_d = 0.84 and S_{td} = 0.129 ($f = 1.60$ rad/s and $\theta_A/2 = 4°$)

Both the analytical peak vorticity $\widehat{\omega}_{peak}(x_c)$ and the experimental peak vorticity fit $\overline{\omega}_{peak}(x_c)$ curves are plotted in Figure 4.25. Deviations from the analytical and the experimental peak vorticity evolution curves can be attributed to the noticeable departure of $\bar{\Gamma}$ from Γ_o at $x/C \approx 4$. The evolution of a vortex from *eqn. (4.22)* assumes a constant value of Γ_o, which is only true for near field vortices.

Peak analytical vorticity error is defined as $\tilde{\omega}_{peak} = |\hat{\omega}_{peak} - \bar{\omega}_{peak}| \,/\hat{\omega}_{peak}$ and is plotted against dimensionless streamwise distance in Figure 4.26. Comparison of with Figure 4.24 suggests that there is a reasonable correlation between the two error values and shows where the breakdown of the constant circulation assumption occurs in terms of the dimensionless streamwise coordinate x_c. As mentioned, this assumption eventually fails due to vortex boundary radii overlap (Ponta, 2010) where vorticity from neighboring vortices having opposite rotation contribute to a steady decrease in circulation with increasing streamwise distance. From Figure 4.22(a) it is possible to see that, at approximately $x_c = 4$, the vortex spacing becomes irregular and, while the radii do not intersect, they do begin to infringe on one another.

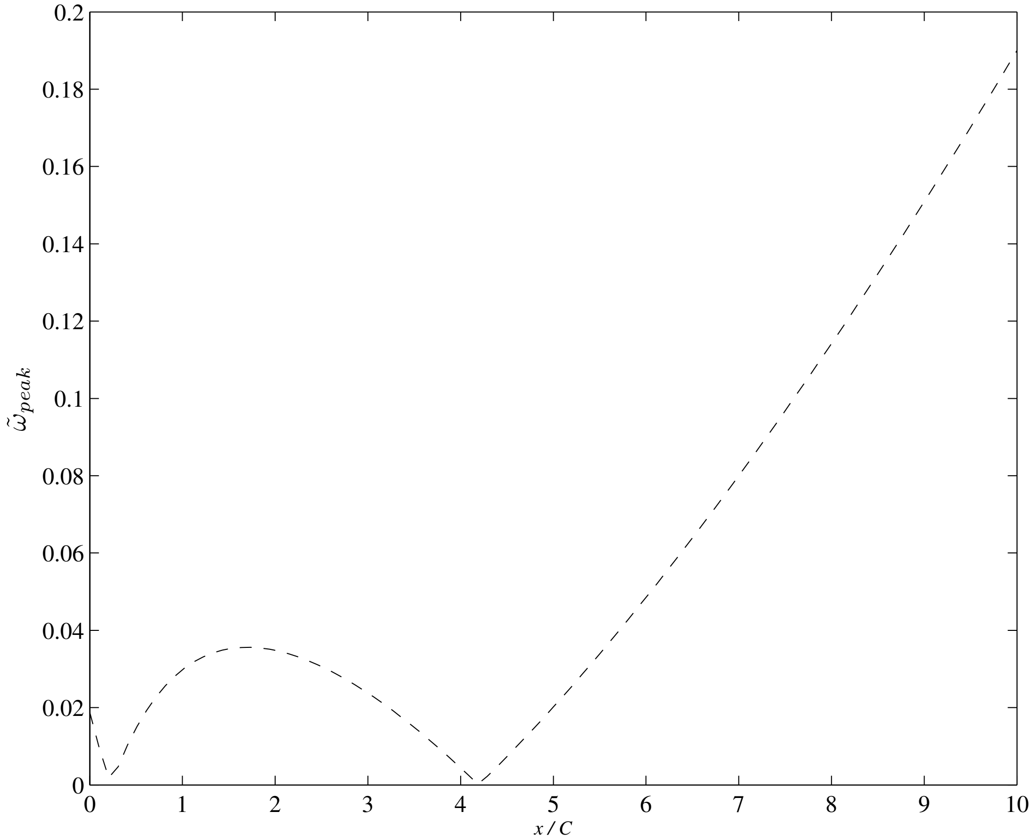

Figure 4.26: Analytical peak vorticity error vs. dimensionless streamwise distance for A_d = 0.84 and S_{td} = 0.129 ($f = 1.60$ rad/s and $\theta_A/2 = 4°$)

The analytical peak vorticity curve is intended to represent a single vortex as it evolves in time however; the vortices in this study are captured at a particular instance in time. As such, the above plots do not portray the life of a single vortex as it travels away from the trailing edge. Instead, they represent a locust of individual and separate vortices as they exist at a precise instance. Inconsistencies in the upstream flow conditions and slight asymmetries in the airfoil alignment can lead to variations in the measured vortex parameters from one oscillation cycle to the next. This leads to discrepancy between the analytical model $\hat{\omega}_{peak}$, which considers a single vortex as it travels away from the airfoil and the experimental fit $\overline{\omega}_{peak}$, which looks at several independent vortices as they exist at different streamwise locations in the wake.

The boundary radii r_v for the measured vortices from case $\mathbf{A_1}$ are expected to grow with increasing streamwise distance. This is mostly due to the transfer of momentum through viscous forces on neighboring fluid particles, effectively advecting the initial circulation of a vortex into adjacent boundaries over time (Ponta, 2010). Substitution of *eqn. (4.22)* into *eqn. (4.10)* and solving for r_v yields the following analytical model for predicting vortex boundary radius:

$$\hat{r}_v(x_c) = \sqrt{\frac{\Gamma_o\left(\frac{4\pi\nu}{\Gamma_o}(1-e^{-1})e^{\beta x_c\left(\frac{C}{v_{drift}}\right)} - \frac{4\pi\nu}{\Gamma_o}(1-e^{-1}) + \left(\frac{\beta}{\omega_o}\right)\right)}{\pi(1-e^{-1})\beta e^{\beta x_c\left(\frac{C}{v_{drift}}\right)}}} \tag{4.23}$$

In Figure 4.27 the vortex boundary radius r_v is plotted against dimensionless streamwise distance x_c, along with the analytical model for radius evolution $\hat{r}_v(x_c)$. The data is fit with the following 2nd order Gaussian function:

$$\bar{r}_v(x_c) = a_1 \exp\left(\left(-\frac{x_c - b_1}{c_1}\right)^2\right) + a_2 \exp\left(\left(-\frac{x_c - b_2}{c_2}\right)^2\right) \tag{4.24}$$

The fit coefficients a_1, a_2, b_1, b_2, c_1 and c_2 are reported in Table 4.3. The vortex radius experimental fit $\bar{r}_v$ as well as vortex radii from the sample field are circled highlighted with red circles in Figure 4.27. The boundary radius fit $\bar{r}_v(x_c)$ is close to the analytical model $\hat{r}_v(x_c)$ for streamwise distances of *x/C* < 4. For *x/C* > 4 the vortices begin to intermingle and several important assumptions from the analytical model breakdown. Specifically the postulation that there are no neighboring vortices to interfere with the vortex under evaluation and consequently, the constant circulation assumption are no longer valid for $x/C > 4$. Beyond this point, the average vortex radius remains constant at $r_v = 12$ mm with vortices as large as $r_v = 16$ mm appearing in the wake.

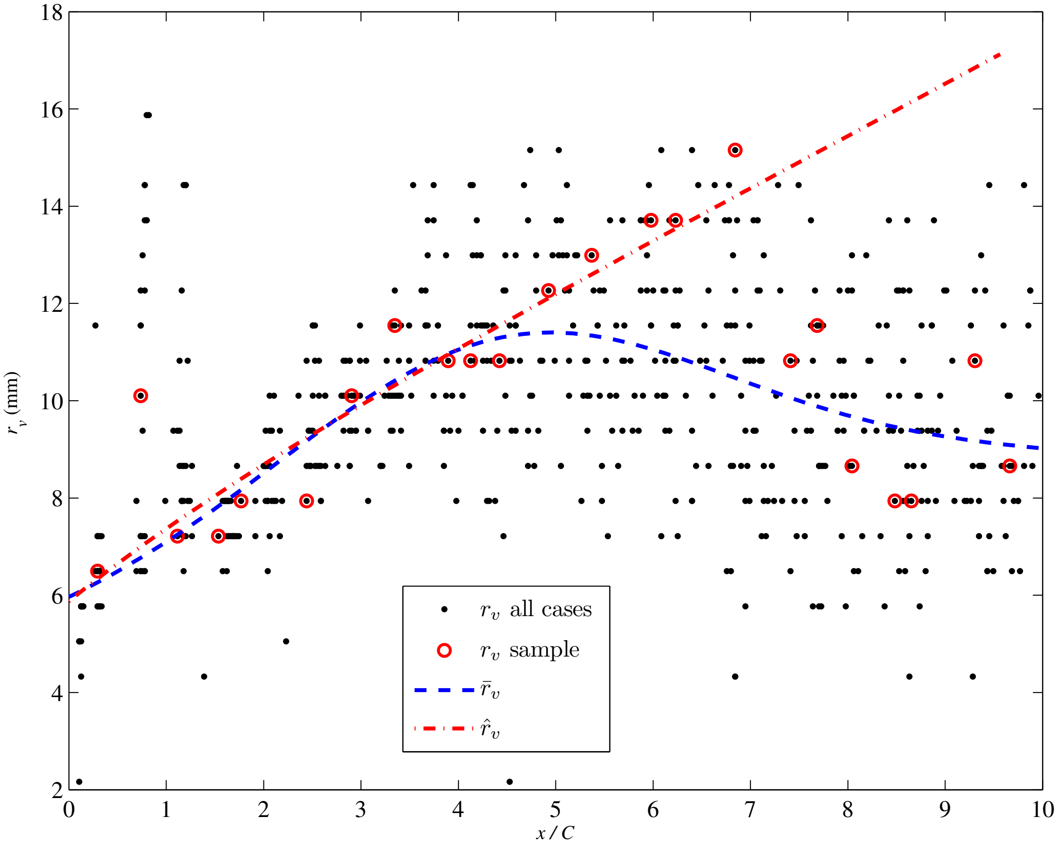

Figure 4.27: Vortex boundary radii r_v vs. dimensionless streamwise distance for $A_d = 0.84$ and $S_{td} = 0.129$ ($f = 1.60$ rad/s and $\theta_A/2 = 4°$)

In Figure 4.28 the dimensionless drift velocity v_{drift}/U_∞ for individual vortices for case $\mathbf{A_1}$ is plotted against the dimensionless streamwise distance x_c. Data points from the case $\mathbf{A_1}$ sample field are highlighted with red circles and the data is fitted with the 2nd order Gaussian function from *eqn. (4.24)*. The relevant fit coefficients are reported in Table 4.3. The normalized free stream velocity of 1 is shown for reference. The figure confirms that the vortices in a 2S_vK wake travel at an average drift velocity lower than that of the free stream (Bohl & Koochesfahani, 2009) and when compared to the wake profile in Figure 4.18, it provides further evidence that the wake profile does in fact resembles a velocity deficit.

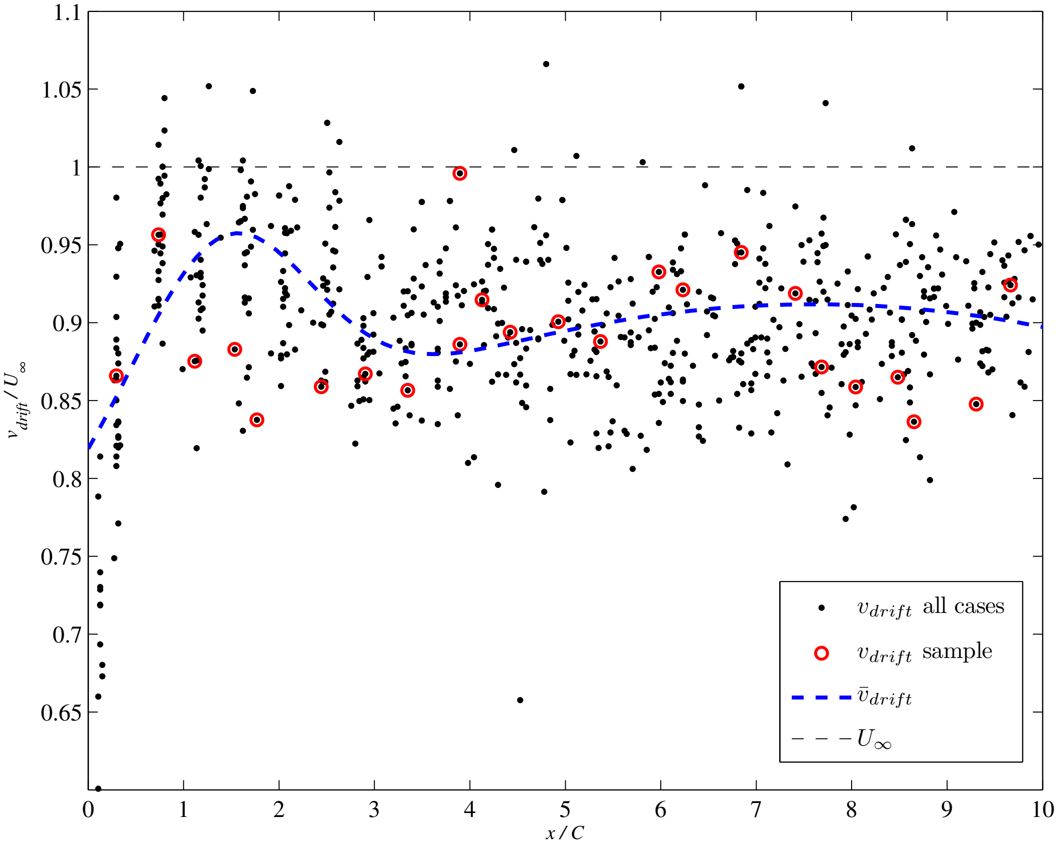

Figure 4.28: Dimensionless streamwise drift velocity v_{drift} vs. dimensionless streamwise distance for A_d = 0.84 and S_{td} = 0.129 ($f = 1.60$ rad/s and $\theta_A/2 = 4°$)

The streamwise vortex spacing S_x is computed as follows:

$$S_x(i) = |x_{core}(i+1) - x_{core}(i)| \tag{4.25}$$

where $x_{core}(i)$ is the streamwise coordinate for the core of vortex i. In Figure 4.29, the normalized streamwise spacing S_x/C is plotted against the dimensionless streamwise coordinate x_c for the 2S_vK wake from case $\mathbf{A_1}$. Also, the data is fit to the following 2nd order exponential function:

$$\bar{S}_x = ae^{bx_c} + ce^{dx_c} \tag{4.26}$$

The relevant fit coefficients are reported in Table 4.3. For *x/C* < 7 the spacing is relatively constant at $S_x = 65$mm.

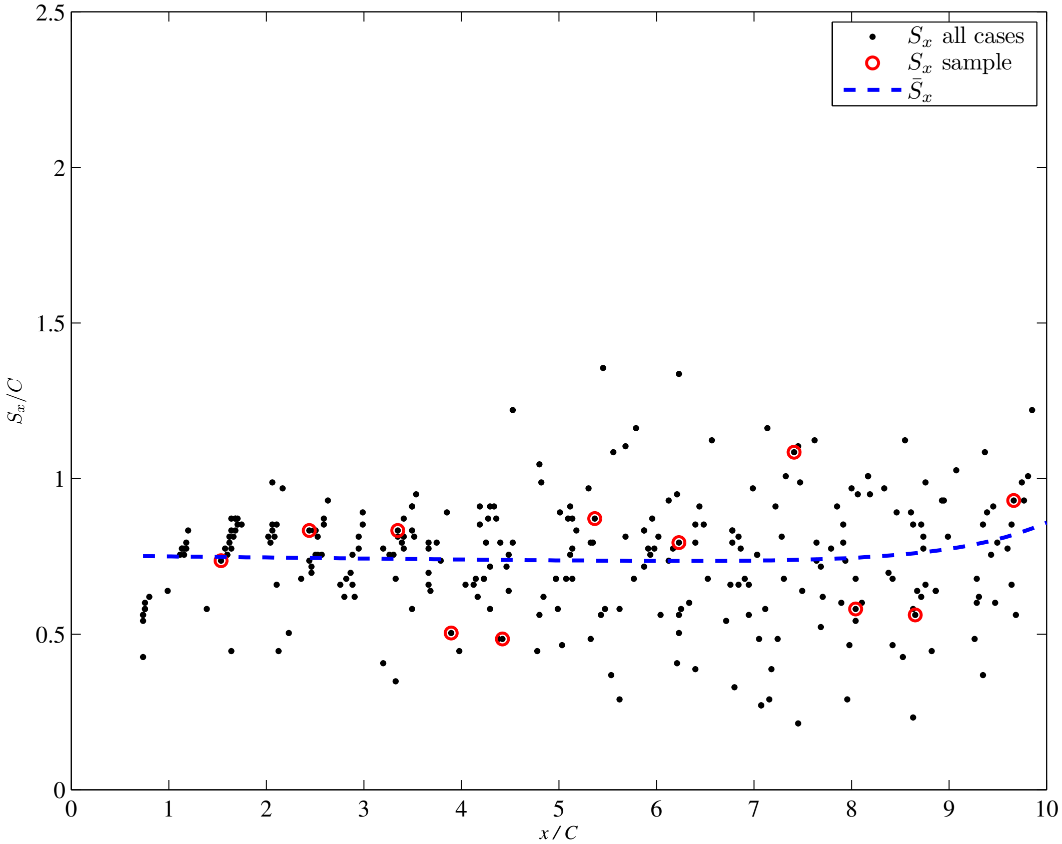

Figure 4.29: Streamwise vortex spacing S_x vs. dimensionless streamwise distance for A_d = 0.84 and S_{td} = 0.129 ($f = 1.60$ rad/s and $\theta_A/2 = 4°$)

The transverse vortex spacing S_y is computed as follows:

$$S_y(i) = |y_{core}(i+1) - y_{core}(i)| \tag{4.27}$$

where $y_{core}(i)$ is the transverse coordinate for the core of vortex i. In Figure 4.30, the normalized transverse spacing S_y/D is plotted against the dimensionless streamwise coordinate x_c for the 2S_vK wake in case $\mathbf{A_1}$ along with highlighted data from the sample field. The data is fit with the exponential function in *eqn. (4.26)* and the relevant fit coefficients are reported in Table 4.3. The data has considerable scatter making it difficult to discern any sort of trend, especially as streamwise distance increases. However, the data does provide a rough idea of the magnitude of transverse spacing, and establishes a means to compare the vortex spacing with other wakes.

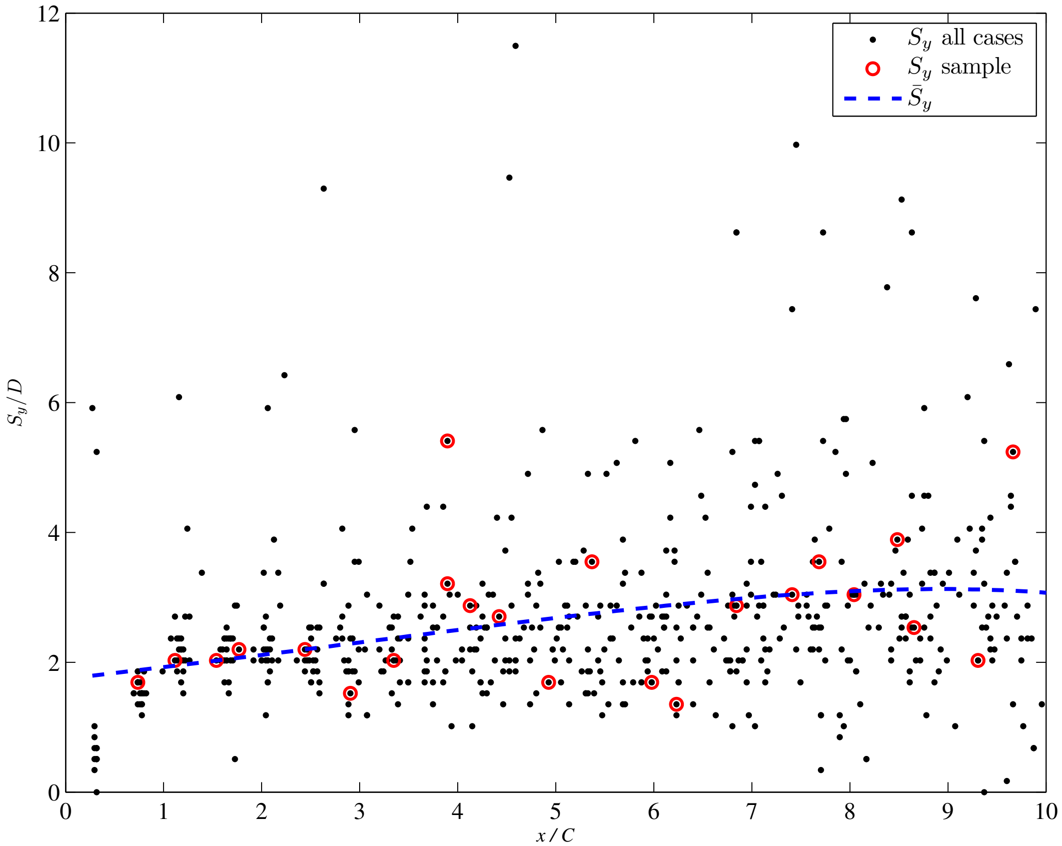

Figure 4.30: Transverse vortex spacing S_y vs. dimensionless streamwise distance for A_d = 0.84 and S_{td} = 0.129 ($f = 1.60$ rad/s and $\theta_A/2 = 4°$)

The fit coefficients for the 2S_vK wake parameters from case $\mathbf{A_1}$ are summarized in Table 4.3. The circulation $\bar{\Gamma}$ has both a positive fit $\bar{\Gamma}_+$ for the vortices with positive rotation and a negative fit $\bar{\Gamma}_-$ for vortices with negative rotation.

Table 4.3:Summary of fit functions and coefficients for the 2S_vK wake from case A_1

Wake Parameter	**Fit function**	**Applicable fit coefficients**					
		a, a_1	*b, b_1*	*c, c_1*	*d, a_2*	*b_2*	*c_2*
$\bar{\boldsymbol{\Gamma}}_+(\boldsymbol{x_c})$	2nd order exponential	-4.94e7	-0.274	4.94e7	-0.274	-	-
$\bar{\boldsymbol{\Gamma}}_-(\boldsymbol{x_c})$	2nd order exponential	-729.9	-0.221	592.5	-5.535	-	-
$\bar{\boldsymbol{\omega}}_{\boldsymbol{peak}}(\boldsymbol{x_c})$	exponential	5.922-9	0.2081	2.975	-	-	-
$\bar{\boldsymbol{r}}_{\boldsymbol{v}}(\boldsymbol{x_c})$	2nd order Gaussian	8.884	9.711	14.02	3.59	4.422	3.098
$\bar{\boldsymbol{v}}_{\boldsymbol{drift}}(\boldsymbol{x_c})$	2nd order Gaussian	0.912	7.600	18.87	0.1365	1.395	1.308
$\bar{\boldsymbol{S}}_{\boldsymbol{x}}(\boldsymbol{x_c})$	2nd order exponential	7982	0.168	-7981	0.168	-	-
$\bar{\boldsymbol{S}}_{\boldsymbol{y}}(\boldsymbol{x_c})$	2nd order exponential	0.7532	-0.0046	6.22e6	1.001	-	-

2S_A wake type (case B_1)

Figure 4.31 illustrates the circulation Γ for the 2S_A wake from case $\mathbf{B_1}$. The data is fitted with the 2nd order Gaussian defined in *eqn. (4.24)* and the relevant fit coefficients are listed in Table 4.4. The vortices from the sample field of case $\mathbf{B_1}$ are highlighted with red circles.

The measured circulation initially increases, then begins to decrease at roughly $x/C = 2$ before reaching a constant value at $x/C \approx 5$. As a result, selecting an appropriate value for Γ_o is more challenging. In order to calculate the analytical peak vorticity, a constant value for initial circulation Γ_o must be assumed. The initial circulation of $\Gamma_o = 366$ mm^2/s estimated with *eqn. (4.18)* in Table 4.2 is higher than the initial experimental Γ from the case $\mathbf{B_1}$ wake shown in Figure 4.31. $\Gamma_o = 300$ mm^2/s is selected instead since it is closer to the experimental data and will produce a better analytical fit $\widehat{\omega}_{peak}(x_c)$ for the wake from case $\mathbf{B_1}$.

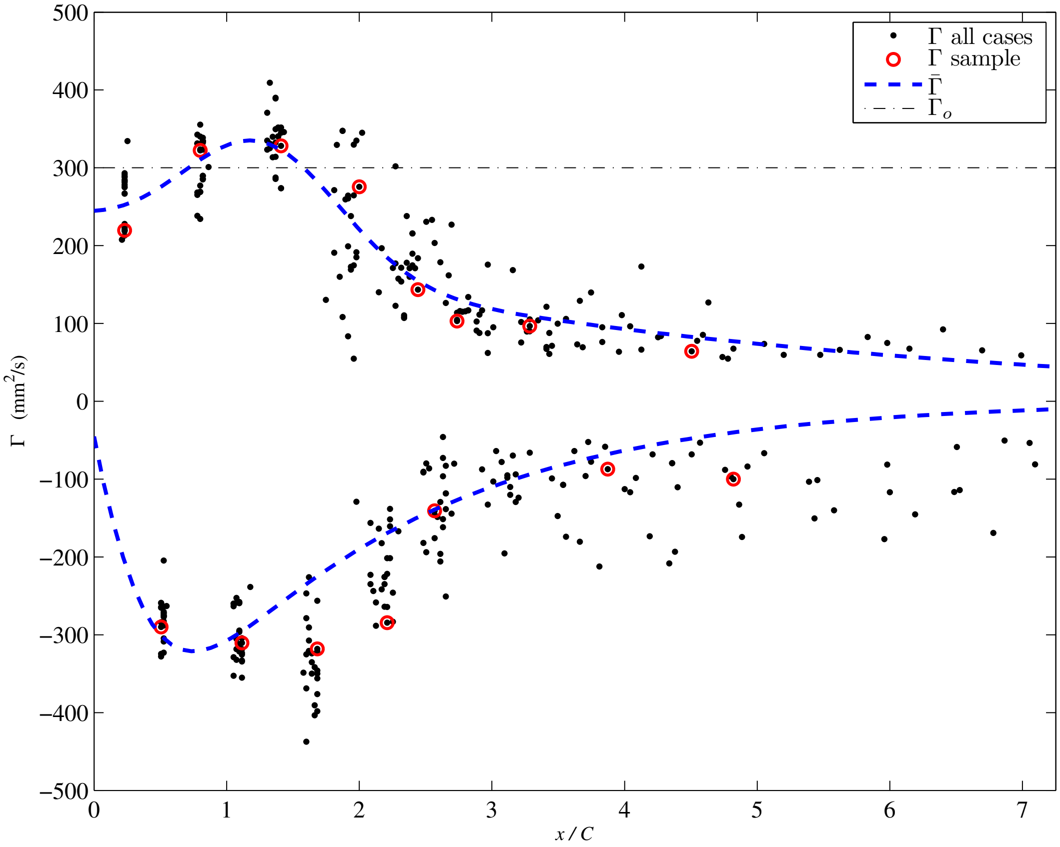

Figure 4.31: Circulation vs. dimensionless streamwise distance for A_d = 0.84 and S_{td} =0.201 ($f = 2.50$ rad/s and $\theta_A/2 = 4°$)

The circulation error $\tilde{\Gamma}_o$ for the wake in case $\mathbf{B_1}$ is shown in Figure 4.33. It is only within 0.05 for streamwise distances of 0.75< *x/C <1.75*; however, it begins to increase appreciably for *x/C* >1.75. This increase is attributed to vortex core overlap (Ponta, 2010) and since the vortices are spaced closer than in the 2S_vK wake (case $\mathbf{A_1}$) this occurs much faster.

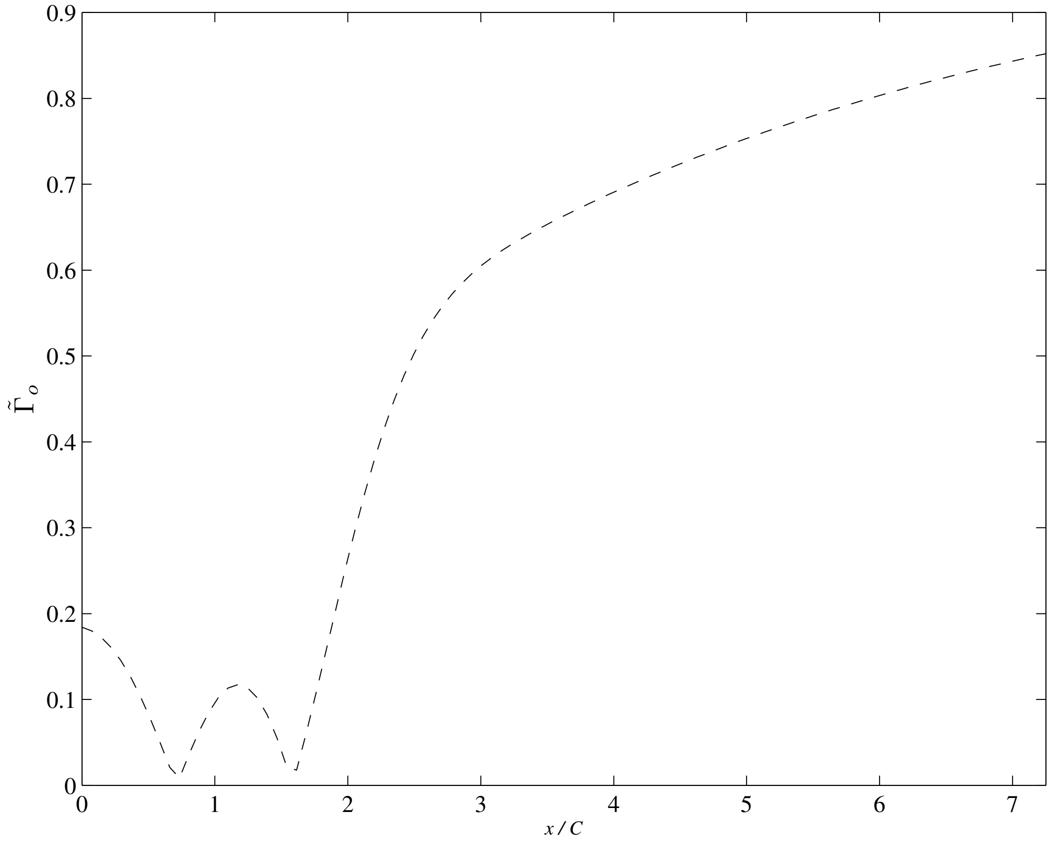

Figure 4.32: Analytical circulation error vs. dimensionless streamwise distance for A_d = 0.84 and S_{td} =0.201 ($f = 2.50$ rad/s and $\theta_A/2 = 4°$)

The evolution of peak vorticity ω_{peak} for the positive vortex row for the 2S_A wake from case $\mathbf{B_1}$ is shown in Figure 4.33. Vortices from the sample field are circled in red. The peak vorticity is fitted to the function from *eqn. (4.20)* and the relevant fit coefficients are reported in Table 4.4. The analytical model for peak vorticity $\widehat{\omega}_{peak}(x_c)$ of positive vortices is estimated with *eqn. (4.22)* where the peak vorticity at $x_c = 0$ is $\widehat{\omega}_{peak}(0) = \omega_o = 8.00$ s^{-1}. The β term, representing the change in axial velocity with the vortex's axial coordinate, was found to be, $\beta = \partial w/\partial z = -0.065$ s^{-1}. This is relatively small compared to the average velocity gradients embodied by the experimental peak vorticity $\omega_\mu = 2.59$ s^{-1}.This effectively confirms the assumption that the wake corresponding to the **B₁** case is predominantly 2D for *x/C < 1.75*.

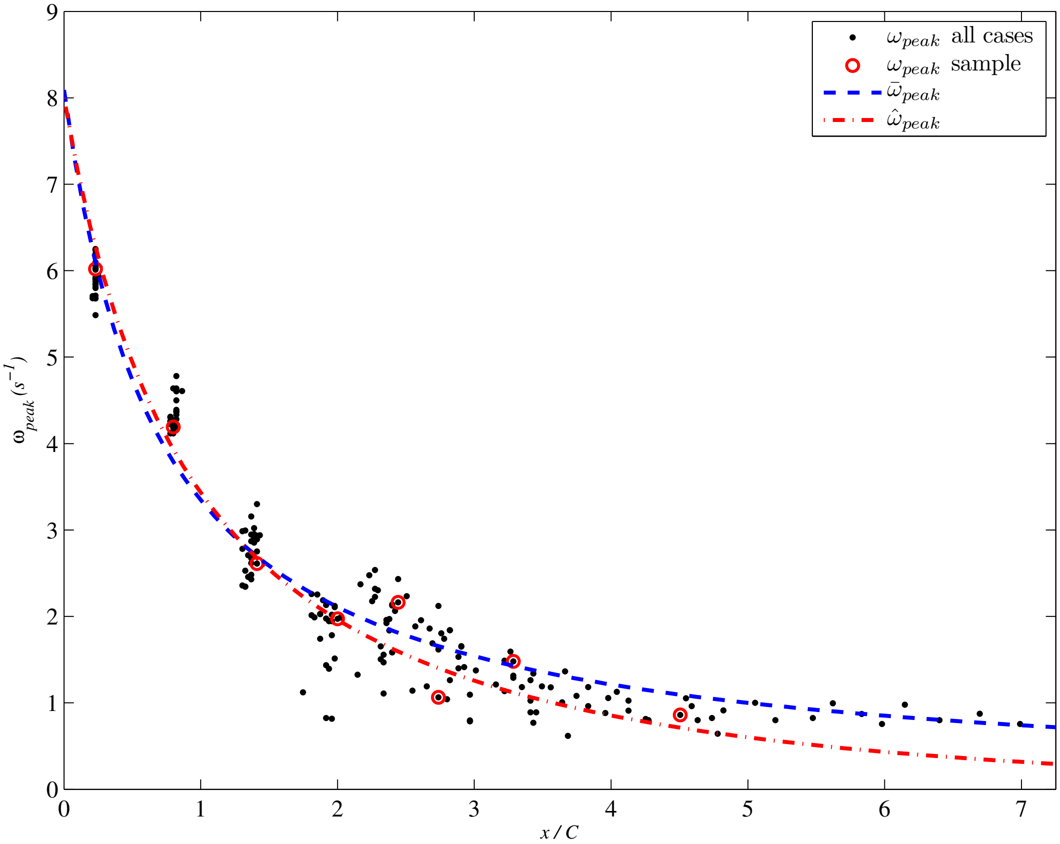

Figure 4.33: Peak positive vorticity vs. dimensionless streamwise distance for A_d = 0.84 and S_{td}=0.201 ($f = 2.50$ rad/s and $\theta_A/2 = 4°$)

Deviation between the analytical curve $\widehat{\omega}_{peak}(x_c)$ and the experimental peak vorticity curve $\bar{\omega}_{peak}(x_c)$ is more prominent in the 2S_A from case **B₁** than in the 2S_vK wake from $\mathbf{A_1}$. Accurate use of *eqn. (4.22)* requires a constant value of Γ_o; however, the circulation in the 2S_A (case **B₁**) is observed not to be constant. In Figure 4.22(b) the wake has considerable boundary radii overlap for $x/C > 5$ and as mentioned, *eqn. (4.22)* considers only a single vortex that is sufficiently far from other structures as to not be affected by their presence. Predicting the evolution of peak vorticity using *eqn. (4.22)* was reasonably accurate for the 2S_vK (case $\mathbf{A_1}$) wake for $x_c < 4$; however, the 2S_A (case $\mathbf{B_1}$) wake violates several important assumptions and cannot be accurately portrayed with the current analytical model for $x/C > 2.5$. The peak vorticity error $\widetilde{\omega}_{peak}$ defined above is plotted against dimensionless streamwise distance for the 2S_A (case $\mathbf{B_1}$) wake in Figure 4.34. Maximum error $\widetilde{\omega}_{peak} = 4$ illustrates the inaccuracies involved when using *eqn. (4.22)* to predict peak vorticity in a wake where circulation varies considerably, and where vortex spacing is tight.

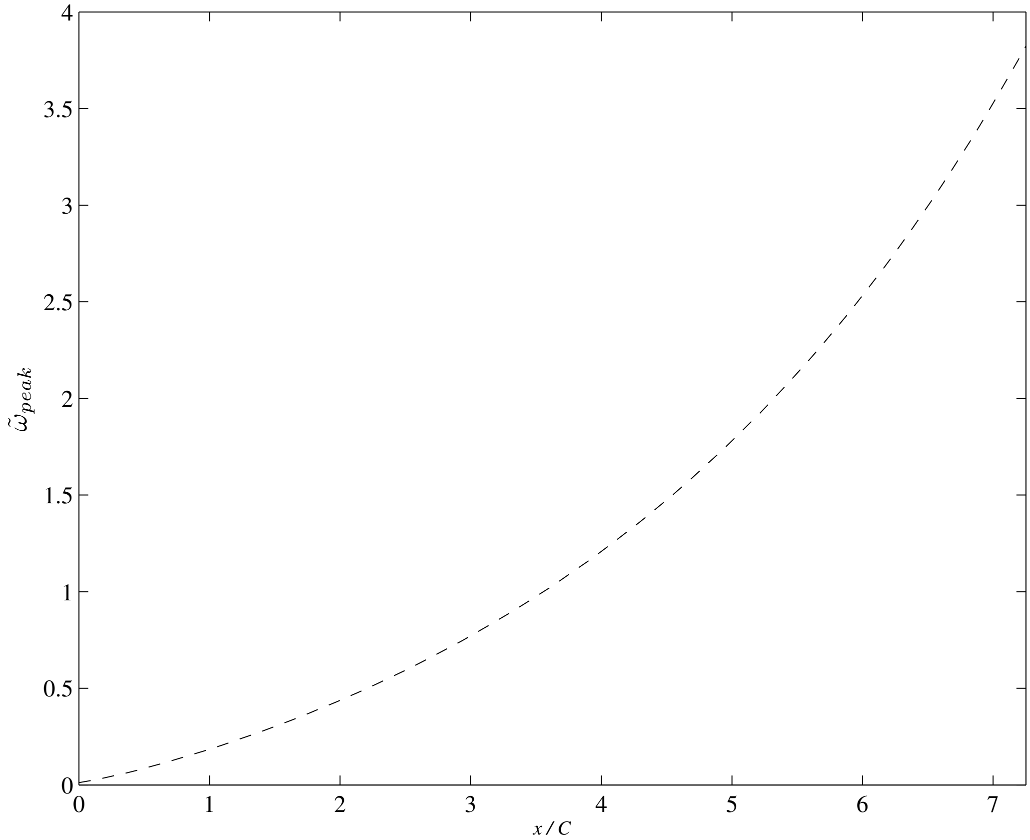

Figure 4.34: Analytical peak vorticity error vs. dimensionless streamwise distance for A_d = 0.84 and S_{td} =0.201 ($f = 2.50$ rad/s and $\theta_A/2 = 4°$)

In Figure 4.35 the vortex boundary radius r_v of the wake from case $\mathbf{B_1}$ is plotted against dimensionless streamwise distance x_c. The analytical model for radius $\hat{r}_v(x_c)$ as a function of streamwise distance is obtained from *eqn. (4.23)* and is plotted along with the 2nd order Gaussian fit $\bar{r}_v(x_c)$ from *eqn. (4.24)*. The relevant fit coefficients are reported in Table 4.4. Vortex radii from the sample field of case $\mathbf{B_1}$ are circled in red. The experimental fit $\bar{r}_v(x_c)$ suggests that for *x/C* < 1.75 the boundary radius increases at a fixed rate and within this distance the analytical model described by $\hat{r}_v(x_c)$ follows it reasonably well.

A comparison with Figure 4.22(b) reveals that *x/C* = 1.75 appears to coincide with the onset of radius overlap. In addition, beyond this point, the vortex spacing becomes disordered and the vortices appear to fall out of streamwise alignment. The analytical model for radius $\hat{r}_v(x_c)$ depends on the constant circulation assumption. This assumption is less applicable for the 2S_A wake (case $\mathbf{B_1}$) than it is for the 2S_vK wake (case $\mathbf{A_1}$) and explains why $\hat{r}_v(x_c)$ from case $\mathbf{A_1}$ appears to correlate better with its experimental data.

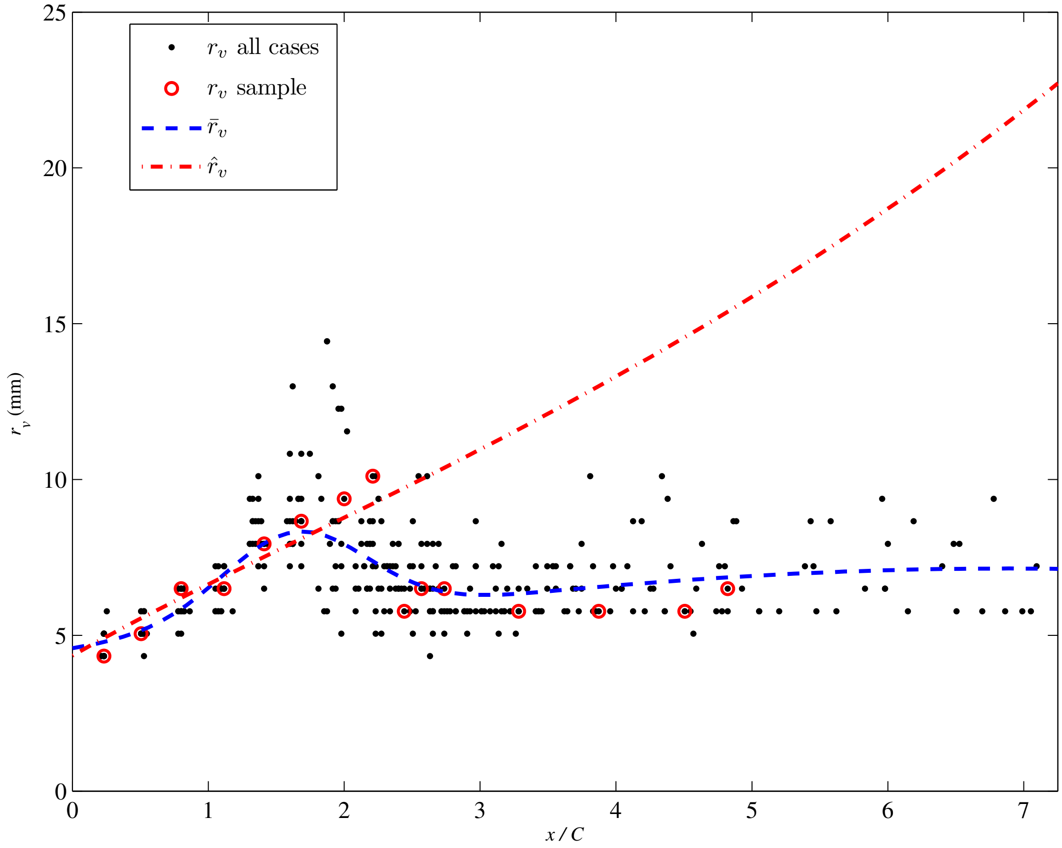

Figure 4.35: Vortex boundary radii r_v vs. dimensionless streamwise distance for A_d = 0.84 and S_{td} =0.201 ($f = 2.50$ rad/s and $\theta_A/2 = 4°$)

In Figure 4.36 the dimensionless drift velocity v_{drift}/U_∞ for individual vortices in the 2S_A wake (case $\mathbf{B_1}$) is plotted against dimensionless streamwise distance x_c. Data points from the sample field are circled in red. The data is fitted with the 2nd order exponential function from *eqn. (4.26)*, and the relevant fit coefficients are reported in Table 4.4. The normalized freestream velocity of 1 is shown for reference. The vortices initially travel downstream faster than the free stream velocity U_∞, but rapidly slow down to sub freestream velocities. The vortices in the 2S_A wake (case $\mathbf{B_1}$) travel, on average, faster than those in the 2S_vK (case $\mathbf{A_1}$) wake but the majority of them still remain lower than the free stream velocity.

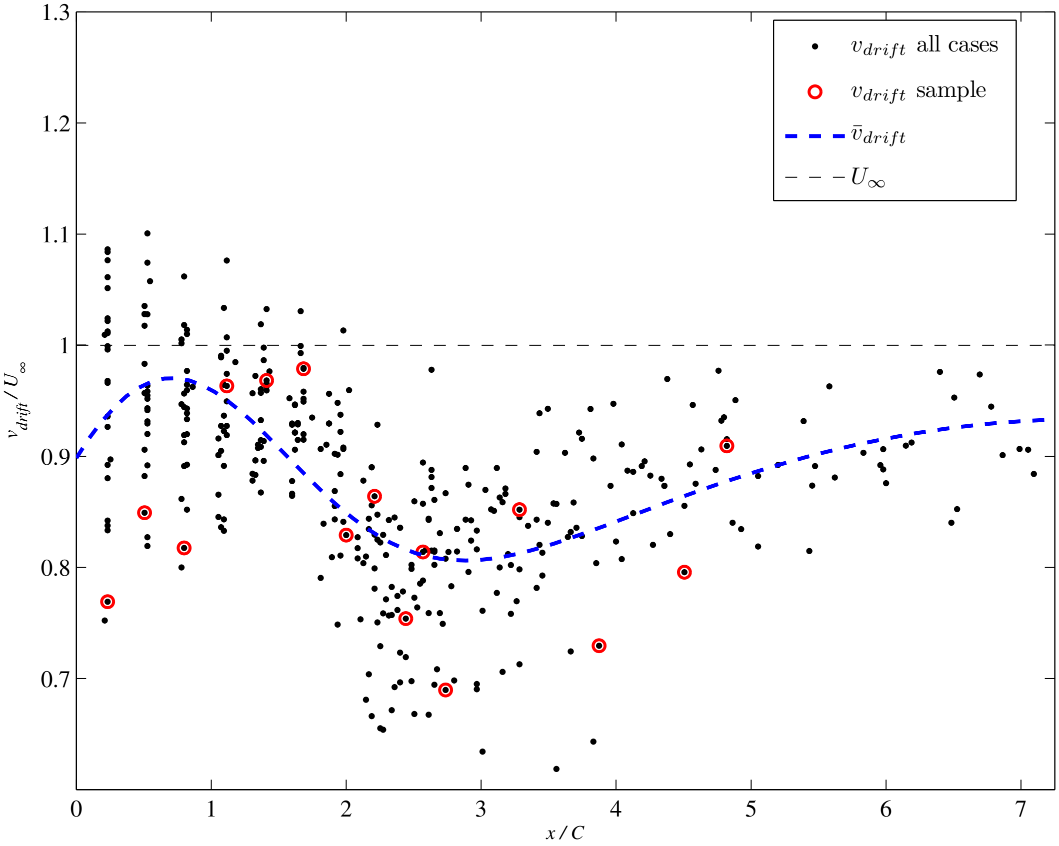

Figure 4.36: Dimensionless drift velocity vs. dimensionless streamwise distance for A_d = 0.84 and S_{td} =0.201 ($f = 2.50$ rad/s and $\theta_A/2 = 4°$)

In Figure 4.37, the normalized streamwise spacing S_x/C is plotted against the dimensionless streamwise coordinate x_c for the 2S_A wake (case **B₁**). For $x/C < 3$ the streamwise spacing remains constant at $S_x/C \approx 0.5$ extending beyond $x/C = 1.75$ where the analytical model breaks down. The vortices in the 2S_A wake (case **B₁**) are expected to have smaller streamwise spacing than in the 2S_vK wake (case **A₁**), since the airfoil is oscillating at a higher frequency for the same flow rate, leading to more vortices shed for the same measure of streamwise distance.

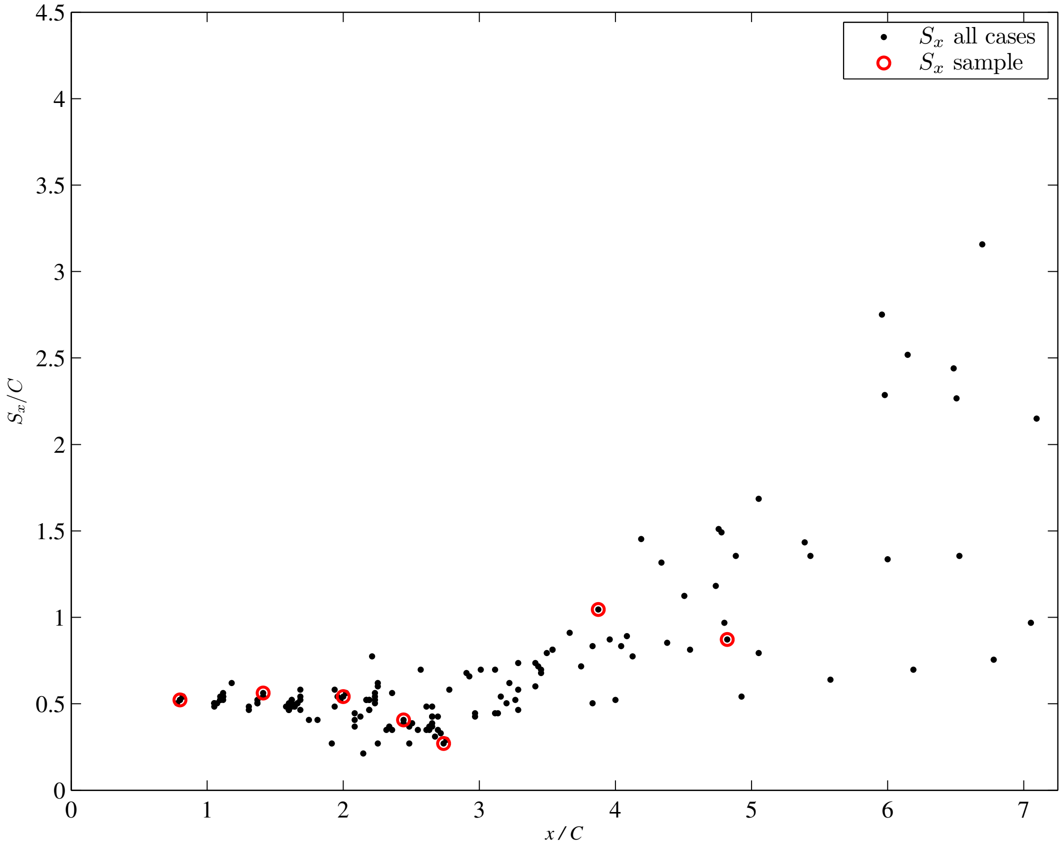

Figure 4.37: Streamwise vortex spacing S_x vs. dimensionless streamwise distance for A_d = 0.84 and S_{td} =0.201 ($f = 2.50$ rad/s and $\theta_A/2 = 4°$)

In Figure 4.38, the transverse normalized spacing S_y/D is plotted against the dimensionless streamwise coordinate x_c for the 2S_A wake (case **B₁**). The 2S_A wake can be viewed as a 2S_vK wake where the two rows of counter rotating vortices are coincident rather than separated by some transverse distance. Therefore, the transverse vortex spacing in a 2S_A wake is expected to approach zero. Figure 4.38 shows that the transverse vortex spacing is close to zero, but only for $x_c < 1.75$. Beyond this limit, the wake breaks alignment as the vortices begin to merge and vortex spatial organization becomes chaotic. This is also observed in Figure 4.22(b).

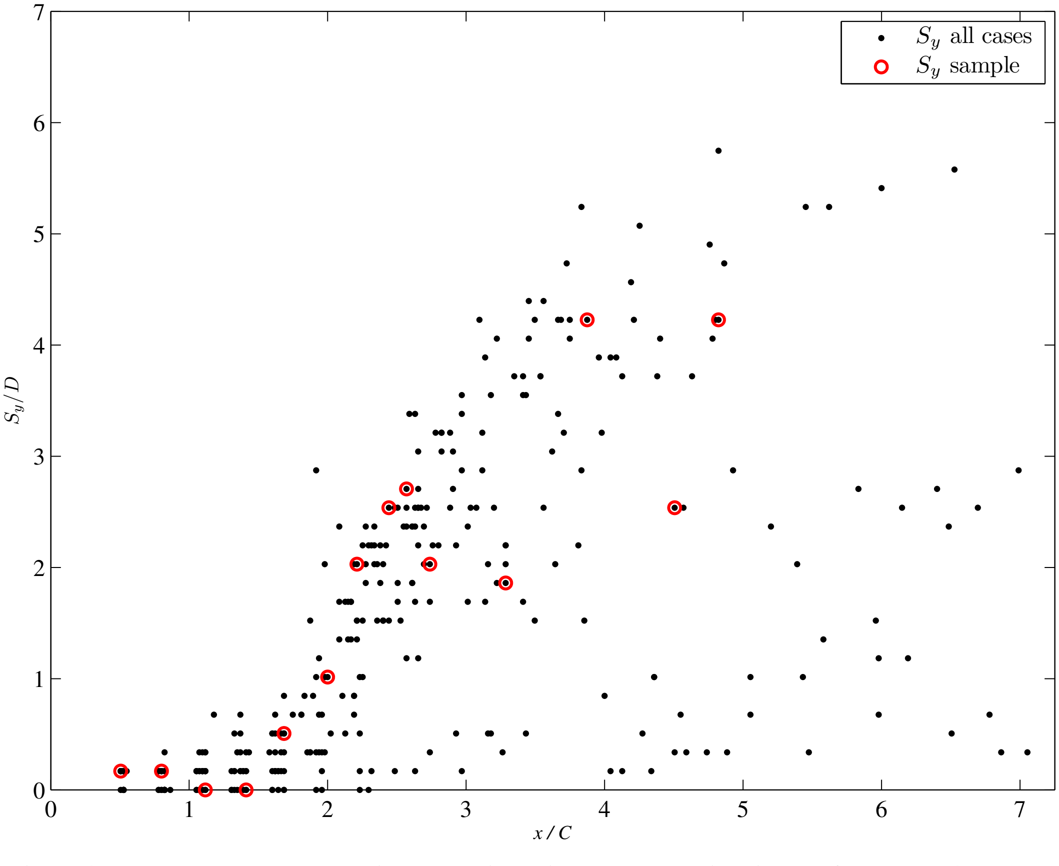

Figure 4.38: Transverse vortex spacing S_y vs. dimensionless streamwise distance for A_d = 0.84 and S_{td} =0.201 ($f = 2.50$ rad/s and $\theta_A/2 = 4°$)

The fit coefficients for the 2S_A wake (case **B$_1$**) parameters are summarized in Table 4.4.

Table 4.4: Summary of fit functions and coefficients for the 2S_A wake

Wake Parameter	**Fit function**	**Applicable fit coefficients**					
		a, a$_1$	*b, b$_1$*	*c, c$_1$*	*d, a$_2$*	*b$_2$*	*c$_2$*
$\bar{\Gamma}_+(x_c)$	2nd order Gaussian	161.9	1.262	0.844	3.75e15	-273.6	49.59
$\bar{\Gamma}_-(x_c)$	2nd order Gaussian	-1.10e5	-27.57	11.9	4337	-1.966	1.365
$\bar{\omega}_{peak}(x_c)$	Custom exponential	2.743e-9	0.1753	8.091	-	-	-
$\bar{r}_v(x_c)$	2nd order Gaussian	2.814	1.637	0.751	7.143	6.903	10.31
$\bar{v}_{drift}(x_c)$	2nd order Gaussian	0.3574	0.4489	1.558	0.9332	7.455	10.6

2S_ivK wake (case C$_1$)

Figure 4.39 illustrates the Circulation Γ for the 2S_ivK wake from case **C$_1$**. The data is fitted to a 2nd order Gaussian curve shown in *eqn. (4.24)*, and the relevant fit coefficients are reported in Table 4.5 . The vortices from the sample field shown in Figure 4.22(c) are highlighted with red circles. It is observed that, the circulation initially increases, then begins to decrease at roughly x/C = 0.75 then remains relatively constant for $x/C > 2$. As with the 2S_A wake from case **B$_1$**, the variability in the circulation data makes it difficult to select a suitable value of Γ_o to be used in the analytical model. The initial circulation estimate computed with *eqn. (4.18)* is used resulting in $\Gamma_o = 410$ mm^2/s which is plotted in Figure 4.39.

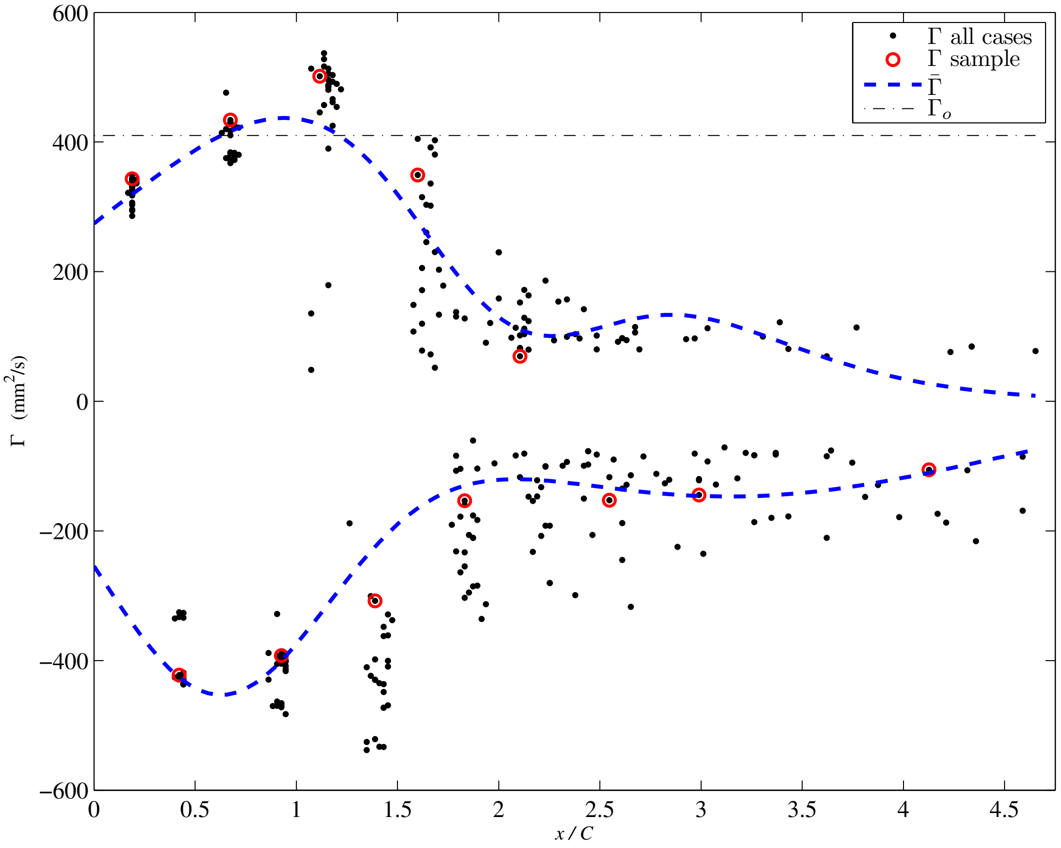

Figure 4.39: Circulation vs. dimensionless streamwise distance for A_d = 0.84 and S_{td} = 0.274 (f = 3.40 rad/s and $\theta_A/2 = 4°$)

The circulation error $\tilde{\Gamma}_o$ for the wake in case $\mathbf{C_1}$ is shown in Figure 4.40. It is only within 0.05 for streamwise distances of 0.5< *x/C <1.4*; however, it begins to increase appreciably for *x/C* >1.4. This increase is attributed to vortex core overlap (Ponta, 2010), Vortices in the 2S_ivK wake (case $\mathbf{C_1}$) have the closest spacing and as a result experience the highest rate of increase for $\tilde{\Gamma}_o$.

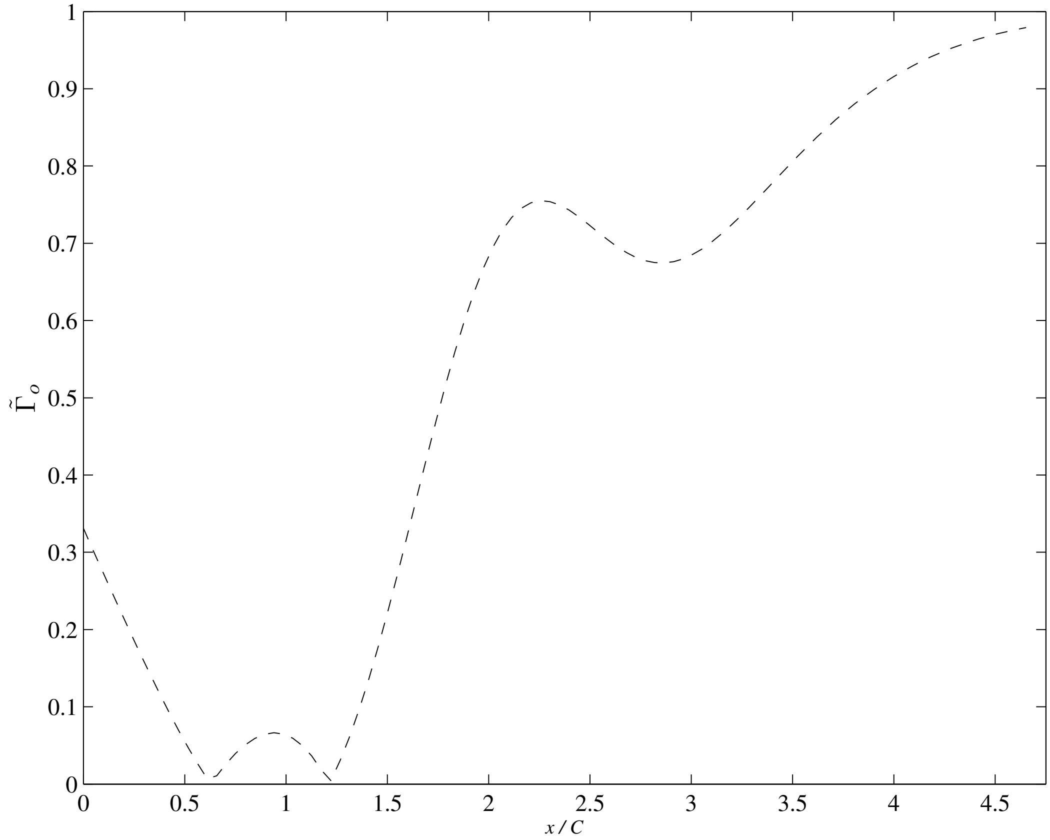

Figure 4.40: Circulation error vs. dimensionless streamwise distance for A_d = 0.84 and S_{td} = 0.274 ($f = 3.40$ rad/s and $\theta_A/2 = 4°$)

The evolution of peak vorticity ω_{peak} for the positive vortex row for the 2S_ivK wake (case **$\mathbf{C_1}$**) is shown in Figure 4.41. Relevant vortices from the sample field in Figure 4.22(c) are circled in red. The data is fitted with the function from *eqn. (4.20)* and the relevant fit coefficients are reported in Table 4.5. The analytical prediction for peak vorticity $\widehat{\omega}_{peak}(x_c)$ for positive vortices is estimated with *eqn. (4.22)* where the peak vorticity at $x_c = 0$ is $\widehat{\omega}_{peak}(0) = \omega_o = 13.25\ \mathrm{s}^{-1}$. The initial circulation of $\Gamma_o = 410\ \mathrm{mm}^2/\mathrm{s}$ is estimated by considering the circulation generated from the flapping motion of the airfoil. Finally, the β

term, representing the change in axial velocity with the vortex's axial coordinate, was found to be, $\beta = \partial w/\partial z = -0.165$ s^{-1}. As with the previous wakes, this is relatively small compared to the in-plane velocity gradients embodied by the experimental peak vorticity of $\omega_\mu =$ 4.42 s^{-1} effectively confirming the assumption that the 2S_ivK wake may be regarded as a 2D flow field.

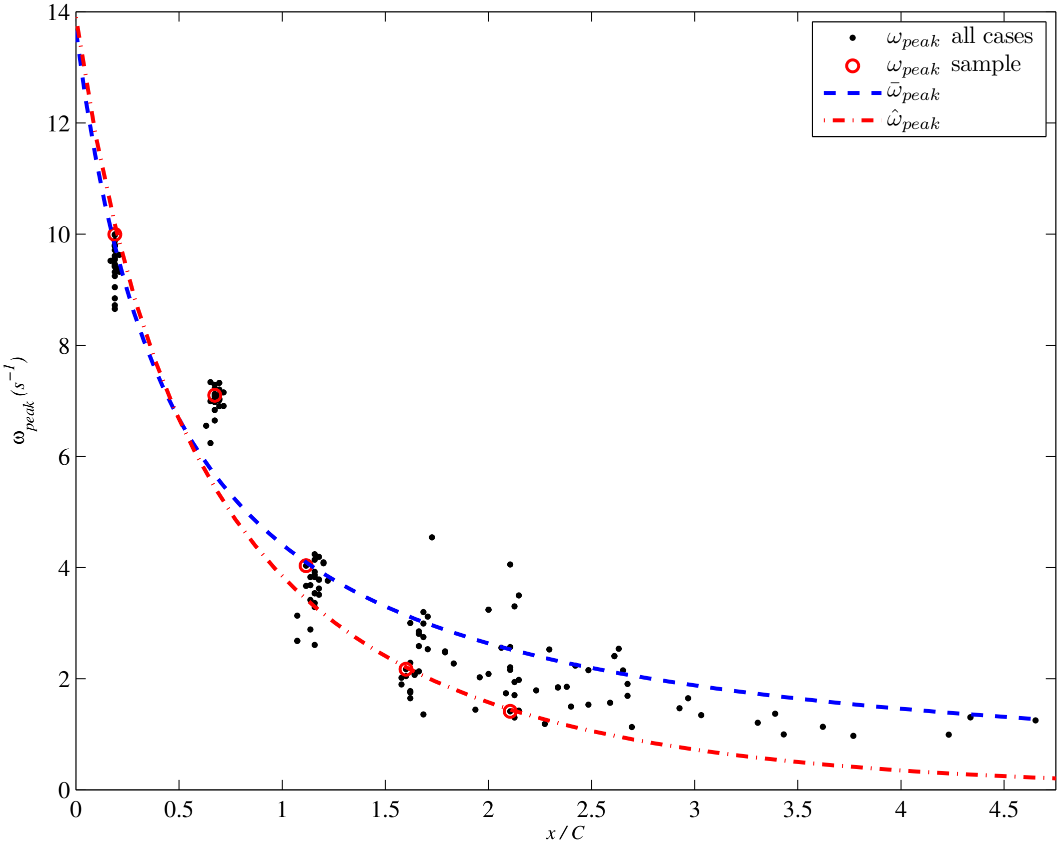

Figure 4.41: Positive peak vorticity vs. dimensionless streamwise distance for A_d = 0.84 and S_{td} = 0.274 (f = 3.40 rad/s and $\theta_A/2$ = 4°)

The analytical peak vorticity curve $\hat{\omega}_{peak}(x_c)$ agrees with the experimental fit $\bar{\omega}_{peak}(x_c)$ for *x/C*< 1. Beyond this limit, the spatial organization of the wake is highly chaotic and similar to the 2S_vK and 2S_A wakes from cases $\mathbf{A_1}$ and $\mathbf{B_1}$ respectively, several important assumptions implied by the analytical model are no longer valid. The peak vorticity error $\widetilde{\omega}_{peak}$ is plotted against dimensionless streamwise distance for the 2S_ivK wake (case **C**$_1$) in Figure 4.42. Comparison with $\widetilde{\omega}_{peak}$ from cases $\mathbf{A_1}$ and $\mathbf{B_1}$ in Figure 4.26 and Figure 4.34 respectively shows that the experimental ω_{peak} data from the 2S_ivK wake (case **C**$_1$) has the largest difference when compared to $\widehat{\omega}_{peak}$ from *eqn.(4.22)*.

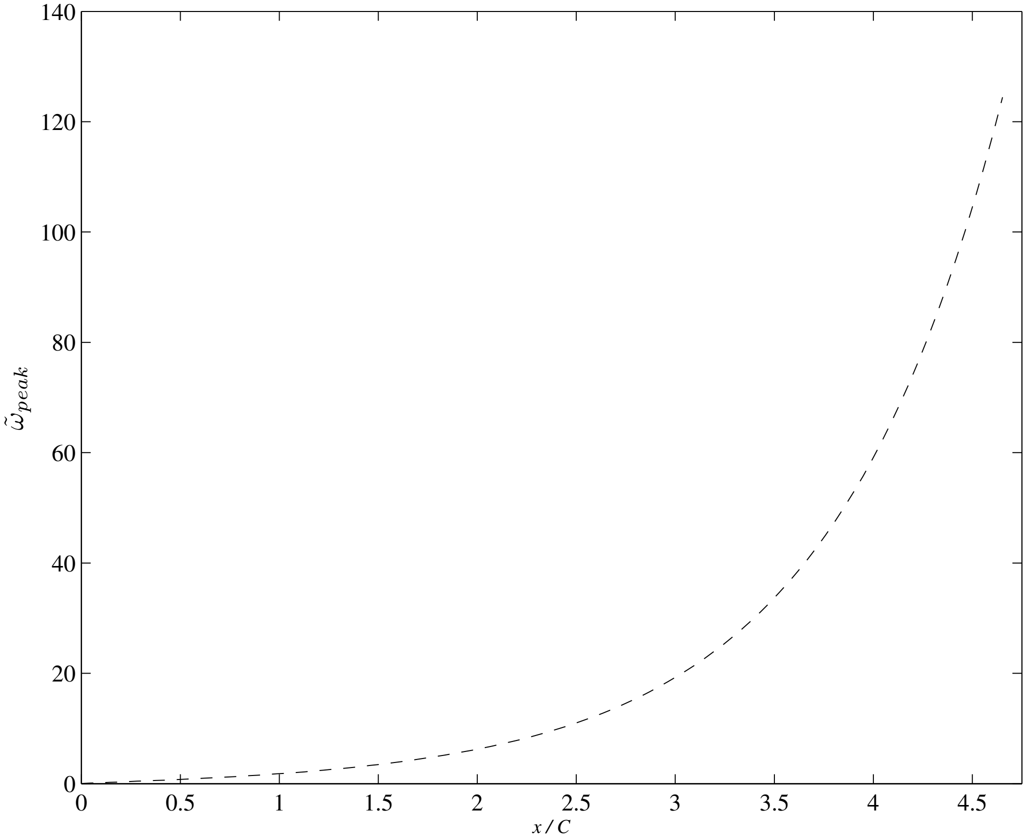

Figure 4.42:Positive peak vorticity error vs. dimensionless streamwise distance for A_d = 0.84 and S_{td} = 0.274 ($f = 3.40$ rad/s and $\theta_A/2 = 4°$)

In Figure 4.43 the vortex boundary radius r_v is plotted against dimensionless streamwise distance x_c, along with the analytical model for radius evolution $\hat{r}_v(x_c)$ obtained from *eqn.(4.23)*. The data is fitted with the 2$^{\text{nd}}$ order exponential from *eqn. (4.26)* and the relevant fit coefficients are reported in Table 4.5. Data points from the sample field in Figure 4.22(c) are circled in red. The analytical model predicting $\hat{r}_v(x_c)$ for the 2S_ivK wake (case **C₁**) generally overestimates vortex radius and its rate of increase. The vortex boundary growth is believed to be strongly limited by the tightly packed spacing of the vortices. This explains why the experimental vortex radii r_v are smaller than the analytical prediction which does not take into account neighboring vortices.

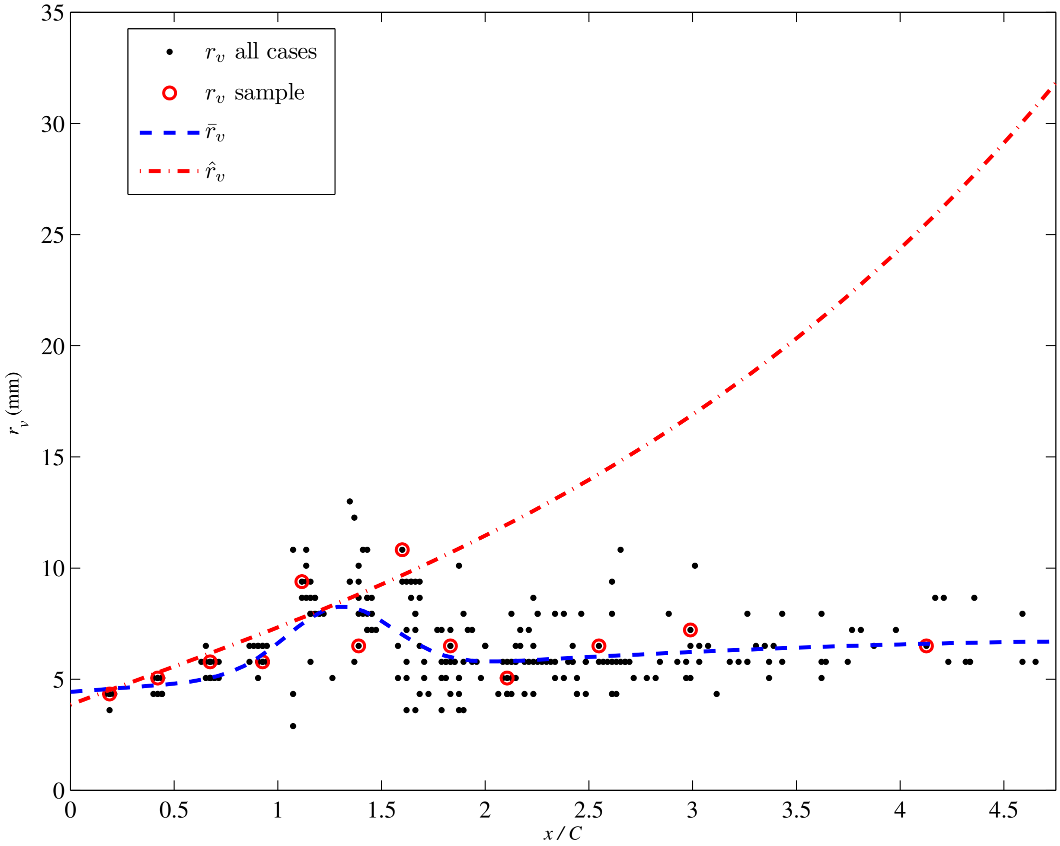

Figure 4.43: Vortex boundary radiu r_v s vs. dimensionless streamwise distance for A_d = 0.84 and S_{td} = 0.274 ($f = 3.40$ rad/s and $\theta_A/2 = 4°$)

In Figure 4.44 the dimensionless drift velocity v_{drift}/U_{∞} for individual vortices in the 2S_ivK wake (case $\mathbf{C_1}$) is plotted against the dimensionless streamwise distance x_c. Data points from the sample field in Figure 4.22(c) are circled in red. The data is fitted with the 2nd order Gaussian function from *eqn. (4.24)* and the fit coefficients are reported in Table 4.5. The normalized freestream velocity of 1 is shown for reference. Figure 4.44 shows that for $x/C < 2$ vortices travel significantly faster than the free stream velocity U_{∞}, and then rapidly slow down to sub freestream velocities. According to the wake profile study, vortices in the 2S_ivK wake (case $\mathbf{C_1}$) are expected to travel faster than the freestream velocity, since unlike the 2S_vK and 2S_A wakes from cases $\mathbf{A_1}$ and $\mathbf{B_1}$ respectively, it is a thrust producing wake. Comparison with Figure 4.18 shows that, on average, the streamwise drift velocity of vortices in the 2S_ivK wake is lower than the centerline velocity magnitude of the time averaged wake profile. However for $x/C < 1.5$ v_{drift} is still considerably higher than the free stream U_{∞} which supports the idea that the 2S_ivK flow field produces thrust.

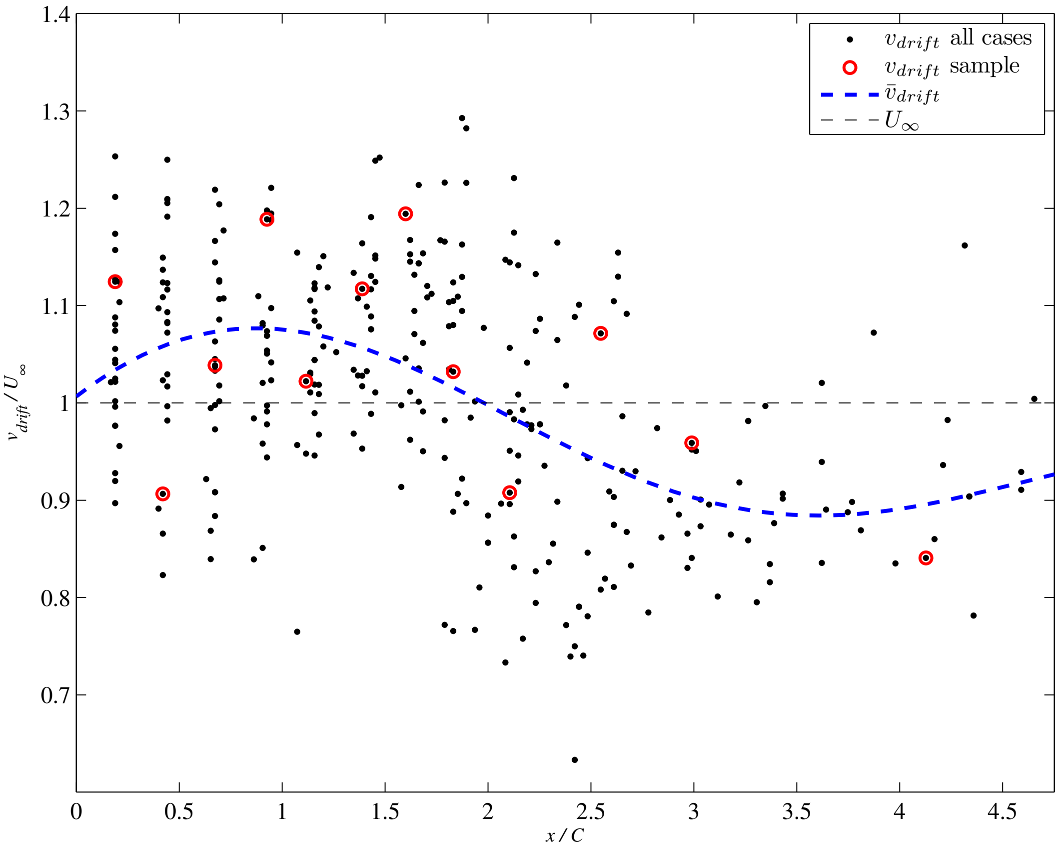

Figure 4.44:Dimensionless drift velocity vs. dimensionless streamwise distance for A_d = 0.84 and S_{td} = 0.274 ($f = 3.40$ rad/s and $\theta_A/2 = 4°$)

In Figure 4.45, the normalized streamwise spacing S_x/C is plotted against the dimensionless streamwise coordinate x_c for the 2S_ivK wake (case **C$_1$**). For $x/C<1.5$ the data has the lowest scatter and remains reasonably constant at $S_x = 25 \pm 15$ mm.

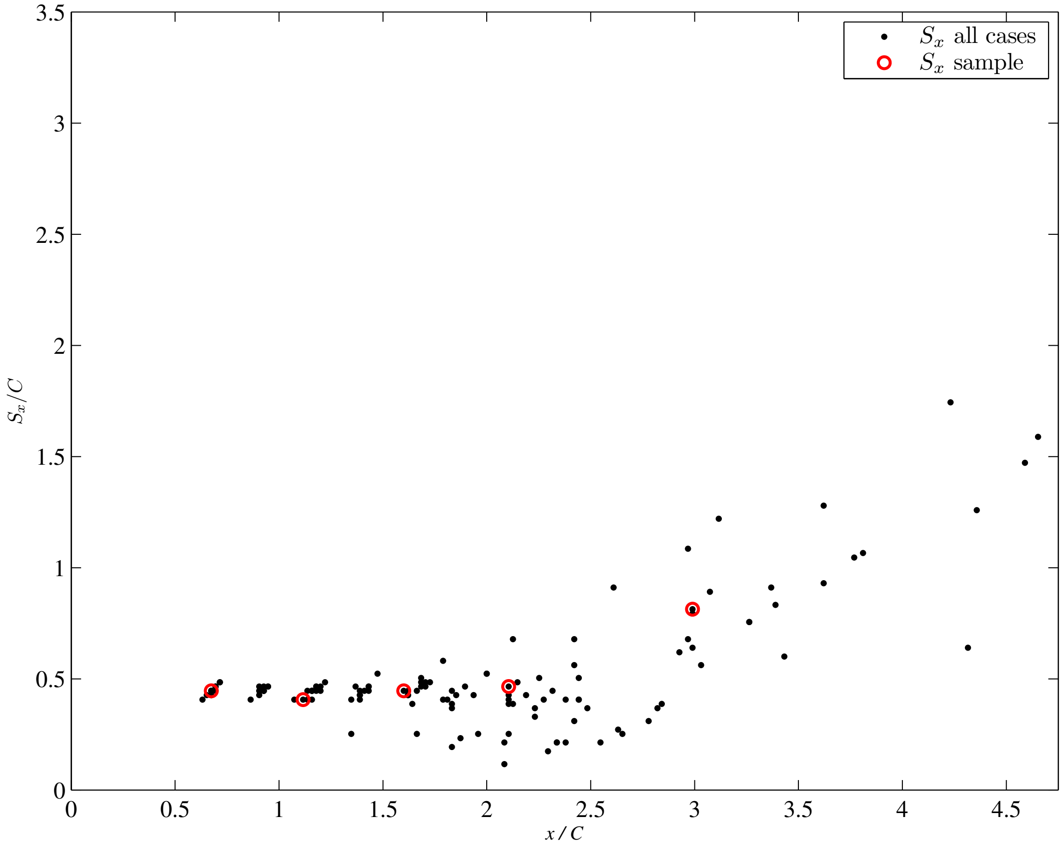

Figure 4.45:Streamwise vortex spacing S_x vs. dimensionless streamwise distance for A_d = 0.84 and S_{td} = 0.274 ($f = 3.40$ rad/s and $\theta_A/2 = 4°$)

In Figure 4.46, the normalized transverse spacing S_y/D is plotted against the dimensionless streamwise coordinate x_c for the 2S_ivK wake (case $\mathbf{C_1}$). Similar to the 2S_vK wake (case $\mathbf{A_1}$), S_y data has considerable scatter making it difficult to identify a trend, especially as streamwise distance increases. The data does however provide a rough idea of the magnitude of transverse spacing, and establishes a means to compare the vortex spacing with other wakes.

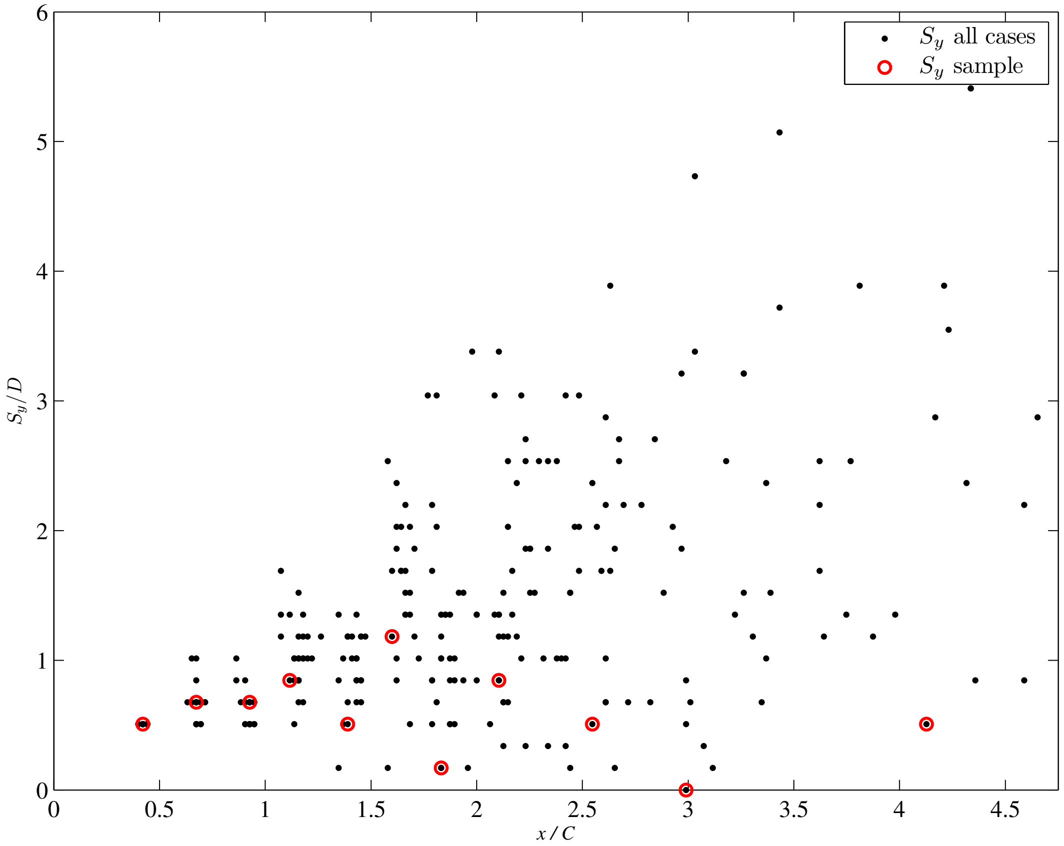

Figure 4.46: Transverse vortex spacing S_y vs. dimensionless streamwise distance for A_d = 0.84 and S_{td} = 0.274 ($f = 3.40$ rad/s and $\theta_A/2 = 4°$)

The various curve fits and corresponding fit coefficients for the 2S_ivK wake (case $\mathbf{C_1}$) parameters presented in the above figures are summarized in Table 4.5.

Table 4.5:Summary of fit functions and coefficients for the 2S_ivK wake

Wake Parameter	**Fit function**	**Applicable fit coefficients**					
		a, a₁	*b, b₁*	*c, c₁*	*d, a₂*	*b₂*	*c₂*
$\bar{\Gamma}_{+}(x_c)$	2nd order Gaussian	-262.3	2.027	0.6877	474.9	1.256	1.695
$\bar{\Gamma}_{-}(x_c)$	2nd order Gaussian	-430.7	0.828	1.102	-146.9	4.304	2.525

$\boldsymbol{\bar{\omega}_{peak}(x_c)}$	Custom exponential	2.84e-7	0.153	13.66	-	-	-
$\boldsymbol{\bar{r}_v(x_c)}$	2nd order Gaussian	6.72	5.257	8.135	2.958	1.3	0.365
$\boldsymbol{\bar{v}_{drift}(x_c)}$	2nd order Gaussian	1.007	0.5379	2.909	0.908	5.888	3.241

Wake comparison

A comparison of important parameters for the three wake types is performed. The circulation Γ, the positive peak vorticity ω_{peak}, the vortex boundary radius r_v, the vortex streamwise drift velocity v_{drift}, the inferred axial velocity gradient β within a vortex are assessed and compared.

There exists a region in the near field of the wake where the spatial organization of the vortices is regular and well structured. In this region there is no apparent boundary region overlap and as a result the vortices are allowed to diffuse naturally into the surrounding fluid (Ponta, 2010). This region is referred to as the organized near field wake ONFR and is annotated in Figure 4.22. In the ONFR, the analytical model agrees with the experimental data. However, beyond this region several governing assumptions break down and the analytical model becomes invalid.

Figure 4.47 shows the experimental circulation curve fit $\bar{\Gamma}(x_c)$ for the 2S_vK, the 2S_A and the 2S_ivK wakes in cases **A₁, B₁** and **C₁** respectively. The 2S_vK wake (case **A₁**) has the lowest initial circulation; which decreases the least over *x/C*=10 downstream. In contrast, the 2S_A and the 2S_ivK wakes (cases **B₁** and **C₁** respectively) have higher initial circulation, which drops below that of

2S_vK (case $\mathbf{A_1}$) at x/C=2. All 3 cases achieve a local maximum in $\bar{\Gamma}$ before decreasing. The local maximum becomes progressively more pronounced as the frequency f is increased. This is due to the different principal sources of circulation on the airfoil. Circulation in the 2S_vK wake is primarily attributed to boundary layer vorticity while circulation in the 2S_A and 2S_ivK wakes is predominantly due to the motion of the trailing edge of the airfoil (Schnipper et al., 2009). As a result, the vortex shedding in a 2S_vK wake takes place in a stable manner since the steady freestream velocity dominates over the trailing edge velocity and the vortex is slowly formed as it advects along the surface of the airfoil. In contrast, vortex shedding in the 2S_A and 2S_ivK wakes is dominated by the highly periodic trailing edge tip velocity and vortices form rapidly at the trailing edge of the airfoil. This gives rise to an extended vortex formation distance that goes beyond the trailing edge of the airfoil and is a potential explanation for the increasingly pronounced local maxima in the circulation data with increasing airfoil frequency f.

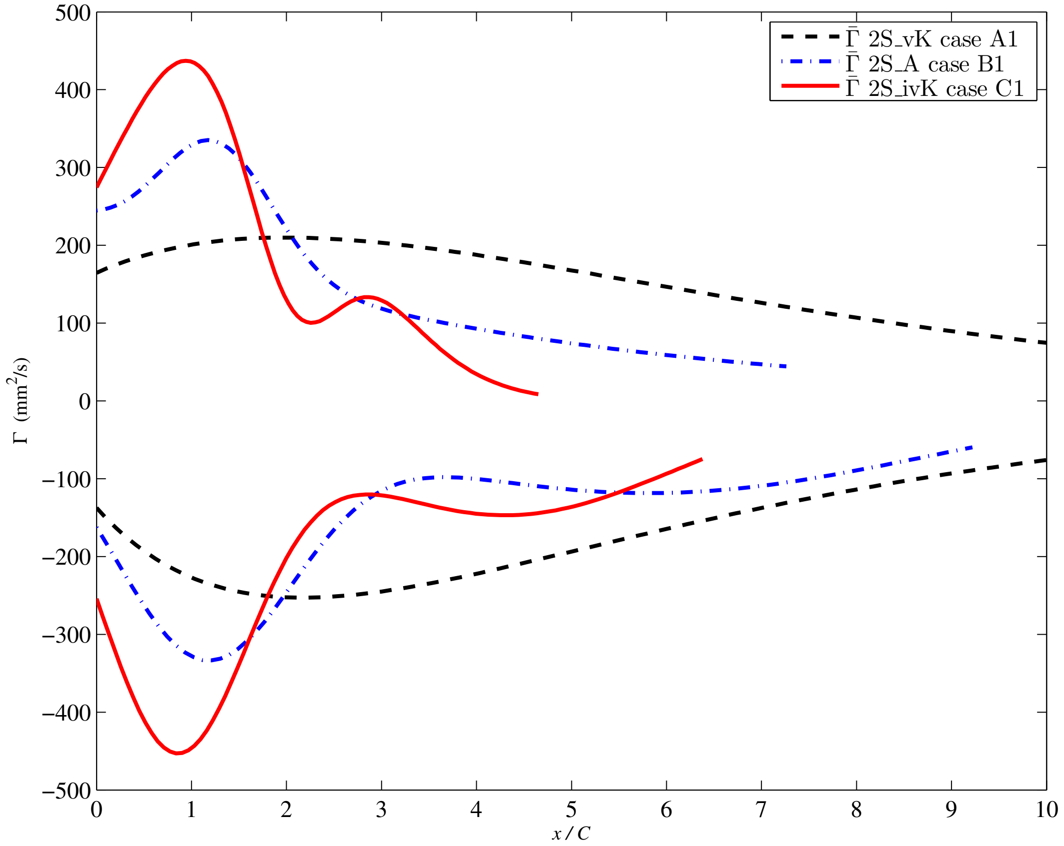

Figure 4.47: Experimental curve fit of circulation vs. dimensionless streamwise distance for the 2S_vK, the 2S_A and the 2S_ivK wakes

Figure 4.48 shows the experimental positive peak vorticity curve fit $\bar{\omega}_{peak}(x_c)$ for the 2S_vK, the 2S_A and the 2S_ivK wakes in cases $\mathbf{A_1}$, $\mathbf{B_1}$ and $\mathbf{C_1}$ respectively. The initial peak vorticity and vorticity gradient is highest for the 2S_ivK wake (case $\mathbf{C_1}$). The lowest initial peak vorticity and the smallest gradient are associated to the 2S_vK wake (case $\mathbf{A_1}$). All wakes eventually reach a relatively constant peak vorticity.

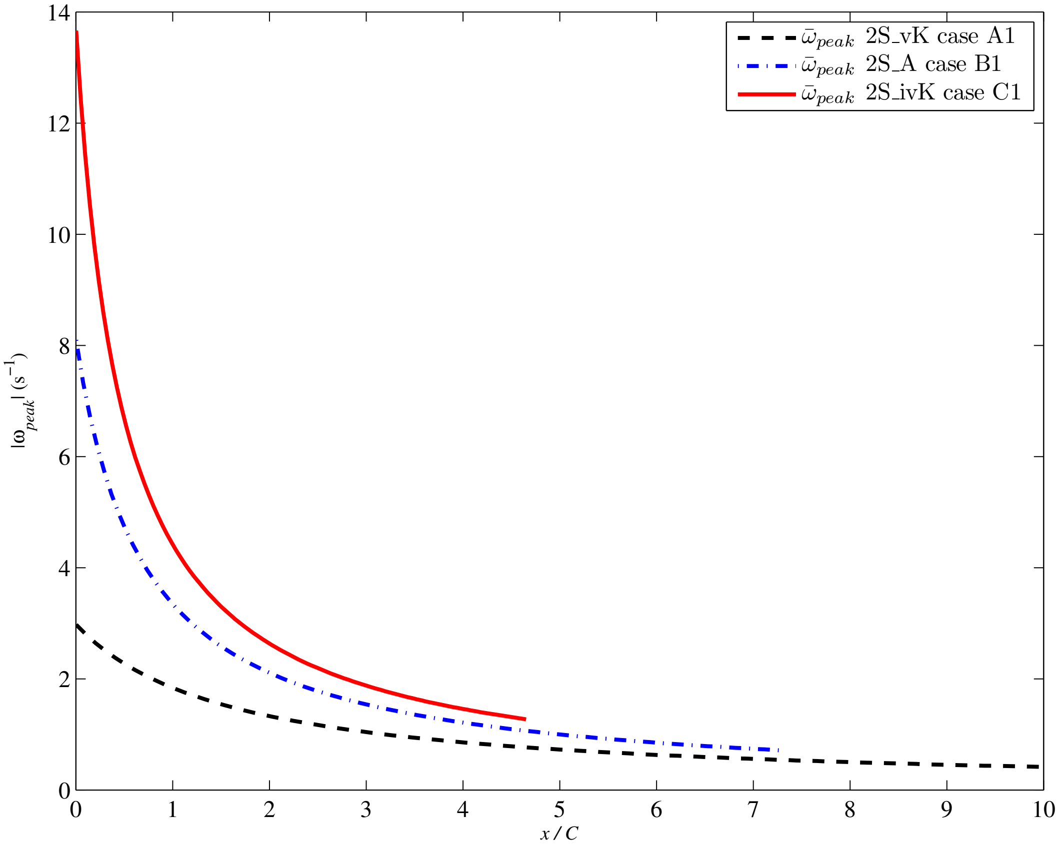

Figure 4.48: Experimental curve fit of positive peak vorticity vs. dimensionless streamwise distance for the 2S_vK, the 2S_A and the 2S_ivK wakes

Figure 4.49 shows the experimental vortex boundary radius curve fit $\bar{r}_v(x_c)$ for the 2S_vK, the 2S_A and the 2S_ivK wakes in cases $\mathbf{A_1}$**,** $\mathbf{B_1}$ and $\mathbf{C_1}$ respectively. Within the ONFR the 2S_vK wake (case $\mathbf{A_1}$) produces the largest vortices followed by the 2S_A (case $\mathbf{B_1}$) and the 2S_ivK wake (case $\mathbf{C_1}$) produces the smallest vortices. For the 3 wakes $\bar{r}_v$ initially increase with *x/C*, then reaches a maximum and decreases to some relatively constant value. The maximum $\bar{r}_v$ occurs at the ONFR. Beyond the ONFR further increase in $\bar{r}_v$ ceases due to neighboring vortices whose boundaries have grown enough to interfere with one another.

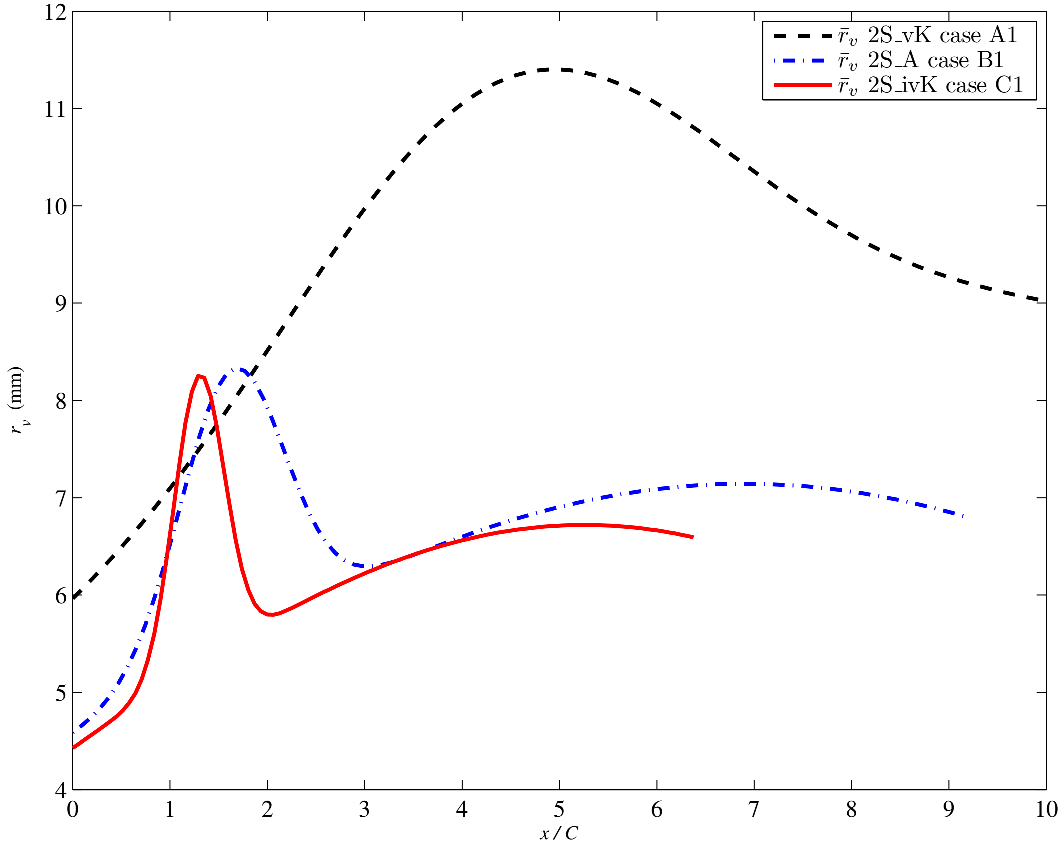

Figure 4.49:Experimental curve fit of vortex boundary radii vs. dimensionless streamwise distance for the 2S_vK, the 2S_A and the 2S_ivK wakes

Figure 4.50 shows the experimental dimensionless streamwise drift velocity curve fit $\bar{v}_{drift}(x_c)$ for the 2S_vK, the 2S_A and the 2S_ivK wakes in cases **A_1, B_1** and **C_1** respectively. The 2S_ivK wake (case **C_1**) produces vortices which travel considerably faster than the free stream, which is expected since it is believed to be a thrust producing wake (Bohl & Koochesfahani, 2009), (Schnipper et al., 2009). Vortices from the 2S_A wake (case **B_1**), while faster than those in the 2S_vK wake (case **A_1**), still remain below the free stream.

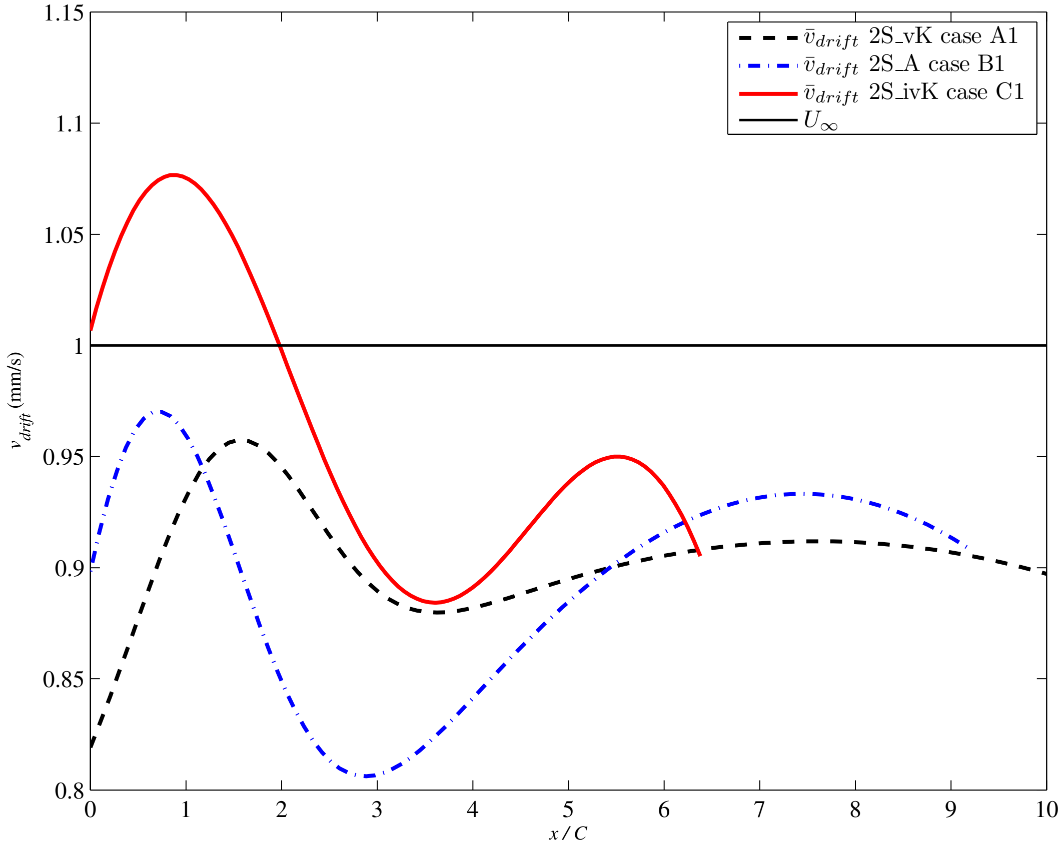

Figure 4.50:Experimental curve fit of streamwise drift velocity vs. dimensionless streamwise distance for the 2S_vK, the 2S_A and the 2S_ivK wakes

Important parameters for the three wake types in cases **A_1, B_1** and **C_1** are summarized in Table 4.6. The axial to in-plane velocity gradient ratio is estimated with $|\omega_\mu/\beta|$ and shows that the flow becomes increasingly three dimensional as the wake progresses toward a forced 2S_ivK wake (case **C_1**). The streamwise coordinate of the ONFR and of analytical agreement are also listed in Table 4.6.

Table 4.6: Summary of important wake parameters for the 2S_vK, 2S_ivK and the 2S_A wakes

Wake	**Γ_o (mm^2/s)**	**ω_o (1/s)**	**β (1/s)**	**$\lvert\omega_\mu/\beta\rvert$**	**Analytical agreement**	**ONFR**
2S_vK	200	2.92	-0.0165	58.33	$x_c < 4$	$x_c < 4$
2S_A	300	8.00	-0.065	39.84	$x_c < 1.75$	$x_c < 1.75$

2S_ivK	410	13.9	-0.165	26.8	$x_c < 0.4$	$x_c < 1.5$

4.5 Conclusions

A NACA 0012 airfoil in a uniform 2D steady flow is forced to oscillate about its aerodynamic center in a sinusoidal manner. The effect of varying the oscillation amplitude θ_A and frequency f was studied by measuring the resulting wake using PIV. The vortex parameters that are evaluated include: circulation Γ, peak vorticity ω_{peak}, vortex boundary radii r_v, vortex streamwise drift velocity v_{drift}, streamwise vortex spacing S_x and transverse vortex spacing S_y.

The spatial organization of vortices in the wake was investigated qualitatively and is used to develop a Re independent (Schnipper et al., 2009) phase map. The phase map is based on dimensionless amplitude A_d and frequency St_d and can be used to categorize the wakes into a 2S_vK, an 2S_A, an 2S_ivK or a 2S_ivKa wake type. PIV is performed for certain points on the phase map (cases $\mathbf{A_1}$, $\mathbf{B_1}$,$\mathbf{C_1}$, $\mathbf{A_2}$, $\mathbf{B_2}$ and $\mathbf{C_2}$ shown in Figure 4.5). These cases illustrate the important wake transitions and were selected such that the different wake types are achieved by only varying amplitude or forcing frequency while holding the other constant.

The PIV results are used to study vortex cross-sectional profiles which showing that the experimental data follows the Burgers vortex model quite closely. This justifies the use of an analytical model for predicting the peak vorticity decay of a vortex. The PIV analysis also suggested that performing vortex detection and characterization on a phase averaged field produces results which increasingly underestimate the magnitude of peak vorticity and circulation with increasing streamwise distance.

Vortex detection is performed for several instantaneous vector fields and this data is used to parameterize the analytical model. The models for the 2S_vK and 2S_A wakes (cases $\mathbf{A_1}$ and $\mathbf{B_1}$ respectively) only agree with the experimental data within the ONFR which is the streamwise coordinate defining the limit of the organized near field region of the wake. The model for the 2S_ivK wake (case $\mathbf{C_1}$) only agrees with the experimental data for x/C<0.4 which is further upstream than its ONFR. The spatial organization of vortices within the ONFR closely resembles that of the ideal wake types shown in Figure 4.1. Further downstream, the wakes become qualitatively different from the ideal wake types since the transverse and streamwise spacing becomes irregular. The streamwise coordinates of the various ONFRs are 4, 1.75 and 1.5 for the 2S_vK, the 2S_A and the 2S_ivK wakes from cases $\mathbf{A_1}$, $\mathbf{B_1}$ and $\mathbf{C_1}$ respectively.

Several studies quantitatively examine many of the wake parameters investigated here for $x/C \leq 1$ and only for the 2S_vK wake type (Bohl & Koochesfahani, 2009), (Godoy-Diana et al., 2009). Other studies that look further downstream (Schnipper et al., 2009) only qualitatively examine the wake. This study considers up to 10 chord lengths downstream and performs a detailed study for the 2S_vK, the 2S_A and the 2S_ivK wakes (cases $\mathbf{A_1}$, $\mathbf{B_1}$ and $\mathbf{C_1}$ respectively). Measurements downstream of the ONFR is more complex than the analytical model causing the analytical model and the experimental data to disagree as expected.

Wake profiles were also generated by averaging several instantaneous velocity fields imaged at a fixed time interval that is different than the oscillation period. These serve to show the transitions from drag inducing wakes, to thrust producing wakes and to investigate how these transitions compare with the qualitative wake organization transitions between the 2S_vK and the 2S_ivK wakes. The 2S_vK (case $\mathbf{A_2}$) wake was found to have a velocity deficit in its wake and therefore induce drag on the airfoil. For $x/C < 2.75$ the 2S_A wake type (case $\mathbf{B_2}$) had a velocity neutral wake and for $x/C > 2.75$ it was shown to have a velocity deficit. Finally, the 2S_ivK wake (case $\mathbf{C_2}$) had a velocity excess and therefore produced a thrust force on the airfoil.

CHAPTER 5: Vortex interaction and wake characteristics of two oscillating airfoils in tandem

5.1 Introduction

The ability to actively control large coherent vortices in an unsteady flow is studied experimentally. The experiment consists of two identical NACA 0012 airfoils in a tandem configuration. The upstream airfoil is referred to as the forefoil and a second downstream airfoil is referred to as the hindfoil. The forefoil is forced to pitch sinusoidally at a fixed frequency and amplitude with the intention of producing a consistent vortical wake comprising of leading edge and trailing edge vortices. The hindfoil executes sinusoidal pitching at the same frequency and amplitude as the forefoil and the effect of changing the relative phase between the two airfoils is studied. The vortex characteristics of the hindfoil wake are evaluated and the circulation magnitude in particular is used to investigate the effect of varying the phase. Two fundamental wakes are studied, one with an oscillation frequency and amplitude of 4 rad/s and 20° *pk-pk* respectively and the other with oscillation frequency and amplitude of 2 rad/s and 40° *pk-pk* respectively. Each of these flows will first be studied independently without the presence of the hindfoil. This produces a reference from which to gauge whether a given hindfoil phase enhances of suppresses vortex strength.

5.2 Background

The study of vortex suppression of a 2S_vK wake through passive control has been studied extensively in the literature. These studies focus on suppressing the unsteadiness of the flow by altering its geometry (Akilli et al., 2005), (Kwon & Choi, 1996), (Shukla et al., 2009). Circular cylinders are typically used to generate the 2S_vK wake since this flow regime is well documented (Akilli et al., 2005)(Kwon & Choi, 1996) and under the right conditions it can provide a robust and reliable source of coherent and well formed vortices. A common geometry modification used in passive control is to attach a longitudinal rigid splitter plate to the trailing edge of the cylinder/structure. Assuming the plate is sufficiently long compared to the cylinder diameter, it is possible to suppress the vortex induced vibrations to lower amplitudes (Akilli et al., 2005). Other related studies have also taken place. These include the effects of rigid splitter plates on the wake of a circular cylinder (Unal & Rockwell, 2006) both experimentally (Akilli et al., 2005) and numerically (Kwon & Choi, 1996). In both cases, suppression is achieved by completely inhibiting communication between the two vortex layers of the 2S_vK vortex street.

An interesting extension to the rigid splitter plate problem is the use of a hinged splitter plate in the wake of the cylinder. In contrast to the rigid splitter plate scenario, a hinged splitter plate only partially inhibits communication between the two shear layers, thus allowing for some level of interaction between the two vortex sheets. Experimental investigation of a splitter plate hinged at the leading edge showed that the main non-dimensional parameters of importance are the splitter plate length to cylinder diameter ratio and Reynolds number (Shukla et al., 2009). Other non-dimensional parameters related to the mass and the stiffness of the splitter plate, as well as the internal structural damping of the hinge are assumed to be small and consequently have little effect on the final results. In that study they were able to show that the splitter plate length to cylinder diameter ratio (*L/D*) is crucial in determining the character and magnitude of the splitter plate oscillations. Also, the splitter plate amplitude increases with Reynolds number at a low range of Reynolds numbers, but reach a saturation amplitude level at higher Reynolds numbers (Shukla et al., 2009). Although characterization of splitter place motion was studied, Shukla et al. (2009) do not study the wake downstream and consequently, make no claims about how a hinged splitter plate may affect the 2S_vK flow generated.

All of the above work represents passive control methods for suppressing the unsteadiness of the flow by altering its geometry. However, the current work aims to reposition vortices and change their strength in a prescribed and desirable manner. This requires the use of active control, which can be further divided into open-loop control, where the active forcing is prearranged and closed loop control, where the forcing is a function of a real-time sensor that responds to the flow. Several studies incorporate closed-loop control namely, Roussopoulos (2006) and Keles (2002) who both use actively driven loudspeakers to force the flow and hotwire sensors to observe the flow. However, more closely related to the current study, Gopalkrishnan et al. (1994) performed an experimental study focusing on active closed-loop control in which they aimed to manipulate fully formed vortices that presumably originate from an unknown source that cannot be altered. In order to accomplish this, the upstream cylinder is replaced with a D-section cylinder allowing for a more customizable wake scheme. The coherent vortices that are generated from it travel downstream until they encounter a sinusoidally pitching and heaving airfoil which attempts to either suppress or enhance the incoming vortices by varying its phase relative to the D-section cylinder. They were able to show that, by changing the phase of the control airfoil, the resulting wake falls into 1 of 3 distinct modes. Either a von Kaman wake with 2 counter-rotating pairs of vortices per oscillation cycle (2P); a suppressed von Kaman wake, where the vortices from the cylinder and the airfoil destructively interfere; or an enhanced 2S_vK wake, where the vortices from the cylinder and those form the airfoil constructively interfere. In modes 2 and 3 the substantial repositioning of the vortices could sometimes result in a 2S_ivK wake. The study of Gopalkrishnan et al. (1994) focuses on the spatial organization of the wake both downstream of the D-section cylinder and of the control airfoil. Some quantitative assessments are made about the spacing and the direction of rotation of the coherent vortices. However, most of the work is centered on qualitative remarks about the flow geometry which is based on experimental kalliroscopic flow visualization results.

The current work aims to complete a quantitative evaluation of several important vortex parameters downstream of the hindfoil's trailing edge. These vortex parameters consist of: vortex boundary radius r_v, circulation Γ and peak vorticity ω_{peak}. The effect of using open-loop control on the hindfoil is quantified by measuring how the vortex parameters change as the phase of the hindfoil is swept through 360°. In addition, novel pressure sensing membranes are installed on the aerodynamic centre of the hindfoil. The real-time pressure data obtained from these sensors, coupled with PIV data obtained from the open-loop control experiments will provide information that will help to later expand the system to a closed-loop controller.

5.3 Experimental Procedure

The experiments take place in the recirculating water channel and with the PIV imaging system described in *Chapter 2*. Several adaptations to the basic experimental setup were required for the current study. The hindfoil was hung vertically into the water channel and downstream of the forefoil. The airfoils have identical geometry, with the exception of the pressure sensing membranes on the hindfoil. They are separated by a distance D_s as shown in Figure 5.1. The angles $\theta_{ff}(t) = (\theta_A/2)\sin(2\pi f t)$ and $\theta_{hf}(t) = (\theta_A/2)\sin(2\pi f t - \Phi\pi/180°)$ expressed in degrees, correspond to the positive angle formed by the chord line and the wake centerline of the forefoil and the hindfoil respectively. Also, Φ is the phase lag of the hindfoil and θ_A is the pk-pk amplitude in degrees of the foils motion.

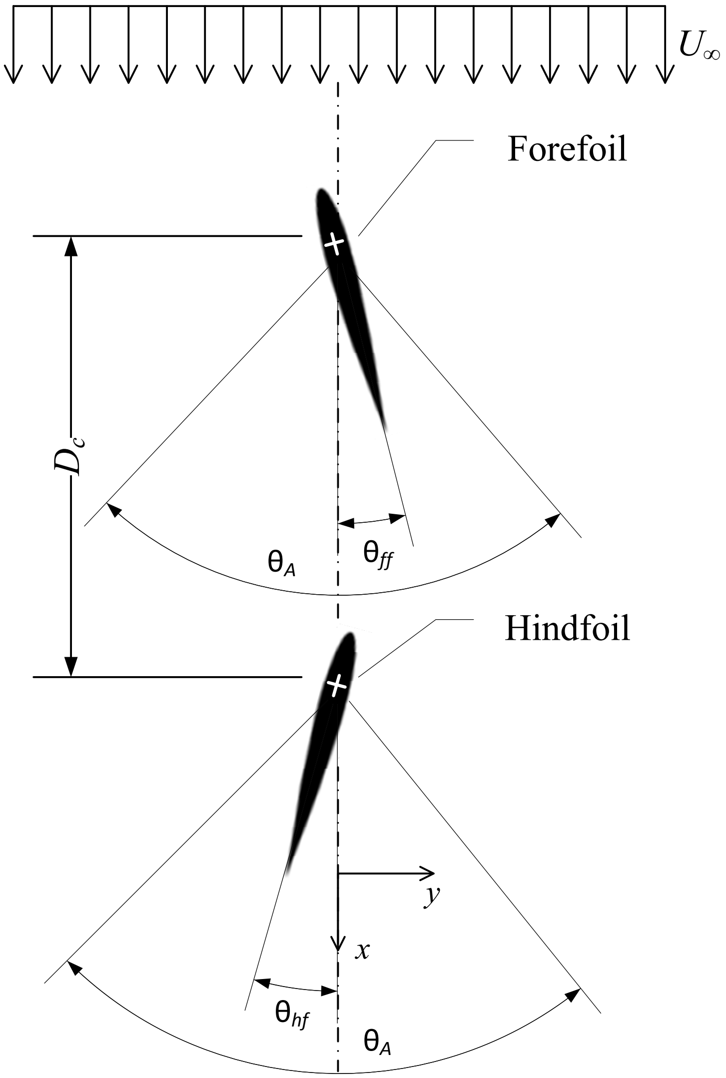

Figure 5.1: A schematic of the tandem airfoil arrangement

In *Chapter 4* the change in axial velocity with $\partial w/\partial z$ was estimated with the analytical model and comparison with the significantly larger in-plane velocities gradients suggests that the flow behind the forefoil is predominantly 2D. As such, the characteristics of the vortical structures traveling past the airfoil are relatively constant along the span of the foil. This led to the development of a span-wise pressure membrane which generates a hydraulic advantage by effectively displacing more air than would a single circular pressure tap under a given pressure differential. The pressure membrane has an inherently larger surface area and under the same pressure will contribute to a stronger voltage output from the differential pressure transducer.

Figure 5.2 shows the forefoil, hindfoil and the pressure membrane in a side view of the test section. The pressure sensing membranes consist of two 5 mm wide × 2.5 mm deep × 200 mm long grooves machined out of the hindfoil. They are symmetric about the hindfoil span and centered on the aerodynamic centre on either side of the airfoil. A 3/32” hole is drilled along the span into the airfoil and penetrates into the machined pressure grooves. The airfoil is wrapped with a thin layer of latex to separate channel water from the air-pressure-measurement, effectively creating two thin flexible membranes on either side of the hindfoil. Brass tubes are inserted into the drilled holes and 1/8” OD flexible plastic tube is fitted over the brass. Minimum length plastic tubes are connected to a differential pressure transducer (Validyne Engineering, DP-138 with an 8-06 diaphragm).

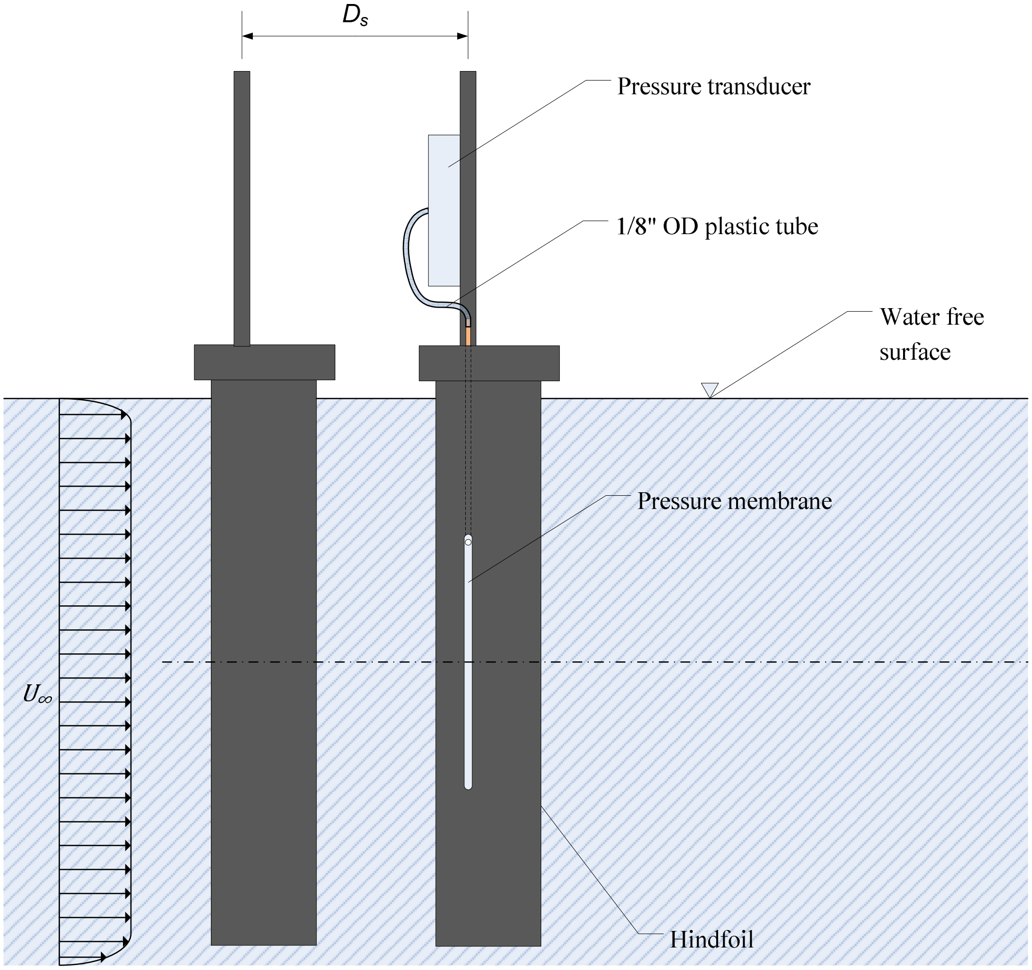

Figure 5.2: Test section schematic showing the forefoil and hindfoil along with the pressure membrane

The pressure membrane deforms dynamically under the pressure fluctuations from the forefoil wake. This displaces the air trapped inside the pressure membrane grooves and consequently moves the diaphragm of the differential pressure transducer producing a measurable change in voltage. This time dependant signal is logged to a data acquisition board (dSPACE Inc, DP-103).

The hindfoil rotates about its aerodynamic center and is driven by a second stepper motor identical to the one used for the forefoil described in *Chapter 2*. The differential pressure transducer is rigidly attached to the stepper motor output shaft. This ensures that the plastic tubes do not deform and move air into the transducer diaphragm cavity as the airfoil oscillates. The oscillation amplitude and frequency of both airfoils are identical and the hindfoil wake is studied at 8 equally spaced points between phase $\Phi = 0°$ and $\Phi = 360°$. Two upstream 2S_vK flow fields are investigated: wake **type A** has oscillation frequency and amplitude of $f = 4\ \mathrm{rad/s}$ and $\theta_A = 20°$ respectively and wake **type B** has oscillation frequency and amplitude of $f = 2\ \mathrm{rad/s}$ and $\theta_A = 40°$ respectively. In both cases the airfoil separation distance and free stream velocity are fixed at D_s = 103.5mm and $U_\infty = 160$ mm/s respectively. PIV is performed for 100 instantaneous flow fields per phase for each of the two upstream flow regimes. The instantaneous PIV data is collected precisely when the hindfoil reaches 0° during a positive rotation. The time dependant pressure signal is logged for 1500 seconds at a time for every phase.

5.4 Vortex characterization

The ability to modify the properties of large coherent vortices in a 2S_vK wake with open-loop control is investigated by studying the effect of changing the phase of the hindfoil relative to the forefoil. Figure 5.3 is a schematic of the anticipated interaction between the upstream 2S_vK wake generated by the forefoil and the sinusoidally forced hindfoil. An incoming upstream vortex interacts with the solid boundary of the hindfoil and the resulting wake downstream of the hindfoil is characterized with PIV measurements.

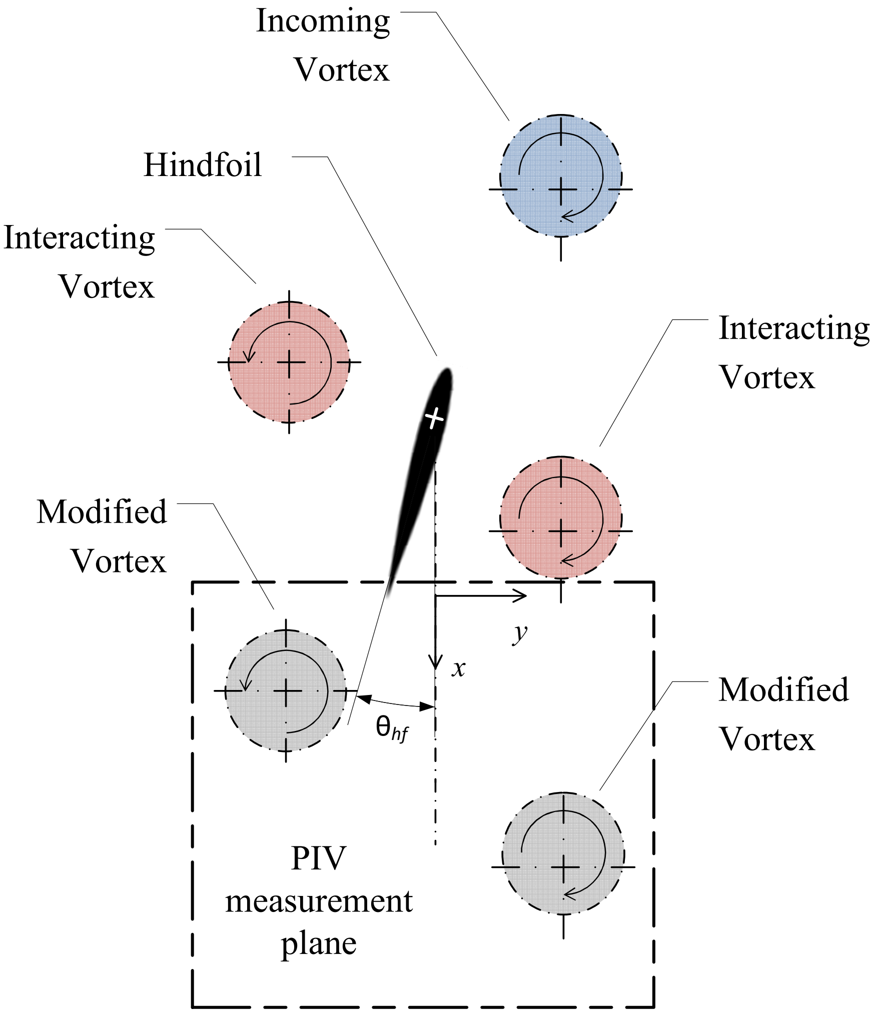

Figure 5.3: Vortex spacing arrangement for tandem airfoil schematic

5.4.1 Single airfoil (forefoil)

Before studying the wake characteristics of the hindfoil, it is first necessary to isolate the forefoil and investigate its wake characteristics independent of the presence of the hindfoil. This creates a reference point from which to compare future tandem wing results.

Wake type A

The phase averaged vorticity field and a sample vorticity field of the single forefoil for wake **type A** is shown in Figure 5.4. There are 6 vortices shed per oscillation cycle, two primary vortices of opposite rotation each surrounded by two same signed vortices of lesser strength on either side. This wake is characterized by a 2P+2S_vK (Schnipper et al., 2009) since the primary vortices are organized in a 2S_vK configuration. The total contribution of circulation from all the vortices in a wake with N_{vtx} vortices of individual circulation Γ_i is defined by:

$$|\Gamma_{total}| = \sum_{i=1}^{N_{vtx}} |\Gamma_i| \tag{5.1}$$

For the wake in Figure 5.4 the mean total contribution of circulation from all the vortices for 100 wakes was $|\Gamma_{total,mean}| = 1.69\times10^4$ mm^2/s. This value will be compared to that of the various tandem wakes.

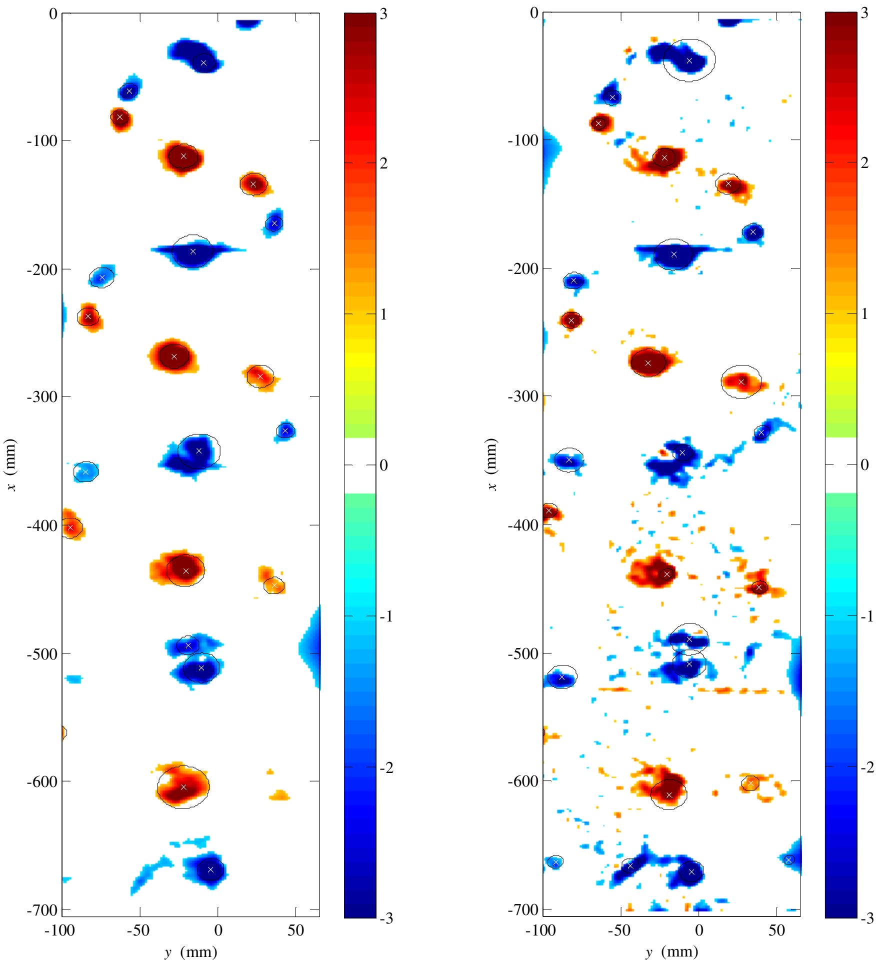

(a) (b)

Figure 5.4: Vorticity field for the wake with oscillation frequency and amplitude of 4 rad/s and $\boldsymbol{\theta_A = 20^\circ}$ With a) showing the phase averaged field and b) showing a sample field. In addition, boundary radii for the detected vortices are shown black circles and the vortex cores are shown as white '×'.

Wake type B

The phase averaged vorticity field of the single forefoil for the wake **type B** is shown in Figure 5.5. The phase averaged field shows four vortices shed per oscillation cycle; two same sign pairs of seemingly equal size and strength staggered in a 2S_vK type arrangement (Schnipper et al., 2009). However, this wake is actually a 4P wake since there are initially 4 pairs of vortices shed per oscillation cycle. The vortices rapidly merge reducing the number of vortices in an oscillation cycle from four pairs to two pairs and the wake for $x \geq -200$ mm resembles a 2P wake. The mean total contribution of circulation from all the vortices for 100 wakes was $|\Gamma_{total,mean}| = 1.1\times10^4$ mm^2/s.

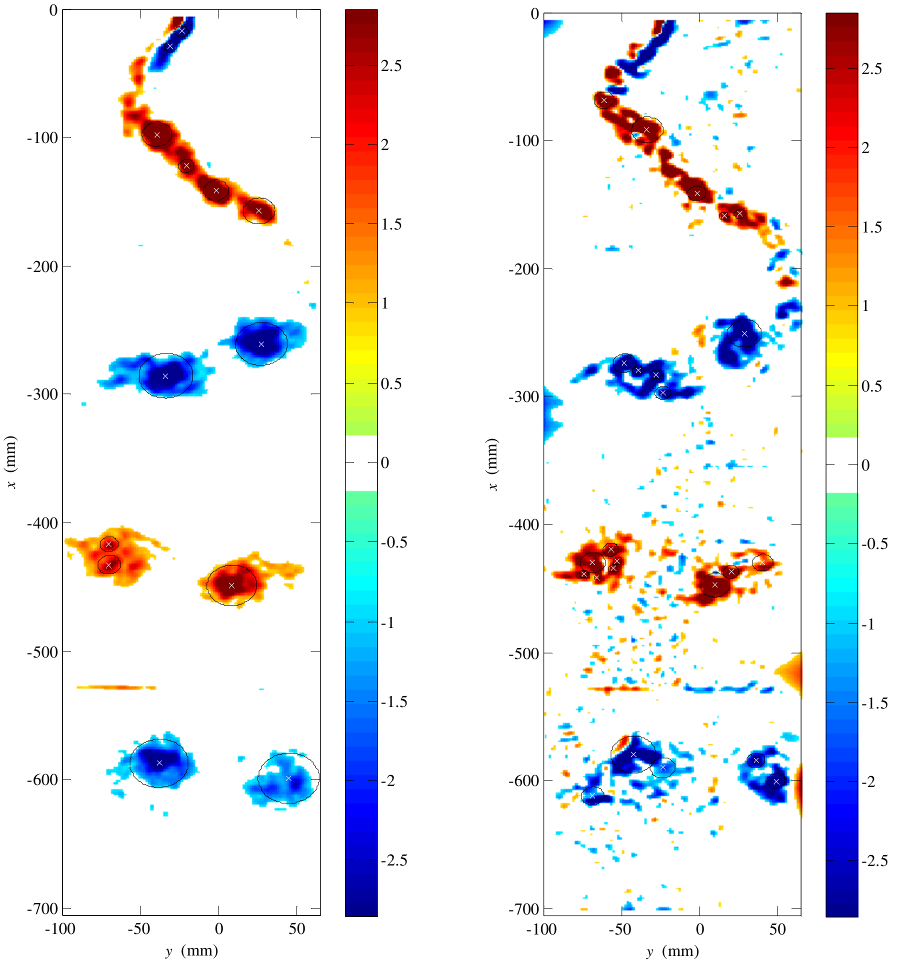

(a) (b)

Figure 5.5: Vorticity field for the wake with oscillation frequency and amplitude of 2 rad/s and $\theta_A = 40°$. With a) showing the phase averaged field and b) showing a sample field. In addition, boundary radii for the detected vortices are shown black circles and the vortex cores are shown as white '×'.

Figure 5.6 shows these wake types A and B on a phase diagram based on dimensionless Strouhal number St_d and dimensionless amplitude A_d defined in *Chapter 4*.

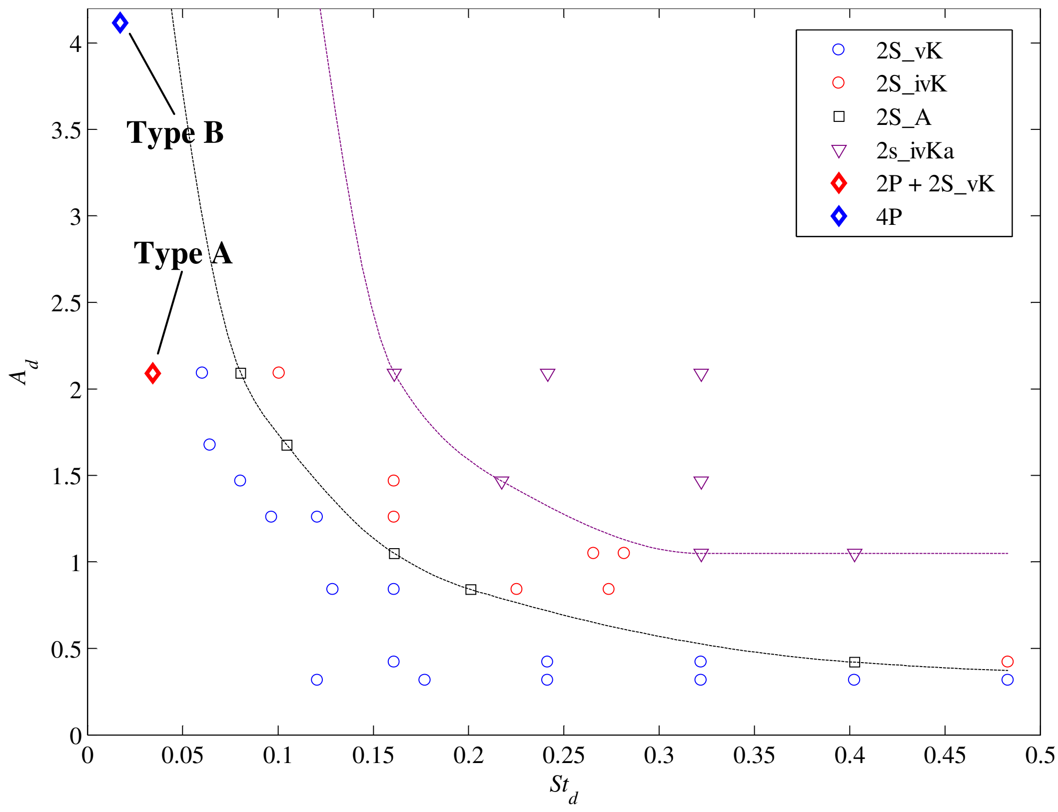

Figure 5.6: Dimensionless Strouhal number St_d based on chord width D, and dimensionless amplitude A_d map out various wake patterns which are the result of several oscillation frequency and amplitude combinations for the NACA 0012 airfoil in steady flow. The black dotted line indicates the boundary where the wake transitions from a 2S_vK to an 2S_ivK wake and the purple dotted line indicates where the wake transitions from 2S_ivK to 2S_ivKa.

5.4.2 Tandem configuration

Wake type A

The phase averaged vorticity field obtained from 100 individual hindfoil wakes from wake **type A** is plotted in Figure 5.7 for phases $\Phi = 0^{\circ}$, $\Phi = 45^{\circ}$, $\Phi = 90^{\circ}$, $\Phi = 135^{\circ}$, $\Phi = 180^{\circ}$, $\Phi = 225^{\circ}$, $\Phi = 270^{\circ}$ and $\Phi = 315^{\circ}$. The vorticity threshold used in the vortex detection is identical to that of the single airfoil scenario and remains constant throughout the various phases. A comparison with the single airfoil wake from Figure 5.4 provides preliminary evidence that the presence of the second airfoil can substantially alter the wake of the single airfoil wake. The vortex locations have been noticeably altered, and continue to change from one phase to another. In the near-field wake there is significant vortex interference as closely spaced vortices of opposite sign intrude upon one another. The wake in this region is highly disorganized making it difficult to track changes between phases. However, as the vortices progress downstream, only the dominant structures remain and it becomes notably easier to study the evolution of a particular vortex through the various phases. For example, the negative vortex at $x = -435$ mm appears to remain unchanged for phases $\Phi = 0° - 180°$, however, at $\Phi = 225°$ it splits into 3 distinct structures before collapsing back into a single vortex at $\Phi = 270°$.

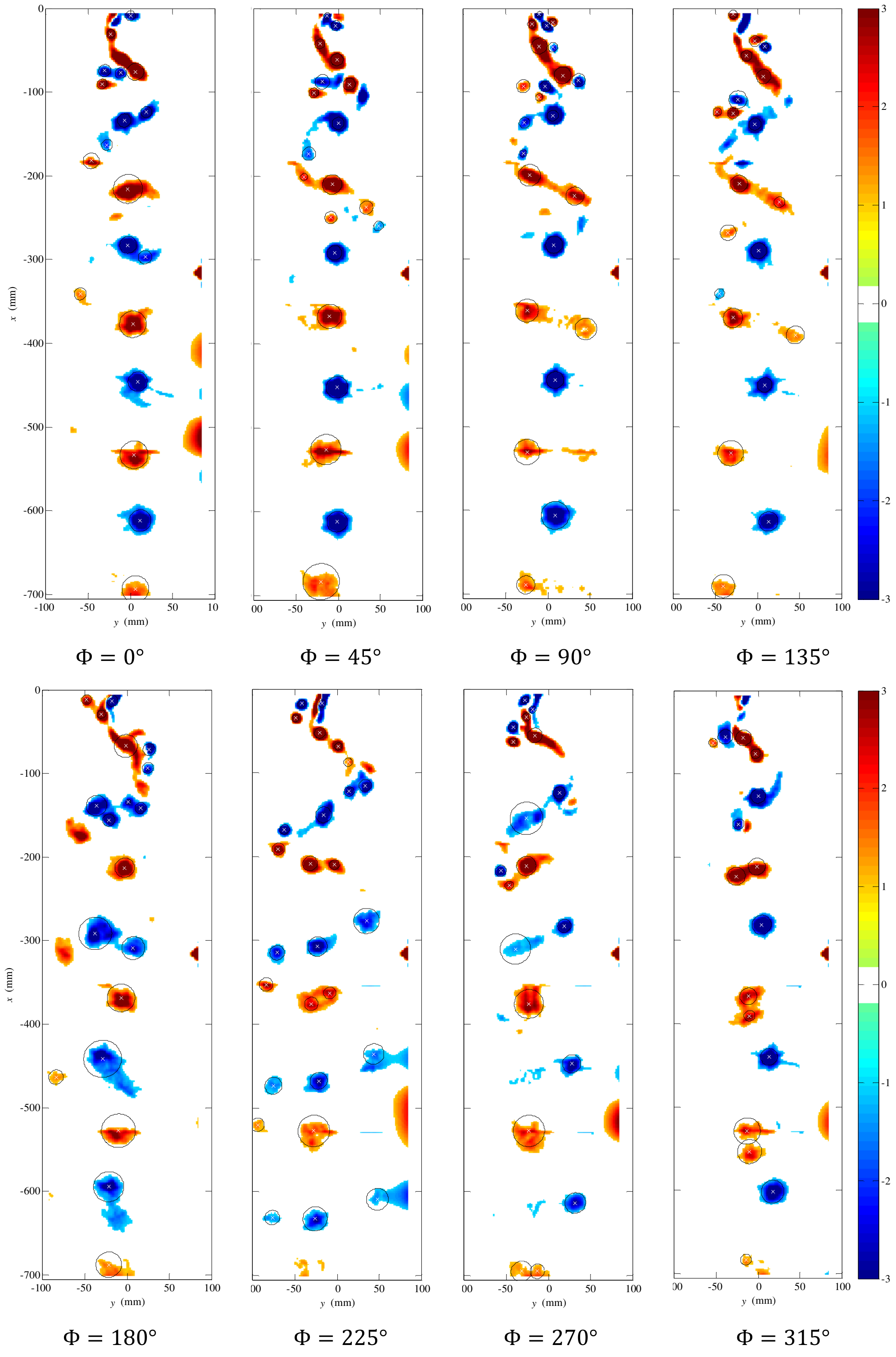

$\Phi = 0°$ $\Phi = 45°$ $\Phi = 90°$ $\Phi = 135°$

$\Phi = 180°$ $\Phi = 225°$ $\Phi = 270°$ $\Phi = 315°$

Figure 5.7: Vorticity field behind the hindfoil of wake type A for 8 phases $\Phi = 0° - 315°$ with detected vortex cores plotted as white x's and boundary radii as black circles.

The total contribution of circulation from all the vortices, computed from *eqn.(5.1)* is averaged over 100 fields and plotted for each of the phases. This along with a cubic interpolated curve and circulation for the single airfoil case is shown in Figure 5.8. The error bars represent two standard deviations in the data.

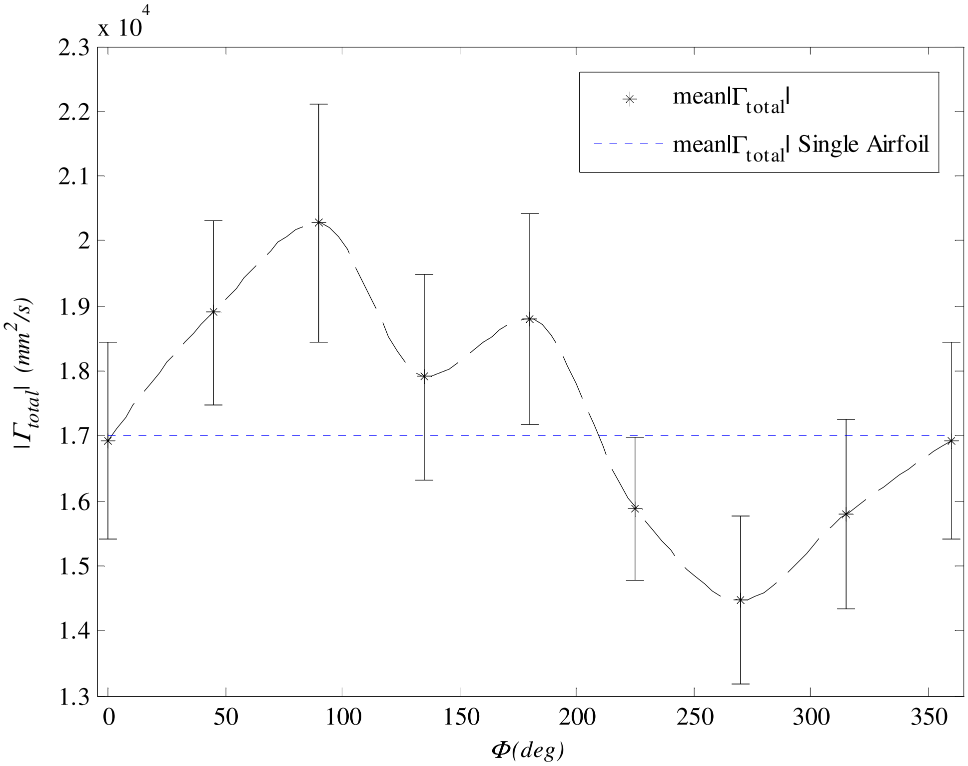

Figure 5.8: Total combined circulation from all of the vortices averaged over 100 fields for each phase along with that of the single airfoil case.

The figure indicates that maximum vortex suppression occurs at phase $\Phi = 270°$, maximum vortex enhancement occurs at $\Phi = 90°$, with a secondary enhancement peak appearing at $\Phi = 180°$. The secondary peak may be explained by investigating the single airfoil case. The single airfoil wake in Figure 5.4 indicates that in addition to the stronger trailing edge vortices, weaker leading edge vortices appear in the wake as a result of large oscillation amplitudes (Bohl

& Koochesfahani, 2009). These vortices are created at the leading edge and advect along the sides of the airfoil causing them to be shed at different hindfoil phases than the trailing edge vortices (Schnipper et al., 2009). It is proposed that a given hindfoil phase may enhance the relatively weaker leading edge vortices while a different phase may enhance the stronger trailing edge vortices.

For a given TIV the detection algorithm may be identifying a sufficiently high number of weak leading edge vortices which produce two distinct enhancement peaks on the tandem phase diagram as seen in Figure 5.8; one corresponding to the strong vortex enhancement phase Φ_{sE} and another for the weak vortex enhancement phase Φ_{wE}. Figure 5.9 is a tandem phase diagram similar to Figure 5.8; however the total circulation $|\Gamma_{total}|$ of only the weak vortices is considered. This figure shows a clear maximum peak at $\Phi = 225°$ and provides evidence supporting the secondary enhancement peak hypothesis presented above.

The distinction between weak and strong vortices is determined by observing the single airfoil case and attempting to find a suitable circulation cutoff which would distinguish leading edge vortices from trailing edge ones. The single airfoil wake from Figure 5.4 is assumed to be a 2P+2SvK wake. Schnipper et al. (2009) describe this type of wake by two counter rotating vortices in a von Karman configuration (2S) which are themselves surrounded by a pair of leading edge vortices (2P) for a total of six vortices per oscillation cycle. Investigation of the single airfoil wake reveals that the circulation of the trailing edge (2S) vortices were all well above 500 mm^2/s while that of the leading edge (2P) vortices were well below 500 mm^2/s. A suitable circulation cutoff for distinguishing the weak leading edge (2P) vortices from the strong trailing edge (2S) vortices is then $\Gamma_{cut} = 500$ mm^2/s.

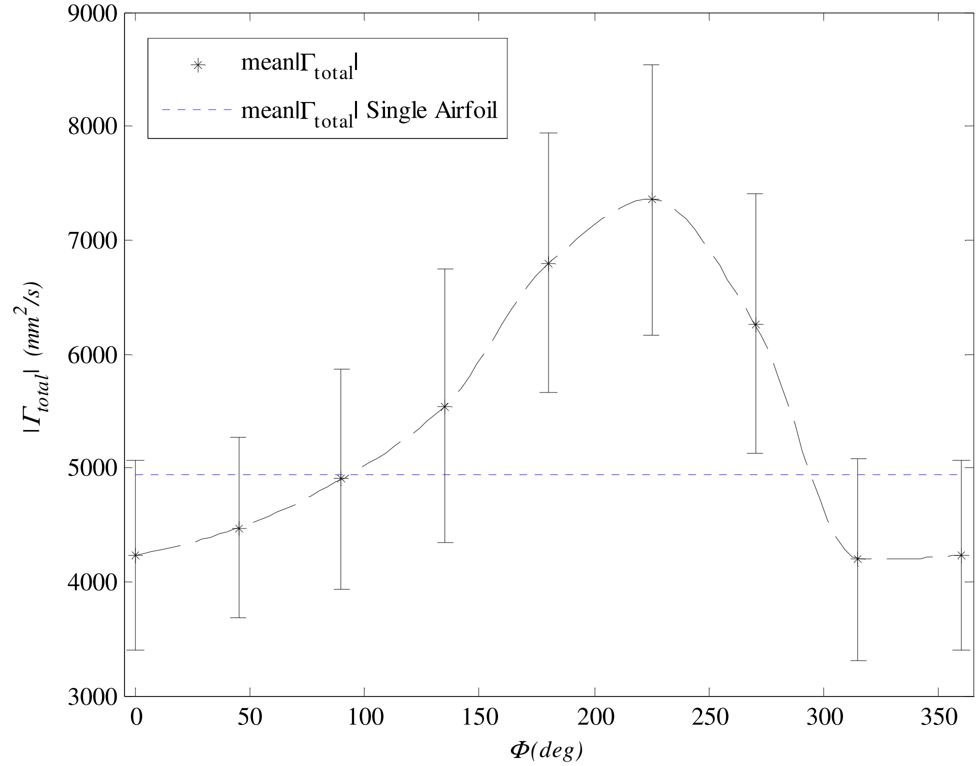

Figure 5.9: Total combined circulation from all of the weak vortices ($\Gamma \leq 500$ (mm^2/s)) averaged over 100 fields for each phase.

Similarly, in Figure 5.10, only the total circulation $|\Gamma_{total}|$ of the strong vortices is considered. The secondary peak at $\Phi = 180°$ seen in Figure 5.8 has flattened out and the curve has well defined maximum and minimum total circulation at $\Phi = 90°$ and $\Phi = 270°$ respectively.

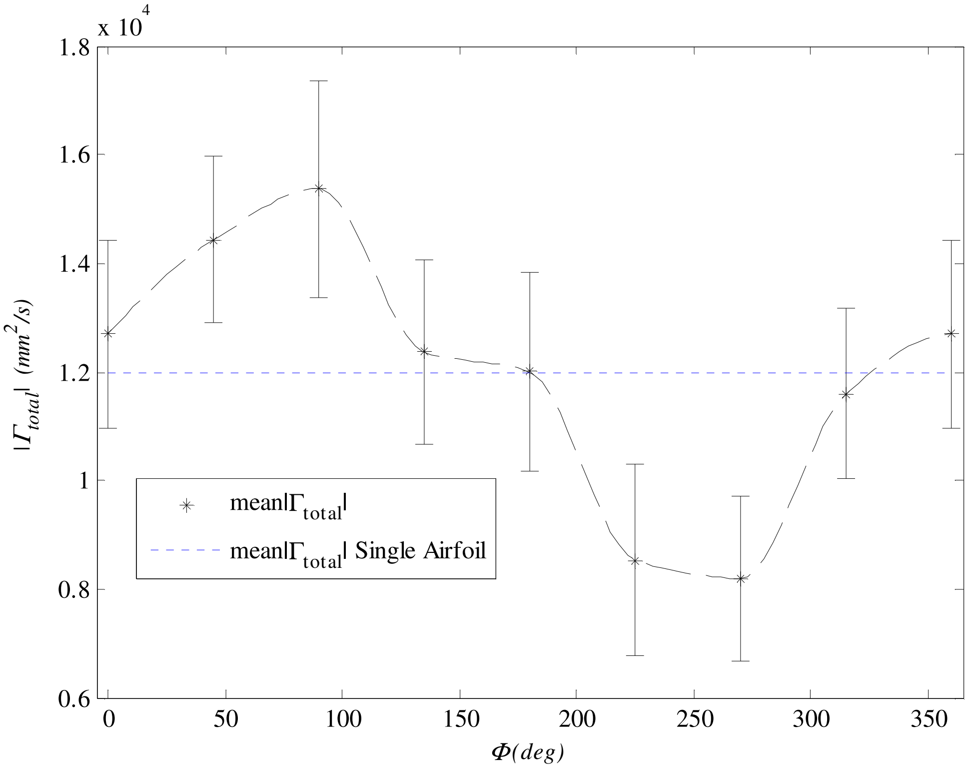

Figure 5.10:Total combined circulation from all of the strong vortices (Γ>500 (mm2/s)) averaged over 100 fields for each phase.

The average number of detected vortices under the given TIV for the 100 fields along with that of the single airfoil is shown in Figure 5.11. The error bars represent two standard deviations. The maximum number of vortices occurs at phase $\Phi = 180°$ and the minimum at $\Phi = 315°$. The highest vortex count occurring at $\Phi = 180°$ contributes to a higher total circulation since more vortices are being summed. This may also contribute to the secondary enhancement peak seen in Figure 5.8.

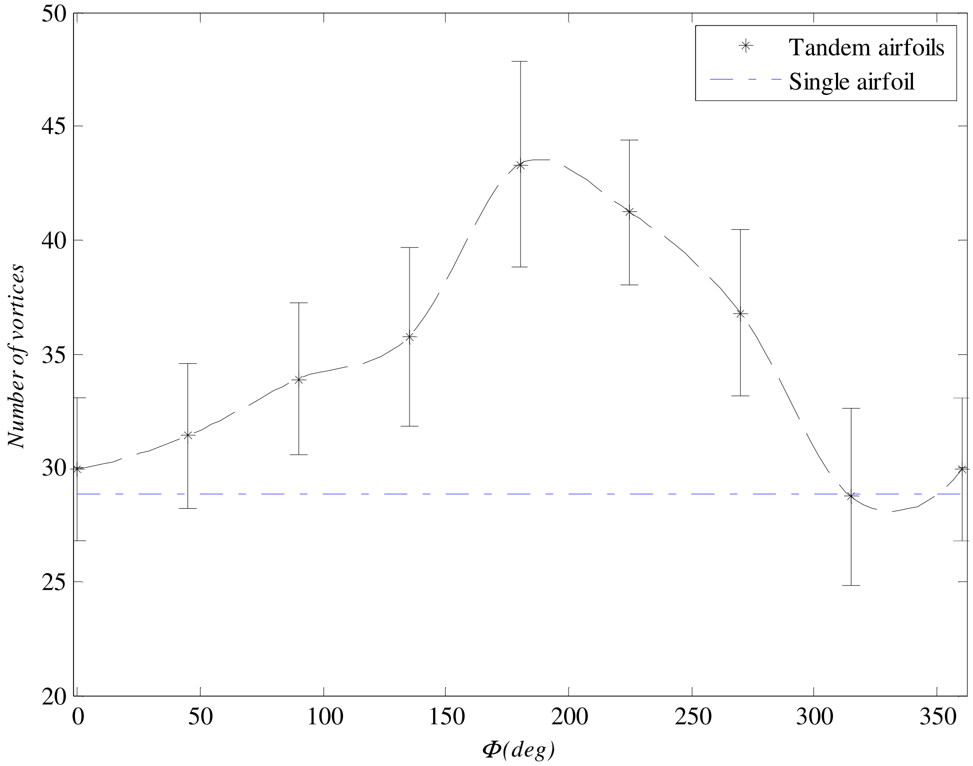

Figure 5.11: Average number of detected vortices vs. the phase of the hindfoil along with the average number of detected vortices for the single airfoil case

Wake type B

The phase averaged vorticity field obtained from 100 individual hindfoil wakes from wake **type B** is plotted in Figure 5.12 for phases $\Phi = 0°, 45°, 90°, 135°, 180°, 225°, 270°, 315°$. The vorticity threshold used in the vortex detection is identical to that of the single airfoil scenario and remains constant throughout the various phases.

A comparison with the single airfoil wake from Figure 5.5 provides preliminary evidence that the presence of the second airfoil can substantially alter the organization of the single airfoil wake. As with the previous wake, the highly unorganized nature of the near-field wake makes it difficult to study the evolution of a particular vortex through the various phases. However, after some finite streamwise distance the vortices cease to interfere with one another, as they are either absorbed constructively by vortices of similar sign, or destroyed by vortices of opposite sign (Gopalkrishnan et al., 1994). Beyond the near-field it becomes increasingly easy to track vortex evolution though the various phases. For example, the positive vortex at $x = -410$ mm inflates slightly from $\Phi = 0^\circ - 45^\circ$, then, at $\Phi = 90^\circ$ it splits into two distinct structures as it migrates slightly downstream. At $\Phi = 135^\circ$, it reaches maximum size and its peak vorticity is noticeably reduced. At $\Phi = 270^\circ$, it continues to shrink in size and peak vorticity all while steadily migrating downstream until it disappears at $\Phi = 315^\circ$.

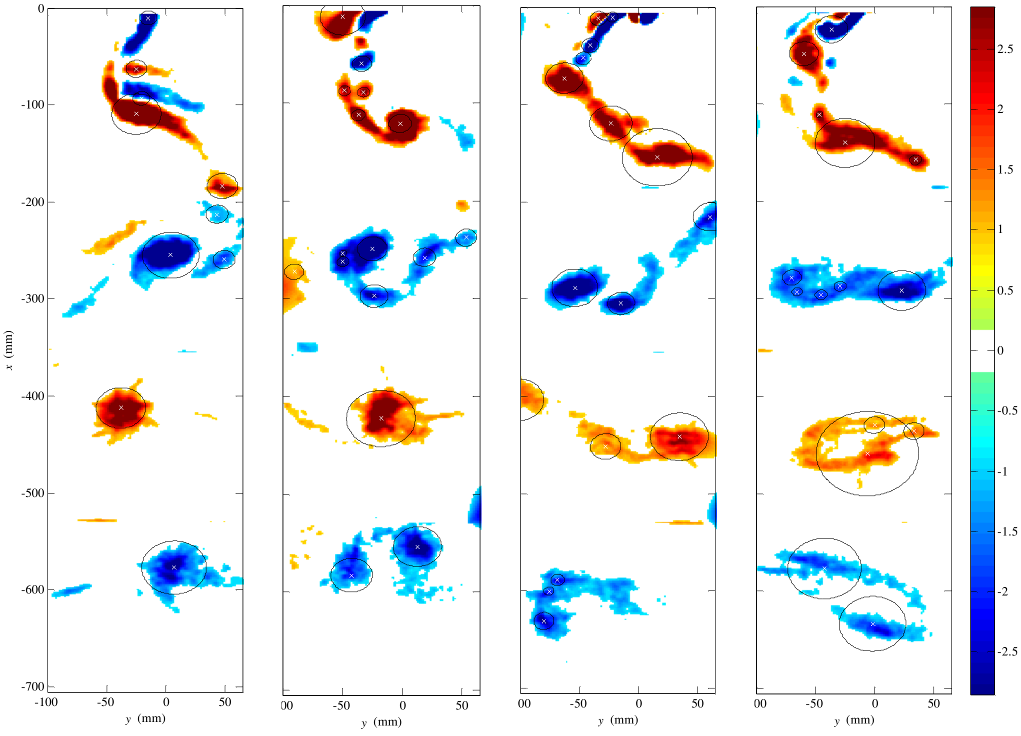

$\Phi = 0^\circ$ $\Phi = 45^\circ$ $\Phi = 90^\circ$ $\Phi = 135^\circ$

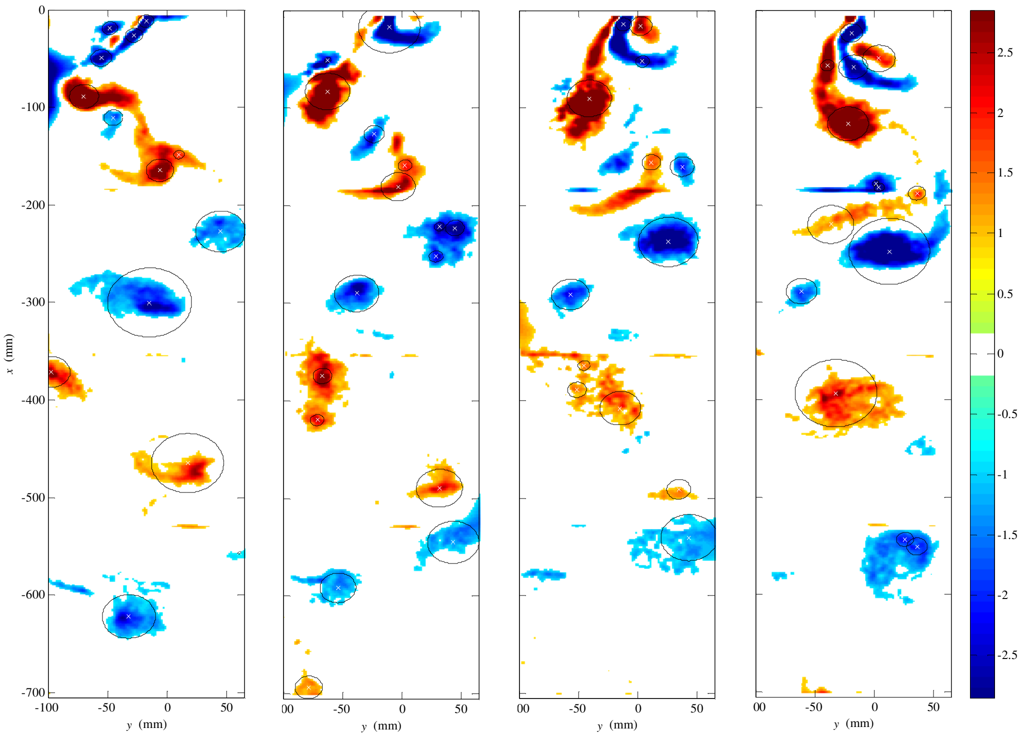

$\Phi = 180°$ $\Phi = 225°$ $\Phi = 270°$ $\Phi = 315°$

Figure 5.12: Vorticity field behind the hindfoil of wake type B for 8 phases $\Phi = 0° - 315°$ with detected vortex cores plotted as white x's and boundary radii as black circles.

The total contribution of circulation from all the vortices, computed from *eqn. (5.1)* is averaged over 100 fields and plotted for each of the phases. This along with a cubic interpolated curve and that for the single airfoil case is shown in Figure 5.13. The error bars represent two standard deviations in the data.

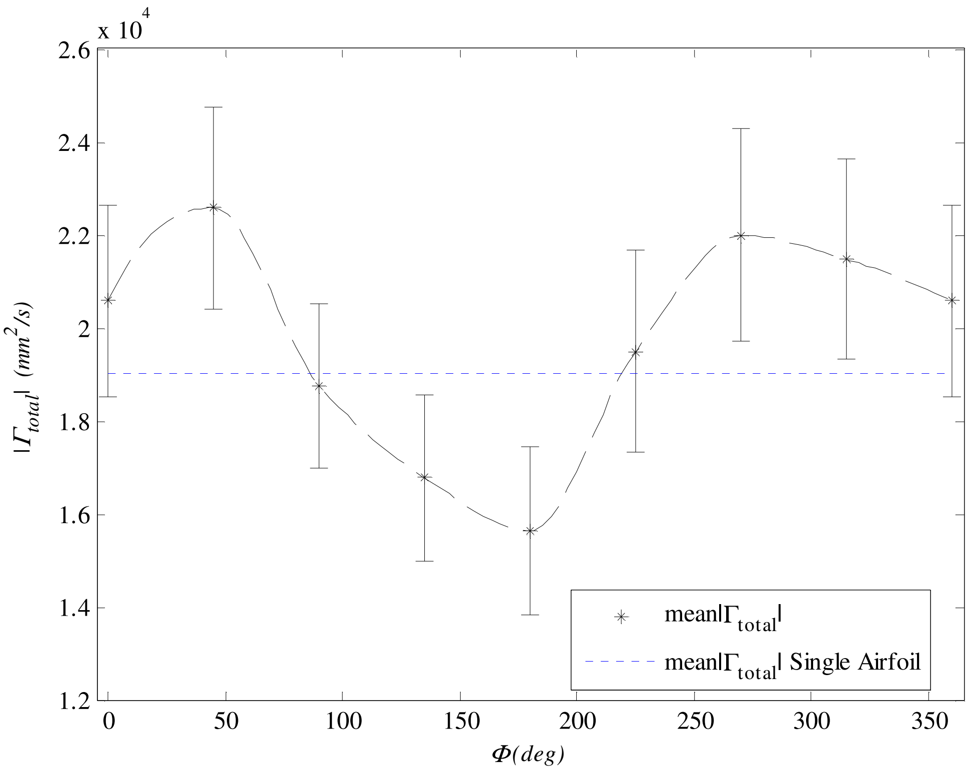

Figure 5.13: Total combined circulation from all of the vortices averaged over 100 fields for each phase along with that of the single airfoil case.

Maximum vortex suppression occurs at phase $\Phi = 180°$, maximum vortex enhancement occurs at $\Phi = 45°$ and a secondary enhancement peak appears at $\Phi = 270°$. Similar to wake **type A**, the secondary enhancement peak may be attributed to enhancement of weak vortices. To verify this, Figure 5.14 shows the total circulation of weak vortices with $\Gamma \leq 500$ mm^2/s. Now a clear peak is visible at $\Phi = 270°$ and this is likely responsible for the secondary enhancement peak seen at the same phase in Figure 5.13.

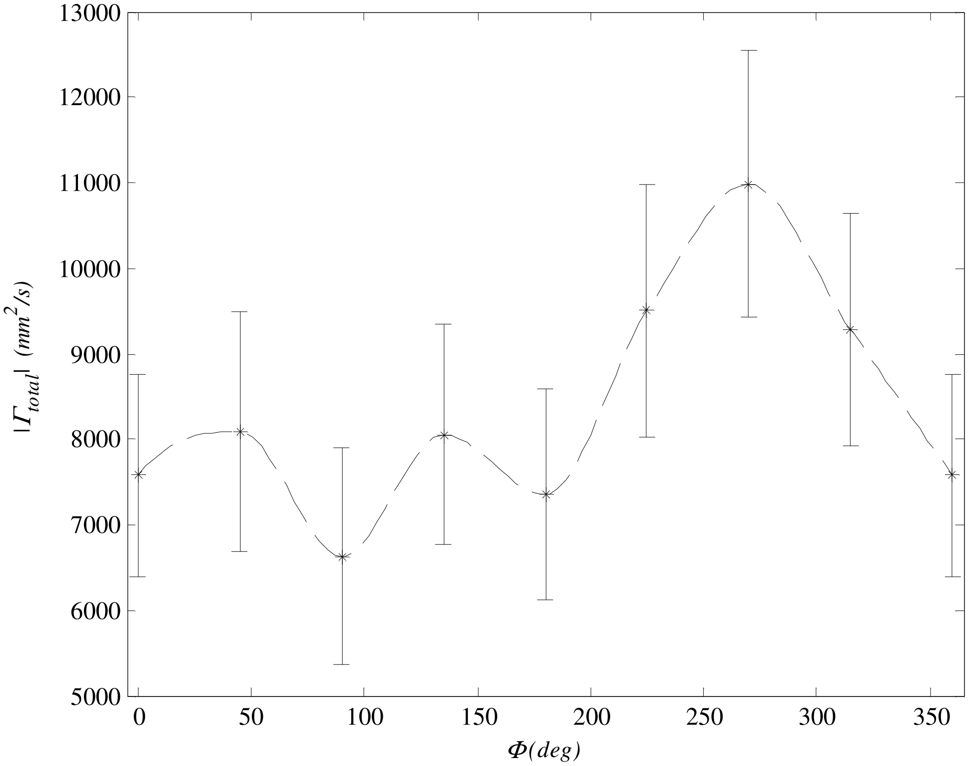

Figure 5.14: Total combined circulation from all of the weak vortices ($\Gamma \leq 500$ (mm^2/s)) averaged over 100 fields for each phase.

To reinforce this, only the total circulation of strong vortices having $\Gamma > 500$ mm^2/s is shown in Figure 5.15. The secondary peak at $\Phi = 270°$ seen in Figure 5.13 is not present and the curve has well defined maximum and minimum total circulation at $\Phi = 45°$ and $\Phi = 180°$ respectively.

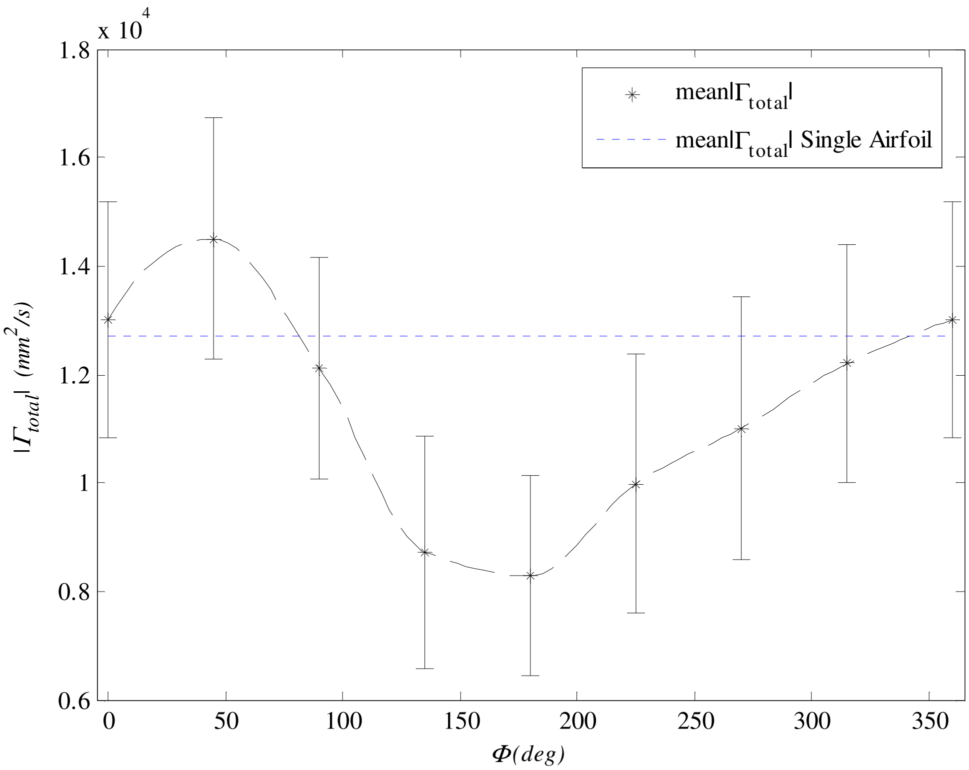

Figure 5.15:Total combined circulation from all of the strong vortices (Γ>500 (mm2/s)) averaged over 100 fields for each phase.

The distinction between weak leading edge and strong trailing edge vortices for wake **type B** was less apparent than it was in the previous wake scheme. Wake **type A** was clearly identified as a 2P+2SvK wake (Schnipper et al., 2009) in which precisely two pairs (2P) of leading edge vortices were shed per oscillation cycle. They were neatly staggered on either side of the stronger von Karman vortices (2S) making it relatively easy to identify them and to select a suitable circulation cutoff Γ_{cut}. Due to the much higher oscillation amplitude, the leading edge vortices in wake **type B** appear to be randomly distributed and tightly spaced around the trailing edge vortices making it more challenging to select an appropriate value for Γ_{cut}. However, the two wake schemes have similar vorticity magnitude, and therefore, $\Gamma_{cut} = 500$ mm^2/s was deemed a suitable choice for wake **type B** as well.

The average number of detected vortices under the given TIV for the 100 fields along with that of the single airfoil is shown in Figure 5.16. The error bars represent two standard deviations. The maximum number of vortices occurs at phase $\Phi = 270°$ and the minimum at $\Phi = 90°$. This figure resembles Figure 5.14 suggesting that the significant increase in vortex count at $\Phi = 270°$ may be the result of an increase in the circulation of weak vortices. Or alternatively, rather than enhancing the weak vortices at $\Phi = 270°$, there are simply more of them appearing in the wake ultimately contributing to a higher total circulation at that phase.

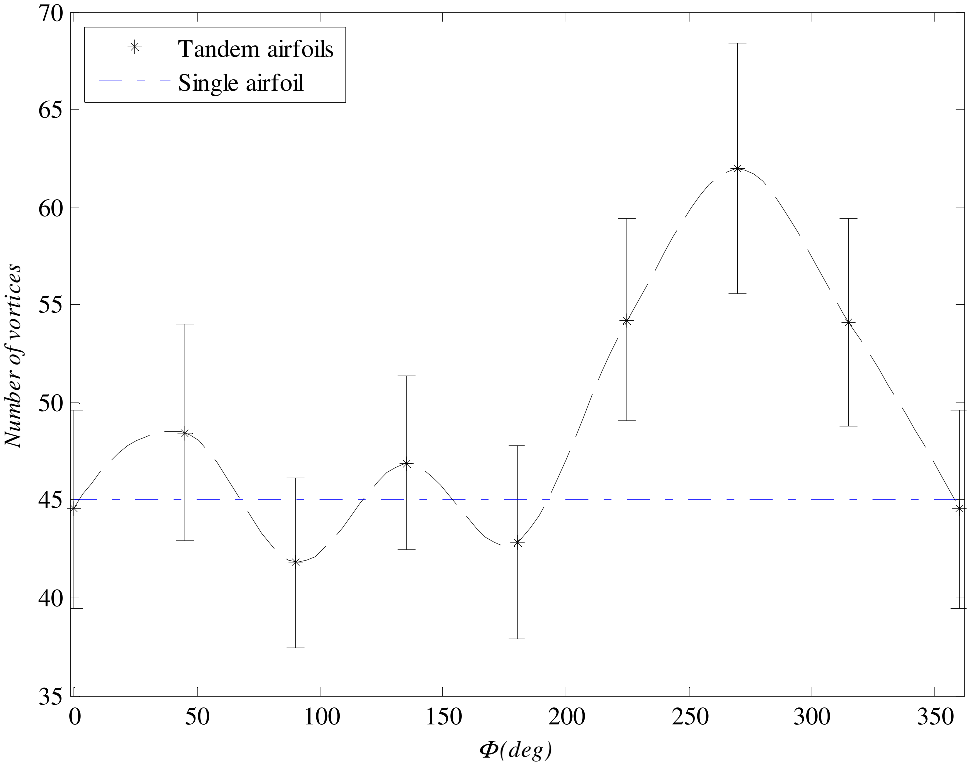

Figure 5.16: Average number of detected vortices vs. the phase of the hindfoil along with the average number of detected vortices for the single airfoil case

5.5 *Differential pressure*

A time dependant voltage output V_{pm}, generated by the differential pressure measured across the pressure membranes, was recorded in real time over 1500 s for each of the various tandem wing phases. Future work aims to distinguish the various pressure signals and attempts to assign them to a unique signature which could later be used to identify the phase difference between the hindfoil and the forefoil if the forefoil motion is unknown.

5.5.1 Signal processing

A Chebyshev type II filter was used to remove high frequency noise in the pressure data. The noise originates from pump-motor vibrations and the 60 Hz grid frequency. The data was collected with a sampling period of $P_s = 2 \times 10^{-4}$s. Smooth operation of the stepper motors requires sufficiently high sample rates, but in order to respect the data storage limitations, data is only collected every 25 samples (referred to as down sampling with $D_s = 25$). This leads to a sample frequency of $f_s = 1/(P_s D_s) = 200$ Hz. A filter of order $N = 10$ was chosen as the lowest order digital Chebyshev type II filter that drops no more than $R_p = 3$ dB in the passband and has a stopband with least $R_s = 80$ dB of attenuation. The passband and stopband edge frequencies, normalized from 0 to 1 (1 corresponds to π radians/sample) are $W_p = 5/(f_s/2) = 0.05$ and $W_s = 8/(f_s/2) = 0.08$ respectively. The filter response is shown in Figure 5.17.

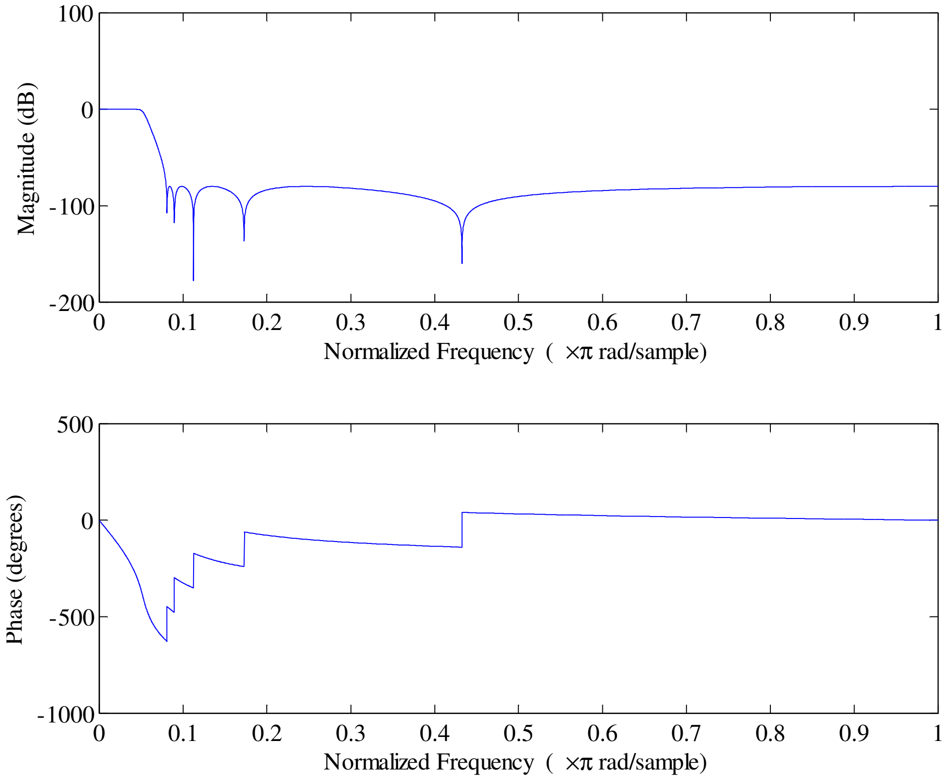

Figure 5.17: Filter response of the selected Chebyshev type II digital filter

5.5.2 Pressure signal

A sample signal V_p taken over 4 airfoil oscillation cycles for wake **types A** and **B** are shown in Figure 5.18 and Figure 5.19 respectively. The sample signals are generated for phases $\Phi = 0°$, $\Phi = 45°$, $\Phi = 90°$, $\Phi = 135°$, $\Phi = 180°$, $\Phi = 225°$, $\Phi = 270°$, and $\Phi = 315°$. The angular position of the hindfoil is shown in blue only for reference and hence its units (degrees) are not shown. They may however be inferred since the amplitude of oscillation is known for both wake regimes.

The signals are comprised of a low frequency, high amplitude component $V_{p,lf}$ and a higher frequency, lower amplitude component $V_{p,hf}$. The total signal is believed to be a linear combination of the two expressed as $V_p = V_{p,lf} + V_{p,hf}$. It is proposed that the low frequency component of the signal is caused by the sinusoidal pitching motion of the hindfoil and that the high frequency component is caused by the vortices generated by the forefoil and the leading edge of the hindfoil. The V_{lf} component is likely the result of the pressure membranes dynamically changing their orientation relative to the upstream flow as the hindfoil oscillates. The $V_{p,hf}$ signal is more difficult to analyze and is the component which makes V_p unique for each phase.

In addition to the shape of the V_p signal, its amplitude also varies according to the phase. The largest pk-pk amplitude of V_p for wake **type A** occurs for $\Phi = 0°$, and the smallest for $\Phi = 180°$. Similarly, The largest pk-pk amplitude of V_p for wake **type B** occurs for $\Phi = 270°$, and the smallest for $\Phi = 90°$. For both wakes the maximum and minimum amplitudes occur 180° apart.

The various signals have distinct shape and amplitude. Therefore, they provide evidence supporting the notion that the phase difference between forefoil and hindfoil may be inferred based on the differential pressure measured across the hindfoil's aerodynamic center.

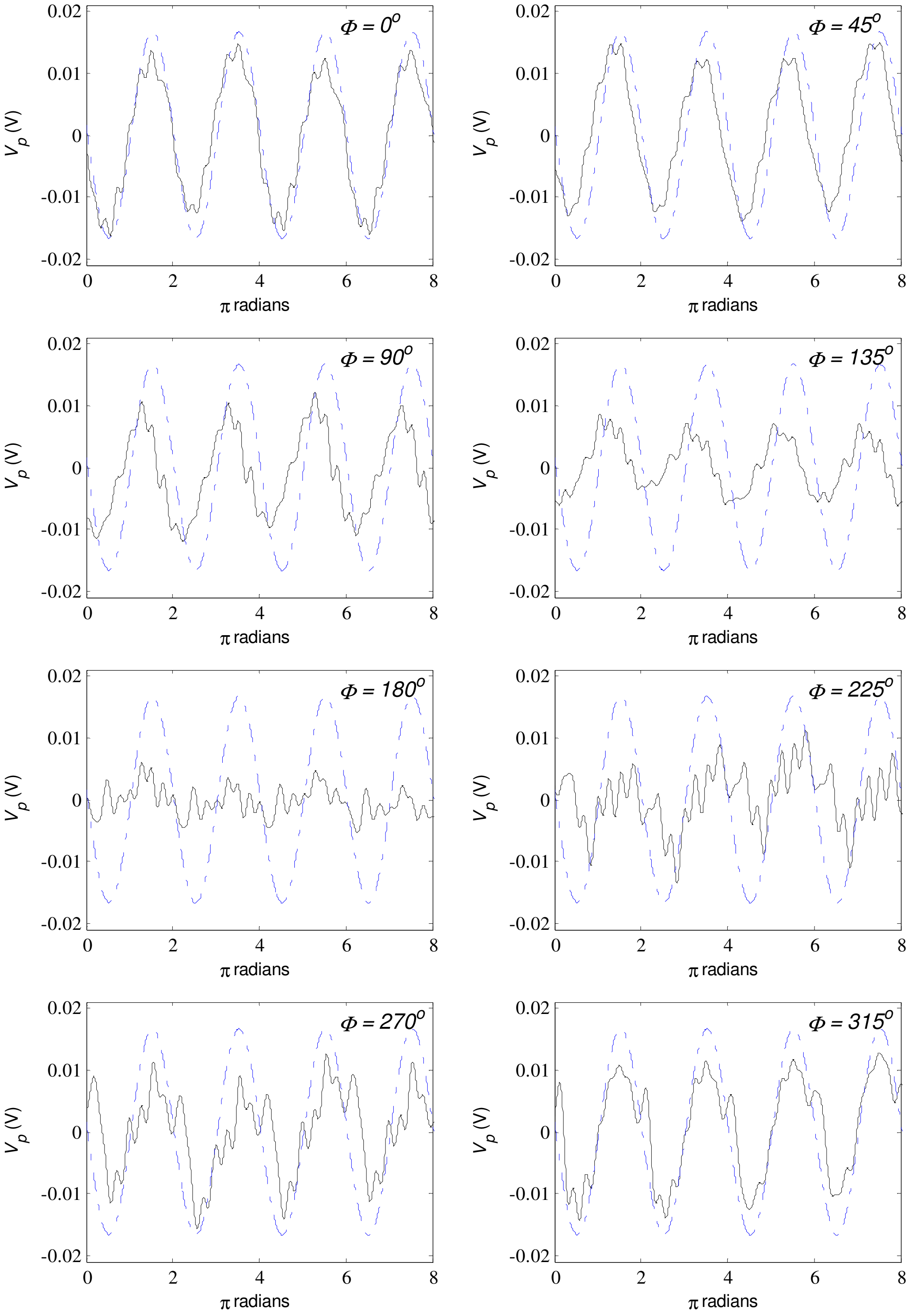

Figure 5.18: Pressure membrane voltage output for various phases for wake type A plotted with the angular position of the hindfoil

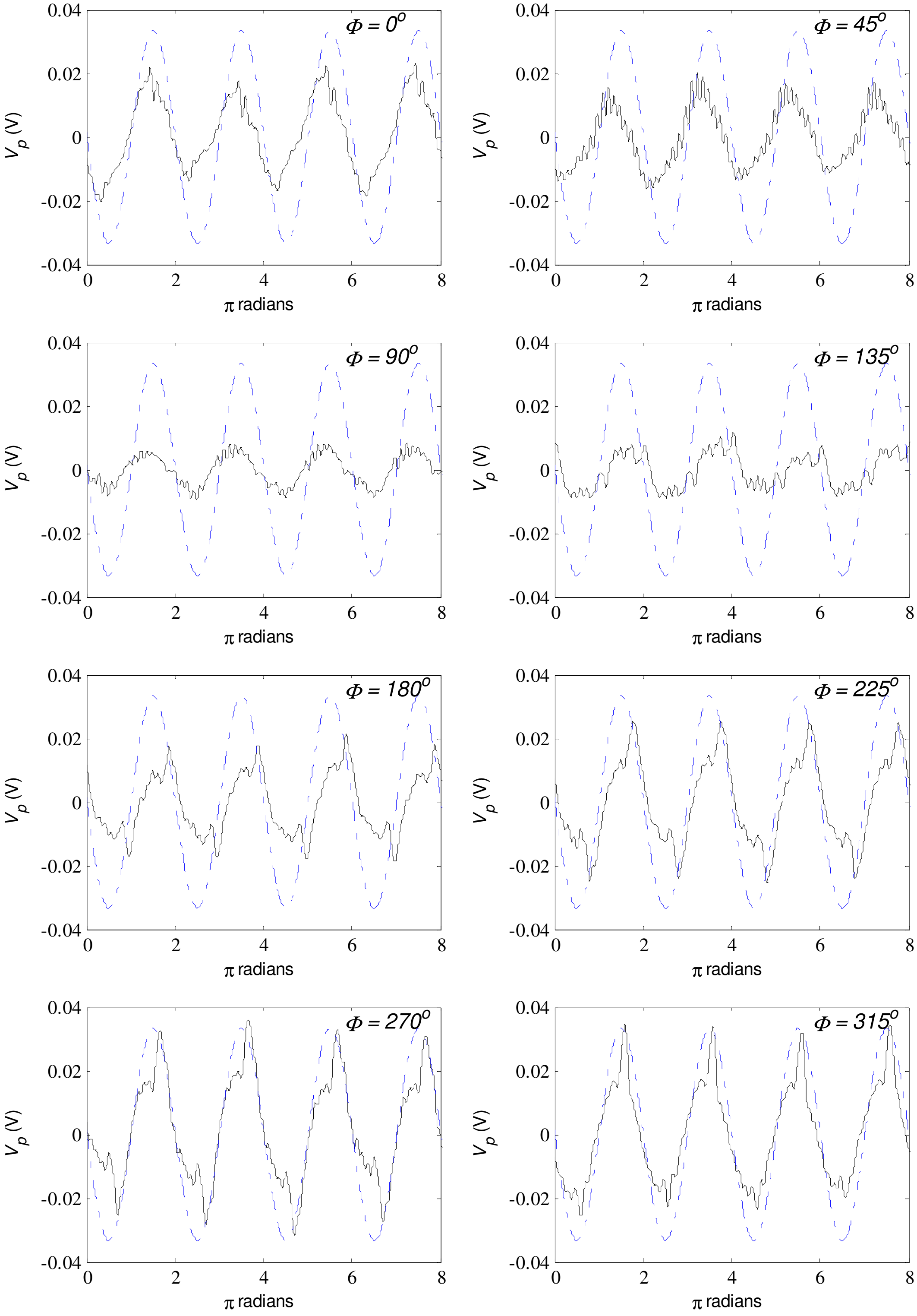

Figure 5.19:Pressure membrane voltage output for various phases for wake type B plotted with the angular position of the hindfoil

5.6 Conclusions

Two identical tandem airfoils were forced to pitch sinusoidally about their aerodynamic centers. The airfoils had the same oscillation frequency and amplitude, but the hindfoil phase relative to the forefoil was varied from 0° to 315° in increments of 45°. The effect of changing the phase was found to substantially modify the strength and arrangement of the hindfoil wake vortices when compared to the wake of the single airfoil. The overall vortex strength for a given wake was quantified by computing the sum of absolute circulation from all of the detected vortices in that wake. A higher value than the reference value obtained from the single airfoil scenario would suggest vortex enhancement and one lower than the reference value would suggest vortex suppression. In wake **type A**, the maximum vortex strength occurred at phase $\Phi = 90°$ and the minimum at phase $\Phi = 270°$. Similarly, in wake **type B** the maximum vortex strength occurred at phase $\Phi = 45°$ and the minimum at phase $\Phi = 180°$. In addition to the primary peaks, there were also smaller secondary peaks. These secondary peaks are believed to be caused by enhancement of leading edge vortices which occur at a different phases than enhancement of the, stronger, trailing edge vortices.

The differential pressure measured across the hindfoil's aerodynamic centre produced a time dependant voltage output. This signal was shown to have a distinct waveform and amplitude for each of the 8 hindfoil phases. This supports the notion that such a signal could be used to deduce the phase difference between the 2 airfoils and ultimately operate in a closed-loop control system.

CHAPTER 6: Conclusions and future work

6.1 Summary

The ability to actively control large coherent vortices in the wake of an unsteady body was studied experimentally. An upstream airfoil produces a predictable and well studied wake which an identical downstream airfoil attempts to actively modify in some prescribed manner. Oscillation of a single airfoil is first characterized and the vortex wake is compared to an analytical model. This section serves to gain an understanding of vortex evolution independent of the control airfoil. The experiments take place in a closed circuit re-circulating water channel and flow measurements are undertaken primarily using the particle image velocimetry (PIV) measurement technique. Custom vortex detection software is developed so that vortices may be accurately identified and characterized in the experimental data.

The flow facility used consisted of an open re-circulating water channel. The airfoils hung vertically into the waterchanel and were driven about the aerodynamic center with micro-stepping motors. The flow was characterized with a commercial PIV system comprising of four dual-frame CCD cameras for imaging, a 2 pulse Nd:YAG laser for illumination and neutrally buoyant hollow glass spheres as seed particles. The raw PIV images were subjected to image preprocessing and the raw vector fields are computed with a multi-pass cross-correlation performed with commercial software (Davis 8.05, LaVision). The raw vector fields were then post processed with the median test to remove spurious vectors. Finally, the 4 individual vector fields were stitched together using custom software and the resulting vector field was further smoothed with a Gaussian low-pass filter.

A vortex detection and characterization algorithm was developed and tested on 2C2D velocity vector fields which characterize the vortex wake of an oscillating airfoil. Vortex detection in experimental data was particularly challenging as it is often accompanied by measurement uncertainty and noise (Saikrishnan, et al. 2006). The high gradients that exist near the centre of the vortex can lead to seeding and correlation issues (Vollmers, 2001). The resulting detection algorithm combined of 3 separate methods in order to automatically interpret the experimental data and to reliably identify the vortical structures. Vorticity and circumferential velocity profile plots confirmed that the CSL algorithm can accurately locate a vortex core, define a vortex boundary radius and to compute its vortex drift velocity. The WA algorithm proved to be a useful automated verification method for recognizing and eliminating false positives diagnosis.

The vortex wake of a single oscillating NACA 0012 airfoil was first investigated. Amplitude and frequency of the airfoil oscillation were found to substantially alter the characteristics of a vortex wake. A *Re* independent phase map served to categorize the wakes and predict, based on dimensionless amplitude and frequency, whether they belong to a von Karman, an aligned, an inverted von Karman or an asymmetric inverted von Karman wake. PIV was then performed for select points on the phase map embodying the important wake transitions. Relevant vortex parameters assessed were; circulation Γ, peak vorticity ω_{peak}, vortex boundary radii r_v, vortex streamwise drift velocity v_{drift}, streamwise vortex spacing S_x and transverse vortex spacing S_y. The PIV results were used to study vortex cross-sectional profiles which provided evidence that validated the Burgers vortex model and led to the derivation of an analytical model for predicting the peak vorticity decay of a vortex. The data agrees with the analytical model for some finite range $x/C <$ ONFR. Where ONFR is the streamwise coordinate defining the limit of the organized near field region of the wake. The spatial organization of vortices in this region is visibly more consistent than it is further downstream. The transverse and streamwise spacing is more regular and the boundary radii inflate at a steady rate. Time resolved wake profiles showed the transitions from drag inducing wakes, to thrust producing wakes. These transitions were found to agree with the qualitative wake transitions between the von Karman, the aligned and the inverted von Karman wakes.

Two identical tandem airfoils were forced to pitch sinusoidally. The hindfoil phase relative to the forefoil was varied in increments of 45°. The effect of changing the phase was found to significantly alter the strength and arrangement of the hindfoil wake vortices. The overall vortex strength for a given wake was quantified by computing the sum of absolute circulation from all of the detected vortices in that wake. This revealed a peak corresponding to maximum vortex enhancement and a crest corresponding to maximum vortex suppression. Finally, a time dependant voltage output signal was obtained from the differential pressure measured across the hindfoil's aerodynamic centre. This signal was shown to have a distinct waveform and pk-pk amplitude for each of the eight hindfoil phases. This supports the perception that such a signal could be used to infer the phase difference between the two airfoils. This signal, or a modified version of it, could potentially be used in a closed-loop control algorithm which attempts to either suppress or enhance the total absolute vortex form an unknown source.

6.2 Future work

Future work in vortex detection consists of improvements to its automation and its ability to accept true negatives. Currently the TIV is selected manually. An automated process in which the TIV is optimized could be developed in the future. This process could be based either on the maximum and minimum absolute vorticity, or alternatively, on some optimization curve generated from multiple TIV values. In the CSL portion of the algorithm, a second choice for the core coordinate could be computed. In the event that a ROI is rejected in the WA algorithm, a second set of streamlines could be generated from a reference frame moving with the second choice core. Such an improvement could lead to enhanced ability to accept true negatives. Finally, in order to test these improvements, a statistical assessment of the vortex detection algorithm should be performed. This would lead to a comparison between the algorithm and the individual algorithms in efforts to understand the advantages of using a combinatorial approach for vortex detection in experimental data.

Future work in the characterization of a single airfoil should include performing stereo PIV. This would produce 3C2D velocity fields rather than

2C2D ones and would allow for the investigation of the axial velocity gradient $\partial w/\partial z$ which, in *chapter 4,* was inferred from the analytical model. Other work would consist of computing drag and thrust predictions based on the time averaged velocity profiles in the wake immediately behind the trailing edge of the airfoil. Finally single frame PIV cross-correlation could lead to time resolved vector fields. These could ultimately lead to experimental data describing the time evolution of a single vortex.

Future work for the wake characterization of two airfoils in tandem focuses mainly on correlating the pressure signal V_p to its respective hindfoil wake. This would make it possible to infer the phase difference between the 2 airfoils with only the pressure voltage signal. This correlated signal, coupled with the discoveries related to maximum vortex enhancement phase and maximum vortex suppression phase, could be used to develop a close-loop control algorithm. This algorithm would ultimately be responsible for either enhancing or suppressing vortices that are shed from an upstream airfoil with unknown motion. Other future work could include measuring thrust and drag on the hindfoil and studying the how it is affected by changing the phase. Finally, in addition to different phases between the airfoils, the effect of changing the hindfoil amplitude relative to that of the forefoil could be investigated.

REFERENCES

Adrian, R. J., & Westerweel, J. (2011). *Particle Image Velocimetry* (1st ed., p. 558). Cambridge University Press.

Akaydin, H. D., Elvin, N., & Andreopoulos, Y. (2010). Energy Harvesting from Highly Unsteady Fluid Flows using Piezoelectric Materials. *Journal of Intelligent Material Systems and Structures*, *21*(13), 1263-1278. doi:10.1177/1045389X10366317

Akilli, H., Sahin, B., & Filiztumen, N. (2005). Suppression of vortex shedding of circular cylinder in shallow water by a splitter plate. *Flow Measurement and Instrumentation*, *16*(4), 211-219. doi:10.1016/j.flowmeasinst.2005.04.004

Ari Sadarjoen, I. (2000). Detection, quantification, and tracking of vortices using streamline geometry. *Computers & Graphics*, *24*(3), 333-341. doi:10.1016/S0097-8493(00)00029-7

Bohl, D. G., & Koochesfahani, M. M. (2009). MTV measurements of the vortical field in the wake of an airfoil oscillating at high reduced frequency. *Journal of Fluid Mechanics*, *620*, 63. doi:10.1017/S0022112008004734

Brown, D. A. R., Jones, P. I. P. N., Middleton, J. C., & Jones, P. N. (n.d.). *Part A□: Measuring Tools and Techniques for Mixing and Flow Visualization Studies*.

Drazin, P. G., & Riley, N. (2006). *The Navier-Stokes Equations: a classification of flows and exact solutions*. *Representation Theory*. Cambridge University Press.

Giaiotti, D. B., & Stel, F. (2006). *The Rankine Vortex Model*. *October*. University of Trieste.

Gibbon, J. (1999). Dynamically stretched vortices as solutions of the 3D Navier–Stokes equations. *Physica D: Nonlinear Phenomena*, *132*(4), 497-510. doi:10.1016/S0167-2789(99)00067-6

Godoy-Diana, R., Marais, C., Aider, J.-L., & Wesfreid, J. E. (2009). A model for the symmetry breaking of the reverse Bénard–von Kármán vortex street produced by a flapping foil. *Journal of Fluid Mechanics*, *622*, 23. doi:10.1017/S0022112008005727

Gopalkrishnan, R., Triantafyllou, M. S., Triantafyllou, G. S., & Barrett, D. (1994). Active vorticity control in a shear flow using a flapping foil. *J. Fluid Mech.*, 1-21.

Gostelow, J. P., Platzer, M. F., & Carscallen, W. E. (2006). On Vortex Formation in the Wake Flows of Transonic Turbine Blades and Oscillating Airfoils. *Journal of Turbomachinery*, *128*(3), 528. doi:10.1115/1.2184354

Honkanen, M., & Nobach, H. (2005). Background extraction from double-frame PIV images. *Experiments in Fluids*, *38*(3), 348-362. doi:10.1007/s00348-004-0916-x

Jeong, J., & Hussain, F. (2006). On the identification of a vortex. *Journal of Fluid Mechanics*, *285*(-1), 69. doi:10.1017/S0022112095000462

Jiang, M. (2002). *Detection and Visualization of Vortices*. Ohio State University.

Jukes, T., & Choi, K. (2009). Active Control of a Cylinder Wake Using Surface Plasma. *IUTAM Symposium on Unsteady Separated Flows and their Control,* (pp. 539-550).

Jung, Y., & Park, S. (2005). Vortex-shedding characteristics in the wake of an oscillating airfoil at low Reynolds number. *Journal of Fluids and Structures*, *20*(3), 451-464. doi:10.1016/j.jfluidstructs.2004.11.002

Keles, R. S. (2002). Active Control of Vortex Shedding in the Far Wake of a Cylinder. *15th ASCE Engineering Mechanics Conference*.

Kwon, K., & Choi, H. (1996). Control of laminar vortex shedding behind a circular cylinder using splitter plates. *Physics of Fluids*, *8*(2), 479. doi:10.1063/1.868801

Lai, J. C. S., & Platzer, M. F. (1999). Jet Characteristics of a Plunging Airfoil. *AIAA Journal*, *37*(12), 1529-1537. doi:10.2514/2.641

Lugt, H. J. (1979). The Dilemma of Defining a Vortex. In U. Müller, K. G. Riesner, & B. Schmidt (Eds.), *Recent Developments in Theoretical and Experimental Fluid Mechanics* (pp. 309-321). Springer.

Madej, A., Babazadeh, H., & Nobes, D. S. (2011). The effect of chamber length and Reynolds number on jet precession. *Experiments in Fluids*, *51*(6), 1623-1643. doi:10.1007/s00348-011-1177-0

Madej, A. M. (2010). *The Experimental Investigation of the Effect of Chamber Length on Jet Precession*. University of Alberta.

Moin, P., & Mahesh, K. (1998). Direct Numerical Simulation: A Tool in Turbulence Research. *Annu. Rev. Fluid Mech.*

Muddada, S., & Patnaik, B. S. V. (2010). An active flow control strategy for the suppression of vortex structures behind a circular cylinder. *European Journal of Mechanics - B/Fluids*, *29*(2), 93-104. Elsevier Masson SAS. doi:10.1016/j.euromechflu.2009.11.002

Nelson, J. M. (2010). *Using Piezoelectric Generation to Harvest Energy From Turbulent Air Flow*. *Policy*. Purdue University.

Ozen, C. a., & Rockwell, D. (2010). Control of vortical structures on a flapping wing via a sinusoidal leading-edge. *Physics of Fluids*, *22*(2), 021701. doi:10.1063/1.3304539

Pagendarm, H.-G., Henne, B., & Rutten, M. (1999). Detecting vortical phenomena in vector data by medium-scale correlation. *Proceedings Visualization '99 (Cat. No.99CB37067)*, 409-552. Ieee. doi:10.1109/VISUAL.1999.809917

Perry, A. E., & Chong, M. S. (1996). Interpretation of flow visualization. *Flow Visualization: Techniques and Examples* (pp. 1-26).

Ponta, F. L. (2010). Vortex decay in the Kármán eddy street. *Physics of Fluids*, *22*(9), 093601. doi:10.1063/1.3481383

Portela, L. M. (1999). *Identification and characterization of vortices in the turbulent boundary layer*. Stanford University.

Prochazka, A., & Pullin, D. I. (1998). Structure and stability of non-symmetric Burgers vortices. *Journal of Fluid Mechanics*, *363*, 199-228. doi:10.1017/S0022112098008866

Raffel, M., Willert, C., Wereley, S., & Kompenhans, J. (1998). *Particle image velocimetry: A practical guide*. New York, NY: Springer-Verlag.

Robinson, S. K. (1991). Coherent Motions in the Turbulent Boundary Layer. *Annual Review of Fluid Mechanics*, *23*(1), 601-639. doi:10.1146/annurev.fl.23.010191.003125

Roussopoulos, K. (2006). Feedback control of vortex shedding at low Reynolds numbers. *Journal of Fluid Mechanics*, *248*(-1), 267. doi:10.1017/S0022112093000771

Saikrishnan, N., Marusic, I., & Longmire, E. K. (2006). Assessment of dual plane PIV measurements in wall turbulence using DNS data. *Experiments in Fluids*, *41*(2), 265-278. doi:10.1007/s00348-006-0168-z

Sarkar, S., & Venkatraman, K. (2006). Numerical simulation of thrust generating flow past a pitching airfoil. *Computers & Fluids*, *35*(1), 16-42. doi:10.1016/j.compfluid.2004.10.002

Schnipper, T., Andersen, A., & Bohr, T. (2009). Vortex wakes of a flapping foil. *Journal of Fluid Mechanics*, *633*, 411. doi:10.1017/S0022112009007964

Seidel, J., Siegel, S., Fagley, C., Cohen, K., & McLaughlin, T. (2009). Feedback control of a circular cylinder wake. *Proceedings of the Institution of Mechanical Engineers, Part G: Journal of Aerospace Engineering*, *223*(4), 379-392. doi:10.1243/09544100JAERO407

Shukla, S., Govardhan, R. N., & Arakeri, J. H. (2009). Flow over a cylinder with a hinged-splitter plate. *Journal of Fluids and Structures*, *25*(4), 713-720. Elsevier. doi:10.1016/j.jfluidstructs.2008.11.004

Strawn, R. C., Kenwright, N. D., & Ahmad, J. (1999). Computer Visualization of Vortex Wake Systems. *AIAA Journal*, *37(4)*, 511–512.

T.L. Hilderman. (2004). *Measurement, modelling, and stochastic simulation of concentration fluctuations in a shear flow*. University of Alberta.

Tang, S., & Aubry, N. (2000). Suppression of Vortex Shedding Inspired By a Low-Dimensional Model. *Journal of Fluids and Structures*. doi:10.1006/j

Unal, M. F., & Rockwell, D. (2006). On vortex formation from a cylinder. Part 2. Control by splitter-plate interference. *Journal of Fluid Mechanics*, *190*(-1), 513. doi:10.1017/S0022112088001430

Vollmers, H. (2001). Detection of vortices and quantitative evaluation of their main parameters from experimental velocity data. *Measurement Science and Technology*, *12*, 1199-1207.

APPENDIX A: Instantaneous streaklines

Instantaneous streaklines characterizing the wake of the oscillating airfoil are generated by injecting a seed particle slurry into the pressure taps of the airfoil. The seed particles consist of 18µm diameter hollow glass spheres and create a dense locust of points which effectively map out streaklines for the given flow field. A laser pulse freezes the motion and illuminates the particles while 4 overhead CCD cameras take instantaneous pictures. The four images are de warped, then stitched together with calibrated offsets to produce one single image. These images are studied and tagged as one of the following wake types: von Karman, Aligned, inverted von Karman, inverted asymmetric von Karman.

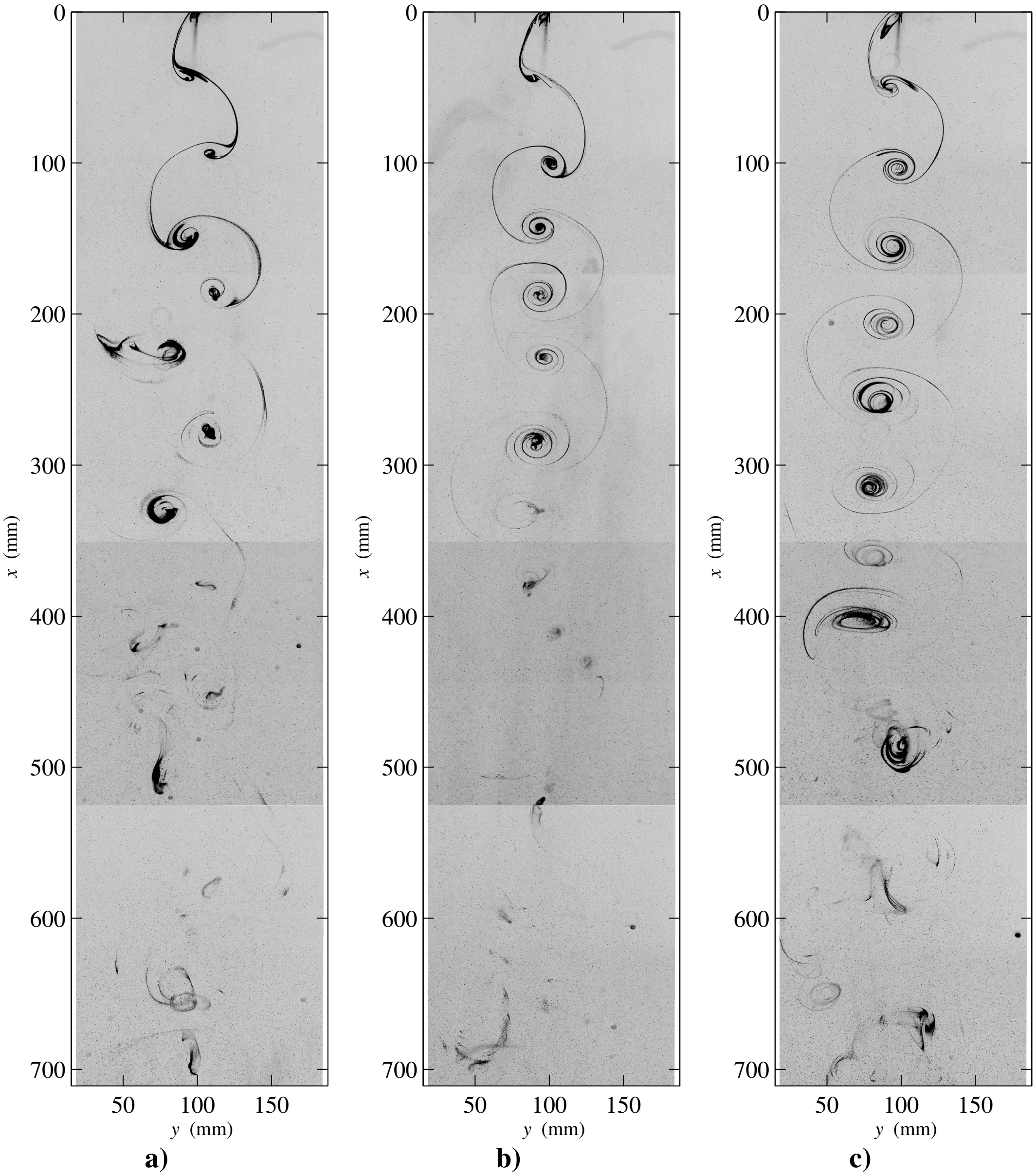

Figure A.1: Instantaneous Streaklines for a) frequency of 1 rad/s and amplitude of 7degrees, b) frequency of 1 rad/s and amplitude of 8degrees and c) frequency of 1 rad/s and amplitude of 10degrees

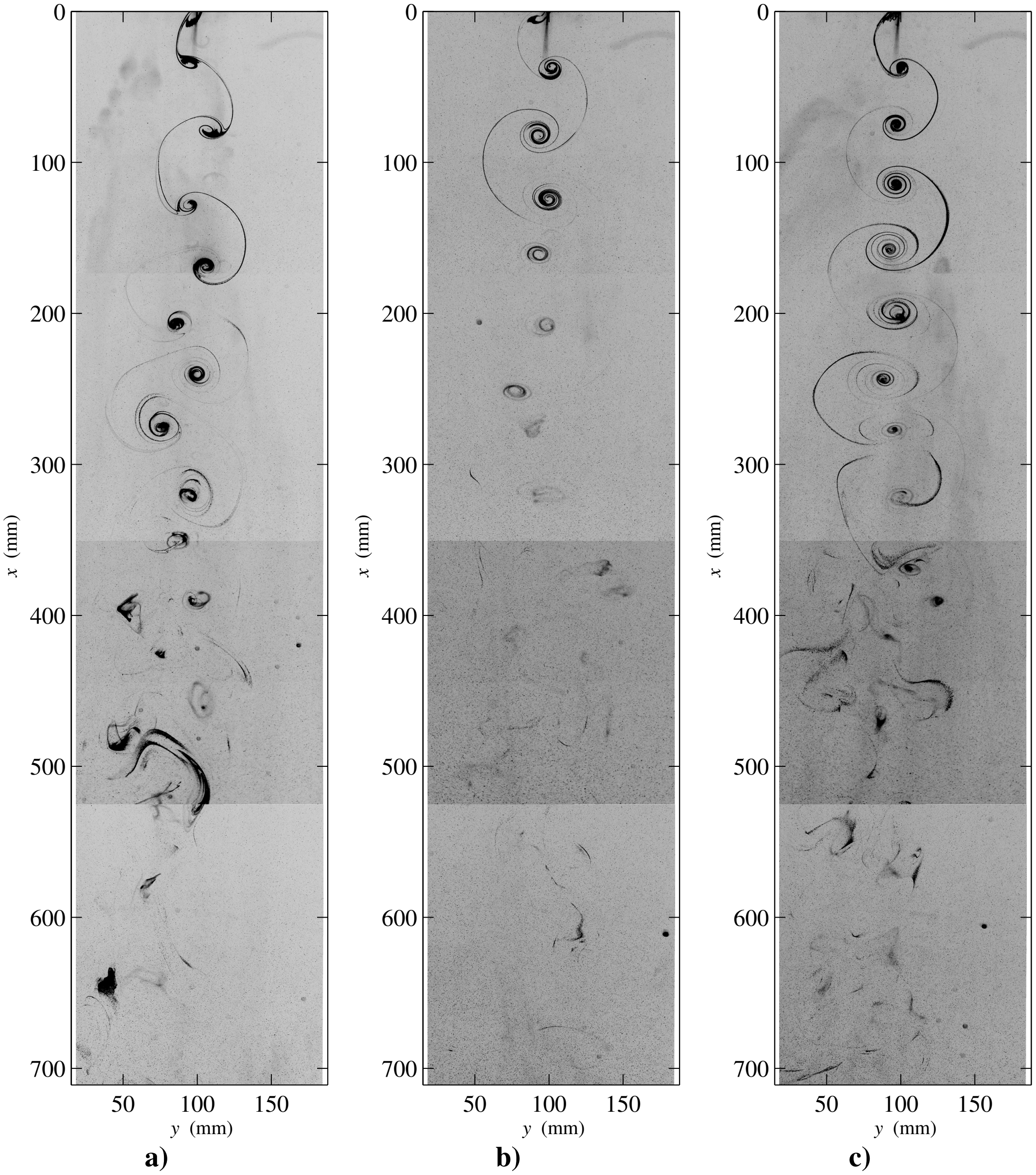

Figure A.2: Instantaneous Streaklines for a) frequency of 1.2 rad/s and amplitude of 6degrees, b) frequency of 1.25 rad/s and amplitude of 10 degrees and c) frequency of 1.3 rad/s and amplitude of 8degrees

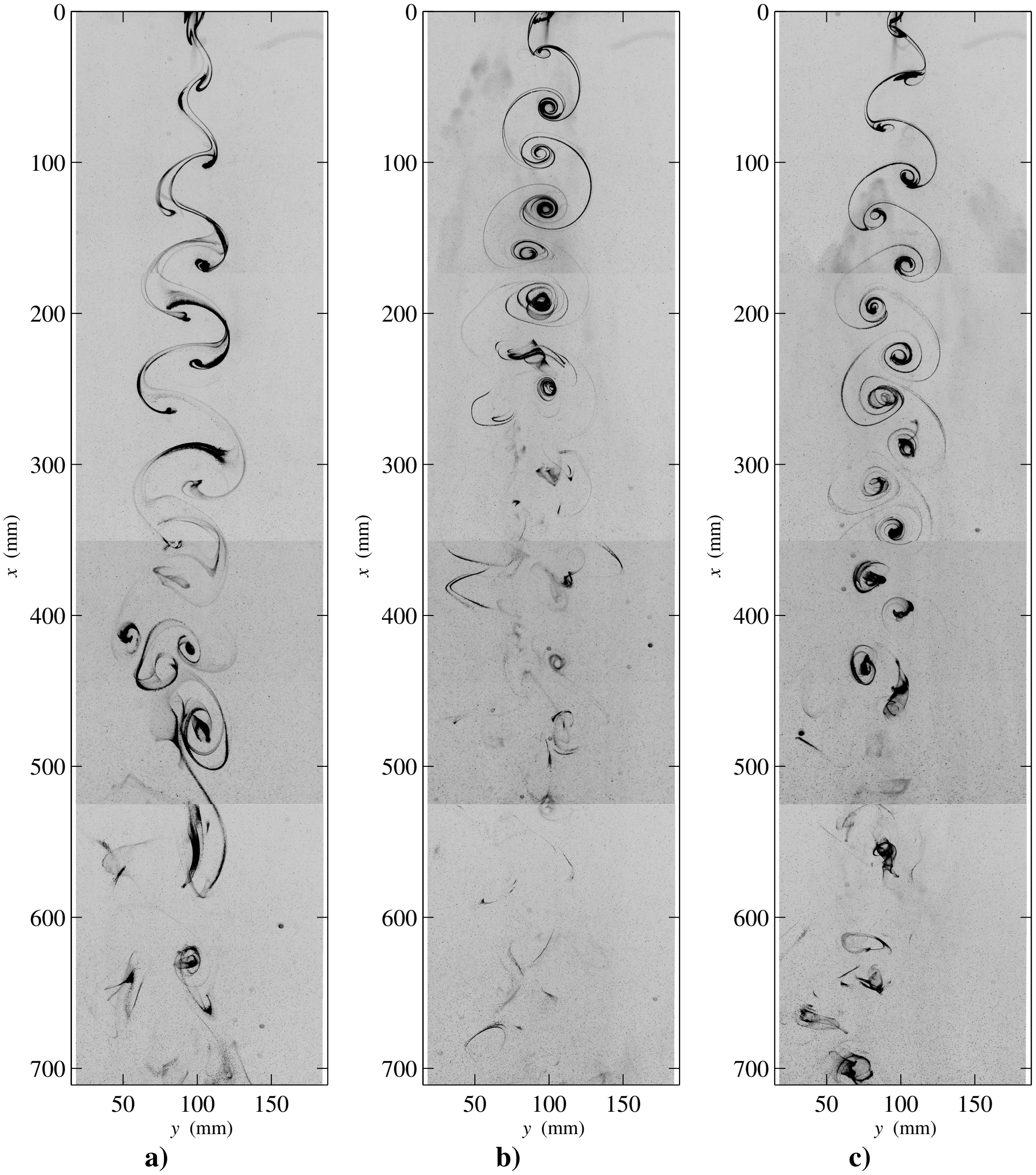

Figure A.3: Instantaneous Streaklines for a) frequency of 1.5 rad/s and amplitude of 1degrees, b) frequency of 1.5 rad/s and amplitude of 6degrees and c) frequency of 1.6 rad/s and amplitude of 4degrees

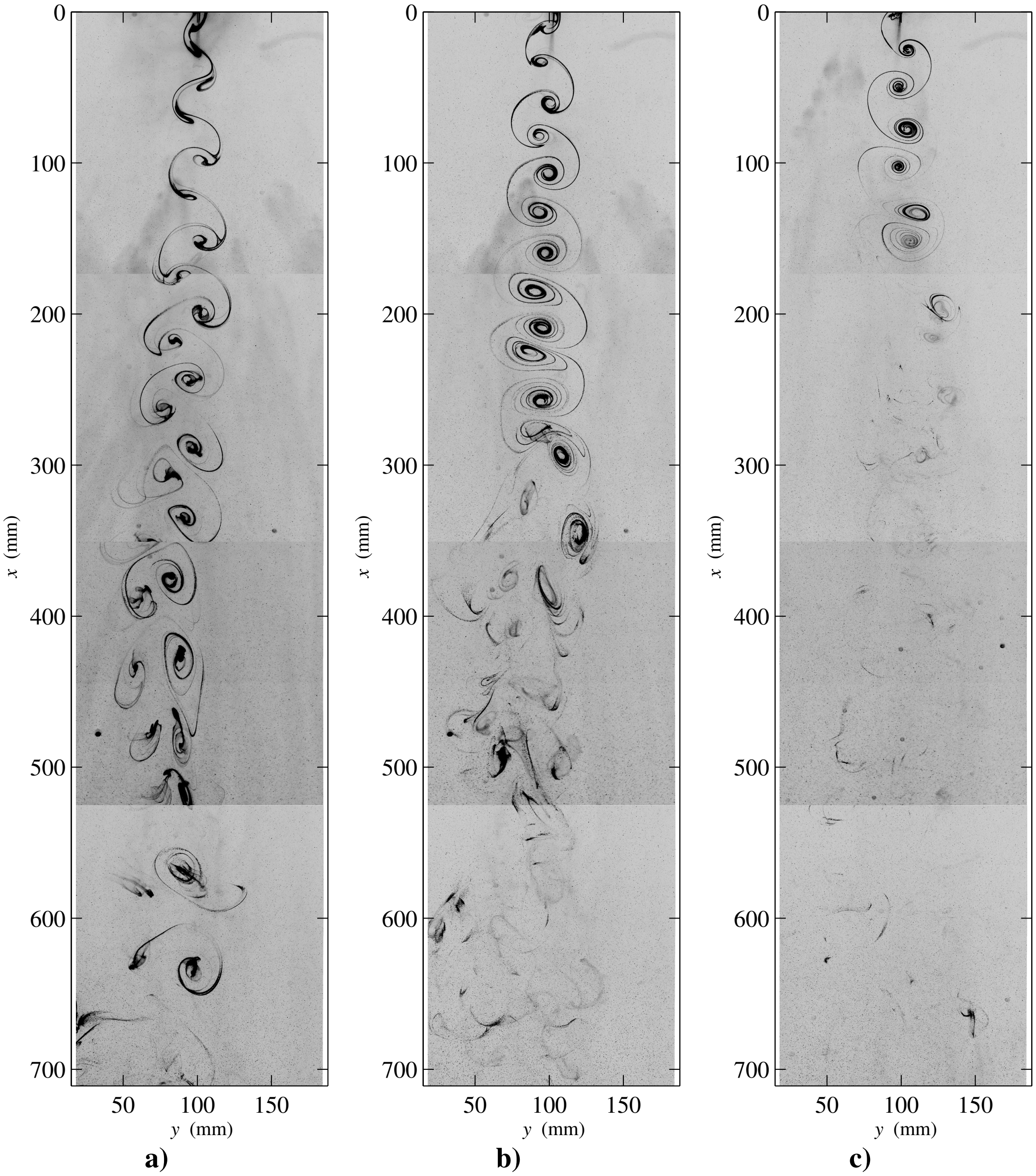

Figure A.4: Instantaneous Streaklines for a) frequency of 2 rad/s and amplitude of 2 degrees, b) frequency of 2 rad/s and amplitude of 4degrees and c) frequency of 2 rad/s and amplitude of 6degrees

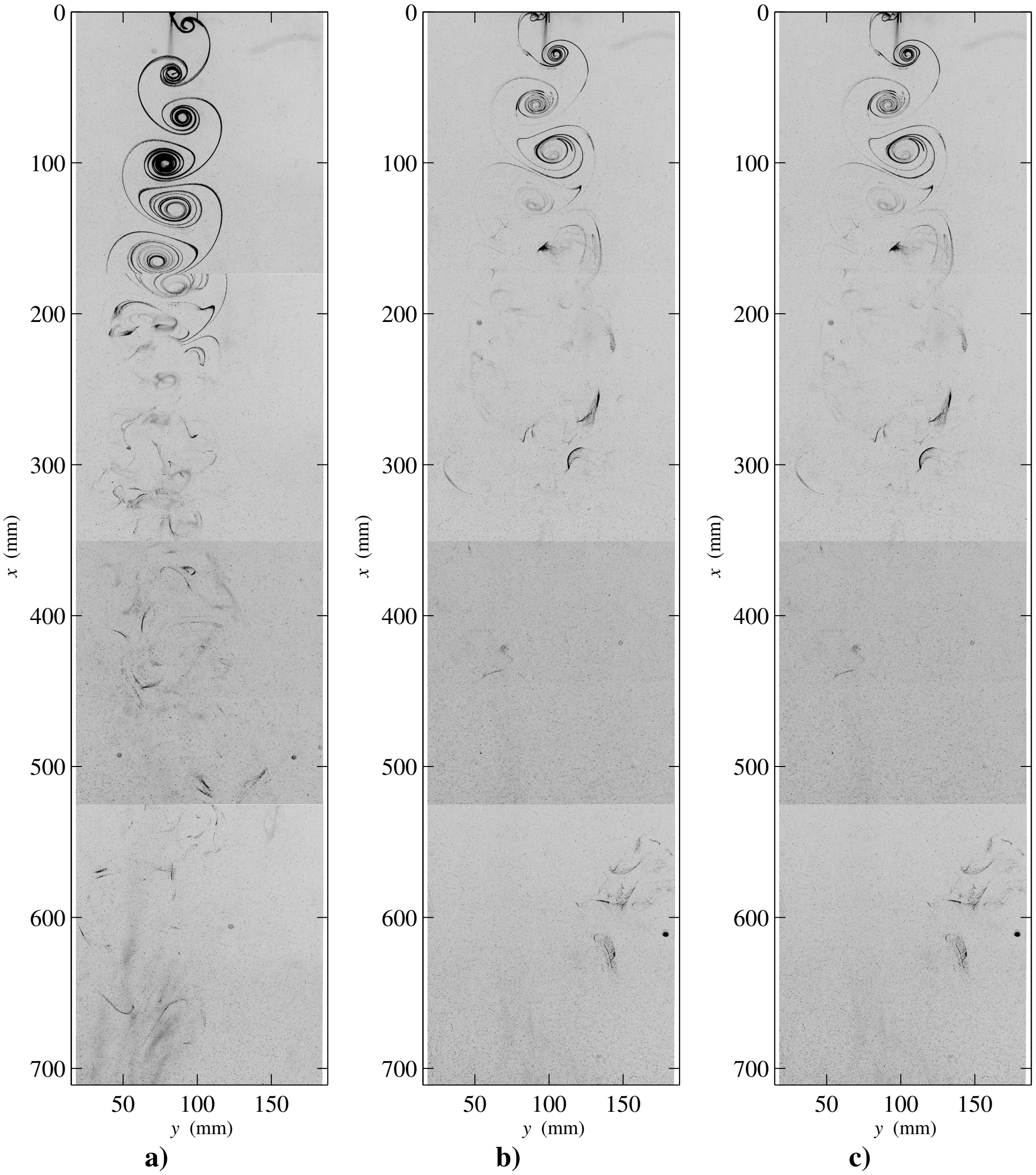

Figure A.5: Instantaneous Streaklines for a) frequency of 2 rad/s and amplitude of 7degrees, b) frequency of 2 rad/s and amplitude of 10 degrees and c) frequency of 2 rad/s and amplitude of 2degrees

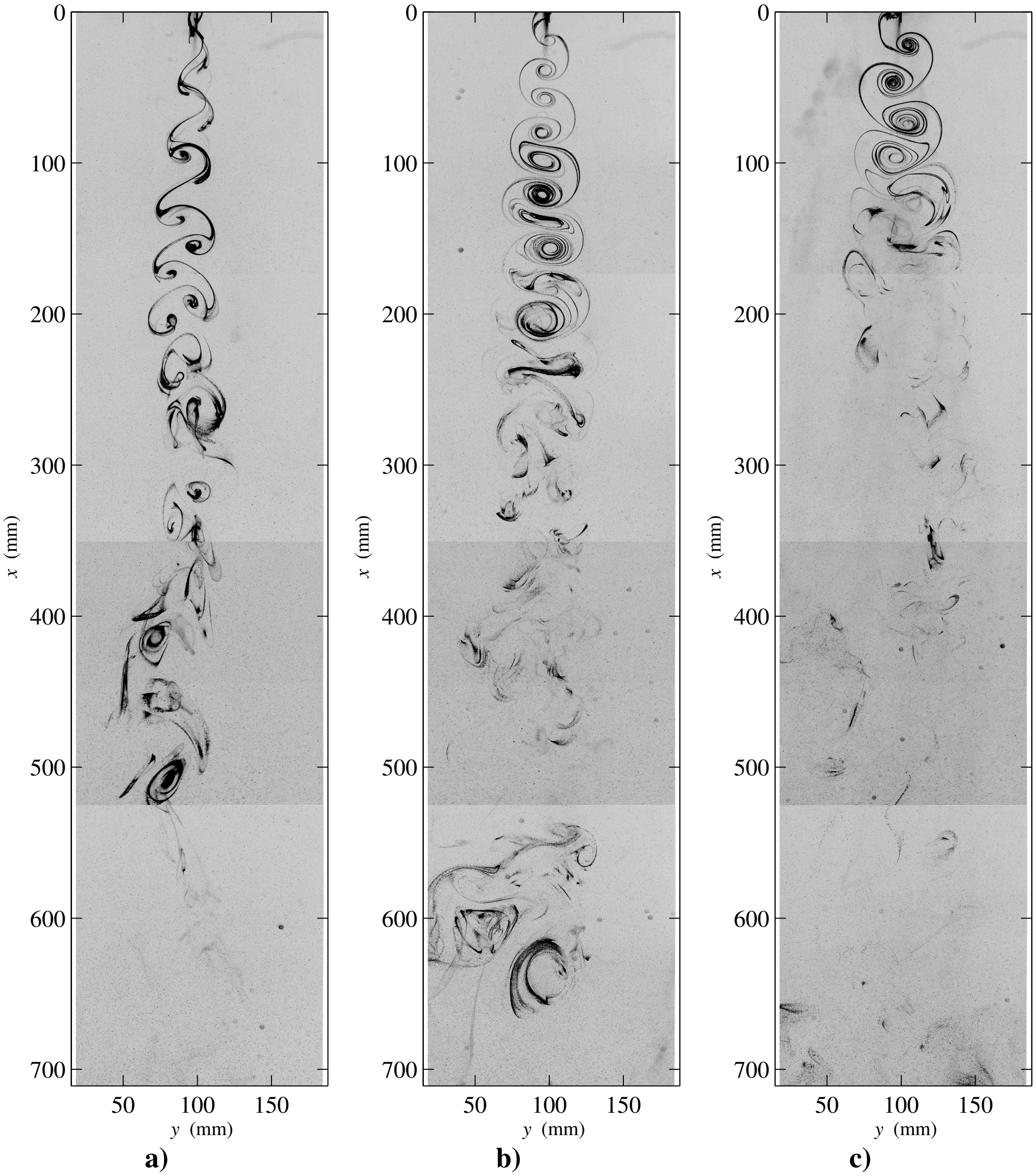

Figure A.6: Instantaneous Streaklines for a) frequency of 2.2 rad/s and amplitude of 1degree, b) frequency of 2.5 rad/s and amplitude of 4degrees and c) frequency of 2.7 rad/s and amplitude of 7 degrees

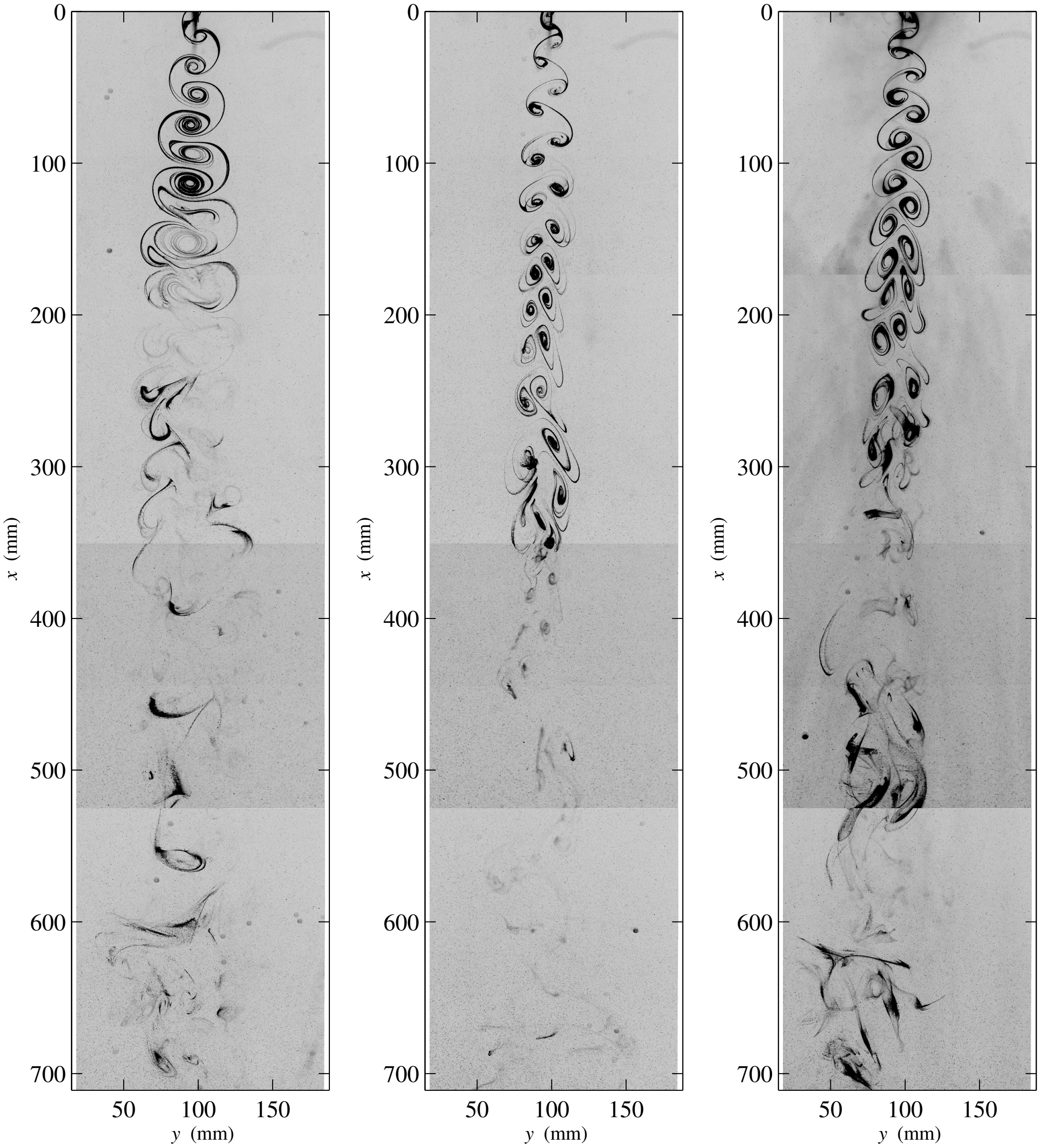

a) b) c)

Figure A.7: Instantaneous Streaklines for a) frequency of 2.8 rad/s and amplitude of 4degrees, b) frequency of 3 rad/s and amplitude of 1degree and c) frequency of 3 rad/s and amplitude of 2degrees

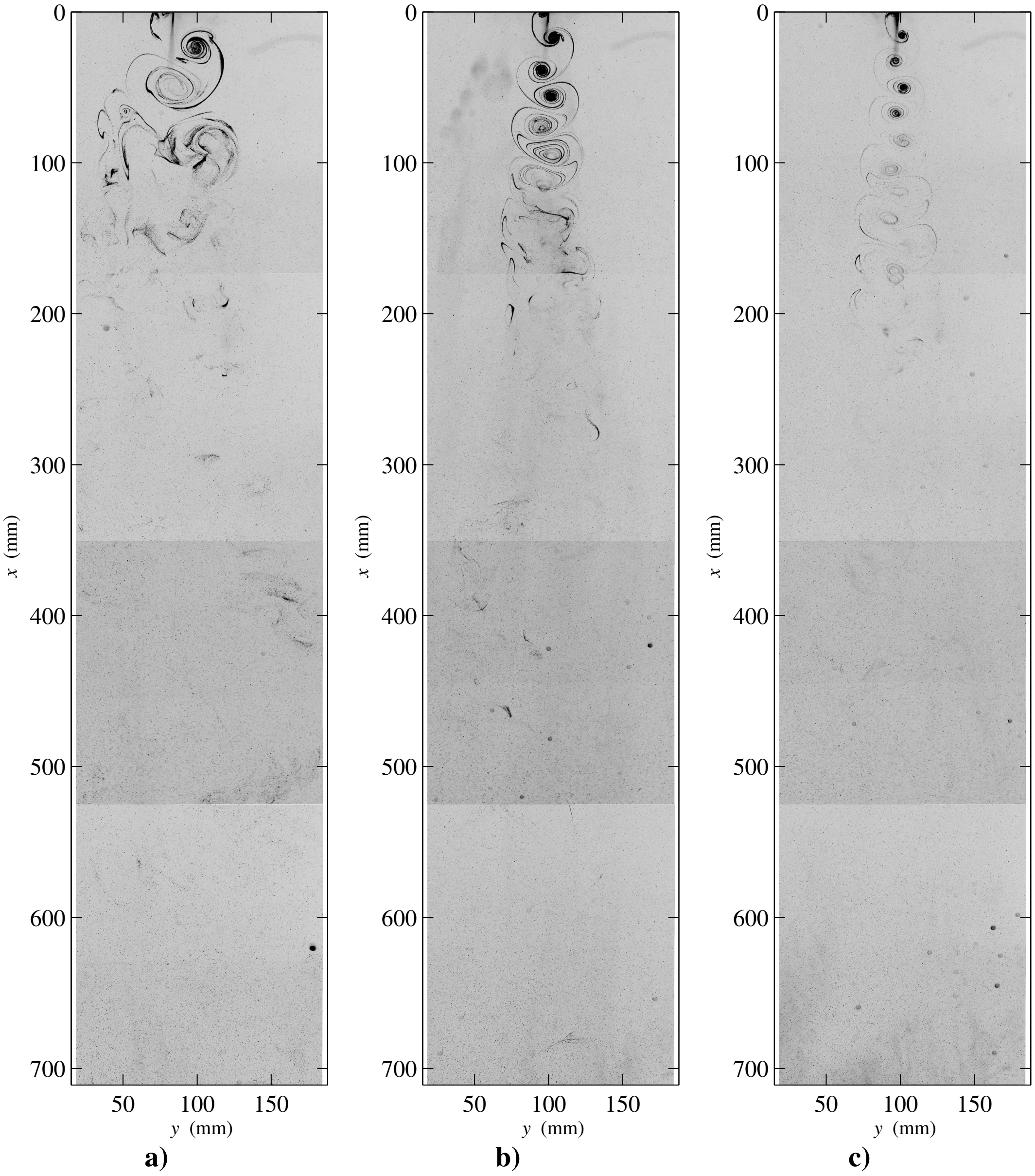

Figure A.8: Instantaneous Streaklines for a) frequency of 3 rad/s and amplitude of 10degrees, b) frequency of 3.3 rad/s and amplitude of 5degrees and c) frequency of 3.4 rad/s and amplitude of 4 degrees

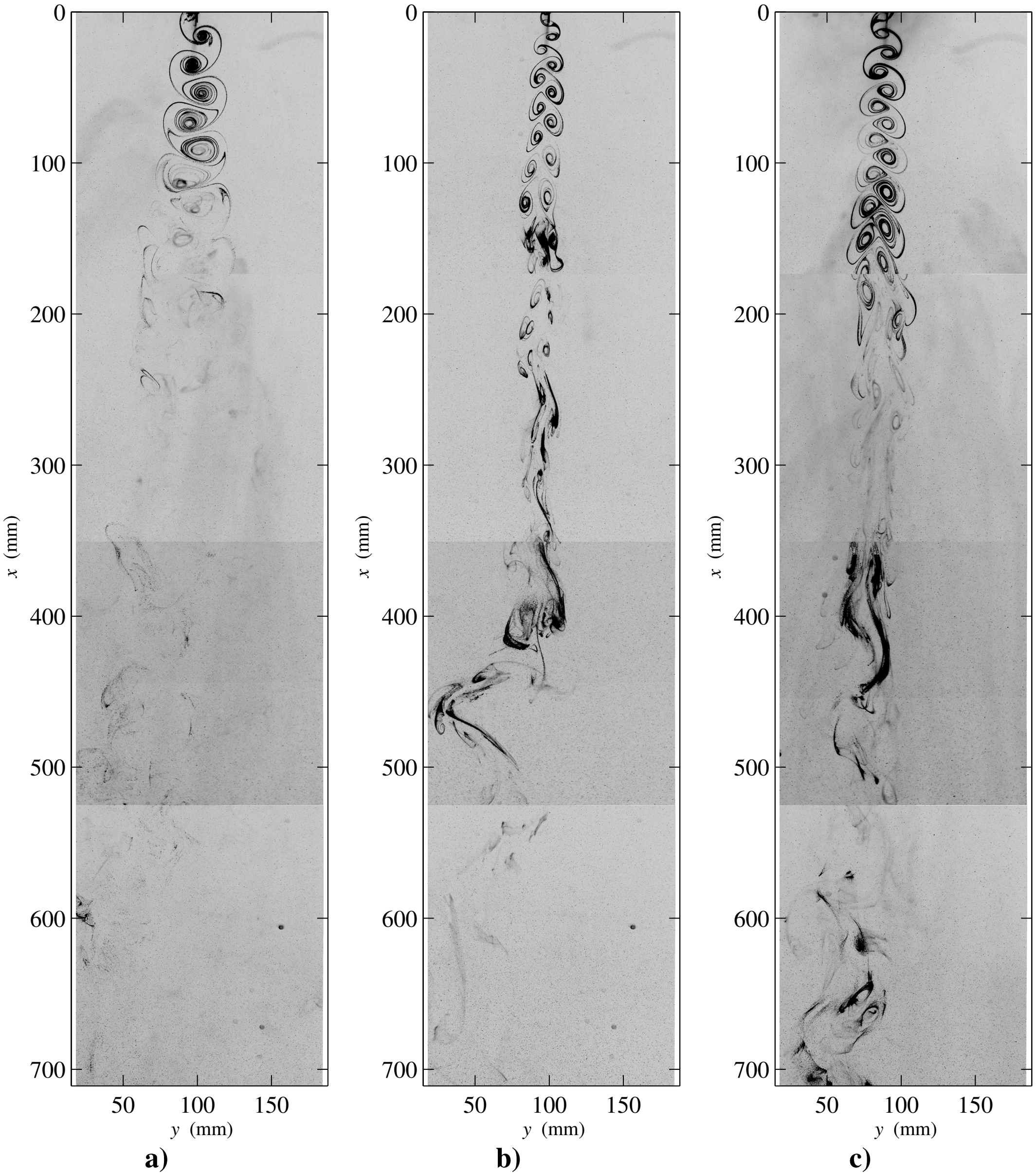

Figure A.9: Instantaneous Streaklines for a) frequency of 3.5 rad/s and amplitude of 5 degrees, b) frequency of 4 rad/s and amplitude of 1degree and c) frequency of 4 rad/s and amplitude of 2degrees

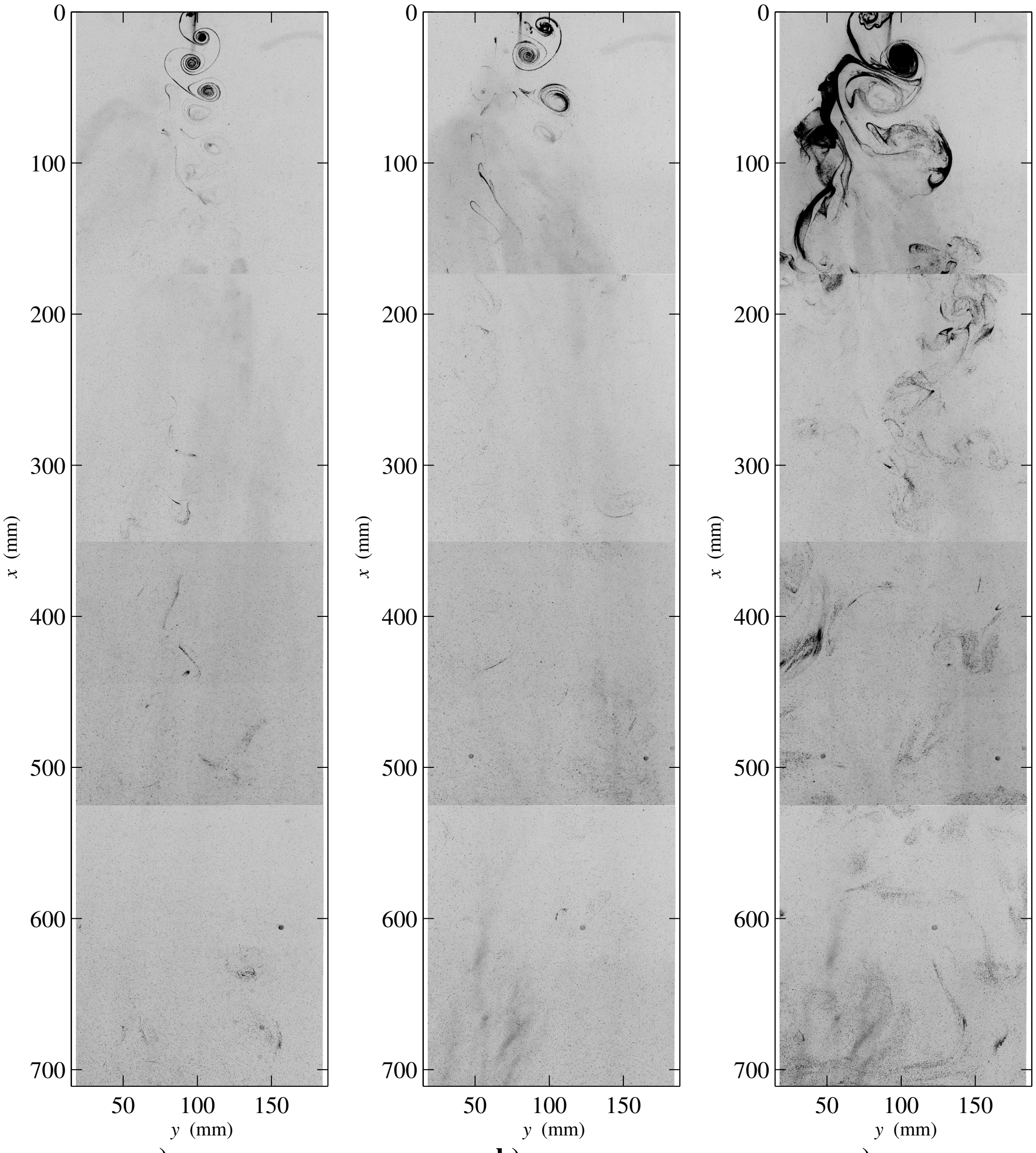

a) b) c)

Figure A.10: Instantaneous Streaklines for a) frequency of 4 rad/s and amplitude of 5 degrees, b) frequency of 4 rad/s and amplitude of 7 degrees and c) frequency of 4 rad/s and amplitude of 10 degrees

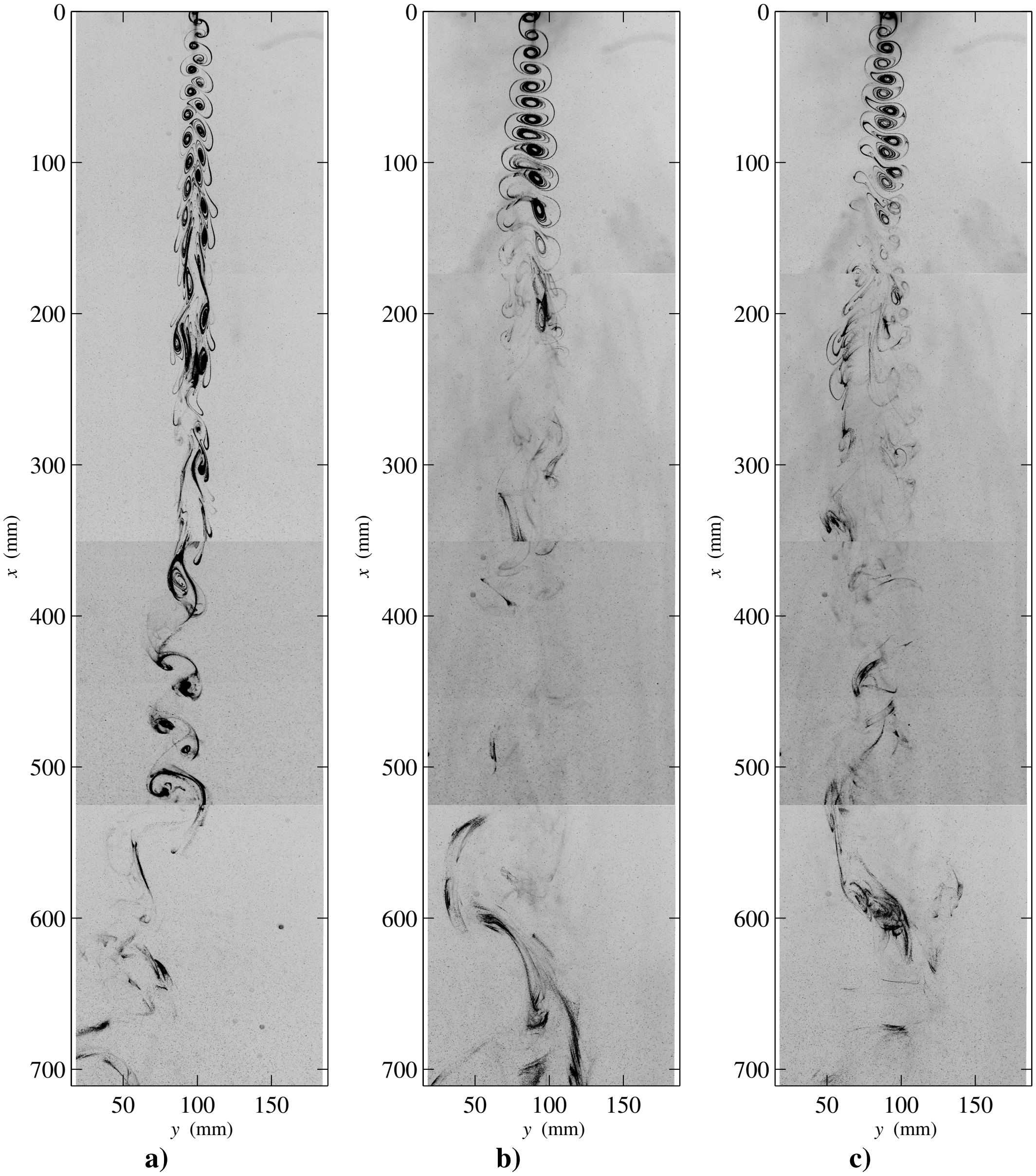

Figure A.11: Instantaneous Streaklines for a) frequency of 5rad/s and amplitude of 1 degree, b) frequency of 5 rad/s and amplitude of 2 degrees and c) frequency of 5.5 rad/s and amplitude of 2degrees

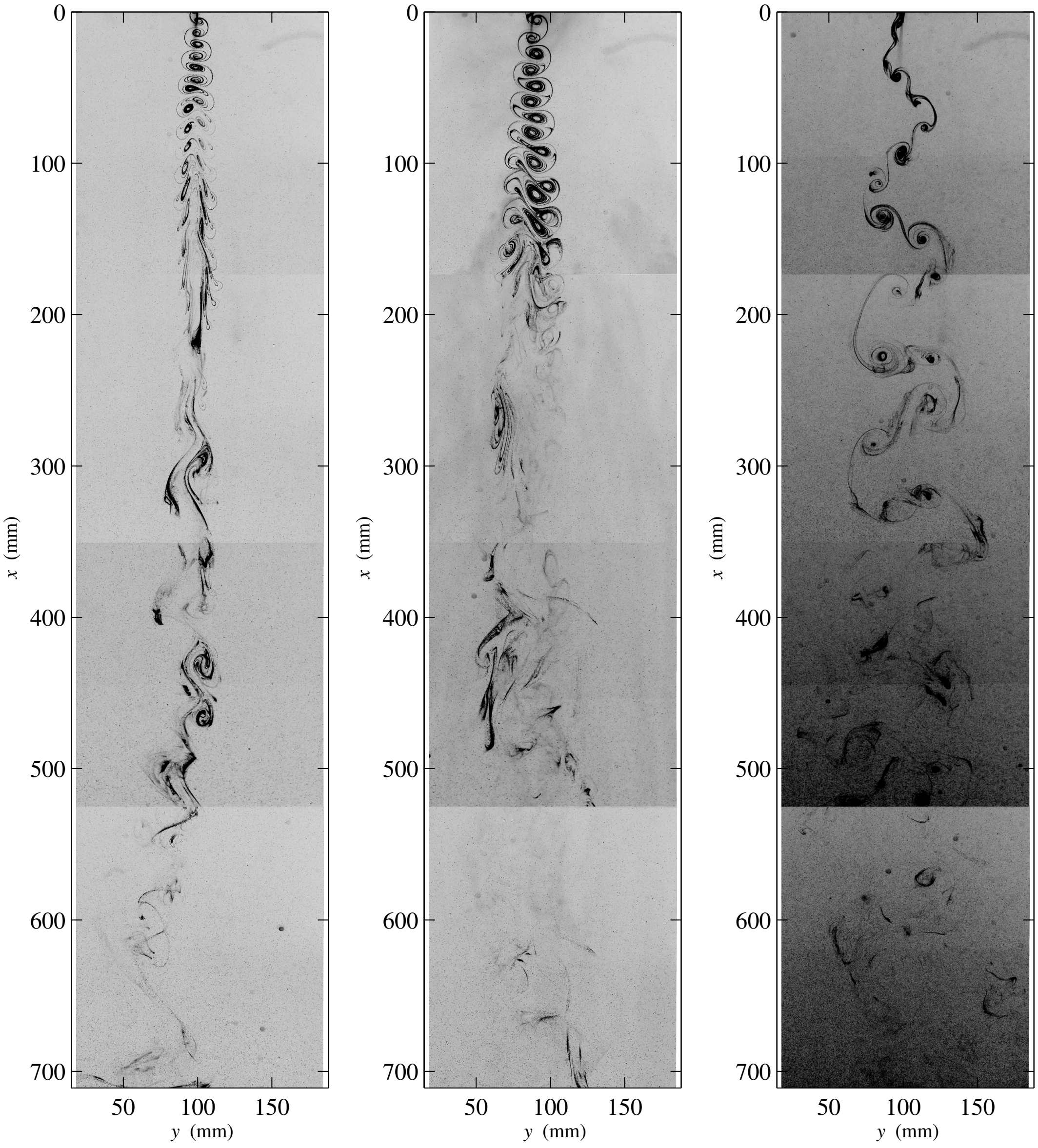

a) **b)** **c)**

Figure A.12: Instantaneous Streaklines for a) frequency of 6 rad/s and amplitude of 1 degree, b) frequency of 6 rad/s and amplitude of 2 degrees and c) frequency of 8 rad/s and amplitude of 4degrees

APPENDIX B: Wake model calculations

The calculations involved in developing an analytical model describing the temporal evolution of peak vorticity for a single vortex is shown below. The 2D vorticity transport equation in cylindrical coordinates assuming incompressible fluid with no concentrated torques or line forces is expressed by:

$$\frac{\partial \omega_z}{\partial t} = \omega_z \frac{\partial w}{\partial z} + \nu \left(\frac{\partial^2 \omega_z}{\partial r^2} + \frac{1}{r} \frac{\partial \omega_z}{\partial r} \right) \tag{B.1}$$

Assuming an axisymmetric vortex with a circular core-region and a Gaussian vorticity distribution described by:

$$\omega(r) = \omega_{peak} \exp\left(-\frac{r^2}{r_c^2} \right) \tag{B.2}$$

Substitution of *eqn.* (B.1) into *eqn.* (B.2) gives:

$$\begin{aligned} \frac{\partial \omega}{\partial t} &= \omega_{peak} \exp\left(-\frac{r^2}{r_c^2} \right) \frac{\partial w}{\partial z} \\ &\quad + \omega_{peak} \nu \left(\frac{\partial^2 \left(e^{-\frac{r^2}{r_c^2}} \right)}{\partial r^2} + \frac{1}{r} \frac{\partial \left(e^{-\frac{r^2}{r_c^2}} \right)}{\partial r} \right) \end{aligned} \tag{B.3}$$

Solving the partial derivatives in the second term on the RHS of *eqn.* (B.3) gives:

$$\begin{aligned} \frac{\partial \omega}{\partial t} &= \omega_{peak} \exp\left(-\frac{r^2}{r_c^2} \right) \frac{\partial w}{\partial z} \\ &\quad + \frac{4\omega_{peak} \nu}{r_c^2} \exp\left(-\frac{r^2}{r_c^2} \right) \left(\frac{r^2}{r_c^2} - 1 \right) \end{aligned} \tag{B.4}$$

Considering $\omega_{peak}(t)$ rather than $\omega(r,t)$ where for a Gaussian vorticity distribution ω_{peak} coincides with $r = 0$. Making the substitution $r = 0$ into *eqn.* (B.4) gives rise to the following expression for the time evolution of peak vorticity:

$$\frac{\partial \omega_{peak}}{\partial t} = \omega_{peak} \exp(0) \frac{\partial w}{\partial z} + \frac{4\omega_{peak}\nu}{r_c^2} \exp(0)\,(0-1)$$

$$\frac{\partial \omega_{peak}}{\partial t} = \omega_{peak} \frac{\partial w}{\partial z} - \frac{4\omega_{peak}\nu}{r_c^2} \qquad \text{(B.5)}$$

The core-region circulation Γ in a vortex over the surface *s* which is the area defining the core-region of the vortex is expressed as:

$$\Gamma = \iint_s \left(\vec{\nabla} \times \vec{v}\right) ds \qquad \text{(B.6)}$$

Where $\vec{v}$ is the 2D velocity field characterizing the vortex and its surroundings and $\vec{\nabla}$ is the gradient operator. Assuming an axisymmetric Gaussian vorticity distribution *eqn.* (B.6) can also be expressed as:

$$\Gamma = \int_0^{2\pi} \int_0^{r_c} \omega_{peak} \exp\left(-\frac{r^2}{r_c^2}\right) r dr d\theta \qquad \text{(B.7)}$$

Solving the outer integral in *eqn.* (B.7)and rearranging:

$$\Gamma = -2\pi\omega_{peak} \int_0^{r_c} r\exp\left(-\frac{r^2}{r_c^2}\right) dr \qquad \text{(B.8)}$$

Solving the remaining integral in *eqn.* (B.8) and rearranging:

$$\Gamma = -2\pi\omega_{peak} \left| -\frac{1}{2} r_c^2 \exp\left(-\frac{r^2}{r_c^2}\right) \right|_{r=0}^{r=r_c} \qquad \text{(B.9)}$$

Applying the bounds of integration *eqn.* (B.9) becomes:

$$\Gamma = -2\pi\omega_{peak}\left[-\frac{1}{2}r_c^2(\exp(0) - \exp(-1))\right] \\ = \pi\omega_{peak}r_c^2(1 - e^{-1}) \tag{B.10}$$

Rearranging and solving for r_c^2:

$$r_c^2 = \frac{\Gamma}{\pi\omega_{\text{peak}}(1 - \text{e}^{-1})} \tag{B.11}$$

Assuming constant circulation with time, $\Gamma = \Gamma_\text{o}$ and substitution of *eqn.* (B.11) into *eqn.*(B.5), gives:

$$\frac{\partial\omega_{peak}}{\partial t} = \omega_{peak}\frac{\partial w}{\partial z} - \frac{4\omega_{peak}\nu\pi\omega_{\text{peak}}(1 - \text{e}^{-1})}{\Gamma_\text{o}} \tag{B.12}$$

Rearranging *eqn.* (B.12) gives:

$$\frac{\partial\omega_{peak}}{\partial t} = \omega_{peak}\left(\frac{\partial w}{\partial z}\right) - \omega_{peak}^2\left(\frac{4\pi\nu}{\Gamma_\text{o}}\right)(1 - e^{-1}) \tag{B.13}$$

Treat $\partial w/\partial z$ and $\left(\frac{4\pi\nu}{\Gamma_\text{o}}\right)(1 - e^{-1})$ as constants so that $\beta = \partial w/\partial z$ and $K = \left(\frac{4\pi\nu}{\Gamma_\text{o}}\right)(1 - e^{-1})$ and substitute into *eqn.* (B.13):

$$\frac{\partial\omega_{peak}}{\partial t} = \beta\omega_{peak} - K\omega_{peak}^2 \tag{B.14}$$

Use separation of variables to obtain a solution to *eqn.* (B.14) by first rearranging then integrating both sides:

$$\int \frac{\partial \omega_{peak}}{\beta \omega_{peak} - K\omega_{peak}^2} = \int \partial t \tag{B.15}$$

To solve the integral requires performing partial fraction reduction of the term inside the integration on the LHS of *eqn.* (B.15) as follows:

$$\begin{aligned} \frac{1}{\beta \omega_{peak} - K\omega_{peak}^2} &= \frac{1}{\omega_{peak}\left(\beta - K\omega_{peak}\right)} \\ &= \frac{A}{\omega_{peak}} + \frac{B}{\beta - K\omega_{peak}} \end{aligned} \tag{B.16}$$

Such that:

$$1 = A\left(\beta - K\omega_{peak}\right) + B\omega_{peak} \tag{B.17}$$

if $\omega_{peak} = 0$ then $A = 1/\beta$ and if $\omega_{peak} = \beta/K$ then $B = K/\beta$ and *eqn.* (B.16) becomes:

$$\frac{1}{\beta \omega_{peak} - K\omega_{peak}^2} = \frac{1}{\beta \omega_{peak}} + \frac{K}{\beta\left(\beta - K\omega_{peak}\right)} \tag{B.18}$$

Substitution of *eqn.* (B.18) into *eqn.* (B.15) gives:

$$\int \frac{\partial \omega_{peak}}{\beta \omega_{peak}} + \int \frac{K \partial \omega_{peak}}{\beta\left(\beta - K\omega_{peak}\right)} = \int \partial t \tag{B.19}$$

Making the substitutions:

$$\Omega = \beta - K\omega_{peak} \tag{B.20}$$

and

$$\partial \omega_{peak} = \frac{\partial \Omega}{-K} \tag{B.21}$$

into the second term on the LHS of *eqn.* (B.19) and performing the integration gives:

$$\frac{\ln(\omega_{peak})}{\beta} - \frac{\ln(\Omega)}{\beta} = t + C \qquad \text{(B.22)}$$

where C is a constant of integration. Then, substituting *eqn.* (B.20) into *eqn.* (B.22) and rearranging gives:

$$\ln(\omega_{peak}) - \ln(\beta - K\omega_{peak}) = \beta(t + C) \qquad \text{(B.23)}$$

After simplifying the logarithmic expression, redefining the constant C and some more rearrangement, *eqn.* (B.23) becomes:

$$\beta t + C = \ln\left(\frac{\omega_{peak}}{\beta - K\omega_{peak}}\right) \qquad \text{(B.24)}$$

Taking the exponent of each side of *eqn.* (B.24), redefining the constant C then rearranging to solve for ω_{peak} gives:

$$Ce^{\beta t} = \frac{\omega_{peak}}{\beta - K\omega_{peak}}$$

$$\beta - K\omega_{peak} = \omega_{peak}Ce^{-\beta t}$$

$$\beta = \omega_{peak}(Ce^{-\beta t} + K)$$

$$\omega_{peak} = \frac{\beta}{(Ce^{-\beta t} + K)}$$

$$\omega_{peak}(t) = \frac{\beta e^{\beta t}}{Ke^{\beta t} - C} \qquad \text{(B.25)}$$

The constant of integration C is found by substituting $\omega_{peak}(0) = \omega_o$ into *eqn.* (B.25) to give:

$$C = K - \beta/\omega_o \tag{B.26}$$

And substitution of *eqn.* (B.26) back into *eqn.* (B.25) gives:

$$\omega_{peak}(t) = \frac{\beta e^{\beta t}}{K e^{\beta t} - K + \left(\frac{\beta}{\omega_o}\right)} \tag{B.27}$$

APPENDIX C: Matlab Code

The code used for data analysis and for generating figures in this thesis is summarized in Table C.1. The table shows the filename along with an abbreviated codename (CC1-CC9). The chapter(s) where the code is used is listed. Finally, the required toolboxes along with any nested functions are listed.

Table C.1: Matlab code summary and description

Filename	Relevant Chapters	Nested Functions & required toolboxes	Description
Vortex_detection_CSLv4_noplot.m (CC1)	2,3	- pivmat toolbox - circle.m	Performs image stitching on 4 individual velocity vector fields as described in chapter 2. Then executes vortex detection and characterization as described in chapter 3 on the global stitched field
Vortex_detection_CSLv5_simulation.m (CC2)	3	- pivmat toolbox - circle.m	Creates a velocity vector field with an axisymmetric Burgers vortex at the centre generated from potential flow theory. Velocity vector white noise can be added to the flow field and the grid resolution can be changed. Vortex detection and characterization as described in chapter 3 is executed
vortex_grid_refinement_simulation.m (CC3)	3	- CC2	Calls on CC2 to generate the plots describing how the core region circulation and radius of the simulated Burgers vortex change with grid resolution and velocity vector white noise.
wake_snapshot.m (CC4)	4		Performs image stitching on 4 individual images. These flow visualisation images were used to qualitatively asses the wake type and categorize them for future use in the phase diagram

Phase_diagram.m (CC5)	4	- Phase Diagram3.xlsx	Generates a phase map from the categorized wake images that were created with CC4. (relevant wake parameters and the resulting classification is stored in Phase Diagram3.xlsx). It then fits cubic splines to the data to map out the transition regions.
Vtx_Flowfield_study_nophaseAvg_v3.m (CC6)	4	- Matlab curve fitting toolbox - CC1	Calls on CC1 to generate the vortex evolution plots describing how several parameters change with *x/C*. It fits curves to the experimental data and shows how they compare to the analytical wake evolution model
Vtx_Flowfield_study_nophaseAvg_v4_Tandem.m (CC7)	5	- CC1	Calls on CC1 to compute the total circulation from the leading edge vortices, from the trailing edge vortices and from both as described in chapter 5. It does this on 100 instantaneous tandem airfoil fields per hindfoil phase Φ then outputs the average total circulation and its standard deviation
Tandem_airfoil_phase_sweep_v2.m (CC8)	5	- CC1 - CC7	Calls on CC7 and generates plots describing the change in total circulation (described in chapter 5) for various phases of the hindfoil. It also plots vertical error bars (1 standard deviation in either direction) and plots the total circulation of the single airfoil case for reference.
Vtx_Flowfield_study_mov.m (CC9)	Defense presentation	- CC1	Makes an animation of the vortex wake by creating frames from the instantaneous vorticity field. It also shows the circular boundaries and core centers of detected vortices.